UNIVERSIDADE FEDERAL DE SANTA CATARINA
CAMPUS TRINDADE
POST-GRADUATE PROGRAM OF MATERIALS SCIENCE AND ENGINEERING

INSTITUT NATIONAL DES SCIENCES APPLIQUÉES - LYON

Vivian Inês dos Santos

Development of Alumina-Toughened Zirconia composites reinforced with carbon nanofibers via Direct Ink Writing

Florianópolis
2023

Vivian Inês dos Santos

Development of Alumina-Toughened Zirconia composites reinforced with carbon nanofibers via Direct Ink Writing

Thesis submitted to the Graduate Program in Materials Science and Engineering of the Federal University of Santa Catarina as a partial requirement for the degree of Doctor of Philosophy in Materials Science and Engineering.

Brazilian supervisor: Prof. Márcio Celso Fredel, Dr. Ing.
French supervisor: Prof. Laurent Gremillard, Ph.D.
Brazilian co-supervisor: Prof. Bruno Henriques, Ph.D.

Florianópolis
2023

Inês dos Santos, Vivian
Development of Alumina-Toughened Zirconia composites reinforced with carbon nanofibers via Direct Ink Writing / Vivian Inês dos Santos ; orientador, Márcio Celso Fredel, orientador, Laurent Gremillard, coorientador, Bruno Henriques, 2023.
232 p.

Tese (doutorado) - Universidade Federal de Santa Catarina, Centro Tecnológico, Programa de Pós-Graduação em Ciência e Engenharia de Materiais, Florianópolis, 2023.

Inclui referências.

Trabalho elaborado em regime de co-tutela.
1. Ciência e Engenharia de Materiais. 2. direct ink writing. 3. alumina-toughened zirconia. 4. carbon nanofibers. 5. additive manufacturing. I. Celso Fredel, Márcio. II. Gremillard, Laurent. III. Henriques, Bruno. IV. Universidade Federal de Santa Catarina. Programa de Pós-Graduação em Ciência e Engenharia de Materiais. V. Título.

Vivian Inês dos Santos

Development of Alumina-Toughened Zirconia composites reinforced with carbon nanofibers via Direct Ink Writing

The present work at the Doctorate level was evaluated and approved, on the 1st of November 2023, by the examining board composed of the following members:

MCF-HDR Elodie Prud'homme, Ph.D.
Institut National des Sciences Appliquées - Lyon

Elisângela Guzi de Moraes, Ph.D.
Universidade Federal de Santa Catarina

Prof. Aldo Roberto Boccaccini, Ph.D.
Friedrich-Alexander-Universität Erlangen-Nuremberg

Prof. Sabrina Arcaro, Ph.D.
Universidade do Extremo Sul Catarinense

Prof. Andrés Fabián Lasagni, Ph.D.
Technische Universität Dresden

Prof. Susana Olhero, Ph.D.
Universidade de Aveiro

We certify that this is the original and final version of the conclusion work that was judged suitable for obtaining the title of Ph.D. in Materials Science and Engineering.

ICP-Edu
Documento assinado digitalmente
Joao Batista Rodrigues Neto
Data: 07/12/2023 15:39:48-0300
CPF: ***.810.989-**
Verifique as assinaturas em https://v.ufsc.br

Coordination of the Postgraduate Program

ICP-Edu
Documento assinado digitalmente
Marcio Celso Fredel
Data: 06/12/2023 22:58:27-0300
CPF: ***.706.459-**
Verifique as assinaturas em https://v.ufsc.br

Prof. Márcio Celso Fredel, Dr. Ing.
Brazilian supervisor

Signature numérique de Laurent Gremillard
DN : cn=Laurent Gremillard, o=CNRS, ou=MATEIS, email=laurent.gremillard@insa-lyon.fr, c=FR
Date : 2023.12.07 20:49:14 +01'00'

Prof. Laurent Gremillard, Ph.D.
French supervisor

Florianópolis, 2023

ACKNOWLEDGMENTS

Anyone who tries to do science alone is doing it wrong. Science thrives on collaboration, both in the development of research projects and of the scientist/research itself. This section is dedicated to thanking those who collaborated with one or both of these topics.

Firstly, I would like to thank my family for their unwavering support. Silvio, Odete, Lilian and Billie constitute a fundamental part of my life. Another support pillar encompasses my circle of friends. I consider myself fortunate to have encountered exceptional people in both Brazil and France. Hence, I extend my gratitude to Paula, Roberta, Francesca, Rafael, Thaiane, Júlia, Fabiane, Stephanie, Carolina, Raouhi, Yiping, Marcelo, Milena, Sylvain, Camille, Asli, Alexandre, Carmem, Mathieu, Timothée, Junxiong, Xavi, Romain, Arthur, Thomas, Léonore and Antoine. Your presence has lightened up my days and, in true friendship fashion, exacerbated the hangovers.

Furthermore, my acknowledgments extend to my supervisors for affording me this opportunity, particularly Prof. Laurent. Some people enter our lives and evolve into wellsprings of inspiration – such is the role that Prof. Laurent has assumed in mine. Within Mateis Lab, any student queried would attest to his extraordinary mentoring skills. His consistent accessibility for brainstorming sessions, along with his provision of constructive feedback, all steeped in an enduring light-heartedness and genuine concern for his students, continue to astonish me. Prof. Laurent, rest assured that this will guide me in my future student mentoring endeavors; thank you for everything.

I would like to conclude these acknowledgements by expressing my gratitude for the funding of this study provided by the Higher Education Personnel Improvement Coordination (CAPES/Brazil), under the CAPES/COFECUB program (process number 88881.665101/2022-01 (Ph936/19)).

I am always at the beginning.

- The Buddha

RESUMO

Há uma demanda crescente por materiais cerâmicos personalizados com formas e propriedades cada vez mais complexas para aplicações de engenharia biomédica, que não podem ser obtidos por meio de técnicas tradicionais de processamento de cerâmica. Nos últimos anos, tem-se dado cada vez mais atenção aos materiais à base de cerâmica produzidos por um método de manufatura aditiva comumente chamado de DIW (*direct ink writing*) ou Robocasting. No entanto, o desafio atual das cerâmicas produzidas por DIW continua sendo a obtenção de uma boa confiabilidade mecânica. Portanto, no primeiro capítulo, esta tese examina o cenário geral do campo de DIW, destacando e analisando os principais resultados dos estudos disponíveis na literatura. Ela também descreve e discute as abordagens mais inovadoras, bem como as estratégias de aprimoramento mecânico e biológico do método DIW. O segundo capítulo da tese apresenta uma caracterização abrangente de pastas compostas por um pó de zircônia tenacificada por alumina (ATZ, 84 vol% Ce-TZP, 8% Al_2O_3, 8% $SrAl_{12}O_{19}$), um defloculante, um ligante, água deionizada e, em alguns casos, nanofibras de carbono (CNFs). O comportamento reológico e as propriedades fundamentais dessas pastas foram determinados e foram realizados testes de capacidade de impressão. Os resultados foram comparados aos critérios/parâmetros de printabilidade estabelecidos e descritos na literatura existente (ϕ, K e FTI). Esses critérios foram considerados adequados para avaliar a capacidade de impressão, embora tenham apresentado algumas limitações na previsão de algumas pastas não imprimíveis. Além disso, foi introduzido um novo critério baseado na taxa de recuperação do módulo de armazenamento, com o potencial de prever a capacidade de impressão com um único teste. O terceiro e último capítulo da tese concentrou-se na fabricação por DIW de filamentos do mesmo compósito de ATZ com e sem CNFs, com o objetivo de aprimorar as propriedades mecânicas por meio de processos cuidadosos de remoção de ligante (*debinding*) e sinterização, bem como a orientação dos CNFs. Foram usados bicos de impressão com diâmetros na faixa de 200 a 840 μm e foram determinadas as condições ideais de *debinding* e sinterização, usando os métodos de sinterização convencional (CS) e *spark plasma sintering* (SPS). A avaliação mecânica dos filamentos incluiu a determinação da tensão de fratura (resistência à flexão), da deformaão de fratura, do módulo de Young e da confiabilidade mecânica (módulo de Weibull). A adição de CNFs, que deveria melhorar as propriedades mecânicas, prejudicou a maioria delas devido à aglomeração desse material. A impressão com bicos menores mostrou melhorias no módulo de Young dos filamentos, com os filamentos de ATZ sinterizados por CS exibindo plasticidade induzida por transformação (TRIP), enquanto os sinterizados por SPS não apresentaram TRIP. As propriedades mecânicas obtidas foram comparáveis ou superiores àquelas obtidas por meio de técnicas convencionais de processamento de cerâmica, como *cold isostatic pressing* e *slip casting*. Da mesma forma, foi obtido um bom nível de confiabilidade mecânica.

Palavras-chave: *direct ink writing*; cerâmica; biomateriais; manufatura aditiva; zircônia tenacificada por alumina; nanofibras de carbono; confiabilidade mecânica.

ABSTRACT

There is a growing demand for personalized ceramic materials with increasingly complex shapes and properties for biomedical engineering applications, which cannot be achieved via traditional ceramic processing techniques. In recent years, increasing attention has been drawn to ceramic-based materials produced by an additive manufacturing method commonly referred to as direct ink writing (DIW) or Robocasting. However, the current challenge of DIW-produced ceramics remains the achievement of strong mechanical reliability. Hence, in the first chapter, this thesis examines the overall scenario of the DIW field, highlighting and analyzing the primary outcomes of studies available in the literature. It also describes and discusses the most innovative approaches, as well as mechanical and biological improvement strategies for the DIW method. The second chapter of the thesis provides a comprehensive characterization of pastes consisting of an alumina-toughened zirconia (ATZ, 84 vol% Ce-TZP, 8% Al_2O_3, 8% $SrAl_{12}O_{19}$) powder, a deflocculant, a binder, deionized water and, in some cases, carbon nanofibers (CNFs). The rheological behavior and fundamental properties of these pastes were determined and printability tests were conducted. The results were compared to established printability criteria/parameters outlined in existing literature (ϕ, K and FTI). These criteria were found to be suitable for assessing printability, although they presented some limitations in predicting some unprintable pastes. Furthermore, a new criterion based on the recovery rate of the storage modulus was introduced, with the potential to predict printability with a single test. The third and last chapter of the thesis focused on the DIW fabrication of filaments of the same ATZ composite with and without CNFs with the objective of enhancing the mechanical properties by careful debinding and sintering processes, as well as the orientation of the CNFs. Nozzle diameters in the range of 200-840 μm were used and optimal debinding and sintering conditions were determined, using both Conventional Sintering (CS) and Spark Plasma Sintering (SPS) methods. The mechanical evaluation of the filaments included the determination of the fracture stress (flexural strength), fracture strain, Young's modulus and mechanical reliability (Weibull modulus). The addition of the CNFs, expected to improve the mechanical properties, hindered most of them because of CNF agglomeration. Printing with smaller nozzles showed improvements in the Young's modulus of the filaments, with ATZ filaments sintered by CS exhibiting transformation-induced plasticity (TRIP), while those sintered by SPS did not. The mechanical properties obtained were comparable to or higher than those achieved through conventional ceramic processing techniques like cold isostatic pressing and slip casting. Similarly, a good level of mechanical reliability was achieved.

Keywords: direct ink writing; ceramics; biomaterials; additive manufacturing; alumina-toughened zirconia; carbon nanofibers; mechanical reliability.

RÉSUMÉ

Il y a une demande croissante de matériaux céramiques personnalisés présentant des formes et des propriétés de plus en plus complexes pour des applications d'ingénierie biomédicale, qui ne peuvent être obtenues par les techniques traditionnelles de traitement de la céramique. Ces dernières années, une attention croissante a été portée aux matériaux à base de céramique produits par une méthode de fabrication additive communément appelée *direct ink writing* (DIW) ou Robocasting. Cependant, le défi actuel des céramiques produites par DIW reste l'obtention d'une grande fiabilité mécanique. Donc, dans le premier chapitre, cette thèse examine le scénario global du domaine de *direct ink writing*, en soulignant et en analysant les principaux résultats des études disponibles dans la littérature. Il décrit et discute également les approches les plus innovantes, ainsi que les stratégies d'amélioration mécanique et biologique de la méthode DIW. Le deuxième chapitre de la thèse présente une caractérisation complète des pâtes composées d'une poudre de zircone renforcée à l'alumine (ATZ, 84 % vol. de Ce-TZP, 8 % Al_2O_3, 8 % $SrAl_{12}O_{19}$), d'un défloculant, d'un liant, d'eau désionisée et, dans certains cas, de nanofibres de carbone (CNF). Le comportement rhéologique et les propriétés fondamentales de ces pâtes ont été déterminés et des tests d'imprimabilité ont été réalisés. Les résultats ont été comparés aux critères/paramètres d'imprimabilité établis dans la littérature existante (ϕ, K et FTI). Ces critères se sont avérés adaptés à l'évaluation de l'imprimabilité, bien qu'ils présentent certaines limites dans la prédiction de certaines pâtes non imprimables. En outre, un nouveau critère basé sur le taux de récupération du module de stockage a été introduit, avec le potentiel de prédire l'imprimabilité avec un seul test. Le troisième et dernier chapitre de la thèse s'est concentré sur la fabrication par DIW de filaments du même composite ATZ avec et sans CNF, dans le but d'améliorer les propriétés mécaniques par des processus de déliantage et de frittage minutieux, ainsi que l'orientation des CNF. Des diamètres de buse compris entre 200 et 840 µm ont été utilisés et des conditions optimales de déliantage et de frittage ont été déterminées, en utilisant les méthodes de frittage conventionnel (CS) et de *spark plasma sintering* (SPS). L'évaluation mécanique des filaments comprenait la détermination de la contrainte de rupture (résistance à la flexion), de la déformation de rupture, du module de Young et de la fiabilité mécanique (module de Weibull). L'ajout de CNF, censé améliorer les propriétés mécaniques, a entravé la plupart d'entre elles en raison de l'agglomération des CNF. L'impression avec des buses plus petites a permis d'améliorer le module d'Young des filaments, les filaments ATZ frittés par CS présentant une plasticité induite par la transformation (TRIP), alors que ceux frittés par SPS n'en présentaient pas. Les propriétés mécaniques obtenues étaient comparables ou supérieures à celles obtenues par les techniques conventionnelles de traitement des céramiques, telles que le *cold isostatic pressing* et le *slip casting*. De même, un bon niveau de fiabilité mécanique a été atteint.

Mots clés : *direct ink writing* ; céramiques ; biomatériaux ; fabrication additive ; zircone renforcée à l'alumine ; nanofibres de carbone ; fiabilité mécanique.

LIST OF ABBREVIATIONS AND ACRONYMS

γ	Surface tension of the suspension
γ_f	Shear strain at the flow point
γ_y	Shear strain at the yield point
$\dot{\gamma}$	Shear rate
$\dot{\gamma}_{max}$	Maximum shear rate
$\varepsilon_{fracture}$	Fracture strain
$\varepsilon_{non\text{-}linear}$	Non-linear strain
ε_{yield}	Yield strain
ε-CL	ε-caprolactone
η	Viscosity
η_{medium}	Viscosity of the medium of the paste
η_r	Relative viscosity
μ-CT	Micro-computed tomography
Ξ	Printability criterion/parameter
ρ	Density
ρ_{air}	Density of air
ρ_{liquid}	Density of the liquid
ρ_{sample}	Measured density of the sample
σ_0	Characteristic strength
$\sigma_{compressive}$	Compressive strength
σ_f	Applied stress
$\sigma_{flexural}$	Flexural strength
$\sigma_{fracture}$	Fracture stress
$\sigma_{x,y}$	Electrical conductivity in the printing plane (x,y)
σ_{yield}	Yield stress
σ_z	Electrical conductivity in the z-direction
τ	Shear stress
τ_f	Flow stress
τ_y or τ_y^{STAT}	Static yield stress
τ_y^{Din}	Dynamic yield stress
φ	Solid content
φ_{max}	Maximum solid content/maximum packing fraction
ϕ	Printability criterion/parameter
[n]	Shape factor
3D	Three-dimensional
3ITT	Three-interval thixotropy test
3PB	Three-point bending
4PB	Four-point bending
AESO	Acrylated epoxidized soybean oil
Al_2O_3	Alumina

ALP	Alkaline phosphatase
AM	Additive manufacturing
ANOVA	Analysis of variance
Ar	Argon
ATZ	Alumina-toughened zirconia
BCP	Biphasic calcium phosphate
BG	Bioactive glasses
BMP-2	Bone morphogenetic protein-2
BMSCs	Bone mesenchymal stem cells
BR	Bone regeneration
BSA	Bull serum albumin
CAD	Computer-aided design
CAMI	Current-assisted metal infiltration
Ce-TZP	Ceria-stabilized tetragonal zirconia polycrystal
CDHA	Calcium-deficient hydroxyapatite
CFRP	Carbon fiber reinforced epoxy composites
CGT	Critical gelation temperature
CIP	Cold isostatic pressing
CMC	Carboxymethyl cellulose
CMT	Critical micellar temperature
CNC	Computed numerical control
CNFs	Carbon nanofibers
CNT	Carbon nanotube
CPO	Calcium peroxide
CS	Conventional sintering
CT	Computerized tomography
CTR	Chance of true relationship
D	Nozzle diameter
$d_{x,y}$	Distance between struts in the same plane (x,y)
d_z	Distance between layers (z-direction)
DCM	Dichloromethane
DIP	Direct inkjet printing
DIW	Direct ink writing
DIW-SC	Direct ink writing-solvent casting
DNGH	Double network granular hydrogel
E	Young's modulus
$E_{compressive}$	Young's modulus under compression
ECM	Extracellular matrix
e.g.	*Exempli gratia* (for example)
F	Probability of failure
F127	Pluronic® F-127
FDM	Fused deposition modeling
FE-SEM	Field-emission scanning microscopy
FEM	Finite element modeling

FTI	Flow transition index – printability criterion/parameter
FVB	Flow-through vascular bundle
g	Gravitational force
G’	Storage modulus
G'_{eq}	Equilibrium modulus
G”	Loss modulus
GNPs	Graphene nanoplatelets
GO	Graphene oxide
h	Height of the printed structure
h_{max}	Maximum printable height
HA	Hydroxyapatite
hBMSC	Human bone marrow-derived mesenchymal stem cells
HEA	2-hydroxyethyl acrylate
HIP	Hot isostatic pressing
HPMC	Hydroxypropyl methylcellulose
HSSGG	High silica sol-gel glass
HUVECs	Human umbilical vein endothelial cells
HV	Vicker’s number of hardness
I_y	Quadratic moment
i.e.	*Id est* (that is)
imCNTs	Ionically modified carbon nanotubes
ISP	*In situ* polymerization
k	Flow consistency parameter
K	Printability criterion/parameter
K_{IC}	Fracture toughness
L	Lower span distance
LLA	L-lactide
LOM	Laminated object manufacturing
LVDT	Linear variable differential transformer
LVR	Linear viscoelastic region
m	Weibull modulus
m_{air}	Mass of the sample in air
m_{liquid}	Mass of the sample in the liquid phase
MA	Maltodextrin
MBG	Mesoporous bioactive glass
mBMSCs	Mouse bone marrow mesenchymal stem cells
mMSCs	Mouse mesenchymal stromal cells
MRI	Magnetic resonance imaging
MSCs	Mesenchymal stem cells
Mw	Molecular weight
n	Flow behavior index
n.d.	Non-disclosed information
nBG	Nano bioactive glass
p	p-value/probability value

P-3B	Piston-on-three balls
P-3DP	Powder-based 3D printing
P-SLM	Powder-based selective laser melting
P-SLS	Powder-based selective laser sintering
PμSL	Projection micro-stereolithography
PAM	Polyacrylamide
PBS	Phosphate buffered saline
PCL	Polycaprolactone
PDC	Polymer-derived ceramic
PEG	Polyethylene glycol
PEI	Polyethylenimine
PEO	Poly(ethylene oxide)
PHA	Poly(hydroxyalkanoates)
PHBHHx	Poly-(3-hydroxybutyrate-co-3-hydroxyhexanoate)
PLA	Poly(lactic acid)
PLGA	Poly(lactic-co-glycolic acid)
PMMA	Polymethylmethacrylate
PPO	Poly(propylene oxide)
PRF	Platelet-rich fibrin
PVA	Poly(vinyl alcohol)
PVP	Polyvinylpyrrolidone
Q	Printing speed
R	Nozzle diameter
R^2	Coefficient of determination
Relat. density	Relative density
rBMSCs	Rat bone mesenchymal stem cells
rGO	Reduced graphene oxide
rhBMP-2	Recombinant human BMP-2
rBMSCs	Rabbit bone marrow stromal cells
rMSCs	Rat mesenchymal stem cells
S-3DP	Slurry-based 3D printing
S-SLS	Slurry-based selective laser sintering
SBF	Simulated body fluid
SC	Slip casting
SEM	Scanning electron microscopy
SiHA	Silicon-substituted hydroxyapatite
SLA	Stereolithography
SLS	Selective laser sintering
SPS	Spark plasma sintering
$SrAl_{12}O_{19}$	Strontium aluminate
SWCNT	Single-walled carbon nanotube
T	Temperature
$t_{sintering}$	Time at the plateau
$T_{sintering}$	Temperature of the sintering plateau

TCP	Tricalcium phosphate
TGA	Thermogravimetric analysis
TRIP	Transformation-induced plasticity
TZP	Tetragonal zirconia polycrystal
UC	Unidirectionally compressed
UV	Ultra-violet
VEGF	Vascular endothelial growth factor
x	Distance from the tensile side of the filament to the neutral axis
XRD	X-ray diffraction
Y-TZP	Yttria-stabilized tetragonal zirconia polycrystal
YSZ	Yttria-stabilized zirconia
ZrO_2	Zirconia

CONTENTS

GENERAL INTRODUCTION

This thesis started to be conceived on October 2019 at the beginning of my Ph.D. journey. It was during this period that Profs. Fredel and Bruno told me about an opportunity for collaborative work with Prof. Laurent at the Mateis Lab in Lyon, France. With a theme completely different from the one I explored in my masters (membranes for guided bone regeneration obtained by electrospinning) and the difficult task of achieving a French level B1 in seven months, I accepted the opportunity.

At that time my familiarity with French was confined to Duolingo lessons (yes, *le chat est noir*). So, with a lot of effort, I passed the proficiency test just in time for my scheduled trip to France in March 2020. Then a pandemic abruptly altered these plans. Everything was postponed, the lab was inaccessible and the first chapter of this thesis was born – a comprehensive literature review. Reading numerous papers daily, collecting and summarizing copious amounts of information, all while isolated from the world and listening to distressing news on the TV, presented its challenges. When circumstances finally improved (September 2021) and I could proceed to France, I realized I was grappling with a burn-out crisis resulting from that tough period. The process of overcoming this psychological and emotional hurdle occurred simultaneously with conducting the experiments detailed in this work. A year and four months later, back in Brazil, I dedicated myself to writing the papers and, consequentially, this thesis, as all the experiments had been finalized. Each chapter within this thesis corresponds to a paper that has either been published or is scheduled for publication. Hence, the three chapters of this thesis:

1) Review paper on the ceramics and ceramic-based composites intended for biomedical engineering applications that had been produced by direct ink writing;
2) Rheological characterization of a paste for direct ink writing composed of alumina-toughened zirconia with and without carbon nanofibers with focus on their printability and the suitability of printability criteria that have been proposed by the literature;
3) Mechanical evaluation of alumina-toughened zirconia filaments with and without carbon nanofibers obtained by direct ink writing.

Each one of them is self-sufficient and, thus, states the research problem, the objectives of the study, previous studies on the same theme and the justifications that led to the choice of the theme. Another paper with the biological characterization of the CNF-containing samples is currently in progress; however, its results were not ready in time for inclusion in this document.

As I'm writing the last sections of this thesis, I come to recognize the tremendous growth that has resulted from this challenging adventure. For that, I'm very grateful. The forthcoming pages depict this scientific journey to the best of my abilities, with the aspiration of providing both insight and enjoyment.

1

CHAPTER 1: CERAMICS AND CERAMIC COMPOSITES FOR BIOMEDICAL ENGINEERING APPLICATIONS VIA DIRECT INK WRITING: OVERALL SCENARIO, ADVANCES IN THE IMPROVEMENT OF MECHANICAL AND BIOLOGICAL PROPERTIES AND INNOVATIONS

1. INTRODUCTION

Additive manufacturing (AM) has intensely improved our ability to produce custom-designed objects with precise dimensions and intricate architectures while ensuring standardization and reproducibility of the manufacturing processes [1,2]. Biomedical materials may also be improved by AM techniques, particularly in two major sets of applications. The first is orthopedic and dental implants, which may take advantage of manufacturing patient-matched devices and also devices that would be problematic to produce otherwise. Tissue engineering is the second area of application that can be beneficiated. Typically, specific porous three-dimensional (3D) supports/scaffolds are required for cells to attach, grow and differentiate themselves into functional tissues or organs [3]. In this regard, AM techniques are specifically remarkable in the production of architectures with porosities of controlled size distribution, from the nanometer to the millimeter scale, which can also be tailored to guide cell growth.

Recent improvements in the biomaterials field, biomedicine and biologic sciences have augmented the use of AM techniques [4], primarily through the customization possibility, a critical factor in this area and one that AM is exceptionally capable of conferring with specific properties and shapes. Recently, AM has been used for diverse medical fields (Fig. 1): drug delivery systems [5]; tissue engineering (customized scaffolds and artificial tissues/organs for transplants) [6,7]; low-cost orthoses and prostheses for developing countries [8,9]; surgical guides for screw insertions [10]; medical instruments for surgery and diagnostics [11]; laboratory equipment (e.g., portable test tools [12] and probes [13]); implants [14,15] and anatomical models for clinical practice [16,17].

Fig. 1. Schematic representation of the application of additive manufacturing in bio-related fields.

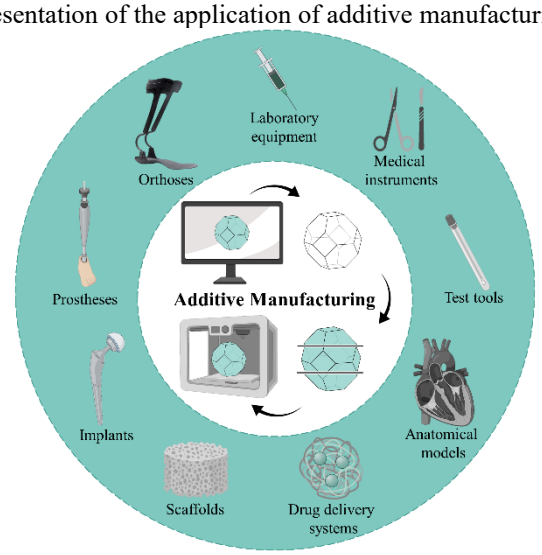

Source: Author.

The significant developments this type of technologies has experienced in a wide range of areas enable the production of objects of all classes of materials (metals, polymers, ceramics and composites), including materials of biological origin [18]. Among these, ceramic additive manufacturing has gained significant research interest due to the limitations of traditional ceramic processing. The increasing demand for ceramic objects with complex morphologies made traditional ceramic processing methods (e.g., casting and molding followed by machining) no longer adequate in some conditions [19,20]. Complex-shaped ceramic components are conventionally fabricated through slip casting (limited by the complexity of the molds) or uniaxial or isostatic pressing (limited by special equipment and tooling), which cannot provide high dimensional accuracy without a costly and time-consuming machining step. Therefore, in addition to a high degree of fabrication freedom, the AM of ceramics draws attention, considering its high efficiency and accuracy in achieving complex structures as well as its ability to tailor composition and microstructure with multifunctional properties [21–23].

There are several AM techniques nowadays, the most used for ceramic materials being schematically illustrated in Fig. 2, based on the different principles of layer formation. The main characteristics of these techniques are displayed in Table 1.

Fig. 2. Schematic representation of the additive manufacturing techniques most used for ceramics.

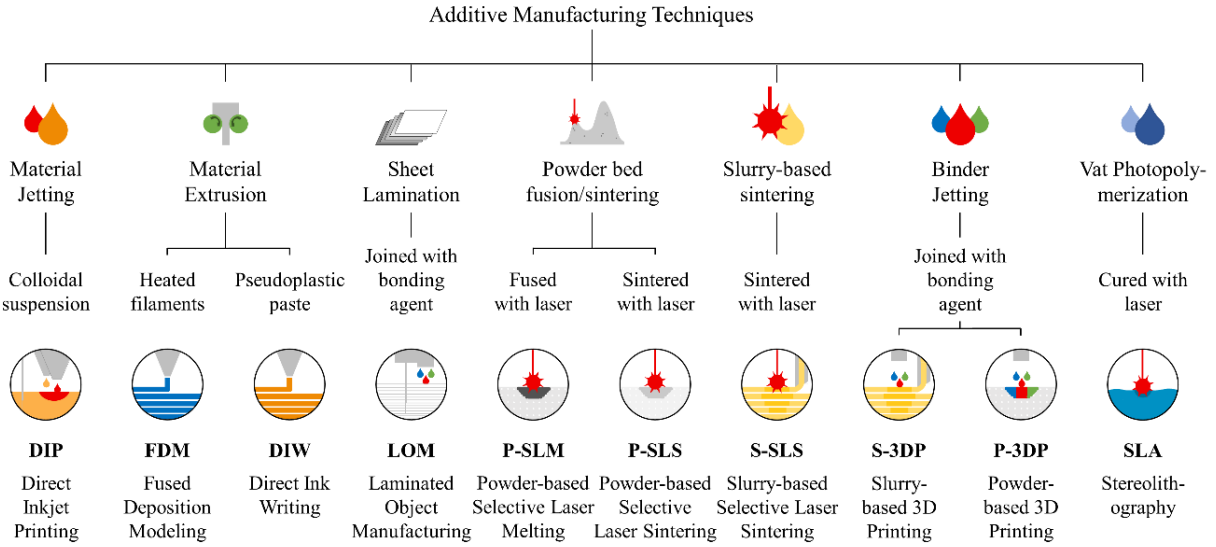

Source: Author.

Table 1. Main characteristics of the additive manufacturing techniques most used for ceramics.

Technique	Feedstock	Piece dimension	Precision (μm)	Dense struts	Dense components	Feedstock preparation cost	Process cost	Direct/ Indirect
DIP	Liquid	S-M	10	Yes	Yes	+++++	++	Direct
FDM	Liquid	S-M	100	Yes	No	+++	+	Direct
DIW	Liquid	S-XL	10	Yes	Yes	++	+	Direct
LOM	Solid	M-L	100	Yes	Yes	+++	++	Indirect
P-SLM	Solid	M-L	100	No	No	+	+++	Indirect
P-SLS	Solid	M-L	100	No	No	+	+++	Indirect
S-SLS	Liquid	M-L	100	Yes	Yes	+	+++	Indirect
S-3DP	Liquid	M-XL	100	Yes	Yes	+	++	Indirect
P-3DP	Solid	M-XL	100	No	No	+	++	Indirect
SLA	Liquid	XS-M	< 1	Yes	No	++++	++	Indirect

Source: Adapted from Zocca *et al.* [21].
XS = 100 μm; S = 1 mm; M = 10 mm; L = 0.1 m; XL = 1 m. Costs are directly proportional to the number of symbols (+) indicated.

A primary ambition of ceramic processing is to elaborate 3D structures with the required functional or mechanical properties, if not both. As can be seen in Fig. 2, multiple AM techniques have been established to expand the variety of available ceramic structures. One extrusion-based printing technique that is of particular interest is direct ink writing (DIW), which was initially developed and patented by Cesarano *et al.* at the Sandia National Laboratories (U.S.A.) in 2000 under the name "Robocasting" [24].

The DIW technology is a widely investigated processing route for ceramics, especially scaffolds. It is based on the extrusion of pastes/suspensions/inks/slurries through a fine nozzle and their subsequential deposition layer-by-layer on a plate to form a controlled 3D architecture [25] – Fig. 3. The composition of these slurries generally includes a liquid carrier (commonly water; with a volume fraction typically greater than 30% but very often surpassing 50%),

polymeric binders/gelling agents (usually < 1%) and a ceramic powder, encompassing the rest of the feedstock [26]. Among the binders and gelling agents, the mostly used are Pluronic® F-127 (a triblock copolymer of PEO-PPO-PEO; PEO: poly(ethylene oxide); PPO: poly(propylene oxide)), PVA (poly(vinyl alcohol)), CMC (carboxymethyl cellulose), HPMC (hydroxypropyl methylcellulose, commercially found as Methocel® F4M), PEG (polyethylene glycol) and PEI (polyethylenimine). A deflocculant is also commonly used to avoid agglomeration of the ceramic particles (e.g., ammonium polyacrylate (commercially known as Darvan®) and polycarboxylic acid (commercial: Dolapix®)). The pastes can be extruded through the nozzle either by a screw system, pneumatic pressure or by the force of a piston. Also, to mitigate the crack/deformation development associated with excessive shrinkage, some studies employ a coating layer on the substrate onto which deposition will take place – some examples are the use of corn syrup [27] and oleic acid [28]. After the deposition, the ink must dry to form a green component, which can then undergo debinding and sintering (if desired).

Fig. 3. Schematic representation of the DIW printing method highlighting its main associated parts and parameters involved in the production of scaffold and dense components.

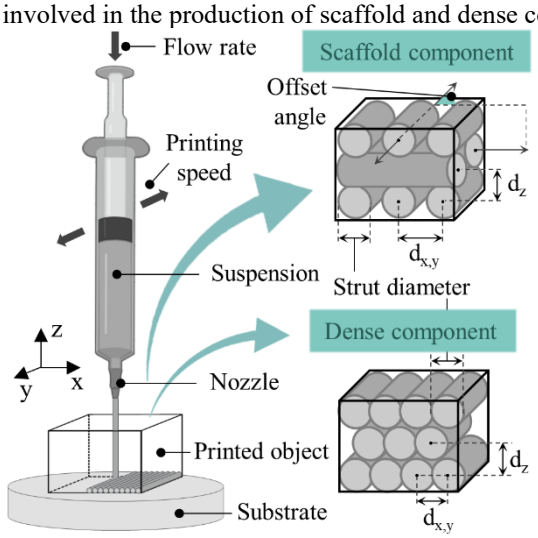

Source: Author.

$d_{x,y}$: distance between struts in the same plane (x,y); d_z: distance between layers (z-direction).

Bone tissue engineering scaffolds fabricated through the DIW technique have shown potential to be stronger than those manufactured by conventional methods – with achieved mechanical strength values 4- to 5-times those obtained for bioactive glass and hydroxyapatite scaffolds with similar porosity prepared by other conventional techniques [29]. The approach also enables the obtention of dense components with densities up to 98%. Among the DIW advantages are the possibility of (1) attaining very fine lattice structures as a result of the low viscosity of the slurry [30], (2) using different extrusion nozzles than the standard circular ones (square, hexagonal or other complex geometries [25]) that can also produce hollow filaments

and (3) orientating high aspect-ratio particles, which is decurrent from the shear stresses associated with the nozzle reduction process – such oriented structures are currently being actively studied [31–33].

Therefore, this fast and non-complex fabrication method is considered a very auspicious approach for biomedical applications, particularly for obtaining ceramic-based bone tissue engineering scaffolds [34,35]. Its simplicity and low cost make DIW also appealing for in-hospital 3D printing. However, to the authors' knowledge, neither an overview of the currently existing DIW-printed ceramic-based components for biomedical engineering applications nor an analysis of their main characteristics exists. This review provides a complete overview of the current state of the art of the ceramic-based components produced by DIW and used for these applications. The studies were categorized by the components' bioactivity and then by their compositions, delivering their most significant findings and outcomes.

2. LITERATURE SEARCH METHODS

2.1. SCIENTIFIC LITERATURE RESEARCH

The scientific literature search was performed using several databases (Scopus, Web of Science) and the search tools provided by several editors (ScienceDirect, SpringerLink, Royal Society of Chemistry and Taylor & Francis). Only general terms were chosen to have a vaster search query, which was not limited to a particular period and included just English articles. Our complete search query was TITLE-ABS-KEY (("direct ink writing" OR "robocasting") AND (LIMIT-TO (LANGUAGE, "English")). The last search was performed on October 11th, 2021.

2.2. ELIGIBILITY CRITERIA

Were evaluated studies that simultaneously fit into three categories, namely, (1) use of the direct ink writing technique as a method of fabrication; articles that merely cite the DIW process were excluded (some authors make distinctions in the nomenclature, sometimes utilizing the term DIW to represent several extrusion techniques, nevertheless, in this review, DIW was considered as a synonym for the "Robocasting" technique), (2) components made from ceramic or ceramic-based composites and (3) targeted for use in biomedical engineering applications, i.e. directly in contact with the patient, whether or not it stays in the body for the

whole period of the examination or treatment. Components that have cells in their inks/slurries (bioinks) and, therefore, are utilized for bioprinting were not considered.

2.3. LITERATURE SEARCH RESULTS

The search returned 4374 scientific articles that, after duplicate exclusion, became 1379, of which the titles and abstracts were examined. Of these, 203 articles fulfilled the eligibility criteria and were selected. The gathered information was considered from different perspectives: the type of structure produced, its application, "bioactivity" and the novelty of the research.

3. LITERATURE DATA ANALYSIS

The distribution of studies regarding ceramic-based materials obtained through the DIW method in the last 15 years and by country can be observed in Fig. 4. It is possible to note an increasing interest in the field, as with additive manufacturing in general. In geographical terms, the main countries publishing studies in DIW ceramic-based biomaterials are the United States of America (U.S.A.) with 19% of the studies, followed by China (15%), Spain (14%), United Kingdom (U.K., 6%), Italy (6%), Portugal (5%), Germany (4%) and Egypt (3%).

Fig. 4. Number of publications of ceramic-based materials produced by DIW in the last 15 years and percentages of studies by country.

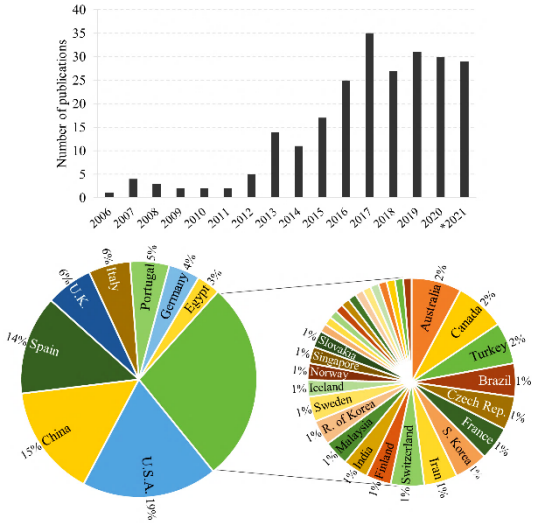

Source: Author.
Asterisk (*) indicates an incomplete year when the review search was conducted.

For this review, the ceramic-based materials for biomedical engineering applications were divided at first into ceramics and composites (Fig. 5). The first group was then classified

into bioinert (comprising mainly alumina and zirconia) and "bioactive" ceramics, which encompassed calcium phosphates (hydroxyapatite (HA) and tricalcium phosphates (TCPs)), bioactive glasses (BG), silicates (calcium silicates and polymer-derived ceramics (PDCs)) and functional ceramics (functionality achieved through protein/drug loading). The composite group was classified according to the materials present, hence, ceramic-ceramic, ceramic-metal, ceramic-polymer, ceramic-hydrogel and functional composites.

Fig. 5. Schematic representation of the classification of ceramic-based materials for biomedical engineering applications.

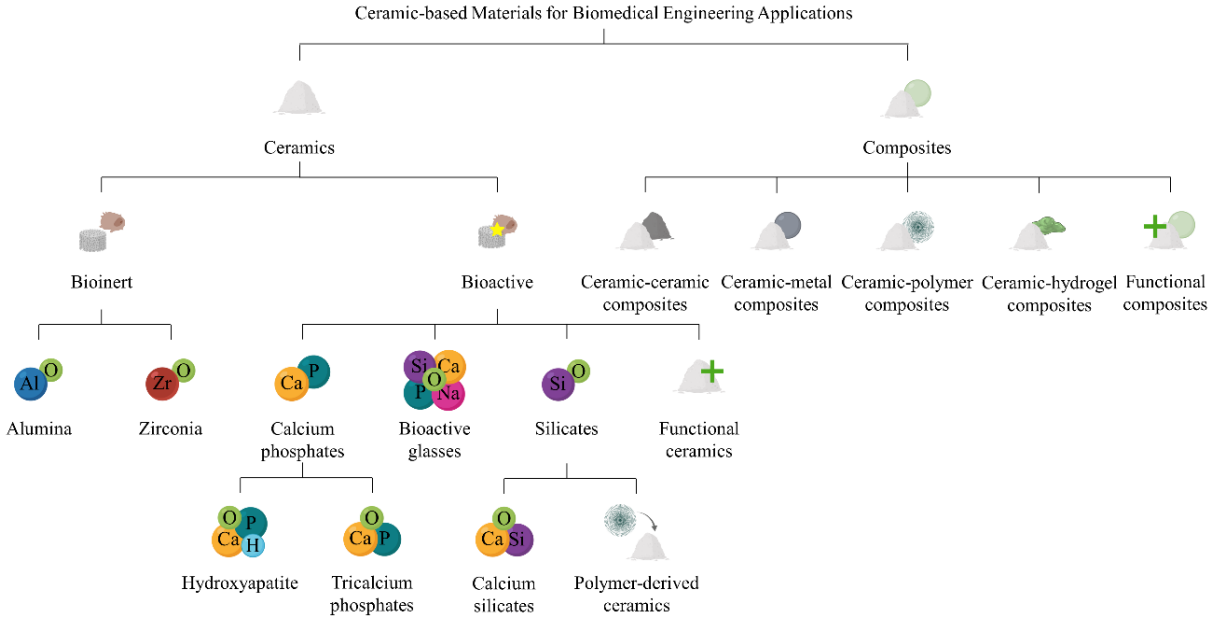

Source: Author.

Such classification enabled the evaluation of the main characteristics of the studies performed in the area; the overall results of this assessment can be observed in Fig. 6. When classified by the type of material, the distribution of studies is primarily similar, with 52% being on ceramic materials and 48% on composites. Bioactive ceramics are the topic of most studies (72%, vs 28% for bioinert), with a clear focus on bioactive glasses (36%), followed by hydroxyapatites (26%), tricalcium phosphates (13%), polymer-derived ceramics (9%), calcium silicates (8%) and functional ceramics (7%). Of the studies involving bioinert ceramics, 56% utilize alumina, 26% zirconia and 18% use other bioinert ceramics.

Fig. 6. Assessment of the main characteristics of the studies on ceramic-based materials produced by DIW for biomedical engineering applications.

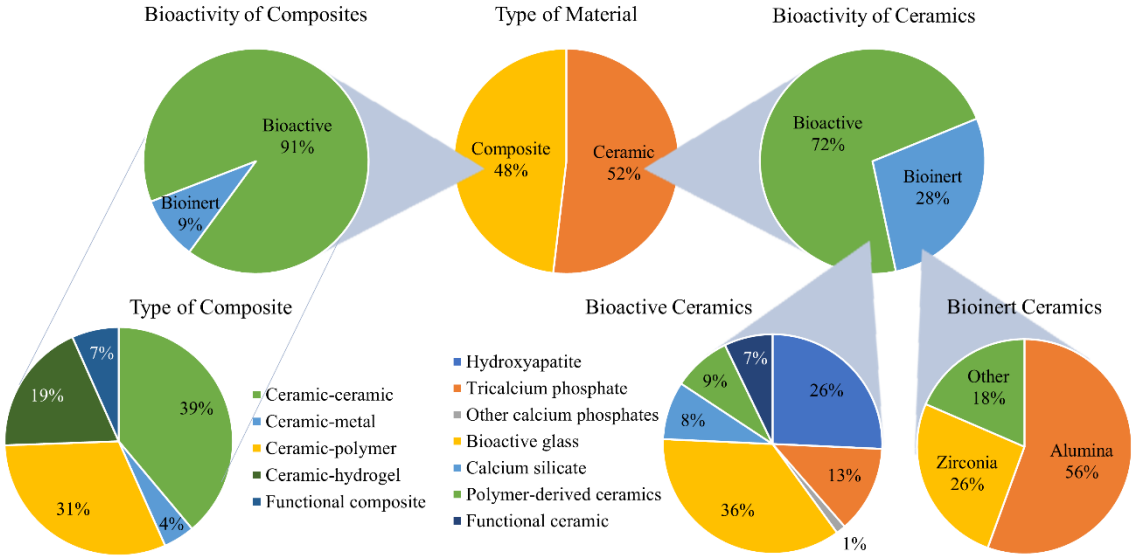

Source: Author.

Regarding the bioactivity in the studies with ceramic-based composites, the dominance of bioactive ceramics is even higher (91%) since the primary characteristics desired by a ceramic addition in a composite proposed for biomedical engineering applications are those related to the bioactivity of the ceramic phase. When classified by the type of materials present in the composite, the most studied are ceramic-ceramic composites (39%), ceramic-polymer composites (31%), ceramic-hydrogel composites (19%), functional composites (7%) and ceramic-metal composites (4%).

The studies can also be assessed in terms of the structure obtained (Fig. 7). The majority of studies (90%) produced scaffolds, whereas only 10% obtained dense structures. This focus on porous structures happens mainly because DIW is intrinsically appropriate for the production of fine filigree structures and allows the fabrication of complex-shaped porous architectures with precise control of the shape, amount and dimension of pores. These characteristics are not achievable by any other technique currently used for the production of porous components.

Considering the dense materials, 78% of them are intended for load-bearing orthopedic applications and 22% for dental applications. As for the scaffolds, as expected, most of them (91%) are proposed for bone regeneration applications, with 5% for the same purpose but also involving drug delivery, 2% for bone regeneration combined with tumor therapy and, tied at 1%, scaffolds for orbital reconstruction and multi-tissue interface.

Fig. 7. Classification based on the structure obtained by the studies on ceramic-based materials fabricated with the DIW technique. Each type of structure is then evaluated in terms of the application for which it is intended.

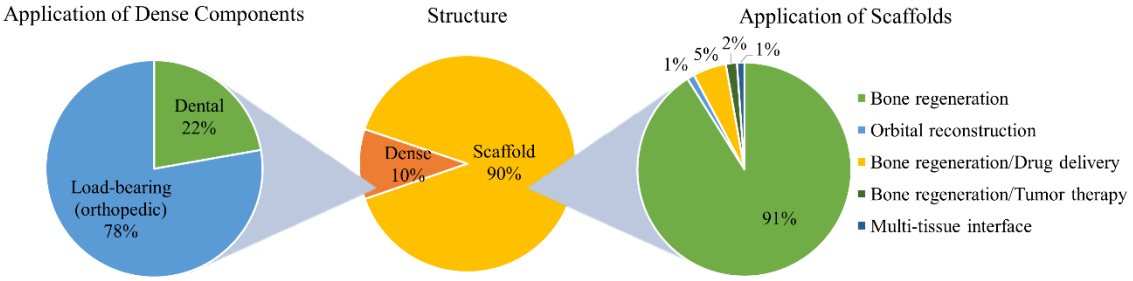

Source: Author.

Each type of structure has different requirements for its proposed applications and will be highlighted separately next.

3.1. SCAFFOLD COMPONENTS

These 3D structures that aim to provide a template for cell attachment and stimulation of *in vivo* bone tissue formation can ideally, through mechanical and biochemical interactions, mimic bone mechanical support, cellular activity and protein production [36,37]. Over the last few decades, a variety of materials has been proposed for bone tissue engineering scaffolds, yet the development of structures with functions analogous to those of natural bone is still a challenge [38].

An ideal scaffold must fulfill specific requirements such as being biocompatible, osteoconductive, ideally biodegradable (with a suitable degradation rate) and possessing mechanical properties similar to those of bone [39–41]. In addition, to enable cell migration and tissue ingrowth, the porosity should be greater than 50 vol% [42–45]. However, there is no consensus regarding the ideal pore size, which has been reported in the literature to range from 1-300 μm [39–41] to suggestions of pores smaller than 500 μm [46], with many intermediate values proposed (larger than 100 μm [42–45], larger than 300 μm [47,48]). A graded porosity can also be advantageous as the porous surface is intended to integrate with the surrounding tissues [49]. Mechanically, the scaffolds should ideally match the properties of the bone/tissue that they plan on substituting or repairing – Table 2.

.

Table 2. Mechanical properties of human bone. Many parameters influence these values (e.g., age, regular physical activity, type of bone), hence their variations in the literature.

Property	Type of bone	
	Cancellous	Cortical
Porosity (%)	30-90 [50]	5-15 [51]
Density (g/cm^3)	0.1-1.0 [52]	1.8-2.2 [52]
Apparent density (g/cm^3)	0.1-1.0 [52]	1.8-2.0 [52]
Compressive strength (MPa)	2-12 [53,54] 7-10 [52]	100-150 [55,56] 170-193 [52]
Young's modulus (GPa)	0.1-5 [55,56] 0.05-0.5 [52]	14-20 [52]
Strain to failure	5-7 [52]	1-3 [52]
Hardness (HV)	30-40 [57]	37-47 [57]
Fracture toughness (MPa.m$^{1/2}$)	0.1 [52]	2-12 [52]

Source: Author.

A variety of methods has been utilized to produce scaffolds, including foaming, particle/salt leaching, phase separation, solvent casting and freeze-drying, but these techniques have limitations in precisely controlling the overall architecture of the structure and its internal pore connectivity. However, when advanced AM techniques such as DIW are considered, precise control of these characteristics is achievable. Patient-specific scaffolds are also attainable, surpassing many of the limitations associated with current fabrication methods and the characteristic irregular shapes of bone defects with a convenient and fast fabrication method [58].

The properties of many ceramic materials, such as relatively high stiffness and bioactivity, make them excellent alternatives to autologous bone grafts to act as temporary frameworks, providing an adequate environment for cell adhesion and proliferation. Nevertheless, obtaining strong mechanical integrity (to allow use in load-bearing applications) while preserving optimal biocompatibility levels, bioactivity, and biodegradability is still a challenge.

This challenge is observable in Fig. 8, which presents the dependence of compressive strength (the most evaluated mechanical property in the field of bone tissue engineering applications) on the porosity of ceramic-based scaffolds produced by DIW. The direct comparison between scaffolds of different materials and morphologies (strut/filament diameter, pore size, pore shape and strut/filament deposition pattern) is not easy. Still, Fig. 8 enables the overall examination of the compressive strength currently achieved: only a few articles report compressive strengths similar to those of cortical bone. Besides, there is a tendency toward stronger scaffolds as porosity approaches 50%, an unexpected finding, as it would be predicted an increasing strength with continuously decreasing porosity.

Fig. 8. Compressive strength *vs.* porosity for ceramic-based scaffolds that were produced via DIW.

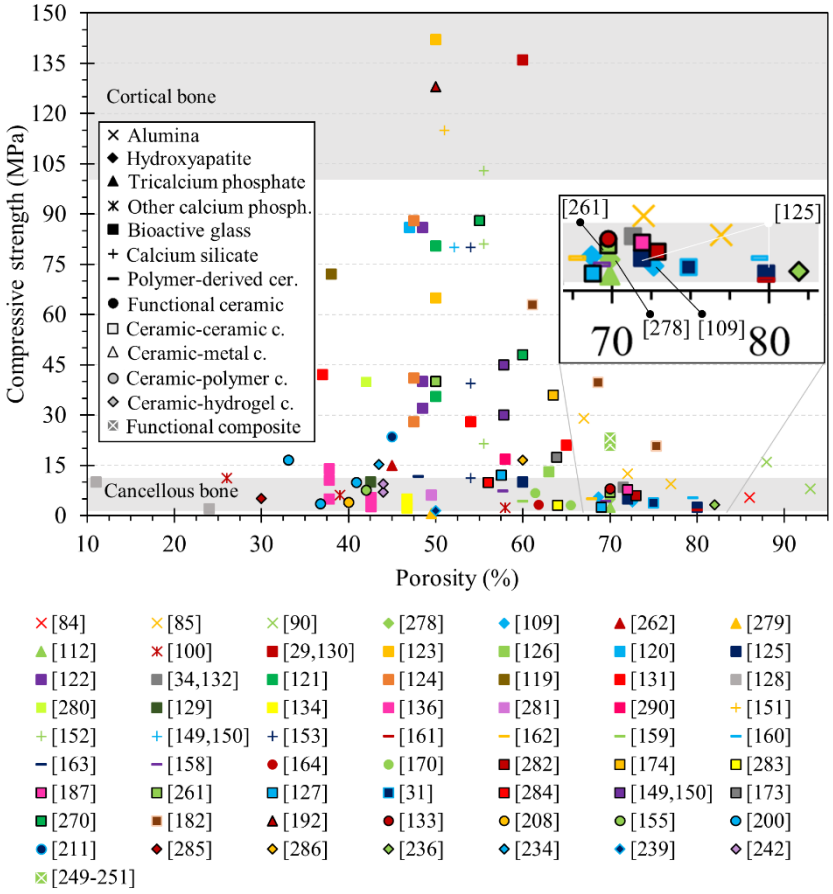

Source: Author.

3.2. DENSE COMPONENTS

Few additive manufacturing (AM) techniques present on the market can produce fully dense ceramic structures. This ability remains a challenge and is the most crucial step to be surpassed so that AM of ceramics establishes itself as more than a niche technology. The AM of dense ceramics, which enables the full retention of the components' superior physicochemical properties and shapes not possible with other techniques, would potentially open new markets for ceramic products. This possibility arises from the fact that AM is not rigorously restrained to the paradigms that usually involve ceramic processing, such as complex machining, low flexibility, limited mold shaping technologies and high processing cost for the production of small lots [21].

Still, some potential issues are associated with the DIW method for the obtention of such components [30,59]. In this technique, the as-printed component contains a high amount of liquid carrier (usually water), which makes the process of drying without cracking difficult – especially for dense components. Besides, the organic content of the paste is usually low (as already mentioned) but still higher than that found in pressed ceramics for example; a fact that

can lead to debinding problems such as cracking or trapped gas inside the printed struts. Furthermore, like all ceramic processing techniques that involve sintering, the process of shrinkage during sintering is unavoidable. These potential issues – drying, debinding and shrinkage during sintering – are the factors that require special care when considering the DIW technique for the fabrication of dense components. To date, different approaches have been proposed to surpass them. The most traditional strategy is to increase the ceramic solid loading content as high as possible [59–62], minimizing shrinkage but requiring optimization to avoid particle agglomeration. Alternatively, techniques that enable the preservation of the printed structure can be combined with DIW, such as the freeze-form extrusion that immediately freezes the printed green body. Studies focusing on binder-free pastes have also been reported [63].

In addition, three different parameters require adjustments when printing dense structures through direct ink writing, namely (1) the center-to-center spacing between adjacent filaments/struts ($d_{x,y}$) and also between layers (d_z) – Peng *et al.* [28] estimate that the optimal line width over height ratio for dense components is ~1.45 – (2) the printing pattern and (3) the material feeding rate. The optimization of these parameters allows the deposited filaments to completely fuse with the adjacent filaments and those underneath them (in the z-direction), minimizing possible defects and cavities [28]. This also requires attaining a narrow range of rheological behavior; for that, a rheological printability criterion was developed in the last years by M'Barki *et al.* [64]. This dimensionless printability criterion (Ξ) is based on the fact that both gravitational and surface forces can distort the printed component; hence, a distortion-free piece could be printed if the dynamic yield stress of the paste is high enough to overcome these two forces. The criterion thus takes into consideration the density (ρ), surface tension (γ) and dynamic yield stress (σ_y^{Din}) of the paste, as well as external parameters such as nozzle diameter (R), height of the structure (h) and the gravitational force (g) – Eq. 1. To produce materials with low deformation, high density and high strength, the parameter Ξ should be close to or higher than 1.

$$\Xi = \frac{\tau_y^{Din}}{\gamma.R^{-1}+\rho gh} \quad (1)$$

These developments/findings are relatively new (2018), demonstrating the increasing interest in producing dense components from DIW and explaining why there have been comparatively few reports on dense ceramic-based components so far. The main characteristics

achieved by dense parts obtained by DIW are shown in Table 3. Although many of these studies report high enough densities, none of them are close to or higher than 99% (as is commonly found in pressed or slip-cast dense components). Besides, as compared to reference materials of the same composition, the reported flexural strengths are usually at least 50% lower while the hardness and toughness are of the same order of magnitude. This indicates the presence of large defects, not related to sintering but rather to the process itself, which, as mentioned, is relatively new for the production of such structures.

Table 3. Mechanical properties and density of ceramic-based dense components produced by DIW.

Material(s)	Year	Relat. density	$\sigma_{compressive}$ (MPa)	$E_{compressive}$ (MPa)	$\sigma_{flexural}$ (3PB) (MPa)	Hardness (HV)	Fracture toughness ($MPa.m^{1/2}$)	Ref.
Alumina*	—	—	—	400 000	≤ 650	2000	4	[65]
Alumina	2016	98%	—	—	145.5 ± 11.5	—	—	[66]
Alumina	2016	97%	—	—	300	—	—	[67]
MgO-doped alumina	2018	>98%	—	—	326	—	—	[68]
Alumina	2019	98%	—	—	—	—	—	[69]
Zirconia*	—	—	—	200 000	≤ 1400	~1200	6-9	[65]
Zirconia (UC)	2020	—	—	—	—	1306 ± 19	5.6 ± 0.4	[70]
Zirconia	2020	—	—	—	—	1175 ± 29	4.5 ± 0.7	[70]
Zirconia (Fully and partially stabilized YSZ)	2018	95-96%	—	—	243	1355	—	[28]
Zirconia (Partially stabilized YSZ)	2019	98.1%	1560	—	489	—	—	[71]
Zirconia	2020	97.1%	—	—	—	1485 ± 32	4.1 ± 0.1	[63]
Titania	2019	91.5%	125	1220-6870	—	—	—	[72]
Hydroxyapatite*	—	—	—	—	—	—	1.0	[65]
Hydroxyapatite	2019	—	—	275	—	—	—	[73]
Silicon carbide	2016	95%	—	—	230	—	—	[67]
Silicon nitride*	—	—	—	—	—	—	10	[65]
Silicon nitride	2017	—	—	—	552 ± 68 (4PB)	—	—	[74]
Silicon nitride /SWCNT (0.2 vol%)	2008	97%	—	—	—	—	8.48	[75]
Ce-stabilized Zirconia/Alumina	2017	~95%	—	—	575	—	—	[76]
β-TCP/BG (45S5)	2018	~90%	—	—	~110	—	—	[77]
BG (13-93)/PLA (infiltrated)	2016	—	105 ± 10	—	—	—	—	[78]
Alumina platelets (oriented)/Epoxy (infiltrated)	2017	—	443.5 ± 8.5	—	—	—	—	[32]
γ-alumina/Silicon oxycarbide (coating)	2019	—	—	—	—	266-300	—	[79]

Source: Author.

Asterisks (*) indicate typical mechanical properties of ceramics produced by conventional methods (pressing) for comparison purposes. Relat.: relative; $\sigma_{compressive}$: compressive strength; $E_{compressive}$: Young's modulus under compression; $\sigma_{flexural}$: flexural strength; 3PB: three-point bending; 4PB: four-point bending; UC: unidirectionally compressed.

4. CERAMICS

4.1. BIOINERT CERAMICS

Bioinert ceramics are a group of materials with good biocompatibility that minimally interact with the body tissues. Also, by the classification proposed by Hench and Ethridge, bioinert ceramics are the ones that "elicit a minimal response in the host" [80]. This class of materials was evaluated in implant applications in the early 1970s as a result of their corrosion resistance, good biocompatibility and stability in the physiological environment. Due to their lack of chemical bonding with human tissues and the need for a second operation after implantation, their use as bone substitutes and scaffolds for bone regeneration – the two main applications of bioceramics – are limited to some extent. Nowadays, they encompass mainly applications in which there is a requirement for dense components.

The DIW studies with the two main bioinert ceramics (alumina and zirconia) are presented in the next sections. In addition, other novel bioinert ceramics such as titanium dioxide, silicon carbide and silicon nitride are featured.

4.1.1. Alumina

Alumina (Al_2O_3) was the first bioceramic extensively used in clinic due to its negligible tissue reaction [81]. Bioinert ceramics based on alumina present nontoxicity and high: chemical inertness, biocompatibility, hardness, mechanical strength and wear resistance. They could, additionally, remain *in vivo* for a long time while maintaining their chemical and physical properties, which match the requirements for implantation and long-term service. These characteristics make them highly promising as bone implants [82].

Nonetheless, due to their bioinertness, not many studies have been conducted on the 3D printing of alumina-based scaffolds for bioengineering applications. Besides, when it comes to dense structures, materials with higher mechanical properties have been developed and gradually took the place that was predominantly of pure alumina structures (e.g., femoral heads of hip implants). Another troublesome factor is powder shaping [83]. Still, some studies performed with DIW have presented dense alumina components with good mechanical properties. Glymond *et al.* [68] conducted one of them with the gelation of alginic acid obtained using Mg ions. The MgO-doped alumina with up to 50 vol% of solid content had 98% relative density and flexural strength of 326 MPa (3-point bending, 3PB)). Al_2O_3 dense structures with

a flexural strength of 300 MPa were, also, successfully fabricated with 97% relative density by Feilden *et al.* [67] using Pluronic F-127® as a binder and solid contents up to 40 vol%.

More recently, innovative approaches for the production of hierarchically porous scaffolds were evaluated utilizing alumina. One promising route to produce scaffolds with porous filaments is the combination of alumina and camphene, in which the latter acts as a pore-forming agent and temporary binder. Moon *et al.* [84] printed a macroporous scaffold with microporous hollow filaments by the co-extrusion of a camphene core with an alumina/camphene shell with subsequent camphene removal (Fig. 9(a-i)). The porosity and mechanical properties of the scaffolds were tailored by controlling the alumina content (15, 20 or 25 vol%). The structure had 500 μm diameter struts, with a porosity of 86 vol% and approximately 5.4 MPa of compressive strength. In another study [85], the same research group combined DIW and freeze casting to produce a macroporous scaffold with elongated and interconnected pores within the filaments (Fig. 9(j-n)). Frozen alumina/camphene filaments were deposited at a stacking sequence of 0°/90° providing 3D interconnected macropores. In contrast, alumina frameworks generated aligned elongated micropores as a replica of camphene dendrites, elongated by the extrusion associated with the DIW method. After the deposition, the structures were freeze-dried and hierarchical porous scaffolds with 67-77% overall porosity and compressive strength from 9.5 to 29.3 MPa were obtained. In this approach, the macro/micro-porous structure and, consequently, the compressive strength could be tailored by adjusting the initial alumina content in the pastes and, as within filament porosity is achieved by solvent removal, this route predominantly leads to open porous anisotropic structures. Still, a challenge for this route is the complete solidification of the paste after extrusion, which could lead to poor bonding between extrusion lines.

Fig. 9. Alumina/camphene scaffolds. (A) Schematic diagram of co-extrusion of a camphene core and ceramic/camphene shell. (B) Representation of macroporous ceramic scaffolds consisting of highly microporous hollow filaments. (C) Representative μ-CT images showing the cross-sectional view of the scaffolds. Representative FE-SEM images of the macroporous alumina scaffolds with highly microporous hollow filaments produced using the alumina contents of 15 vol% (D, G), 20 vol% (E, H) and 25 vol% (F, I), evidencing the cross-sections (D, E, F) and the microporous alumina struts (G, H, I) [84]. (J) Schematic diagram of 3-D alumina/camphene co-extrusion process. (K) Porous ceramic scaffold with 3-D interconnected macropores and aligned micropores. Representative FE-SEM images of macro/micro-porous alumina scaffolds produced using various alumina contents of 15 vol% (L), 20 vol% (M) and 25 vol% (N). It is possible to observe that aligned microporous alumina frameworks developed parallel to the extrusion direction [85].

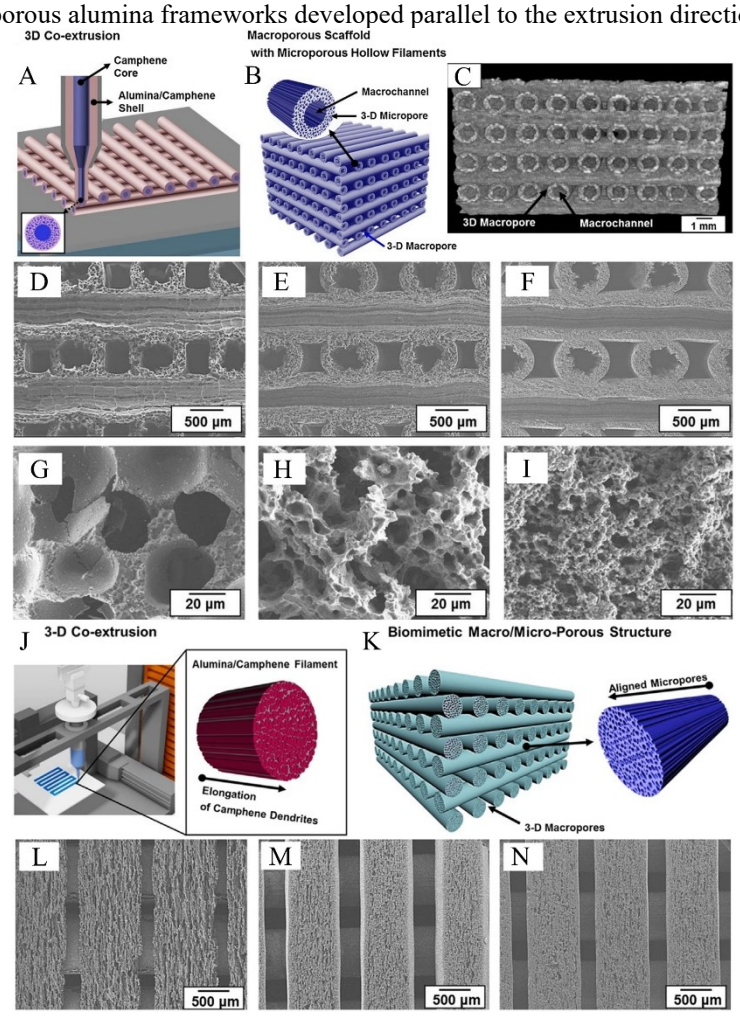

Source: Adapted from [84,85].

A versatile approach to attain mechanically stable highly porous ceramics based on capillary suspensions was developed in 2013 by Dittmann *et al.* [86,87] with alumina suspensions. Capillary suspensions are fluid/fluid/solid systems with a strong particle network structure, in which the particles stay together due to capillary forces induced by liquid bridges of the secondary fluid. This fact alters the rheology of the system and stabilizes the suspension. Therefore, the bulk fluid can be extracted from the suspension without the particle network collapse (backbone of the later sintered part) as, if the pair of fluids is appropriately chosen, the remaining liquid bridges between the particles guarantee the structure's integrity. A wide range of pore structures is attainable with this processing route with very high repeatability, including

porosities and pore size ranges that were previously hard to obtain (e.g., porosity higher than 50% and median pore diameter by volume lower than 10 μm); in their study, Dittmann *et al.* achieved α-alumina scaffolds with porosity higher than 60% and pore sizes smaller than 10 μm.

For DIW, capillary suspensions of α-alumina were prepared by Maurath *et al.* [88] – Fig. 10. In their study, hexagonal honeycomb structures bioinspired in balsa wood presented 60-88% overall porosity with fully open-porous struts (45-60% porosity and pore sizes < 6 μm). For the bulk phase, palm wax (1.1 vol%) was dissolved in a mixture of paraffin (48.6 vol%) and mineral spirits (50.3 vol%), whereas the second phase was a mixture of 50 vol% D(+)-sucrose in water. The printing suspensions were prepared by mixing the alumina particles with the bulk phase with the subsequent addition of the second phase; solid contents used were 23 or 31 vol%. The suspensions showed excellent printing behavior and structures with small spanning elements and high aspect ratios (height/width = 4–11) were printed on a glass slide coated with polyethylene glycol (PEG), which was wetted with water to form a lubrication layer. The hexagonal honeycomb hierarchical structures demonstrated exceptionally high specific strength under compression and significantly increased the strength-density range that sintered capillary suspensions had reported. The distinctly lower sensitivity of strength on the honeycombs' density caused them to be mechanically more efficient than bulk specimens from capillary suspensions; moreover, their specific strength was superior by a factor of ~2-3 when compared to the strength of cast specimens (slip-casting). As expected, the honeycomb structures behaved anisotropically under compression, with the compressive strength in-plane (~3 MPa) being ~2-3 times higher than that of out-of-plane.

Fig. 10. α-Alumina scaffolds from capillary suspensions inspired in balsa wood [88]. (A) Schematic illustration of the processing route with the open-porous structure of the sintered struts being based on the open-porous network of capillary suspension that serves as a precursor for the ceramic part. (B) and (C) Hexagonal honeycomb structures. (D) Relative compressive strength vs. relative density for honeycomb scaffolds and other 3D printed ceramics and glasses with fully open-porous struts. $\sigma_{ts,m}$: tensile strength of the matrix. (E) Compressive strength as a function of density. The graph shows data for honeycomb scaffolds with constant strut porosity (ε_s) of ~57% and slip-cast specimens based on capillary suspensions [87]. The dependence of strength on the density of the 3D printed samples fits well with the scaling laws for in-plane and out-of-plane loaded hexagonal honeycomb structures [89].

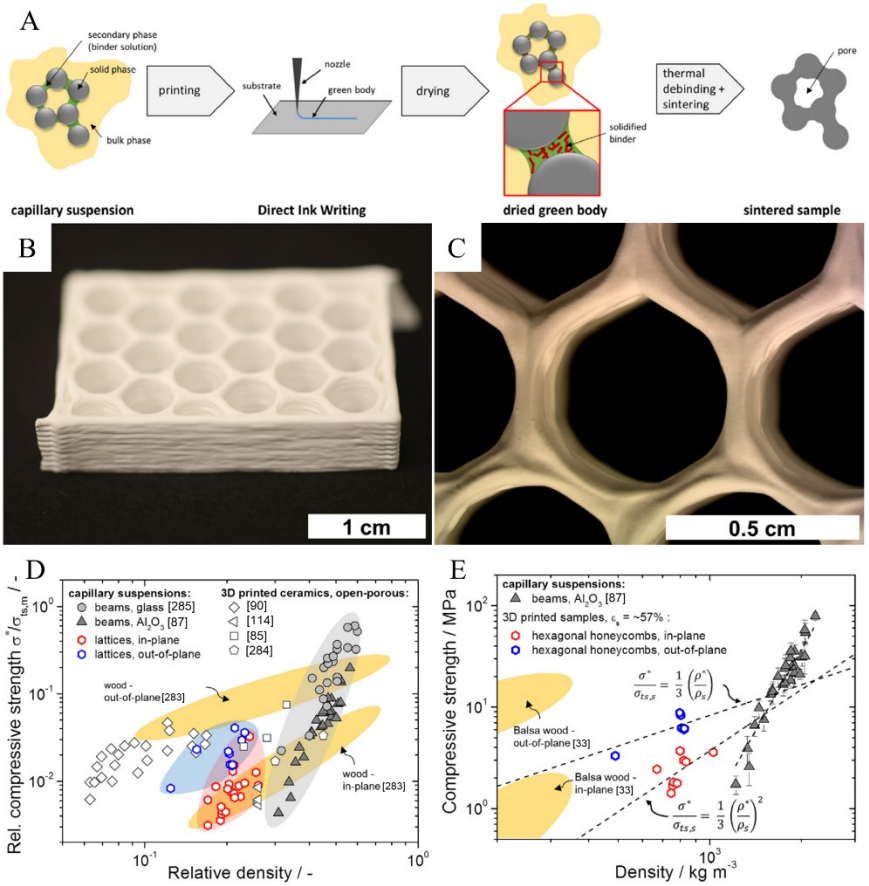

Source: Adapted from [87,88].
σ*: compressive strength; $\sigma_{ts,s}$: tensile strength of the struts; ρ*: overall density; ρ_s: density of the strut.

In the recent past, a new concept of 3D printing hierarchically structured ceramic solids by DIW with inks based on ceramic foams has been developed – named direct foam writing – and was employed by Minas *et al.* [90] for bioengineering applications. In their study, by the appropriate modification of alumina powders with short amphiphiles, ultrastable emulsions/foams with suitable DIW rheological properties were attained, which allowed the obtention of hierarchical alumina scaffolds with controlled pore size distribution and porosity (Fig. 11). In this combination of emulsion/foam templating and DIW, the mm-sized pores are determined by the interfilament distance, whereas the process parameters of the emulsification control the μm-sized macropores. The interconnectivity degree and the pore sizes of the emulsion/foam templated scaffolds were regulated by the addition of an interface-active molecule (partially hydrolyzed poly(vinyl alcohol) (PVA)), leading to the droplets stabilization

through a combination of the effect of particles and PVA molecules. The resulting structures had compressive strengths of 8 and 16 MPa for porosities of 93 and 88%, respectively. Therefore, this multiple-length scale porous architecture improved the scaffolds' mechanical efficiency as it maximized strength and minimized weight. The scaffolds occupied a thus far empty area of the strength-density diagram (blue symbols of Fig. 11(c)) – fact possible by utilizing a minimum solid content; just enough to create a load-bearing percolating network of struts at various length scales. The study obtained structures with porous filaments with 17.4 ± 12.9 μm average pore sizes (38 vol% Al_2O_3 and 0.01 mmol·g^{-1} valeric acid), as well as closed pore structures with much finer pores, 5.0 ± 2.8 μm, with a narrower size distribution (42 vol% Al_2O_3 and 0.04 mmol·g^{-1} propionic acid) and structures with 4.6 ± 2.2 μm interconnected pores with homogeneously dispersed 1.7 ± 0.6 μm windows between them (46 vol% Al_2O_3, 0.08 mmol·g^{-1} propionic acid, and 1 wt% PVA). As a result of the high stability of the particle-stabilized emulsions and foams, the authors could also combine inks with different droplet/bubble sizes, enabling local control of the pore sizes' spatial distribution and good bonding between the differing inks (Fig. 11(f-h)). Overall, the study showed that the combination of emulsion/foam templating and DIW is a versatile route for the production of hierarchical porous ceramics with complex geometries and multiporosity features with unprecedentedly high strength-to-weight ratios. By utilizing surface-active particles and PVA as stabilizers, either closed or open porosities can be attained, respectively, with the macroporosity's independent control at the mm and μm scales. Besides, it was demonstrated that similarly to biological materials, the load-bearing solid-phase hierarchical organization leads to improved macroporous structure mechanical efficiency. Still, further studies are demanded so that the porous hierarchical structures can cover a broader range of porosities, pore sizes and pore morphologies to enable the full exploitation of these promising structures.

Fig. 11. Alumina hierarchically structured scaffolds. (A) Schematical illustration of the processing of the hierarchical porous ceramics prepared by emulsion/foam templating and DIW. (B) Schematic illustration of the stabilization mechanism of the emulsions/foams. (C) Compressive strength vs. relative density of the Al_2O_3 porous scaffolds: with dense filaments (Δ); with closed porosity (□); with open porosity obtained with the addition of PVA (○); and prepared by direct foaming (⁕, Studart *et al.* [91]). (D) SEM images of: (top row/green) foam-templated architecture with closed porosity (38 vol% Al_2O_3 and 0.01 mmol.g^{-1} valeric acid); (middle row/red) emulsion-templated structure with closed porosity (42 vol% Al_2O_3 and 0.04 mmol.g^{-1} propionic acid); (bottom row/blue) PVA-containing emulsion-templated structure with open porosity (46 vol% Al_2O_3, 0.08 mmol.g^{-1} propionic acid and 1 wt% PVA). (E) Illustration of the compression test of scaffolds with (i) dense filaments, (ii) closed porosity and (iii) open porosity. (F) Images of concentric ring structures with increasing tilting degrees made through multiporosity printing of two different alumina-based inks. One of the inks was stained with Nile Blue A to ease visualization in the wet state. (G,H) SEM images of sintered porous structures showing the transition zone of the two different inks. The local structure can be deliberately tuned to show (i) dense alumina, (ii) closed pores or (iii) open pores.

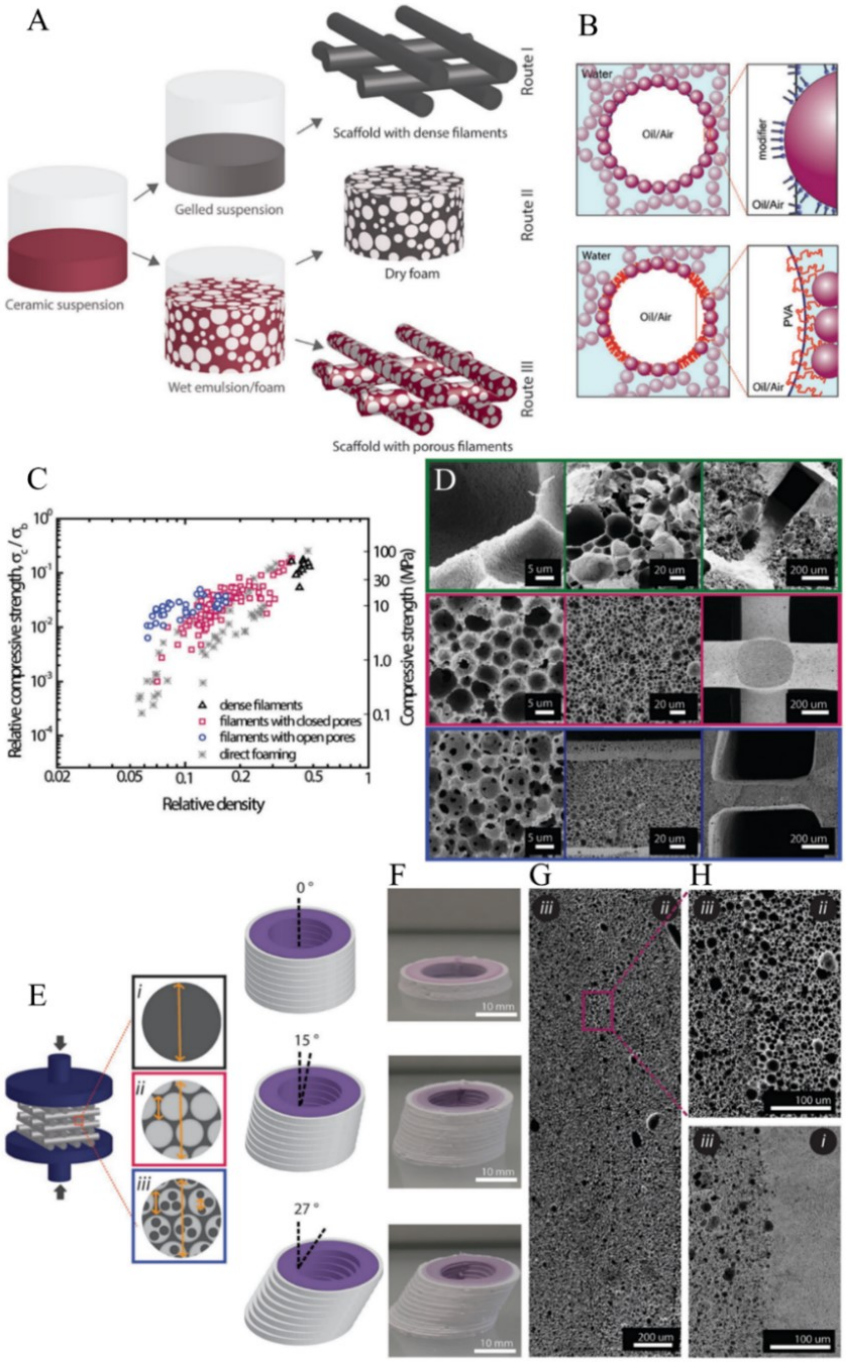

Source: Adapted from [90].

4.1.2. Zirconia

Zirconium dioxide (zirconia, ZrO_2) is another bioinert ceramic and materials based on it are among the most useful in the biomedical field. This extended use is due to its excellent mechanical properties (when compared to other ceramics, i.e., the highest toughness and strength among oxide ceramics [92,93]) and almost complete biological inertia. As a result of these properties, zirconia-based materials stand out in orthopedic and dental applications. Regarding structures developed by DIW, dense pieces for such uses are the most studied.

Dense components and scaffolds of zirconia (fully and partially stabilized YSZ (yttria-stabilized zirconia)) were designed with low-solid-content pastes (< 38 vol%) in a study by Peng *et al.* [28]. Relatively low sintering temperatures (1400 °C) could be achieved using precursors with higher specific surface areas. High relative densities were also obtained (95-96%). The overall content of organic additives was lower than 2 wt%; but, a high linear shrinkage (up to 33%) was observed. The authors utilized a non-toxic releasing agent (e.g., oleic acid) to coat the printing substrate to release the strain between the substrate-green body and to mitigate crack/deformation development associated with excessive shrinkage. Some defects/voids larger than 200 μm were found, which the authors attributed either to trapped air or releasing agent (oleic acid) between filaments in the first extrusion layer. Another hypothesis was that of materials' under-extrusion during the DIW process, which, after sintering, caused cracks. These defects could have diminished the mechanical properties, as the dense components and scaffolds had, respectively, flexural strengths (3PB) of ~243 and ~57 MPa – values that at their highest reached merely 22% of the flexural strength reported for CY3Z-P (3 mol% yttria-stabilized zirconia with high chemical purity) (3PB after compaction) [94]. Yet, the structures presented an elevated hardness of up to 1355 (HV).

When considering dental applications, zirconia dense components were examined by Branco *et al.* [70] to tribologically assess the pair of human teeth/zirconia produced by DIW, focusing on enamel wear mechanisms. Besides, the density, porosity, crystalline structure, hardness and toughness were compared with unidirectionally compressed (UC) zirconia. The DIW paste was composed of 3 mol% Yttria partially stabilized tetragonal zirconia powder (80 wt%), 2.4 wt% D(-)-fructose, 0.19 wt% Zusoplast® C92 and 0.03 wt% (relative to the solids) Dolapix® CE 64. The chewing simulation tests showed that both sample groups did not suffer any wear and that the antagonist cusps were worn similarly. In addition, the DIW samples had superior surface roughness (241 ± 16 nm) and slightly lower fracture toughness (4.5 ± 0.7 $MPa.m^{1/2}$) and lower hardness (1175 ± 29, HV) than UC samples (62 ± 4 nm, 5.6 ± 0.4

$MPa.m^{1/2}$, 1306 ± 19 (HV)). This fact was attributed to the higher porosity of the DIW components (superficial: 3.9 ± 1.7%; cross-cut: 1.2 ± 0.1%) compared to the UC ones (superficial: 0.3 ± 0.16%; cross-cut: ~0). The authors considered, as most of the properties between the two groups were similar, that DIW seems a promising method to obtain personalized zirconia dental implants, especially given the overall tribological behavior. Still, further clinical studies are required.

A study by Rodrigues *et al.* [63] also obtained zirconia dense components for dental applications from binder-free pastes that were sintered at 1500 °C for 2 h and that reached 97.1% of relative density. Pastes with 86-90 wt% of solid content were printable and the structures could reach a hardness of 1485 ± 32 (HV) and 4.1 ± 0.1 $MPa.m^{1/2}$ of fracture toughness. It was also found that brushing the component's green surface assisted in the obtention of a surface finish within the standards for dental prostheses. Even though further studies are required to ensure the structures' tribological and mechanical reliability, an environmentally friendly, cost-effective and personalized production of dental prosthetic components by DIW is closer to reality.

4.1.3. Other bioinert ceramics

Although most studies on DIW bioinert ceramics are on alumina and zirconia, other bioinert ceramics have been produced by DIW for biomedical engineering applications. For example, Chen *et al.* [72] conducted a study on optimizing the rheological properties of titania (TiO_2, with 72 wt% solid loading) inks containing sodium hexametaphosphate and sodium alginate to produce dense structures. The resulting pieces had 91.5% relative density, achieving a compressive strength of 125 MPa and elastic modulus of 1.22-6.87 GPa. In addition, silicon carbide (SiC) dense components were produced by Feilden *et al.* [67] with solid contents up to 40 vol%, 95% of relative density and 300 MPa of flexural strength.

Silicon nitride (Si_3N_4) has also been printed by DIW into dense [74] and scaffold [95] structures. The dense components reported by Zhao *et al.* [74] were printed with pastes containing Si_3N_4 powder, two sintering additives (Y_2O_3 and Al_2O_3) – resulting in 20 vol% solid content –, 0.9 wt% of Methocel® F4M and a combination of high and low molecular weight PEI (2.5 wt% high and 2.5 wt% low). The printed components were debinded at 300 and 600 °C with a 2 h hold in each temperature, subsequentially sintered at 1700 °C for 2 h in a N_2 atmosphere and then hot isostatic pressed (1700 °C, 2 h, N_2 atmosphere, 200 MPa of pressure). The obtained dense structures presented 552 ± 68 MPa of flexural strength (4-point bending,

4PB). On the other hand, scaffolds produced by Sainz *et al.* [95] were sintered either under a controlled N_2 atmosphere or by SPS (Spark Plasma Sintering) in a conventional graphite furnace. Aside from the Si_3N_4 powders, the pastes had high and low molecular weight PEI (50 wt%), 5 wt% Methocel® F4M and Darvan® 821 (n.d. (non-disclosed) quantity). They were printed with 330 μm nozzles in a paraffin oil bath, calcinated at 650 °C for 2 h and then sintered as described at 1700-1750 °C for 30-60 min. Different sintering aids (Y_2O_3, Al_2O_3, and SiO_2) were utilized, obtaining a strut diameter of 245-283 μm, linear shrinkage of ~18-24% and porosity of ~60% with 650-700 μm pore sizes. Compressive strength values showed a dependence with the β-Si_3N_4 phase content and reached ~60 MPa in structures containing over 69% of β-Si_3N_4 content. Besides, the scaffolds' bioactivity was affected by the phase composition of the grain boundary, with the highest bioactivity being observed for the composition $90Si_3N_4$-$4.11Y_2O_3$-$3.13Al_2O_3$-$2.76SiO_2$ (in wt%) (high amount of grain boundary YAlSiO glassy phase). Good affinity with albumin proteins was demonstrated by AFM (Atomic Force Microscopy) evaluations, which revealed protein adsorption after only 5 seconds of BSA (bovine serum albumin) solution exposure.

4.2. BIOACTIVE CERAMICS

Bioactive ceramics are materials that react once in contact with physiological fluids, forming bone-like hydroxyapatite layers and, consequentially, a strong chemical bond to bone tissues [96]. For this reason, several bioactive ceramics are of great clinical interest for biomedical engineering applications, such as calcium phosphates, bioactive glasses and calcium silicates.

4.2.1. Calcium phosphates

Calcium phosphates are ceramic materials with calcium (Ca^{2+}) and phosphate ions, which can be orthophosphates (PO_4^{3-}), metaphosphates (PO^{3-}), pyrophosphates ($P_2O_7^{4-}$) or sometimes carbonate or hydroxide ions [97]. They are well-known bioactive ceramics due to their compositional similarity with teeth and bone. One of their essential characteristics is the calcium (Ca) to phosphorus (P) ratio that influences their dissolution rate, which increases as the Ca/P ratio decreases [98], as can be observed in Table 4 for some calcium phosphates of interest. The Ca/P ratio also controls their bioactivity; a ratio of 1-2 has been shown to favor the osteoblasts' viability and ALP (alkaline phosphatase) production [99].

Table 4. Calcium phosphate materials of interest, their Ca/P ratio and dissolution properties.

Chemical name (mineral name)	Symbol	Chemical formula	Ca/P ratio	Solubility product
Monocalcium phosphate	MCP	$Ca(H_2PO_4)_2 \cdot H_2O$	0.50	1.00×10^{-3}
Dicalcium phosphate dihydrate (Brushite)	DCPD	$CaHPO_4 \cdot 2H_2O$	1.00	1.87×10^{-7}
Dicalcium phosphate (Monetite)	DCP	$CaHPO_4$	1.00	1.26×10^{-7}
Octocalcium phosphate	OCP	$Ca_8H_2(PO_4)_6 \cdot 5H_2O$	1.33	5.01×10^{-15}
Tricalcium phosphate	TCP	$Ca_3(PO_4)_2$	1.50	2.83×10^{-30}
Hydroxyapatite	HA	$Ca_{10}(PO_4)_6 \cdot (OH)_2$	1.67	2.35×10^{-59}
Tetra-calcium phosphate	TTCP	$Ca_4O(PO_4)_2$	2.00	—

Source: Adapted from [97].

Some promising alternatives to calcium phosphates have been recently studied and a good category is that of compounds containing magnesium phosphates (MgP), such as newberyite ($Mg(PO_3OH \cdot 3H_2O)$) and struvite ($NH_4MgPO_4 \cdot 6H_2O$). Cao *et al.* [100], for example, focused on newberyite, struvite and brushite ($CaHPO_4 \cdot 2H_2O$) scaffolds with a two-step cementation process and light MgO as starting material. The DIW paste was composed of MgO powder (~27 vol% solid content) and a 13 wt% aqueous Pluronic® F-127 solution and was printed with 300 μm nozzles. After the DIW assembly, the green structures were soaked in a diammonium phosphate ($(NH_4)_2HPO_4$) solution and then in distinct phosphate solutions to convert the structures into newberyite, struvite, and brushite. The structures had a porosity of approximately 39, 58 and 26%, respectively, and compressive strengths of ~6.1, ~2.4 and ~11.2 MPa. The struvite scaffold was the only one that induced cytotoxicity, a fact that the authors attributed to the strong alkaline environment that was developed during its degradation process. On the other hand, the newberyite and brushite scaffolds presented cytocompatibility and good *in vitro* degradation.

Still, hydroxyapatites and tricalcium phosphates are by far the most studied calcium phosphates for tissue engineering applications both in general and with the DIW method and will be highlighted in the following sections.

4.2.1.1. Hydroxyapatite

Hydroxyapatite (HA, $Ca_{10}(PO_4)_6 \cdot (OH)_2$) is a naturally occurring calcium phosphate and the most prominent biomaterial for bone tissue engineering applications [101]. Its Ca/P ratio is 1.67, which presents better biocompatibility than other calcium phosphates (β-TCP included) and also other well-known materials for bone regeneration (e.g., Bio-Oss®) [102]. Recent studies have shown it to be a very appropriate implant material, especially for scaffolds with strength comparable to that of cancellous bone, showing compressive strengths up to 5.1

± 0.5 MPa in addition to having been proven beneficial for human mesenchymal stem cell growth [103,104].

Regarding HA's use with the DIW processing method, a study by Miranda *et al.* [105] found that the compressive strength of HA scaffolds was doubled (~110 ± 35 MPa) after 2 weeks of immersion in SBF, which allowed it to reach values similar to those of cortical bone with a similar dry density. This remarkable increase was due to the growth of bone-like apatite on the HA struts' surface; the same experiment was conducted with β-TCP scaffolds, but their compressive strength remained unaltered. These pastes encompassed Darvan® C (n.d. quantity), Methocel® F4M (HPMC, n.d. quantity), PEI as a gellifying agent (n.d. quantity) and the ceramic powder, which in the case of HA represented a solid content of 35 vol% and in that of β-TCP 45 vol%. Thus, SBF immersion could be a simple and inexpensive mechanism to enhance the surface properties and, consequentially, the mechanical performance of scaffolds from apatite-forming materials.

The drying method of freeze-drying after the DIW process was evaluated by Martínez-Vázquez *et al.* [106], who produced HA scaffolds with 45 vol% solid content; the DIW pastes also presented Darvan® C (1.5 wt% relative to powder content), Methocel® F4M (n.d. quantity) and PEI (4 vol% relative to liquid content). The final structures were printed with a 410 μm nozzle and presented a porosity of ~73% and compressive strength of 5.3 ± 0.4 MPa. The microporosity's size and morphology within the filaments were significantly affected by the sintering temperature and the drying method. Larger (1-10 μm) dendritic-like microporosity was associated with the freeze-drying method, which improved the biological response; on the other hand, conventional drying improved the compressive strength of the scaffolds. The latter was also enhanced by higher sintering temperatures, even though cell proliferation behavior deteriorated. Therefore, the use of freeze-drying after DIW printing was found to be a mechanism that does not severely reduce the compressive strength of HA-derived scaffolds while enhancing their biological performance.

Natural occurring hydroxyapatite has also been employed with the DIW process. Mocioiu *et al.* [107] compared powders and DIW structures of HA from natural sources (whelk shells of *Rapana thomasiana*) with synthetic HA. It was found that the formation of nanostructured HA was independent of the raw material utilized and that natural HA from whelk shell lacked *in vitro* cytotoxicity and had similar cell viability to that of synthetic HA, thus opening a new explorable path in the field.

Ca-deficient (CDHA) and Si-substituted HA (SiHA) scaffolds have been reported by Matesanz *et al.* [108] with 90% relative density and 50 MPa of compressive strength. The pastes

encompassed 30 vol% of solid content, 2.5 wt% Darvan® C, Methocel® F4M (7 mg/mL of liquid) and PEI (4 vol% relative to the liquids); printing took place with 500 μm nozzles. The study evaluated bone cell growth for both HA types, either treated at 700 or 1250 °C. It was found that scaffolds treated at 700 ºC had higher surface areas and porosities. In contrast, scaffolds treated at 1250 °C had higher cell proliferation and differentiation, implying that CDHA and SiHA structures treated at high temperatures have better tissue response. This inferior cell response associated with a low-temperature treatment could result from poorly sintered surfaces that could generate a loss of cell anchorage. In addition, CDHA and SiHA scaffolds treated at 1250 ºC presented better mechanical properties and lower fibrinogen and albumin adsorption.

The DIW method was also utilized by Raymond *et al.* [109] when developing a hydrothermal method for the consolidation of α-TCP scaffolds and comparing it to a biomimetic treatment, in which there is no need for high-temperature sintering. They analyzed three different scaffold architectures (honeycomb, orthogonal and orthogonal rotated) and found that the hardening process related to the hydrolysis of α-TCP into CDHA in the hydrothermal method was significantly accelerated with the total reaction time going from 7 days to 30 minutes. This short period could allow the fabrication of on-demand scaffolds within a few hours, counting the time required for patient imaging, scaffold architecture selection, printing, consolidation and sterilization. The new hydrothermal treatment preserved the architectural integrity and nanostructure features of the scaffolds. Still, it reduced the compressive strength by 30% due to β-TCP residual presence (4.1 MPa compared with 5.5 MPa for the biomimetic treatment). The reliability was also decreased with the Weibull modulus of 5.6 for hydrothermally-immersed scaffolds and 8.8 for those treated biomimetically. Both treatments were proven appropriate for patient-specific bone grafts, given the rMSC (rat mesenchymal stem cell) colonization of the scaffolds.

4.2.1.2. Tricalcium phosphate

Tricalcium phosphate (TCP, $Ca_3(PO_4)_2$) is another calcium phosphate that is vastly used as a biomaterial. There are three main phases: α, α’ and β; with β-TCP being the primary phase at low temperatures and α and α’ being formed at high temperatures. The Ca/P ratio of TCP is 1.5, therefore, lower than HA, having a consequentially higher biodegradation rate. The additive manufacturing of TCP has mainly been applied to produce 3D scaffolds for bone tissue engineering applications.

In a study by Tovar *et al.* [110], β-TCP scaffolds with ~58.6% porosity and 38.8 MPa flexural strength (3PB) were produced. The printing paste had varying solid content from 42 to 50 vol%, 1.5 wt% Darvan® 821A, Methocel® F4M (7 mg/mL of liquid) and PEI as gellifying agent (5 mg/mL). No adverse immune responses were shown in the histological analysis at the same time that it revealed progressive bone remodeling within the scaffold and a gradual decrease of the scaffold's volume over time. The μ-CT (μ-computed tomography) images registered directional bone ingrowth, with increased bone formation over time. Newly regenerated bone presented reduced elastic modulus statistically homogenous and analogous to native bone at the three-time points analyzed (8, 12 and 24 weeks). In contrast, negative control samples presented limited healing at 8 weeks and hardness was shown to be equivalent to 24 weeks native radial bone.

β-TCP hollow cylindrical scaffolds were obtained through DIW by Lopez *et al.* [111]. The printing paste had 46 vol% of solid content, 1.45 wt% Darvan® 821A, Methocel® F4M (7 mg/mL of ceramic) and PEI (5-6.67 mg/mL). The DIW procedure occurred with 250 μm nozzles into paraffin oil, followed by debinding at 400 and 900 °C and sintering at 1100 °C for 4 h. The printing direction was chosen so that the axis of the tube would be parallel to the printing substrate. They were able to restore adult rabbit, critical-sized, mandibular defects to a level comparable to the native bone after 8 weeks of implantation. Histological and SEM (scanning electron microscopy) analyses revealed directional bone ingrowth into the scaffold interstices, with healing pathway origins tracked to defect walls and marrow spaces. New bone growth and scaffold resorption at scaffold/bone interfaces were also observed.

Casas-Luna *et al.* [112] focused on the effect of different sintering trajectories on β-TCP scaffolds. To obtain the printed structures, a mixture of monetite and hydroxyapatite was incorporated in a 40 wt% aqueous Pluronic® F-127 solution in a 1:1 ratio (wt) and deposited with struts of 450 μm of diameter. Fast and reactive pressure-less sintering at 1100 and 1200 °C could be achieved with fast-heating rates of 100 $°C.min^{-1}$ (10 min) in air or vacuum atmosphere, which resulted in superior densification with no significant grain growth. Furthermore, elastic modulus and hardness increased 8 times compared to conventional sintering alongside an increase of 1.5-2.5 times in the compressive strength (1-4 MPa). This superior mechanical performance's primary reason is the struts' higher densification, which implies that the β-TCP densification rules its mechanical performance instead of the grain size refinement. The fast heating rates induced no deformation of the 3D structure and there was no compromise of the macroporosity, as pressure-less sintering allows it to be preserved. Overall, the highest compressive strength was attained for scaffolds sintered at 1200 °C in vacuum.

Seitz *et al.* [113] evaluated TCP (50 wt% solid content) scaffolds utilizing an aqueous solution of dextrin (20 wt%) and saccharose (2.5 wt%) as printing binders. The structure intended for bone regeneration had mesh sizes of 150-750 μm, with 60 vol% micro and ~35 vol% macroporosity. The authors highlighted that optimal printing characteristics were achieved with a composition of 4 wt% binders and 2 wt% deflocculants. Nevertheless, the compressive strength remained an issue, as it was below 1 MPa.

A very well-known thermo-reversible gel (Pluronic® F-127) has also been considered by Franco *et al.* [27] to prepare β-TCP scaffolds. The pastes (n.d. solid content) contained the gel, which had low viscosity at low temperatures (i.e., the extrusion ones) and that, once deposited in a warm (60 °C) paraffin oil bath, underwent quick gelation. They found that, as the Pluronic® content was increased (3.8-15.6 vol%), strut microporosity varied in a wide range (25-43%) and that the flexural strength decreased accordingly from ~115 to ~89 MPa. The alumina substrates onto which the scaffolds were printed were coated with a double hydrophobic (permanent marker)-hydrophilic (corn syrup) layer, which promoted adhesion during the printing process but dissolved in a controlled way afterward, facilitating sample removal and avoiding the generation of stresses associated with drying and sintering. The scaffolds' strut diameter was approximately 80 μm and the relative density reached 99%.

4.2.2. Bioactive glasses

Bioactive glasses (BGs) are ceramic materials that contain SiO_2, Na_2O, P_2O_5 and CaO in different ratios. Most of them are based on silica (to form the glass network), with an amount of calcium and phosphorous (for new bone growth) and a glass modifier (e.g., sodium) [114]. Bioactive glasses have been one of the most promising bioceramics for bone tissue engineering since their 1969 breakthrough invention by Hench *et al.* due to their excellent *in vitro* and *in vivo* bioactivity [115,116]. Because of their wide compositional range, several types of BG have been studied, among which are 45S5, 47.5B, 58S, 13-93, 13-93B3, 2B6Sr and 6P53B – their compositions are displayed in Table 5. As it is not in the scope of this review to address the advantages and limitations of each bioactive glass system, a good discussion of this subject can be found in [117].

Table 5. Compositions of the most commonly utilized bioactive glasses.

Bioactive glass	Composition (wt%)							
	SiO_2	Na_2O	CaO	K_2O	MgO	P_2O_5	B_2O_3	SrO
45S5	45	24.5	24.5	–	–	6	–	–
47.5B	45.34	9.85	17.82	14.96	6.40	5.64	–	–
58S	58	–	33	–	–	9	–	–
13-93	53	6	20	12	5	4	–	–
13-93B3	–	5.5	18.5	11.1	4.6	3.7	56.6	–
2B6Sr	15.5	5.4	17.8	10.8	1.2	4.1	36.2	9.0
6P53B	52.7	10.3	18	2.8	10.2	6	–	–

Source: Author.

Bioactive glasses commonly have poor mechanical properties, not being suitable for load-bearing applications. However, scaffolds developed by additive manufacturing techniques, such as the DIW method, have been reported to attain an average elastic modulus and compressive strength similar to those of cortical bone, a fact promising for their application in loaded bone defects. These good properties are one reason why there have been so many studies with the DIW of bioactive glasses. The main features of the studies highlighted in this review are presented in Table 6 according to their glass synthesis technique and described in the sequence. A fact worth highlighting is that for sol-gel-derived BGs to exhibit *in vitro* behavior, both composition and structure are important, whereas the behavior of melt-derived BGs presents a direct dependence on composition [118].

Table 6. Comparison of melt-quenched and sol-gel bioactive glass scaffolds produced via DIW.

Glass synthesis	Glass type	Sintering temperature (°C)	Strut diameter (μm)	Pore size (μm)	Porosity (%)	Compressive strength (MPa)	Ref.
Melt-quenching	13-93	700	330	120	33-43	88 ± 20	[119]
				300 × 150	47 ± 1	86 ± 9	[120]
	13-93	700	~200	200 40-60 × 150	50	80.4	[121]
	2B6Sr	620				35.6	
	13-93	700	260 ± 10	260 × 140	47-50	86 ± 9	[122]
	13-93B3	560				40 ± 10	
	13-93B3 oriented	565				32 ± 9	
	13-93	690	300 ± 20	420 ± 30	50	142 ± 20	[123]
	13-93B3	560				65 ± 11	
	13-93	700	330	300	47 ± 1	88 ± 7	[124]
	13-93B3	560				28 ± 11	
	13-93 + 13-93B3	560				37-45	
	45S5	600	400	200	80	2.5	[125]
		800	360	180	72	5	
		1000	300	150	60	10	
		1000	200	100 × 250	63	13	[126]
		550 (Ar)	~400	~100-150 × 250	69	2.5	[127]
		1000 (Ar)			57.5	12	
		550	359 ± 9	-	24 ± 7	~2	[128]
		1000	306 ± 10	-	11 ± 7	~10	
	47.5B	600	300	150-180	42.5 ± 4.5	~10	[129]
	6P53B	700	≥ 50	500	60	136 ± 22	[29,130]
	FastOS®BG	800	~370	200	37	42	[131]
				300	54	28	
				500	65	21	
Sol-gel	Sr-MBG*	-	400	400	69-74	8-9	[34,132]
	MBG	-	250	300-400	70	5-12	[133]
	HSSGG	800	383	270	46.7 ± 1.8	5.4	[134,135]
				370		3.5	
				460		2.6	
	HSSGG + 5 wt% La^{3+}	800	380	270	42.6 ± 1.2	5.4	[136]
				370		3.5	
				460		2.6	
	HSSGG + 5 wt% Cu^{2+}	800	380	270	37.8 ±1.5	13.9	
				370		10.6	
				460		4.9	
	$Ca_7Si_2P_2O_{16}$	1400	Core (220-500)/shell (450-950)	-	55-85	1-4.5	[137]

Source: Author.

Asterisk (*) indicates composition 57.2SiO_2-7.5P_2O_5-35.3 (SrO + CaO), mol% with 0, 5, 10 or 20% of Ca substituted with Sr.

Bioactive silicate 13-93 glass scaffolds were developed by Xiao *et al.* [119] for the comparison of a grid-like microstructure to a porosity gradient (inner region with higher porosity and outer region with less porosity). This structure was intended to mimic the microstructure of long human bones, improving their flexural strength without significantly reducing the compressive strength and *in vivo* bone infiltration ability. Finite element modeling (FEM) was utilized to simulate the mechanical response in compression and flexion with the required microstructure predicted by FEM later produced and evaluated in four-point bending

and compression to validate the simulations. The DIW paste utilized had 40 vol% of solid content mixed with a 20 wt% aqueous Pluronic® F-127 solution and, after printing and drying, the scaffolds were debinded and sintered at 600 °C and 700 °C for 1 h, respectively. Scaffolds with a porosity gradient microstructure had flexural strength (34 ± 5 MPa) that was over twice the strength of the uniform grid-like microstructure (15 ± 5 MPa) alongside an also higher compressive strength (88 ± 20 MPa, with uniform grid-like microstructure scaffolds having 72 ± 10 MPa). Twelve weeks after the scaffolds' *in vivo* implantation in non-critical-sized rat calvarial defects, the extent of new bone infiltration showed by the histomorphometric analysis within the scaffolds with porosity gradient (37 ± 16%) was comparable to that of the grid-like scaffolds (35 ± 6%). The amount of BG-HA conversion in these 12 weeks was around 21% and, overall, the evaluations validated the FEM predictions. In summary, the study found that porosity gradient scaffolds that better mimic the microstructure of long human bones have enhanced mechanical properties and analogous *in vivo* bone infiltration capacity to uniform grid-like scaffolds.

Liu *et al.* [120] also used the DIW method to prepare 13-93 silicate glass scaffolds and performed a complete mechanical evaluation. They used the same composition as the previous study (40 vol% of solid content mixed with a 20 wt% aqueous Pluronic® F-127 solution), printed through a 410 μm nozzle and with the same debinding (600 °C) and sintering (700 °C for 1 h) conditions. The resulting scaffolds had 98 ± 1% relative density, 47% porosity, pore width of 300 ± 10 μm (deposition plane) and pore height of 150 ± 10 μm (z-axis). Under flexural loading, the strength, modulus and Weibull modulus were 11 ± 3 MPa, 13 ± 2 GPa and 6, respectively – with strength and modulus close to the lower end of those of cancellous bone. Under compression, the strength, modulus and Weibull modulus were 86 ± 9 MPa, 13 ± 2 GPa and 12, respectively – close to cortical bone values. A mean fatigue life of approximately 106 cycles was found for the scaffolds tested under compression either in air (room temperature) or in PBS (phosphate buffered saline) at 37 °C under 1-10 or 2-20 MPa cyclic stresses. There was a distinct reduction in the scaffolds' compressive strength during the first 2 weeks of SBF (simulated body fluid) immersion and *in vivo* implantation, but this decrease was slighter after that. Scaffolds immersed in SBF for up to 12 weeks had brittle mechanical behavior, whereas scaffolds implanted in rat subcutaneous sites changed their mechanical response from brittle to elastoplastic within 2-4 weeks. Furthermore, in comparison to scaffolds immersed in SBF *in vitro*, those implanted *in vivo* presented a more accelerated compressive strength deterioration due to a faster *in vivo* hydroxyapatite conversion.

Silicate 13-93 and borosilicate 2B6Sr scaffolds were reported with the same microstructure and compared by Jia *et al.* [121] with autografts (positive control) and empty defects (negative control) in critical-sized segmental defects in rabbit femur for extended periods. Both 13-93 and 2B6Sr scaffolds had 40 vol% of solid loading, the same macropore size and open porosity (50%) and compressive strengths of 80.4 and 35.6 MPa, respectively. Both scaffolds showed excellent osteogenic ability through histological analysis, comparable to that of autografts. The 2B6Sr scaffolds had a slightly faster degradation rate after 3 and 9 months of *in vivo* implantation than the 13-93 scaffolds. No visible interface was distinguishable in the three groups at 9 months post-implantation, exhibiting complete bone healing and bone-implant integration – the defects stayed unhealed after the same period in the empty group. The three groups also showed improved bone formation and regenerated bone hardness with increasing *in vivo* implantation time. After 9 months, the new bone hardness was comparable to that of the host bone. The 2B6Sr scaffolds and autografts had substantially higher bone formation than the 13-93 scaffolds; this higher 2B6Sr osteogenic capacity could be attributed to its faster degradation and, therefore, the release of soluble ions (including Sr which has a potent osteostimulatory effect). Finally, both groups of scaffolds had their ability to support angiogenesis confirmed by immunohistochemical analysis, without any significant difference between all groups after 9 months.

Bi *et al.* [122] printed scaffolds of 13-93, 13-93B3 and 13-93B3 with an oriented microstructure (13-93B3 (OR)), evaluating their critical-size segmental defects healing capacity and comparing them to autografts. The DIW pastes of 13-93 encompassed 40 vol% solid content and 20 wt% aqueous Pluronic® F-127 solution, whereas the 13-93B3 pastes were made with 40 vol% of solid content, 12.8 vol% ethyl cellulose, 4.3 vol% PEG and 42.9 vol% ethanol; this difference was due to the higher reactivity of the latter. All structures obtained had a porosity of 47-50%. The 13-93, 13-93B3 and 13-93B3 (OR) scaffolds had good mechanical properties with compressive strengths of 86 ± 9, 40 ± 10 and 32 ± 9 MPa, respectively. The results showed that the new bone percentage of defects implanted with the BGs (25-28%) as well as the total von Kossa-positive area (32-38%) and the new blood vessel area (4-8%) did not present a significant difference from the autografts (38, 40 and 5%, respectively; $p=0.05$). Besides this, the percentage of new cartilage formed in the 13-93 scaffolds (18%) was significantly higher than that formed in 13-93B3 (8%) and autografts (8%) ($p=0.02$). The autografts and all three bioactive glass scaffolds integrated well with bone, and supported angiogenesis, new bone growth and conversion to HA, with no significant difference between them.

Gu *et al.* [124] designed silicate (13-93) and borate (13-93B3) bioactive glasses as well, in addition to a combination of them (13-93 + 13-93B3) with volume fractions varying from 0 to 100%. The silicate and borate scaffolds were made with the same composition as the paste of the previous study, had 330 μm strut diameters and 47% porosity (300 μm pore sizes). As for the scaffolds made of a combination of the bioactive glasses, they were either composed of an inner region of 13-93 BG (3.8 mm of diameter) with a thin outer layer of 13-93B3 (0.4 of thickness) or an inner region of 13-93 BG (diameter of 3.3 mm) and a thick outer layer of 13-93B3 (0.65 of thickness). The glass phase (13-93:13-93B3) in the scaffolds was 67:33 (vol%) for the first group and 50:50 (vol%) for the second group. The study showed that increasing 13-93B3 volume fractions decreased the *in vivo* bone regeneration capacity, with the new bone percentage in the defects with 13-93 scaffolds (6 weeks: 23 ± 4%; 12 weeks: 28 ± 8%) being significantly higher than in the defects with 13-93B3 scaffolds (6 weeks: 6 ± 4%; 12 weeks: 9 ± 7%). After 12 weeks of *in vivo* implantation, the 13-93 glass was merely partially converted into hydroxyapatite, while the 13-93B3 glass was nearly fully converted after 6 weeks. The authors estimated that the lower capacity to support bone regeneration of the 13-93B3 scaffolds could be related to the high concentration of boron released from their rapid conversion to HA. In mechanical terms, an increasing amount of 13-93B3 led to reduced compressive strengths and elastic moduli, with pure 13-93, pure 13-93B3 and the composite of both presenting compressive strengths of 88, 28 and 41 MPa, respectively.

The same silicate (13-93) and borate (13-93B3) bioactive glasses' scaffolds were also compared by Deliormanli *et al.* [123], in biological and mechanical terms. The 13-93 BG pastes contained 45 vol% of solid content, 20.1 vol% of ethyl cellulose acting as a binder and 6.8 vol% of PEG acting as a plasticizer, whereas the 13-93B3 BG pastes had 40, 12.8 and 4.3 vol%, respectively; the solvent used was ethanol. The scaffolds obtained had strut diameters of 300 ± 20 μm and approximately 50% porosity with pore sizes of 420 ± 30 μm. It was found that the borate 13-93B3 scaffolds, when immersed in SBF, had a faster conversion into a hydroxyapatite-like material than the silicate 13-93 scaffolds but also presented a more pronounced reduction in strength with immersion time. Excellent mechanical properties were observed, especially for the silicate 13-93 scaffolds with a compressive strength of 142 ± 20 MPa, a value that decreased to 79 ± 32 MPa after 50 days of immersion in SBF. The borate 13-93B3 scaffolds, in comparison, had a compressive strength of 65 ± 11 MPa that was reduced to 8 ± 4 MPa after the same period in SBF. The weight loss of the borate and silicate scaffolds after 60 days in SBF was 56 and 5.7%, respectively, with the conversion product consisting of an amorphous calcium phosphate material. The same group also made a supplementary study

[138] to evaluate different pore sizes' effects on the biological response. The pore widths assessed were 300 ± 10, 600 ± 20 and 900 ± 50 μm and were shown to have little impact on angiogenesis and tissue infiltration after 4-week implantation, with no histological difference in the fibrous tissue formed and no significant difference in the *in vivo* total area of blood vessel formation.

A comparative study of 45S5 bioactive glass scaffolds with 45 vol% solid content (with 1 wt% carboxymethyl cellulose (CMC)), either fully amorphous (sintered at 550 °C) or mostly crystalline (sintered at 1000 °C), has also been performed [128]. The amorphous scaffolds had a slightly wider strut diameter (359 μm) and higher porosity (24%) when compared to the crystalline scaffolds (306 μm and 11%). The amorphous scaffolds also exhibited faster calcium carbonate/phosphate precipitation and improved *in vitro* degradation, facts attributed to faster volumetric diffusion of the involved species through the amorphous structure. However, cell proliferation of the amorphous scaffolds was not higher than that of the crystalline ones – structures that, as expected, also had a better mechanical performance with the compressive strength of amorphous scaffolds being ~2 MPa compared to ~10 MPa of crystalline scaffolds. The mechanical degradation after SBF immersion was initially faster for amorphous scaffolds (due to their faster reaction kinetics) but with longer immersion periods, slightly accelerated in glass-ceramic scaffolds due to the crack generation in the mineralization layer. Through *in vitro* tests with MC3T3 osteoblastic cells, the study found that sintering 45S5 scaffolds at 1000 °C, causing their densification and crystallization, enables the improvement of cell proliferation and long-term *in vitro* cell viability by the prevention of an excessively fast ion release from the bioactive glass scaffold.

Fu *et al.* [29,130] examined 6P53B bioactive glass scaffolds with 30 vol% solid content. This BG composition was a modified version of the original 45S5 glass, mainly designed to enlarge the sintering window without crystallizing the glass. The mixture of BG particles (particle size (D50) of 1.2 μm, 30 vol%) and 20% Pluronic® F-127 solution was printed with 100 or 250 μm on an alumina substrate within a paraffin oil reservoir at 40 °C, subsequently dried and sintered at 700 °C. The hydrogel-based glass ink resulted in a structure with 500 μm pores and completely dense struts with diameters over 50 μm. The scaffolds' porosity attained was 60%, similar to that of cancellous bone (50-90%), whereas the compressive strength of the scaffolds achieved 136 MPa, a value comparable to human cortical bone – an impressive achievement. Even with the reduction due to the weight loss during the 3-week SBF immersion, the compressive strength remained high (77 MPa).

Olhero *et al.* [131] developed an alkali-free FastOs®BG scaffold of a diopside-fluorapatite-tricalcium phosphate system (38.49SiO_2-36.07CaO-19.24MgO-5.61P_2O_5-0.59CaF_2, mol%). The DIW slurry had 47 vol% of solid content, Aristoflex® TAC as a gelling agent and hydroxypropyl methylcellulose (HPMC) as a binder. The study encompassed the optimization of the rheological behavior, focusing on the effects of the particle size distribution and type and amount of processing additives. It was found that attrition milling was the most efficient grinding method to obtain fine particles and that the particle size distribution, as expected, was a vital characteristic for the packing efficiency of the glass powders, their rheological flow behavior and maximum attainable solid loading. The distinguished processing and sintering ability of the BG scaffolds resulted in good mechanical properties. Scaffolds with 200 μm pore sizes had 37% porosity and 42 MPa of compressive strength, whereas those with 300 μm had 54% and 28 MPa and those with 500 μm pore sizes presented 65% porosity and strength of 21 MPa. These compressive strength values were comparable to those of cancellous bone.

Mesoporous bioactive glass (MBG) is a usual nomenclature for bioactive glasses with hierarchically porous structures (ordered mesopores and regular macropores). These glasses also have great potential for bioengineering applications due to their enhanced surface area and unique pore structures, compared to conventional BG, which enable the loading of drugs or osteogenic agents for bioactivity improvement [139]. With that in mind, Zhang *et al.* [34,132] produced strontium-containing MBG (57.2SiO_2-7.5P_2O_5-35.3(SrO+CaO), mol%) scaffolds with 0, 5, 10 or 20% of Ca substituted with Sr. The Sr-MBG powders were prepared through sol-gel methods, added to an aqueous 10% PVA solution and printed into scaffolds with ~69-74% porosity and ~400 μm pore sizes. It was found that, with increasing Sr substitution, the structures had a slower ion dissolution rate and higher potential to stabilize the pH of the environment. The Sr-MBG scaffolds presented good apatite-forming ability and stimulated the proliferation and differentiation of osteoblastic cells (MC3T3-E1) and the formation of new blood vessels in critical-sized rat calvarial defects in 8 weeks. The study also showed a sustained drug delivery property of the Sr-MBG scaffolds, with dexamethasone being used as a model drug. Besides, their compressive strength was around 8-9 MPa, which could be maintained to ~7 MPa after 7 days of SBF immersion. Overall, the advantages of good bone-forming bioactivity and compressive strength, controlled ion release and drug delivery possibility make the Sr-MBG scaffolds promising for bone regeneration applications.

Angiogenesis is a factor crucial for bone defect healing, especially for critical-size defects. It is predicted that since the blood vessels transport nutrients and oxygen to sustain

healthy bone growth, angiogenesis improvement should also increase osteogenesis. In this regard, stimulated angiogenesis has been found directly interrelated to the presence of copper (Cu) ions [140,141], which have improved angiogenesis in full-thickness skin wounds and subcutaneous sites in rodents by the delivery of Cu ions by borate bioactive glass scaffolds [142,143]. Therefore, Lin *et al.* [144] produced Cu-doped 13-93 bioactive glass scaffolds by DIW with 0 to 2 wt% CuO additions to evaluate if the release of inorganic ions could be a viable alternative to the use of growth factors for tissue healing improvement. The scaffolds were obtained by printing pastes with 40 vol% of solid content mixed with a 20 wt% aqueous Pluronic® F-127 solution with subsequent drying, debinding at 500 °C and sintering at 700 °C for 1 h. The results showed that when *in vitro* immersed in SBF, the release of Cu ions into the medium took place in a dose-dependent manner and the scaffold was partially converted to hydroxyapatite. The CuO additions of 0.4 and 0.8 wt% did not affect the proliferation, ALP activity (MC3T3-E1 cells) and the percentage of new bone that infiltrated the scaffolds (46 ± 8%) after 6 weeks in rat calvarial defects, but all three characteristics were inhibited by the 2 wt% CuO additions, with the percentage of new bone being 0.8 ± 0.7%. On the other hand, the new blood vessel area in the fibrous tissue infiltrating the scaffolds improved with the CuO doping and was significantly superior in scaffolds with 2 wt% CuO. Regarding their biocompatibility, doping with up to 0.8 wt% CuO did not affect it, but 2 wt% CuO additions to the 13-93 scaffolds were toxic to the cells and detrimental to bone regeneration; nonetheless, the study highlighted that even higher Cu additions have been proven nontoxic in other studies [144]. Still, the authors foresaw that the addition of clinically safe doses of growth factors (i.e., BMP2) could be a more efficient method than Cu doping silicate bioactive glass scaffolds in the regeneration of bone defects.

A high silica sol-gel glass HSSGG ($64.4SiO_2$-$4.9Na_2O$-$21.53CaO$-$9.09P_2O_5$, wt%) scaffold was also evaluated after being produced by DIW by Ben-Arfa *et al.* [134,135]. Usually, sol-gel BG powders present high volume fractions of micro- and meso-porosities, a fact that can be detrimental for colloidal processes such as DIW since the powders can adsorb a significant fraction of the dispersing medium, consequently impairing the paste dispersion and flow. To reduce this dispersing liquid uptake, prevent the excessive exposure of the surface area to the liquid and achieve a relatively high solid loading (≤ 40 vol%), sintering at 800 °C for 2 h was used to obtain a small portion of fine pores (mesopores < 30 nm) in the powders. The printing paste was obtained by gradually dispersing the powder into a 1.1 wt% aqueous CMC solution. The BG powders underwent partial crystallization with complete heat treatment (calcination and sintering), hindering extensive densification upon sintering. Hydroxyapatite

formation was observed after 72 h of SBF immersion. The scaffolds had 383 μm strut diameters and a considerable fraction of open micro-porosity (~36%) was left in the struts after sintering. This notable micro-porosity level limited the scaffolds' compressive strength (~5 MPa for those with 300 μm macro-pore sizes). However, it was prone to improve the *in vitro* and *in vivo* behavior of the scaffolds in tissue engineering and bone regeneration applications. In a complementary study, Ben-Arfa *et al.* [136] took a step further with the same HSSGG sol-gel glass and evaluated the effect of ion doping with Cu^{2+} and La^{3+} on the slurry printability and the scaffolds' mechanical properties. The doping ions, especially La^{3+}, acted as glass modifiers and led to fewer silica polymerization extents, which favored the glass powder milling and the obtention of smaller mean particle sizes. Mechanically, the addition of La^{3+} induced a slight improvement (7-18%) in the compressive strength (≤ 5.4 MPa); however, a much more significant improvement (up to 221%) was observed with the Cu^{2+} addition, achieving compressive strengths up to ~14 MPa. This difference in mechanical enhancement could be attributed to ionic radii differences. Copper has a much smaller ionic radius (0.73 Å) when compared to La (1.06 Å) [145], alongside a lower valence, granting Cu a higher diffusion coefficient, which makes it an effective sintering aid that enhances the densification and, by consequence, the mechanical properties. Therefore, glass doping showed itself as an approach for improving the mechanical properties of scaffolds for bone regeneration applications.

In an interesting study, Luo *et al.* [137] designed a composite scaffold of hollow struts from a solution of alginate and water-soluble PVA combined with bioactive glass nanoparticles ($Ca_7Si_2P_2O_{16}$) with dexamethasone. The preparation of the printing paste involved mixing the bioceramic and alginate powders with a 20 wt% Pluronic® F-127 solution. After printing, the scaffolds were sintered at 1400 °C for 3 h. A coaxial 3D printing strategy was utilized to obtain the multi-oriented hollow channels of the BG/alginate scaffolds, which presented high surface area and porosity (~55-85%) with a compressive strength of ~1-4.5 MPa – higher than that obtained in their previous study with MBG involving solely cross-linking and not sintering [146]. Usually, scaffolds with a single type of macropore (as those made of hollow struts) have comparably low pore surfaces and porosity with limited availability of nutrients and oxygen in the center of the scaffold. Nonetheless, the obtained structure of hollow struts improved cell attachment and proliferation, promoted *in vivo* bone ingrowth with the formation of bone tissue even in the center of the scaffolds and led to better control of the degradation rate.

4.2.3. Silicates

4.2.3.1. Calcium silicates

Calcium silicates are another type of bioceramic that has drawn much attention for bone regeneration applications because of their outstanding bioactivity. They can be divided into binary ($CaO–SiO_2$), ternary ($CaO–MgO–SiO_2$) and quaternary ($SrO–ZnO–CaO–SiO_2$) systems, but the calcium silicate that has by far been the most used alongside the DIW method for bone regeneration is wollastonite ($CaO–SiO_2$) due to its great bone repair potential [147,148]. This vast utilization is endorsed by the studies highlighted next.

Shao *et al.* [149,150] compared Mg-substituted (~10%) wollastonite-based scaffolds with three other groups of bioceramics scaffolds (pure wollastonite, β-TCP and bredigite). The DIW pastes had 56.5 wt% solid content mixed with a 6% PVA solution and the printing procedure was conducted with 450 μm nozzles. They found that the Mg-substituted wollastonite scaffolds had the largest pore sizes but the lowest porosity (52.1%), primarily due to the considerable shrinkage during sintering. Additionally, these scaffolds were the ones that had the highest osteogenic capability among the four groups evaluated, corroborating the wollastonite's great potential for bone repair stated in the literature. Mg-doped (10 wt%) wollastonite scaffolds with excellent mechanical properties and porosity of 51% (350 μm pore sizes) have been achieved in another study [151]. In this investigation by Liu *et al.*, the pastes were similar to that of the previously described study with 55.5 wt% of solid content mixed with a 6% PVA solution; these were printed through 450 μm nozzles, dried for 24 h at 60 °C and sintered at 1100 °C for 3 h. The Mg-doped wollastonite's compressive strength (~115 MPa) was over 4-fold higher than that of pure wollastonite scaffolds (~26 MPa) and presented a compressive modulus of 800 MPa. The doped scaffolds had accelerated new bone growth (6-18 weeks) and an elastoplastic response to match the rabbit femur's strength (10-15 MPa) after 18 weeks which was mechanically outstanding. They also experienced mild resorption and their pore walls had a constant phase conversion of calcium silicate into biological apatite.

One characteristic imperative for optimizing bone repair in calvarial defects is the scaffold's side-wall pore architecture. With this in mind, Shao *et al.* [152] examined scaffolds with 53-58% porosity of wollastonite or Mg-doped (6%) wollastonite to evaluate the role of this characteristic on the scaffolds' mechanical properties and osteogenic capacity. The DIW pastes presented 57.4 wt% of solid content mixed with a 6% PVA solution. After the printing procedure with 450 μm nozzles, the scaffolds were dried at 80 °C. The study encompassed two

different layer deposition modes – single-layer printing (SLP, 0°/90°) and double-layer printing (DLP, 0°/0°/90°/90°) – both undergoing a sintering process of one or two steps (one-step: plateau at 320 °C for 45 min and 500 °C for 60 min with a target temperature of 1150 °C for 3 h and natural cooling; two-step: heating to 1150 °C, holding for 45 min, rapidly cooling down to 1060 °C in 10 min and holding for 3h). It was found that the processes of Mg doping and two-step sintering were particularly advantageous for the enhancement of the flexural (~6–18 MPa) and compressive strengths (~25–103 MPa) of the calcium silicate scaffolds. The SLP scaffolds presented a high *in vivo* osteoconduction at an early stage (4 weeks), but for a long-time stage (8-12 weeks), the DLP scaffolds had a higher osteogenic capacity. Even though this higher osteogenic capacity in the long-term was linked to DLP pure wollastonite scaffolds, those DLP with Mg addition displayed excellent fracture resistance and appreciable new bone tissue ingrowth. The study revealed that Mg doping and two-step sintering are two encouraging approaches to improve the mechanical strength of calcium silicate scaffolds and hold promise for the 3D printing of thin-wall porous scaffolds to treat craniomaxillofacial bone defects.

An adjustable component distribution was obtained by Jin *et al.* [153] utilizing core-shell structures to print scaffolds. With this strategy, the scaffolds printed had a wollastonite shell and a core that could be wollastonite or Mg-doped wollastonite (4 or 10% of Mg-substituting Ca ratio). To obtain the printing pastes, the ceramic powders were separately dispersed in 6% PVA solutions and printed with coaxially-aligned nozzles with core and shell interior diameters of 400 and 900 μm, respectively. The scaffolds were dried at 80 °C for 24 h and sintered at 1150 °C for 3 h. The resulting structures had 50-58% porosity, 750 μm-diameter struts and improved mechanical properties with increasing Mg content. Wollastonite, 4 wt% Mg-doped and 10 wt% Mg-doped wollastonite presented compressive strengths of 11.2, 39.4 and 80 MPa, respectively – an increase attributed to enhanced sintering properties and denser struts with higher Mg percentage. After 14 days of SBF immersion, all the core-shell samples formed an apatite layer, indicating their bioactivity. Overall, these different distributions in the core-shell structures led to tunable strength and degradation. Their study and many others have proven the core-shell approach promising for tailoring component distribution, microstructures, and, consequently, mechanical and biological properties [153–155].

An unusual configuration with a hierarchical structure of "hot-dog-like" scaffolds of a different calcium silicate – akermanite ($Ca_2MgSi_2O_7$) – was developed by Li *et al.* [156] through a combination of DIW and bidirectional freeze-casting. The structure consisted of hollow tubes ("bread", ~1 mm pore size) embedded by struts ("sausage", ~500 μm diameter) with uniformly aligned lamellar micropores. The scaffold, which had a varying solid content of

20, 30, 40 and 50 vol% (with also 2 wt% of PVA and 1 wt% of sodium polyacrylate), presented 28 to 43% porosity and had excellent drug and protein loading and releasing abilities. The study found that the designed structure could deliver icariin (a model osteogenic drug) as well as a large molecule protein such as bull serum albumin (BSA) and that this controlled delivery and the hierarchical structure itself helped improve the *in vivo* bone-forming bioactivity.

4.2.3.2. Polymer-Derived Ceramics

Polymer-derived ceramics (PDC) are materials made from preceramic polymers converted into ceramics through controlled heat treatments. The PDC route involves shaping the polymer (e.g., DIW method), then its crosslinking or gelling and later its conversion into ceramic through pyrolysis at adequate temperatures (usually higher than 800 °C), a process that breaks the C-H bonds, releasing CH_4, H_2 or other volatile compounds, forming an inorganic material [157].

The polymeric precursors, mainly Si- or B-based, make it possible to obtain a wide range of ceramic materials such as silicon-oxycarbide (SiOC), silicon-carbonitride (SiCN), silicon-oxycarbonitride (SiOCN), silicon-boron carbonitride (SiBCN), silicon nitride (Si_3N_4), silicon-carbide (SiC) and boron nitride (BN) [157]. These PDCs are the most recognized ones, nevertheless, many other ceramics can be produced by the PDC route.

The obtention of porous-structured ceramics through polymeric precursors has many advantages over the conventional sintering of ceramic powders. These include (1) the lower temperatures required for the polymer-to-ceramic conversion; (2) the fact that the shaping of the polymer precursors can be made with inexpensive polymer-forming techniques, as is the case of DIW and (3) the possibility of achieving intermediate products with a combination of the ceramic-like properties and the polymeric nanostructure (“Ceramers”), by heating at temperatures that are within the polymer-to-ceramic transformation range [157].

Some technological challenges related to polymer-derived ceramics remain. The most crucial is the release of gaseous species during the preceramic polymer pyrolysis, in addition to its associated shrinkage, which impedes the direct fabrication of bulk structures. There are strategies to minimize these issues (i.e., adding reactive or inert fillers), but the manufacture of fully dense pieces is still a challenge. Nevertheless, polymer-derived ceramics have been increasingly investigated and are considered promising materials for the fabrication of scaffolds for bioengineering applications. Some interesting studies encompassing PDCs are featured in the next paragraphs

A preceramic polymer (MK, polymethylsilsesquioxane), alongside reactive fillers ($MgO/Mg(OH)_2$ and $CaCO_3$), composed the paste utilized by Dasan *et al.* [158] to fabricate akermanite ($Ca_2MgSi_2O_7$) hierarchically porous scaffolds by DIW. First, the MK polymer was dissolved in isopropyl alcohol and mixed with fumed silica in an amount corresponding to a ratio between MK-derived silica and FS of 9:1 (wt). Then, active oxide fillers were incorporated into the paste in quantities corresponding to a $CaO:MgO:SiO_2$ molar ratio equal to 2:1:2 – equivalent to stoichiometric akermanite ($Ca_2MgSi_2O_7 = 2CaO{\cdot}MgO{\cdot}2SiO_2$). The use of MgO (nano) and $CaCO_3$ micro-particles as reactive fillers produced crack-free scaffolds that either had dense or porous struts. The first group (scaffolds with dense struts) had a porosity of ~58% and 7.3 MPa of compressive strength, whereas the latter (scaffolds with porous struts) had ~69% and 4.2 MPa. The authors also added hydrated sodium borate ($Na_2H_4B_4O_9{\cdot}nH_2O$) to the paste with a triple purpose. It helped in attaining phase purity and eliminating cracks (it formed a liquid phase upon firing, granting structural integrity and phase evolution) and enabled the achievement of hierarchically porous structures as the release of water vapor could happen at low temperatures, therefore, before the ceramic transformation. Hence, the complex porosity distribution produced by formulations encompassing hydrated sodium borate could be utilized for the obtention of a new generation of glass-ceramic scaffolds.

Fiocco *et al.* [159] also utilized the PDC route while designing scaffolds of calcite surrounded by an amorphous silica binding phase with 56-64% porosity and 300 μm strut diameters (410 μm nozzles). The paste had a weight balance of $SiO_2/CaCO_3$ of 35/65 (wt%) and, to obtain it, fumed silica powders were mixed with MK (polymethylsilsesquioxane) in isopropyl alcohol, with subsequent incorporation of $CaCO_3$ micro-sized powders. It was printed within a vegetal oil bath, then primarily cross-linked at 350 °C and ceramized in air at 600 °C. The low temperature used for the thermo-oxidative decomposition (i.e., conversion of polymer into amorphous silica) is far lower than the usual temperatures for silicone-derived ceramics and avoided calcite decomposition. The silica-bonded calcite scaffolds had compressive strengths of 2.9-5.5 MPa, good *in vitro* bioactivity and cell adhesion and proliferation abilities, making them suitable candidates as scaffolds for the regeneration of cancellous bone defects.

Fu *et al.* [160] focused on β-dicalcium silicate ($\beta\text{-}Ca_2SiO_4$) scaffolds with a porosity of ~78-81% and 400 μm pore sizes from a preceramic silicone resin (polysilsesquioxane) loaded with $CaCO_3$ active filler. The paste was made by dissolving the silicone resin in isopropyl alcohol and adding the $CaCO_3$ powder (Ca/Si molar ratio of 2:1), whereas printing took place with 400 μm nozzles and varying angles between successive layers of 0°, 60° and 120°. The scaffolds were sintered at 1000, 1100 and 1200 °C and presented excellent apatite

mineralization ability. The study found that higher sintering temperatures significantly improved the compressive strength (5.2 ± 0.7 MPa) of the scaffolds and stimulated the rat bone mesenchymal stem cells (rBMSCs) adhesion and proliferation as well as the alkaline phosphatase activity and the osteogenic-related gene expression of the cells.

Hardystonite ($Ca_2ZnSi_2O_7$) polymer-derived scaffolds with 350 μm-diameter struts and approximately 80% of porosity have also been produced through DIW by Zocca *et al.* [161]. They assessed the influence of the heat-treatment atmosphere on the crystalline phase assemblage, morphology and compressive strength. The DIW paste was achieved by dispersing fumed silica (1.9-2.5 wt%) in isopropyl alcohol, adding a preceramic polymer (MK - polymethylsilsesquioxane, 20.3-26.4 wt%) and then ceramic fillers ZnO (12.8-16.7 wt%) and $CaCO_3$ (31.6-41 wt%); some printing pastes also had some hardystonite powder as a filler (21.2 wt%). The preceramic polymer and the fumed silica added had the double purpose of reacting with the filler to form the hardystonite phase upon heat treatment and granting adequate rheological properties – the first acted as a polymeric binder, increasing the viscosity and the latter formed a network of colloidal agglomerates of silica, inducing a "gel-like" behavior. A 410 μm nozzle was used to print the structures in a sunflower oil bath. The scaffolds were cross-linked at 200 °C and then treated with two different heat treatment atmospheres: air or nitrogen. The heat treatment performed in air developed the aspired hardystonite phase. In contrast, the heat treatment in nitrogen formed wollastonite polymorphs, a fact attributed to zinc oxide carbothermal reduction followed by metallic zinc evaporation. The addition of a hardystonite inert filler eliminated almost entirely the crack presence in the ceramized scaffolds and the final structures presented mechanical properties suitable for non-load-bearing bioengineering applications (compressive strength of 1.6 ± 0.3 MPa).

Polymer-derived hardystonite has been the focus of Elsayed *et al.* [162] as well. They obtained B-doped hardystonite ($Ca_2Zn_{1-x}B_{2x}Si_{2-x}O_7$) scaffolds through air thermal treatment of silicone resins. The printing paste was achieved by the dissolution of the preceramic polymer MK (27 vol%) in isopropyl alcohol, its mixture with fumed silica and subsequentially with $CaCO_3$, ZnO and dehydrated colemanite. The DIW procedure took place with 410 μm nozzles in a sunflower oil bath and, after drying, the scaffolds were cross-linked at 200 °C for 1 h and heat treated at 950 °C for 1 h. The calcium borate added to the silicone-based mixture acted, upon firing, as a micro-sized oxide reactive filler, granting a liquid phase, promoting ionic interdiffusion and developing B-containing hardystonite-based structures with ~68% of porosity. Even though the developed scaffolds were fired at a lower temperature than other previously obtained silicone-derived hardystonite structures (usually 1200 °C), the B-doped

hardystonite scaffolds showed a substantial enhancement of the mechanical properties, presenting compressive strength of ~5 MPa.

In another study [163], the same group developed Sr/Mg-doped hardystonite ($Ca_{1.4}Sr_{0.6}Zn_{0.85}Mg_{0.15}Si_2O_7$) scaffolds with a porosity of 48 ± 1%. For that, the preceramic polymer (MK, 28 vol%) was dissolved in isopropyl alcohol, mixed with fumed silica and then with the fillers ZnO, $CaCO_3$, $SrCO_3$ and $Mg(OH)_2$. Printing (840 μm nozzle) happened in air, with subsequential cross-linking at 200 °C. The silicone resins and the reactive fillers were thermally treated in air at 1100 °C for 1 h. Fine glass powders were used as additional fillers, not modifying the overall phase assemblage due to their chemical similarity with the PDC. They enhanced the densification, mechanical properties and integrity of the structures. The scaffolds presented good compressive strengths (11.6 ± 3.2 MPa) and the preliminary cell evaluations showed that the Sr/Mg-doped hardystonite scaffolds had better biocompatibility and bioactivity than pure hardystonite ones.

4.2.4. Functional ceramics

As was observed in the previous sections, many studies have been focused on optimizing the pore structure and chemical composition of porous bioceramic scaffolds for bone tissue engineering. Recently, they have been modified with the use of various functional materials, which developed a variety of functional scaffolds for bone tissue engineering. Different functionalities can be achieved via protein/drug loading, influencing the structure, surface, and interface of the scaffolds, all factors that affect their biological properties. In this regard, direct ink writing has been proven an appealing method to print materials with such sensitive components as it does not utilize high-energy illumination or heat. Thus, many studies have been conducted in printing functional ceramics with DIW; some of these studies that had interesting outcomes, were innovative or both are shown in the sequence.

During the surgical treatment of bone tuberculosis, the lesion site excision produces defects in the bone structure. Regeneration of these defects is improved by the utilization of 3D scaffolds embedded with anti-tuberculosis drugs. With that in mind, Yuan *et al.* [164] used the DIW method to obtain β-TCP scaffolds with the anti-tuberculosis drugs Rifampin and Isoniazid. They evaluated their microstructures and mechanical and biological performances (Fig. 12). After printing the paste (β-TCP, paraffin microspheres (2-8 μm diameter, added to produce a microscopic pore structure), citric acid, potassium hydrogen phosphate, silica and magnesium oxide) at 37 °C with a 500 μm nozzle, the structures were sintered for 2 h at 1100

°C and the anti-tuberculosis drugs were loaded on PLGA (poly(lactic-co-glycolic acid)) microspheres by different steps of centrifuging. The scaffolds had ~62% total porosity, of which 42.5% corresponded to macro-porosity (400 μm pores) and ~19.5% to micro-porosity (2-8 μm pores). The compressive strength achieved was ~3.3 MPa. Besides, the scaffolds presented excellent *in vitro* biocompatibility and a degradation rate matching the osteogenesis biological process. The *in vivo* studies showed that the microspheres could effectively and stably release the anti-tuberculosis drugs for 90 days with concentrations that killed tuberculosis-causing bacteria (*M. tuberculosis*). The scaffolds also allowed the survival and good migration of rat bone mesenchymal stem cells (rBMSC), indicating successful bone repair and regrowth. The study had some limitations, such as the lack of precise control of the microspheres' content and the fact that the degradation study did not consider the action of osteoclasts and macrophages. Although additional analyses are required for their optimization for *in vivo* environments, the β-TCP scaffolds loaded with Rifampin and Isoniazid have shown an encouraging approach for bone regeneration following tissue resection in the cases of bone tuberculosis.

Fig. 12. β-TCP scaffolds loaded with Rifampin and Isoniazid. (A) Scaffold model (S=P=500 μm; W=400 μm; H=5 mm; L=11.3 mm). (B) SEM image of drug-loaded β-TCP support with microspheres (50x). (C) *In vitro* drug release profile. (D) pH change of SBF over time as the scaffold degrades. (E) 500x and (F) 1000x SEM images of rBMSC adhesion to the scaffold.

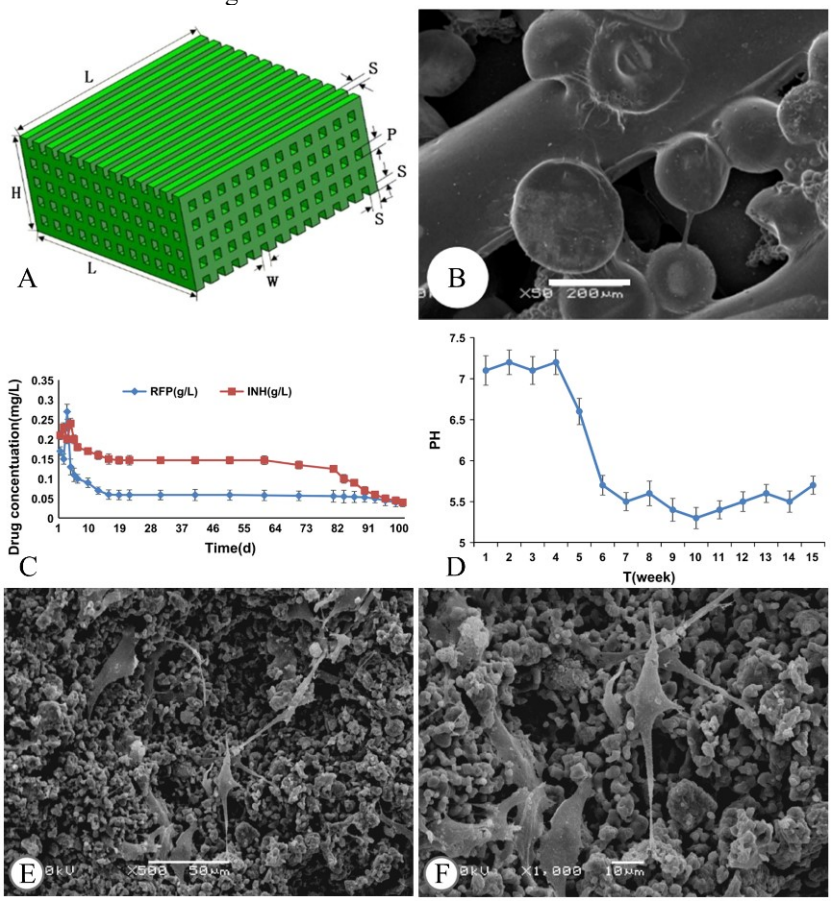

Source: Adapted from [164].

Growth factors can significantly improve scaffolds' bioactivity due to their signaling proteins' function in bone healing [165,166]. One of the most used growth factors for bone tissue engineering applications is bone morphogenic protein (BMP)-2 due to its osteoinductive capacity, which is efficient in the formation of ECM (extracellular matrix) and promotion of the differentiation of MSCs (mesenchymal stem cells) into osteoblasts [165].

The appealing properties of BMP-2 draw the attention of Liu *et al.* [167,168]. They investigated the new bone-forming ability of 13-93 bioactive glass scaffolds (solid content of 40 vol%) mixed with a 20 wt% aqueous Pluronic® F-127 solution, printed with 410 μm nozzles, debinded at 600 °C and sintered at 700 °C for 1 h. The structures had 47% of porosity and were pretreated in a K_2HPO_4 (dipotassium hydrogen phosphate) solution – to convert a thin surface layer (~5 μm) of the glass to hydroxyapatite – or pretreated in K_2HPO_4 and loaded with BMP-2 (1 μg/scaffold). The bioactive glass conversion to HA, bone regeneration and blood vessel formation in non-critical-sized rat calvarial defects were evaluated for 6 [167], 12 and 24 weeks [168] and compared to as-fabricated scaffolds. Scaffolds pretreated with K_2HPO_4 had significantly higher new bone formation at 6 weeks post-implantation when compared to as-fabricated scaffolds, a fact attributed to the high surface area of the formed hydroxyapatite surface layer, which improves protein adsorption and osteogenic ability [167]. Nevertheless, no significant difference in bone regeneration was found in longer implantation times (i.e., 24 weeks) between the as-fabricated and pre-treated scaffolds [167,168]. These discoveries highlighted that, at early implantation times, the pretreatment of scaffolds with K_2HPO_4 could improve their protein adsorption and osteogenic and bone-forming ability, but, in the long term, scaffolds not treated with K_2HPO_4 had a faster conversion to HA; this aspect was able to increase their bone regeneration ability. In comparison, at all three implantation times, scaffolds loaded with BMP-2 presented a significantly higher bone regeneration capacity. They were almost entirely infiltrated with lamellar bone within 12 weeks, with the formation of marrow-rich bone – a typical outcome of bone growth induced by BMP-2. In terms of blood vessel formation, at 6 and 12 weeks post-implantation, the number and area of blood vessels in the new bone infiltrating the BMP2-loaded scaffolds were significantly higher than those of the as-fabricated and pretreated scaffolds. Still, no significant difference was found in these two characteristics among the three groups at 24 weeks. It was also found that neither the pretreatment nor the BMP-2 loading affected the BG-converted-to-HA fraction at 24 weeks, which was ~30% and that the bone regeneration capacity of BMP-loaded scaffolds was independent of the pretreatment period (1-6 days) in the K_2HPO_4 solution. In summary, the

conversion of a surface layer of the BG to hydroxyapatite and the loading of surface-treated scaffolds with BMP-2 could significantly enhance bone regeneration capacity.

Bone morphogenetic protein 2 (BMP-2) was also examined by Dellinger *et al.* [169] utilizing hydroxyapatite scaffolds for its delivery. The paste had 48 vol% of solid content, 1.25 wt% Darvan® 821A, Methocel® F4M (2.5 mg/mL of liquid) and 1-octanol; this paste was mixed with polymethylmethacrylate (PMMA) micro-spheres to promote controlled microporosity (27.5 vol% HA and 27.5 vol% PMMA). After printing, the HA scaffolds, which had 415 μm of strut diameter, were sintered for 2 h at 1300 °C with subsequent incorporation of 10 μg of BMP-2 for their *in vivo* characterization in goat metacarpal and metatarsal bones for 4 and 8 weeks. The results showed that the BMP-2 presence improved the scaffolds' osteogenesis, with a higher percentage of the scaffolds filled with bone tissue at 4 and 8 weeks – histological evidence of more complete healing. Suggestions that the adjacent bone influenced differently the HA/BMP-2 microporous scaffolds properties than the non-microporous scaffolds were found by the internal dark blue staining of the first group and reported for the first time. Furthermore, even though bone healing was not influenced by micropores alone as confirmed by histological measures, the micropores' interconnectivity enabled ECM (extracellular matrix) infiltration into the scaffolds' struts, indicating that the matrix can infiltrate the whole scaffold, not only the macropores. This fact would lead to a more thorough incorporation of bone into the scaffold and, consequently, a more complete defect healing.

Following the same line, Zhou *et al.* [170] recently printed β-TCP scaffolds with a biomimetic vascular hierarchical structure and rhBMP-2 (recombinant human BMP-2) coating to improve the scaffolds' vascularity (Fig. 13). For that, the paste for the DIW procedure had 45 vol% solid content, 2.5 wt% Darvan® C, Methocel® F4M (7 mg/mL) and PEI (0.8 vol% relative to the liquids). After printing, the scaffolds were debinded at 400 °C for 1 h, sintered at 1200 °C for 1 h and then coated with rhBMP-2 pre-dissolved in a gelatin-acetic acid solution. The design of the scaffold had a central vascular channel of 2 mm in diameter and 6 side branch channels of 1 mm in diameter with 450 μm of spacing between them. Upon embedding of femoral axial vascular bundles, the vascular hierarchy significantly increased the scaffold's overall vascularity. Compared to conventional TCP scaffolds, the designed multi-channeled β-TCP scaffolds led to the formation of bone-like tissue and suitable blood vessels through their structure at 4 weeks of implantation. Particularly, more uniform vascularized bone was found 2 weeks post-implantation in scaffolds coated with rhBMP-2 and embedded with a flow-through vascular bundle (FVB). The scaffolds' compressive strength was significantly reduced as a result of the side channels and, notably, the central channels; the latter facilitated structural

failure in that direction. Still, the strengths were close to 3 MPa in all directions, that is, within the range of compressive strengths of cancellous bone.

Fig. 13. rhBMP-2-coated β-TCP scaffolds with embedded autologous vascular bundles. S: conventional TCP scaffolds; CS: multi-channeled β-TCP scaffolds; CS+LVB: multi-channeled β-TCP scaffolds with ligated vascular bundle; CS+FVB: multi-channeled β-TCP scaffolds unligated/flow-through vascular bundle.(A) Computer-aided-design (CAD) of β-TCP scaffolds with bionic vascular access through biomimetic vascular channels; (B) Schematic representation of the fabrication of the channeled scaffolds and insertion of the autologous vascular bundle for accelerating vascularization and osteogenesis; (C) SEM image of the CS branch pattern; (D) Representative μ-CT images for neo-vasculogenesis and neo-osteogenesis within scaffolds implanted in rabbit vastus medialis pocket at week 2 (S-conventional scaffold; CS-channeled scaffold; LVB-ligated vascular bundle; FVB-flow-through vascular bundle); (E) Total porosity of the scaffolds; (F) Compressive strength; (D) rhBMP-2 release profile of S and CS scaffolds (in PBS); Alkaline phosphatase (ALP) assays for (H) 3 h, (I) 1 day and (J) 21 days (insignificant difference (ns $p > 0.05$), and significantly different from control (*$p < 0.05$, and **$p < 0.01$); Quantitative analysis of neo-vasculogenesis and neo-osteogenesis at week 2 through estimation of (K) vessel volume/tissue volume, (L) vessel number, (M) bone volume/tissue volume and (N) cancellous number ($n = 5$; significant effect of the treatment: *$p < 0.05$ and ***$p < 0.001$; significant effect compared to S+BMP2 group: @$p < 0.05$ and @@$p < 0.01$; CS+BMP2 group: #$p < 0.05$; and CS+LVB+BMP2 group: & $p < 0.05$).

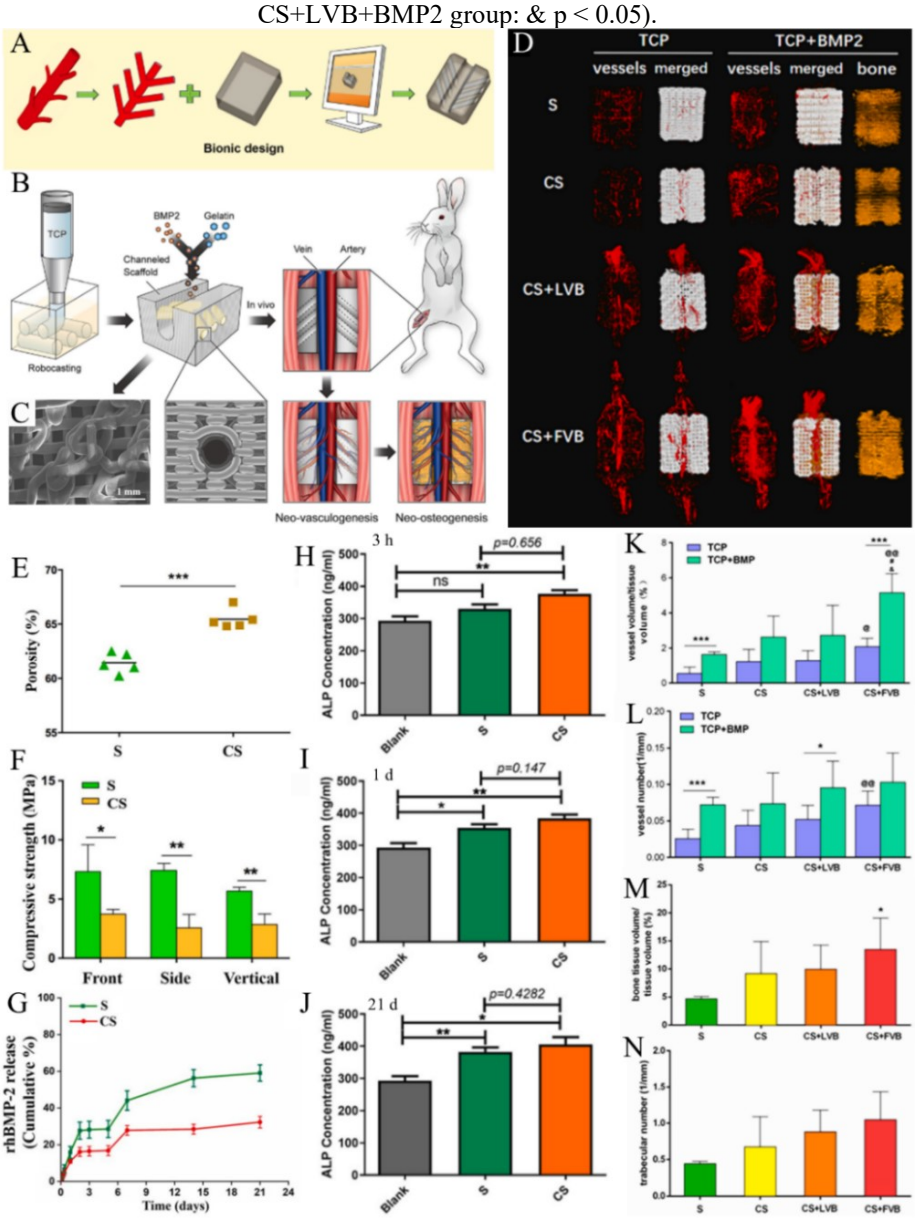

Source: Adapted from [170].

5. CERAMIC COMPOSITES

The three-dimensional printing of pure ceramics has known much progress in the last years with the creation and diffusion of the DIW method. Later on, the utilization of composites grew as technology and knowledge naturally progressed. This development stands mainly on optimizing the paste characteristics, which can be its printability, processability, mechanical properties and bioactivity [171]. Evidently, this optimization depends on the material that is being added to the ceramic ink. The advantages granted for each type of composite are described in the sections to come.

5.1. CERAMIC-CERAMIC COMPOSITES

The development of ceramic-ceramic composites has taken place to alleviate the disadvantages of mono-component materials by combining two or more bioceramics. The most well-known ceramic-ceramic composite is biphasic calcium phosphate (BCP), in which hydroxyapatite (HA) and tricalcium phosphate (TCP) are combined in various ratios to overcome the excessively low biodegradation rate of the first, tailoring its biodegradability. This combination has been proven beneficial in several studies; in the particular case of powder-based 3D printing (P-3DP), Detsch *et al.* [172] found that BCP scaffolds have similar cell viability but higher cell proliferation when compared to pure HA or β-TCP scaffolds.

When it comes to ceramic-ceramic composites produced by DIW, additions of nanoplatelets and fibers have been reported alongside the incorporation of low-melt glasses [173,174] to aid the sintering process and improve the mechanical properties. By far, carbon-based additions (especially graphene oxide (GO)) are the ones that have been mainly utilized [31,127,175–180] – these are further explored in the subitem of this section. Some studies encompassing ceramic-ceramic composites are featured next.

Goyos-Ball *et al.* [76] investigated dense components and scaffolds of 10 mol% ceria-stabilized zirconia and alumina composites (35 vol% of solid content) using Pluronic® F-127 (25 wt%). The scaffolds were printed with 580 μm nozzles, had round lattices of 200 μm pore size and 30% porosity and presented compression strengths comparable to cortical bone, reaching almost 200 MPa. The dense components showed a maximum flexural strength of 575 MPa, 82% of the flexural strength values of conventionally processed 10CeTZP-Al_2O_3. Moreover, the printed parts showed good chemical stability, negligible wear, no cytotoxicity

and induced osseous differentiation. As a result of their high structural integrity, the CeTZP-Al_2O_3 composites could be used for load-bearing regeneration applications [181].

Yttrium-stabilized zirconia scaffolds coated with hydroxyapatite by slurry infiltration were obtained by Kocyło *et al.* [182], in which, to suppress the reaction at 1200 °C between ZrO_2 and HA upon sintering, a fluorapatite (FA) intermediate layer was introduced. The paste had 39.5 vol% of solid content, in addition to deionized water, Dolapix® A88 (dispersant, 1.26 vol%), glycerin (to avoid premature drying) and alginic acid sodium salt (binder, 1.73 vol%). Printing took place with nozzle diameters of 580 μm. It was shown, by XRD (x-ray diffraction) evaluations, that the FA intermediate layer indeed prevented the HA-ZrO_2 reaction and suppressed the HA decomposition. The resulting coating was relatively microporous, ~20 vol%, with a 20 μm total thickness. The structure was sintered at 1450 °C for 2 h, had ~580 μm filament diameters, porosities of approximately 61, 69 and 75 vol% and compressive strengths of ~63, 40 and 21 MPa, respectively. The study found that the scaffolds with the FA/HA layers exhibited better bioactivity than those with the HA/HA coating as well as a slower dissolution rate.

Houmard *et al.* [183] designed biphasic calcium phosphate (BCP) scaffolds for load-bearing bone substitute applications with two different ratios of HA/β-TCP: 60/40 and 20/80. These composites were added to 20 wt% aqueous Pluronic® F-127 solutions and were printed with nozzle diameters varying from 200 to 610 μm. The obtained structures had 25-80 vol% porosity and compressive strength in the range of 3-50 MPa. The immersion tests performed in static SBF and water revealed no significant weight loss of the scaffolds after 5 months; the Ca and P dissolution of the 60HAP/40β-TCP scaffolds was approximately 20 times higher than that of pure HA. The study also exposed the fact that, at similar volume porosity, the compressive strength of the sintered structures increased with decreasing strut diameters.

In a well-acknowledged study, Roohani-Esfahani *et al.* [184] produced scaffolds of a composite of Sr-doped hardystonite (Sr-$Ca_2ZnSi_2O_7$), gahnite ($ZnAl_2O_4$) and a glass phase with four pore geometries and evaluated the mechanical response (Fig. 14). The paste s had a solid content of 45 vol%, with a hydroxypropyl methylcellulose solution (HPMC, 1 wt%), sodium polyacrylate (1 wt%, deflocculant) and a polyethyleminine (PEI) solution (10 wt%, Mw~25,000). The structures with different pore geometries (hexagonal, curved, rectangular and serrated/zig-zag) were printed with a 600 μm nozzle and had varying porosities of ~50, 55, 60 and 70% with pore sizes of 450, 550, 900 and 1200 μm, respectively. The scaffolds had compressive strengths comparable to cortical bone (Fig. 14(g)). Of particular interest, those with hexagonal pores had high fatigue resistance (compressive cyclic load of 1-10 MPa with

1,000,000 cycles), flexural strength (30 MPa) and failure reliability when compared with scaffolds with conventional architecture pores. The strength found was 150-fold higher than that reported for polymeric and composite scaffolds with similar porosity (data gathered by the authors (Fig. 14(g,h))) and also 5-fold higher than the strengths reported for ceramic and glass scaffolds with similar porosity as well. Therefore, through pore geometry optimization, the study demonstrated a general approach to enhance the scaffolds' mechanical strength, producing highly porous and strong glass-ceramic scaffolds for bone regeneration applications.

Fig. 14. Sr-doped hardystonite/gahnite/glass scaffold. CAD design models (left column) and SEM images of the evaluated scaffolds (Scale bars: 500 μm unless stated otherwise). Designs: (A) Hexagonal, (B) Curved, (C) Rectangular and (D) Zigzag. (E) SEM images of the fracture surface of the Sr-HT-Gahnite scaffold showing no microporosity in the struts. (F) Microstructure of Sr-HT-Gahnite scaffolds consisting of three phases: Sr-HT grains, $ZnAl_2O_4$ crystals and an intergranular glass phase. (G) Compressive strength vs. porosity of the scaffolds with distinct pore geometries. (H) Flexural strength of Sr-HT-Gahnite scaffolds with hydroxyapatite and bioactive glass scaffolds. Each point style corresponds to a different literature value.

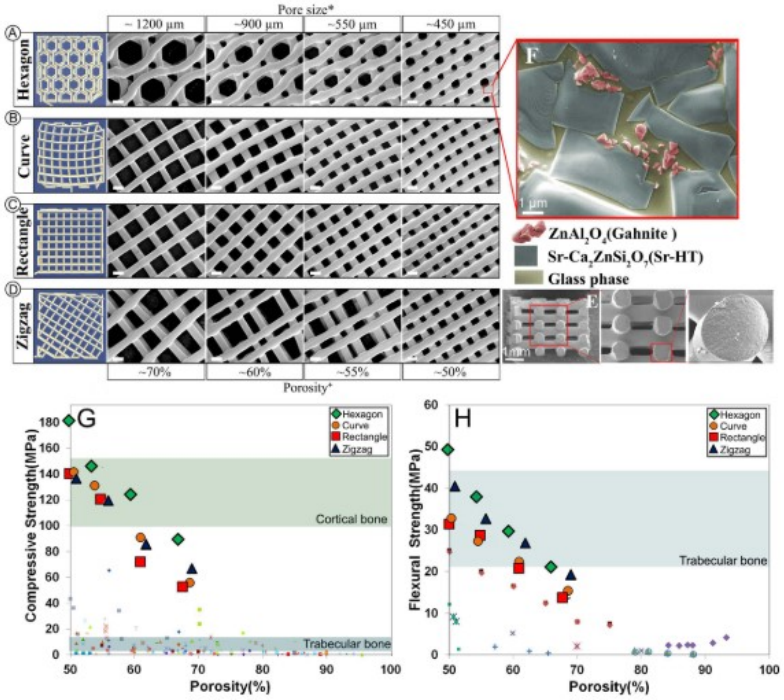

Source: Adapted from [184].

One significant clinical challenge within bioengineering applications is the treatment of malignant bone tumors, as these situations demand the simultaneous removal of tumor tissues and regeneration of bone defects. To address this need, porous bifunctional 3D scaffolds are utilized to incorporate functional materials to accomplish more functionalities, such as photothermal therapeutic and magnetic hyperthermia properties. In this concern, Wang *et al.* [185] combined DIW and a hydrothermal method to prepare bifunctional scaffolds by the *in situ* growth of molybdenum disulfide (MoS_2) nanosheets on akermanite (AKT) printed scaffolds. Pluronic® F-127 (6.39 wt%) and alginic acid sodium (4.09 wt%) were added to the

AKT powders (63.94 wt%) to ensure a homogeneous printable paste. After printing with 580 μm nozzles, the MoS_2 nanosheets' growth on the surface of the struts, through the hydrothermal process, was performed to endow the scaffolds with photothermal therapeutic potential. The MoS_2-modified AKT scaffolds (MS-AKT) had a rapid increase in their temperature under near-infrared irradiation (NIR), which decreased the viability of osteosarcoma and breast cancer cells and inhibited *in vivo* tumor growth. This photothermal temperature could be modulated by varying the scaffold's size, the laser power density and the MoS_2 content. In addition, the MS-AKT scaffolds could support cell attachment, proliferation and osteogenic differentiation (bone mesenchymal stem cells (BMSCs)) besides inducing *in vivo* bone regeneration, showing themselves as a promising clinical strategy in the treatment of tumor-induced bone defects.

In an interesting study, He *et al.* [186] developed diopside ($MgCaSi_2O_6$) scaffolds coated with Cu-doped bredigite ($Ca_7Mg(SiO_4)_4$) or Cu-doped akermanite ($Ca_2MgSi_2O_7$) with good bioactivity, stability and antibacterial potential for application as a new orbital filler/implant (i.e., a medical prosthetic that replaces orbital volume and allows some realistic movement of the prosthetic eye). The paste was also comprised of a 10 wt% PVA solution and, for the DIW procedure, nozzle diameters of 400 μm were utilized. The calcium-magnesium silicate materials were sintered at 1150 °C for 3 h and had ~52% of porosity with ~350 μm pore sizes. The diopside scaffolds had minimal degradation after 12 weeks of *in vivo* incubation. The Cu-doped coatings (5 mol% of Ca was substituted by Cu) produced significant angiogenesis effects, vastly beneficial for neovascularization, especially in the case of Cu-doped bredigite coatings. Thus, the utilization of diopside-based scaffolds modified with functional coatings of Ca-Mg silicates in the retention of orbital prostheses is likely to enhance the patient's prosthesis acceptance due to their improved retention and stability.

Shao *et al.* [149,150] manufactured scaffolds of magnesium-doped wollastonite (CSi-Mg_{10}) combined with β-TCP for bone regeneration application, based on computed tomography (CT) images. A fraction of 10% of Ca was substituted by Mg in wollastonite (β-$CaSiO_3$) and the composite was comprised of 15% β-TCP (CSi-Mg_{10}/TCP_{15}). The DIW pastes had 56.5 wt% solid content mixed with a 6% PVA solution and were printed with nozzle diameters of 450 or 500 μm. The study also encompassed different heating schedules of sintering, such as one-step (1SS) and two-step sintering (2SS); the same as utilized in another study of the group with wollastonite and Mg-doped wollastonite [152]. CSi-Mg_{10}/TCP_{15} that underwent 1SS and 2SS had 57.8% porosity and compressive strengths of 45 and 30 MPa, respectively. The mechanical characterization also demonstrated that the addition of β-TCP to Mg-doped wollastonite induced a ~50% decrease in the scaffolds' compressive strength, but the values were still 5-fold

higher than those of TCP under the same sintering conditions. Notably, the CSi-Mg_{10} scaffolds had a considerably high compressive strength (> 80 MPa) and the 2SS schedule was shown more favorable for the improvement of the flexural strength than the 1SS (90.1 over 82.1 MPa, respectively); both strengths were 10-fold higher than the obtained for TCP scaffolds (~7.8 MPa). A significantly higher osteogenic capability was found for CSi-Mg_{10}/TCP_{15} composite scaffolds after 8 weeks compared to pure CSi-Mg_{10} and β-TCP scaffolds, reaching ~35% new bone tissue after 12 weeks of implantation.

Wollastonite has, typically, challenging densification by ordinary sintering techniques with relative densities generally below 90% - a fact that compromises its mechanical properties. To overcome this difficulty, Elsayed *et al.* [187] produced wollastonite-diopside scaffolds with a glass-assisted sintering approach. The scaffolds were obtained via a PDC route from silicone resin and inorganic fillers (calcium carbonate ($CaCO_3$) and dolomite ($CaMg(CO_3)_2$)) with printing nozzles of 410 μm and a printing medium of sunflower oil to prevent nozzle clogging. The resulting structure had strut diameters of ~520-590 μm and 68-76 vol% porosity. The utilization of silicone in the ink formulation was based on its double effect of control of ink rheology and the development, upon heat treatment, of wollastonite and diopside crystalline phases. A glass of the same oxide composition (W-D glass) was fabricated as fine powders and used as an additional filler (10 wt%). This addition allowed the attainment of stronger scaffolds (~8 MPa of compressive strength (68 vol% porosity)) as a result of increased viscous flow upon firing, which diminished the micro-cracks in the struts of the scaffolds that were generated by preceramic polymer decomposition. The W-D glass addition had no negative impact on the phase assemblage; conversely, the density increased with increasing glass content. Also, the substantial crystallization from the glass devitrification and resin/filler interaction enabled excellent shape retention after firing. Overall, the study demonstrated that, even if added in low content, the W-D glass incorporation led to a notable enhancement of the scaffolds' compressive strength due to their superior integrity and homogeneity.

In that same line, Shao *et al.* [150] developed wollastonite scaffolds with a bioactive glass-assisted sintering strategy. The paste with 56.5 wt% solid content was mixed with a 6% PVA solution and printed with a 500 μm nozzle. The chosen bioactive glass (34.40 $CaO{\cdot}46.05$ $SiO_2{\cdot}15.35$ $Na_2O{\cdot}0.78$ $P_2O_5{\cdot}3.42$ B_2O_3, mol%) with a low melting point was added in 1, 2 or 3 wt%. Different pore shapes were studied with sintering at 1080 °C showing an associated shrinkage of ~21% and a scaffold with 60% final porosity. The highest compressive strength was related to honeycomb pores (~88 MPa), approximately 83% higher than that of rectangular pores (~48 MPa). Also, scaffolds with the BG addition showed a significant strength

improvement after SBF exposure, a behavior notably superior to pure wollastonite scaffolds. Biologically, the *in vitro* hydroxyapatite forming ability with BG was similar to that of those without the addition. The study results highlight the substantial reinforcement of the bioactive glass addition to the long-term structural stability and strength reliability.

Wang *et al.* [174] also utilized a low-melt BG-assisted sintering approach to enhance the akermanite scaffolds' mechanical properties. The akermanite/BG (NCS-B, $CaO{\cdot}SiO_2{\cdot}Na_2O{\cdot}P_2O_5{\cdot}B_2O_3$) composite structures were obtained by printing with 400 μm nozzles of pastes of the powder mixed with a 0.9 wt% aqueous CMC solution, which was then dried at 65 °C and sintered at 1050 and 1100 °C for 3 h. The composite scaffolds had final porosity of 62-65% with ~327-340 μm pore sizes and compressive strength of ~36 MPa – ten times higher than that of pure akermanite scaffolds, showing potential for the regeneration of load-bearing segmental bone defects. The composite scaffolds presented slower *in vitro* biodegradation in Tris buffer, which did not significantly affect their strength over a long period (6 weeks). It was shown that the BG incorporation in the amount of 40% had considerable apatite forming ability in the *in vitro* SBF immersion tests, comparable to that of pure akermanite. In addition, the BG reinforcement considerably improved the structural and strength reliability in SBF, a fact that is advantageous for the enhancement of osteogenic cell activity and bone regeneration. Overall, the investigation demonstrated that a 4 wt% B_2O_3-containing 45S5 BG analog could reinforce akermanite scaffolds at a 20-40 wt% content.

The same research group also obtained a composite scaffold of diopside ($CaMgSi_2O_6$) with the addition of a low-melt bioactive glass ($28CaO{\cdot}45SiO_2{\cdot}4P_2O_5{\cdot}18B_2O_3{\cdot}5CuO$) to assist the sintering process, which was performed at 1150 or 1250 °C [173]. The diopside-BG powder was added to a 6% PVA solution resulting in solid content of 57.9 wt%; 400 μm nozzles were utilized. The incorporation of 5 or 10% BG enhanced the compressive strength of the diopside scaffolds sintered at 1150 °C. The *in vitro* tris buffer immersion evaluation unveiled that after 8 weeks, the scaffolds had a minimal mass loss (< 3.5%) and that, with an adequate amount of B_2O_3-rich CuO-containing bioactive glass (10%) and an appropriate sintering temperature (1150 °C), the scaffolds presented enhanced compressive strength and appreciable stability. After 2-6 weeks of *in vivo* implantation beneath rabbit *panniculus carnosus* muscles, the BG-reinforced diopside scaffolds showed significantly higher angiogenesis ability than pure diopside structures. Particularly, an appreciable angiogenesis response was found for scaffolds with 10% BG additions and sintered at 1150 or 1250 °C. Steam autoclaved scaffolds had excellent contact-active inhibition against bacterias such as *Staphylococcus aureus* and *Pseudomonas aeruginosa*, whereas as-sintered scaffolds presented no antibacterial effect.

Overall, the BG-reinforced diopside scaffolds had an open porosity of 62.5-65.3%, 15.5-19.4 MPa of compressive strength and favorable antibacterial, physicochemical and biological performance.

5.1.1. Ceramic composites with carbon-based reinforcements

As mentioned above, carbon-based materials are by far the most used reinforcements in ceramic-ceramic composites produced via DIW. This is mainly due to the excellent mechanical properties of these materials, perhaps the most targeted improvement in ceramic materials. In addition, good electrical conductivity can be developed with their incorporation. This property has been proven beneficial since electrical stimulation can be used to induce osteointegration after implantation [188,189]. Some studies on the incorporation of carbon-based materials and their main characteristics and results are featured next.

In a couple of papers, Franchin *et al.* [31,175] studied composite scaffolds of silicon carbide (SiC) and aligned chopped carbon fibers (> 30 vol% and 17-21 vol%, in each paper, respectively) with a preceramic polymer (poly(methyl-silsesquioxane)) acting both as a polymeric binder and ceramic source. The paste also contained a dispersant (DISPERBYK®-180) and hydrophobic fumed silica; the printed process was conducted with two nozzle diameters (410 or 580 μm). The structures presented a porosity of approximately 75 vol% and 4 MPa of compressive and 30 MPa of flexural (4PB) strengths. Some issues related to the hindering of the matrix shrinkage during pyrolysis by the fibers' presence were found. These resulted in cracks perpendicular to the filament axis but were solved by adding SiC powder as a passive filler and optimizing the preceramic polymer content, significantly reducing the defects after ceramization. The addition of the aligned chopped carbon fibers was very advantageous. They improved the scaffolds' fracture toughness, which presented fiber pull-out at the fracture surface and a non-catastrophic failure once the maximum stress was reached. The study demonstrated the DIW process's potential to produce anisotropic structures with improved toughness and strength in specific directions by the fiber alignment granted.

Román-Manso *et al.* [176] evaluated silicon carbide (SiC)/graphene nanoplatelets (GNPs) composite scaffolds with an oriented structure. The solids content utilized was 42-44 vol%, the dispersant used was a mixture of high (Mw= 25000 $g.mol^{-1}$) and low (Mw= 2000 $g.mol^{-1}$) molecular weight PEI (4 or 5 wt%), with methylcellulose (5 wt%) acting as binder and Darvan® A821 as flocculation agent (0.3 wt%). The structures had 5, 10 or 20 vol% of GNP content, were printed with nozzles of 330 μm diameter and, after drying, were densified by

pressureless SPS at 1800 °C. The scaffolds displayed a core/shell structure since GNPs were parallel aligned to the filament wall in the shell (c-axis perpendicular to the extruding direction, as expected). Such a structure had a compressive strength of 10-50 MPa and directional electrical conductivities – $\sigma_{x,y}$ values ≤ 611 $S.m^{-1}$ and σ_z ≤ 273 $S.m^{-1}$ (axes defined by the directions of extrusion and pilling up). Both this and the previously mentioned study highlight the DIW potential in orienting high aspect ratio phases through the shear stress associated with the nozzle reduction process.

In a work carried out by Jakus *et al.* [177], a composite scaffold of hydroxyapatite/graphene (1:1, vol%) displayed good bioactivity, flexibility and electrical conductivity. The paste with a solid content of 25-40 vol% and binder (PLGA) content of 10-40 vol% was printed with conical or cylindrical nozzles with diameters of 100, 200, 400 or 1000 μm. The composite was shown to support cell viability and proliferation (mesenchymal stem cells) and to significantly upregulate the neurogenic and osteogenic gene expression over 14 days. The resulting composite had mixed characteristics of the two individual systems, but these properties did not necessarily follow a linear rule of mixtures; the microstructural and mechanical properties were more similar to those of graphene, whereas the electrical conductivity was not so much. The induction of MSCs' osteogenic and neurogenic gene expression alongside combined mechanical properties from both individual systems was a strong indication that the HA/graphene composites and their variations are suitable candidates for application in transition zones between two distinctive tissue types.

Eqtesadi *et al.* [127] developed scaffolds composed of melt-quenched 45S5 bioactive glass with additions of reduced graphene oxide (rGO) platelets (0-3 vol% content). The composites with 35 vol% solid content, CMC binder (2 wt%) and 400 μm strut diameters were pressureless sintered at 550 or 1000 °C in an Ar (argon) atmosphere to preserve the nature of the reinforcements while ensuring consolidation. The 45S5 BG densification was improved with the Ar utilization as sintering atmosphere, but this increase did not extend to the compressive strength, which was similar to scaffolds fabricated in air. On the other hand, the rGO addition was detrimental to the densification of the 45S5 bioactive glass, but, interestingly, their addition with contents up to 1.5 vol% improved toughness and compressive strength. The best results were obtained for 1 vol% rGO additions, which induced a fracture toughness enhancement of ~850% (550 °C, ~1 $MPa/m^{1/2}$) and 380% (1000 °C, ~1.6 $MPa/m^{1/2}$) and a compressive strength increase of ~290% (550 °C, ~10 MPa) and 75% (1000 °C, ~22 MPa). Overall, scaffolds sintered at 500 °C in Ar had a compressive strength of 2.5 MPa (0 vol% rGO) and 10 MPa (1 vol% rGO), while those sintered at 1000 °C had 12 MPa (0 vol% rGO) and 22

MPa (1 vol% rGO). As it is notable, the improvement produced was dependent on the sintering temperature and was greater at 550 °C. This improved mechanical performance, determined by a good dispersion and strong interaction of rGO and the BG matrix, was not accompanied by a bioactivity deterioration and could be very useful for tissue engineering applications.

The same research group also incorporated graphene oxide (GO) nanoplatelets (0-4 vol%) into a bioactive glass (13-93) and obtained composite scaffolds that were pressureless spark plasma sintered (SPS) at 650 °C [178] – same strut diameter (400 μm), solid (35 vol%) and binder (2 wt%) content were used. The vacuum in SPS favored the viscous flow, which enabled densification levels comparable to those of conventional air sintering but at significantly lower temperatures and durations (650 °C for 15 min in SPS compared to 700 °C for 60 min in conventional sintering [190]). On the other hand, the viscous flow was hindered by the GO platelets' addition hampering the bioglass' densification. Despite this, their addition up to a specific content improved the 13-93 BG scaffolds' mechanical performance in terms of compressive strength (45-90 MPa) and, remarkably, toughness (8 $MPa.m^{1/2}$, estimated by the area under the load-displacement curve from 3PB divided by sample volume), which was within or even surpassed that of dense cortical bone. The best performance was achieved with the incorporation of 2 vol% GO with ~894% toughness and ~26% compressive strength improvements; at higher contents, the nanoplatelets agglomerated and, alongside increased porosity, decreased the obtained mechanical enhancement. The mechanical reinforcement attained is similar to that achieved by polymeric full infiltration/impregnation of analogous DIW scaffolds [78], with the difference that, in this case, the macroporosity and osteoconductive surface – both vital for bone tissue ingrowth and regeneration – were preserved.

In a study by Wu *et al.* [179], scaffolds of β-TCP coated with a uniform layer of graphene oxide (GO) were evaluated in terms of their *in vitro* and *in vivo* osteogenic capacity and also the molecular mechanisms behind this ability. The β-TCP powder (n.d. solid content) alongside a PVA binder (n.d. quantity) was printed into scaffolds which were then simply soaked in a GO/water paste (sonicated for 4 h) followed by heat treatment (100 °C), comprising the GO-modified β-TCP structures (β-TCP-GRA). The GO coating significantly stimulated cell proliferation, alkaline phosphatase activity and osteogenic gene expression of human bone marrow-derived mesenchymal stem cells (hBMSCs). The mechanism behind this β-TCP-GRA osteogenic induction was likely to be the activation of a signaling pathway of the hBMSC cells (called Wnt/β-catenin). This activation is caused by protein absorption and by the interaction of bioactive groups (e.g., OH- and COO-) and the nano-apatite layer induced by GO with the

cells. The GO coating also led to improved new bone formation *in vivo*, a signal of the GO stimulatory effect on *in vivo* osteogenesis, which makes GO coating on β-TCP scaffolds an encouraging approach for bone tissue engineering applications, especially for large bone defects' regeneration.

In the following study [180], the same group developed GO-modified β-TCP/Fe_3O_4 magnetic composite scaffolds for bone tumor therapy. The scaffolds were printed with the same paste and conditions as the previous study and then soaked in a GO or GO-Fe paste; this way, the graphene oxide was coated on the scaffolds' surface without the GO dispersion issues. After coating 8 times, the final Fe_3O_4 content in the composites was no more than 1%. The resulting β-TCP scaffolds with surface modification of Fe_3O_4 nanoparticles/GO nanocomposite layers (Fe_3O_4 particles wrapped by GO sheets) had triangle pore morphology with 300-500 μm pore sizes and ~50 % porosity. The low Fe_3O_4 content (≤ 1%) endowed the scaffolds with superparamagnetic behavior and hyperthermal effects. The scaffolds' temperature could be modulated from 50 to 80 °C under an alternating magnetic field (15 min), controlled by the Fe_3O_4 content and magnetic field intensity. This excellent hyperthermal effect of the composite scaffolds resulted in over 75% cell death of osteosarcoma cells (MG-63) *in vitro*. Besides, the β-TCP-Fe-GO scaffolds significantly improved osteogenic gene expression (OCN, OPN, Runx2 and BSP) and alkaline phosphatase (ALP) activity of rabbit bone marrow stromal cells (rBMSCs) as well as significantly increased rBMSCs proliferation when compared to pure β-TCP scaffolds. The latter happened by the synergistic effect of GO and released Fe ions. The overall results demonstrate that the Fe_3O_4 presence endowed the GO-modified β-TCP/Fe_3O_4 scaffolds with exceptional magnetic properties and magnetothermal effects. This fact, alongside their excellent osteogenic capabilities, exposes their potential for application in the regeneration and therapy of bone defects resulting from bone tumors.

Bone regeneration and tumor therapy were also the intended application of the free carbon-embedding larnite scaffolds investigated by Fu *et al.* [191]. The polymer-derived larnite/carbon scaffolds composed of active fillers ($CaCO_3$) and a preceramic silicon resin (Fig. 15) had 400, 600 and 800 μm pore sizes, 60° offset between layers and compressive strengths of 4.8 ± 0.5 MPa. The structures stimulated the expression of osteogenesis-related genes, such as OCN, ALP and Runx-2, in rat bone mesenchymal stem cells (rBMSCs) in addition to the promotion of new bone formation in critical-sized rat calvarial defects; showing better bone regeneration ability than pure larnite scaffolds. The larnite/C scaffolds presented an excellent photothermal effect that could kill human osteosarcoma cells (MNNG/HOS) *in vitro* and inhibit

tumor growth in nude mice *in vivo*, highlighting their potential for applications involving both bone regeneration and tumor therapy abilities.

Fig. 15. Larnite/carbon scaffolds and their *in vivo* photothermal effect. (A) Heating curves of the larnite and larnite/C-3 scaffolds (treated at 1200 °C for 3 h) with 808 laser irradiation in nude mice and (B) their corresponding infrared thermal images. *In vitro* cellular response of the larnite and larnite/C scaffolds. (C) LSCM (laser scanning confocal microscopy) image of rBMSCs seeded on larnite and larnite/C-3 scaffold with cell nuclei and cytoskeleton stained with DAPI and rhodamine-phalloidin (scale bar 10 μm) (D) Proliferation of rBMSCs cultured for 1, 3 and 7 days (n=3). (E) ALP activity of rBMSCs cultured for 7 and 14 days (n=3). (F) ECM mineralization (red) and ALP (blue) staining of rBMSCs (scale bar: 7.5 mm and 100 μm). Osteogenesis-related gene expression of (G1) ALP, (G2) OCN and (G3) Runx-2 by qRT-PCR analysis for 3 and 7 days (n=3).

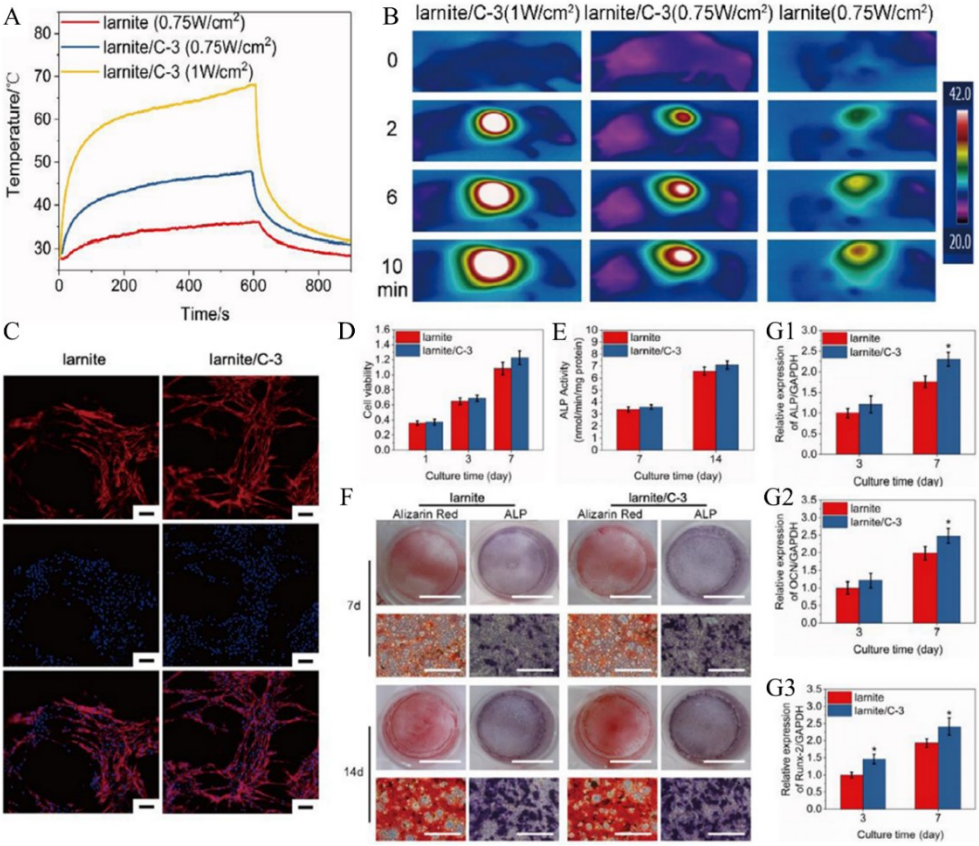

Source: Adapted from [191].
Asterisks (*) indicate a significant difference, $p < 0.05$.

5.2. CERAMIC-METAL COMPOSITES

There are not many studies on ceramic-metal composites produced through DIW; they represent only 5% of all composites. The primary objective of combining metal phases with ceramic materials is the improvement of the mechanical properties of the latter. Some metals that have been applied in ceramic-metal composites are titanium, incorporated as fibers, and magnesium, which is mainly infiltrated in the ceramic structures produced. Some prominent studies encompassing these materials are highlighted next.

In a study by Thomas *et al.* [192], scaffolds of bioactive glass (13-93) were reinforced with titanium (Ti) fibers to increase their mechanical properties to fit load-bearing bone repair applications. The Ti fibers utilized had a diameter of ~16 μm and lengths of ~2-200 μm. The DIW paste had a solid content of 40 vol% and also encompassed 4-4.4 vol% of a thickening agent (Methocel® F4M, hydroxypropyl methylcellulose), 2 vol% of Darvan® C and varying concentrations of Ti fibers (0, 0.2, 0.3 or 0.4 vol%). The composite ink was deposited in a heated plate and the obtained structure had ~50% porosity with pore sizes varying from 400 to 800 μm. The study found that the 0.4 vol% addition of Ti fibers enhanced the scaffolds' fracture toughness by ~70% (from ~0.5 to 0.8 $MPa.m^{1/2}$) and the flexural strength by ~40% (from ~10 to 15 MPa (4PB) – comparable to that of human cancellous bone (10-20 MPa) [193,194]). Besides reinforcing the scaffold, the Ti fibers' addition did not inhibit its bioactive properties and HA formation, as the *in vitro* evaluations showed.

The infiltration of a TCP scaffold with pure commercial Mg through the CAMI method (current-assisted metal infiltration) was performed by Casas-Luna *et al.* [195] to develop biodegradable load-bearing implants. The TCP powder was mixed with a 30 wt% aqueous Pluronic® F-127 solution ensuring a solid content of 62.5 wt% (~30 vol%). The resulting paste was printed with 250 μm nozzles and the printed component had 350 μm of distance between same-plane adjacent filaments. The scaffolds were sintered at 1100 °C for 5 h, with subsequent infiltration of the Mg in a spark plasma sintering equipment (CAMI, 1 kN, 670 °C for 1 min under vacuum with a heating rate of 100 °C/min). The study showed a good magnesium interpenetration with even small pores (< 2 μm) being filled and possible dissolution of Ca into the molten Mg. The latter was presumed due to the formation of intermetallic $CaMg_2$, nevertheless, a continuous and well-defined interface between the ceramic-metal phase was observed. The degradation rate of the Mg-TCP interpenetrated composite was approximately 3 times slower than that of pure Mg. The XRD analysis showed no TCP chemical degradation, a fact attributed to the atomic substitution of Mg and Ca atoms. Since the fast degradation rate is one of the main concerns related to Mg-based implants, TCP scaffolds infiltrated with such high corrosion-resistant magnesium alloys may be a good alternative to slow the degradation rate, hence guaranteeing suitable mechanical properties during the bone healing period.

5.3. CERAMIC-POLYMER COMPOSITES

Ceramic-polymer composites stand out for tissue engineering applications since they combine the ceramic phase's favorable bioactivity and mechanical strength with the flexibility,

toughness, and biodegradability granted by the polymer phase [196]. By far, the most utilized polymers in ceramic-polymer composites obtained by DIW are PCL (polycaprolactone) and PLA (poly(lactic acid)), whereas the most used ceramics are bioactive glasses, HA and β-TCP, due to their excellent osteoconductivity. This polymeric phase can act as a binder during the printing process (not encompassed in this section), be applied as a matrix with ceramic phase reinforcements, and coated on or infiltrated in the scaffolds (Fig. 16). In this paper, components were considered as infiltrated if they have undergone fully infiltration (i.e., loss of macroporosity), whereas components were considered as coated if they had the external surface of their struts coated (preserving macroporosity), whether the coating had slightly infiltrated the accessible porosity of the strut or not. Intuitively, there are no debinding or sintering cycles in such cases, unless the infiltration/coating takes place after the sintering of the component. The most distinguished studies involving DIW and ceramic-polymer composites are presented in the following sections, alongside their main outcomes.

Fig. 16. Schematic illustration of the different types of polymer-ceramic composites.

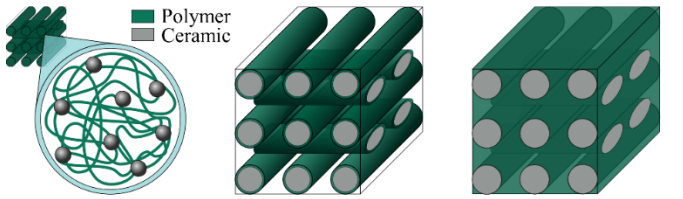

Source: Author.

5.3.1. Composites with polymeric matrix

The simplest way to benefit from the mechanical and degradability properties of polymers in ceramic-polymer composites is to use such materials as the matrix of the composite. Some interesting studies that evoked this approach are featured in the next paragraphs.

A ceramic-polymer composite with a polymeric matrix was developed via DIW by Wang *et al.* [197]. In their study, the local delivery of copper ions (Cu^{2+}) from a Cu-doped bioactive glass (Cu-S53P4, $53SiO_2{\cdot}4P_2O_5{\cdot}19CaO{\cdot}23Na_2O{\cdot}1CuO$, wt%) – known for its angiogenic potential – was combined with printed PCL (polycaprolactone) scaffolds. A viscous PCL solution in acetone acted as a carrier for the BG microparticles, achieving a homogeneous ink that was solidified in a cold ethanol bath (phase exchange of PCL from acetone to ethanol). The compositional PCL:BG weight ratios were 4:1, 2:1 or 1:1. The Cu-BG/PCL scaffolds had

filament diameters of 207-232 μm, apparent porosity of 60%, precipitation of an HA-like layer on the strut surface and compressive Young's modulus that ranged from 7 to 13 MPa; the latter, alongside the scaffolds' cytotoxicity, was dependent on the Cu content. It was found that the BG doping with Cu^{2+} induced a higher expression of early osteogenic marker genes (i.e., RUNX2a) but reduced the expression of late osteogenic marker genes (i.e., OSTEOCALCIN and DLX5), which demonstrated a Cu^{2+} suppressing effect on the hBMSCs osteogenic differentiation. The rising content of BG and Cu in the composite had a reducing impact on the ALP activity of hBMSCs. Additionally, in a coculture of HUVECs (human umbilical vein endothelial cells) and hBMSCs, the BG/PCL and Cu-BG/PCL scaffolds supported vascularization and tubule network formation when compared to the pure PCL scaffolds. Unexpectedly, the ions Cu^{2+} released from the composite did not influence the tubule formation.

In addition to the commonly used polymeric binders, PHBHHx (poly-(3-hydroxybutyrate-co-3-hydroxyhexanoate)), a member of the PHA (poly(hydroxyalkanoates)) family, has had its biodegradability and biocompatibility proven as well as better elastomeric properties and, as so, has been applied for drug delivery matrices, biodegradable sutures, injectable implant systems and artificial nerve conduits [198]. With this in mind, Zhao *et al.* [133] printed MBG/PHBHHx composite scaffolds and obtained great biological outcomes. To produce the scaffolds, PHBHHx powder was dissolved in a chloroform and dimethyl sulfoxide mixture of solvents (20:80, vol) with subsequent incorporation of the MBG particles in mass ratios of 3, 5 or 7 (MBG/PHBHHx). The printed structures were transferred to a ventilated oven at 37 °C to evaporate the solvents. The resulting scaffolds presented 250 μm filament diameter, ~70% porosity with pore sizes in the range of 300-400 μm and compressive strength (~5-12 MPa) – ~200 times that of polyurethane foam-templated MBG scaffolds. Biologically, compared to the polymer-bonded MBG control group (i.e., MBG/PVA scaffolds), the MBG/PHBHHx scaffolds had better bioactive and osteogenic properties, faster apatite-forming ability and promoted the adhesion, proliferation and differentiation of human bone marrow-derived mesenchymal stem cells (hBMSC). Furthermore, at 8 weeks post-implantation in critical-size rat calvarial defects, the MBG/PHBHHx scaffolds stimulated bone regeneration and largely repaired the defects, according to μ-CT, histology and sequential fluorescence labeling analyses. In addition, they exhibited a controlled *in vivo* degradation rate and potential to stabilize the pH of the environment that increased with increasing PHBHHx ratio.

In a couple of recent papers, Mondal *et al.* studied in a couple of papers different compositions of hydroxyapatite (HA)/acrylated epoxidized soybean oil (AESO) (also known as SOEA – soybean oil epoxidized acrylate) with either PEGDA (polyethylene glycol

diacrylate) or HEA (2-hydroxyethyl acrylate) intended for biomedical applications. In the first study [199], they evaluated AESO/HA/PEGDA (49:30:21, vol%) ethanol- and acetone-based pastes that were printed as filaments with nozzles diameters varying from 210 to 840 μm and then UV cured (Irgacure® 819 photoinitiator). A significant improvement of mechanical properties was found when printing with smaller nozzle diameters, with a 2-fold increase of the ultimate tensile stress when the needle diameter was decreased by a factor of 4. Filaments printed with nozzles of 840 and 210 μm diameters had ultimate tensile stresses of ~26 and ~49 MPa and moduli of ~885 and ~1700 MPa, respectively. These enhanced properties were attributed to fewer defects and increased crystallinity. Hence, the study found that the AESO/HA/PEGDA nanocomposites' extrusion through narrow nozzles improved their mechanical properties; still, further optimization is required to attain robust mechanical properties suitable for repairing bone defects.

In their sequel study, Mondal *et al.* [200] reported scaffolds with the only difference being the compositions: AESO/HA (80:20, vol%), AESO/HA/HEA (40:20:40, vol%) and AESO/HA/PEGDA (72:20:8, vol%). An ultrasonic homogenizer was utilized and UV curing was performed during layer-by-layer deposition. Curing and good dispersion of the nHA in the polymeric matrices during printing were successfully attained and, after 14 and 21 days of *in vitro* culture, the structures supported cell proliferation and osteogenic differentiation. Still, each ink's functional groups' nature influenced the mechanical properties and cytocompatibility, possibly by the additional hydrogen bonding in HEA. The structures composed of AESO/HA, AESO/HA/HEA and AESO/HA/PEGDA had, respectively, porosities of ~33, ~41 and ~37%, compressive strengths of ~17, ~10 and ~3.5 MPa, compressive moduli of ~110, ~55 and ~55.5 MPa and toughness of ~1.7, ~1.0 and ~0.1 MPa. Through the HEA addition, the cell adhesion, proliferation and osteogenic differentiation (BMSCs) were improved, as well as the rheological properties and printability of the ink, leading to high-fidelity homogeneous scaffolds. However, the HEA incorporation also significantly reduced the nHA dispersion and the scaffolds' strength and elastic modulus of the scaffold. The incorporation of PEGDA, on the other hand, improved nHA dispersion, while it did not enhance the rheological and mechanical properties and downregulated the cells' osteogenic differentiation compared to AESO alone and AESO/HEA.

A combination of methods made by Yun *et al.* [201] allowed the obtention of mesoporous bioactive glass (MBG)/PCL composite scaffolds. This hierarchical porous structure with three-level multiscale porosity was developed by the formation of giant macropores (~200 μm) via the DIW technique, mid-size macropores (2–9 μm) by the salt leaching method (NaCl) and mesopores (5 nm) via triblock copolymer templating method

($EO_{100}PO_{65}EO_{100}$, Pluronic® F-127). The printing paste was achieved by mixing NaCl granules (25-33 μm) with MBG powders (with Pluronic® F-127 dissolved in it during its synthesis), which were then mixed with a PCL chloroform-dissolved suspension; the final composition had the weight ratios of 0.6:1 = MBG:PCL and 0.5-1:1 = NaCl:PCL). The MBG/PCL scaffold fabrication involved printing with a 500 μm nozzle onto a chilled substrate and then immersing the scaffolds in deionized water to leach the NaCl out. It was found that the application of the salt leaching technique with NaCl-sized controlled granules to the DIW method increased the porosity effect as well as the molding capabilities. The additional macro-pore formation in the struts positively affected the *in vitro* cell activity and bone-forming bioactivity. The MBG/PCL scaffolds had a well-interconnected pore structure, adequate compressive strength for bone repair (2-4 MPa), good *in vitro* bioactivity and apatite-forming ability. Additionally, depending on the NaCl content, the structures showed unique sponge-like properties with softness and easy pliability while maintaining better mechanical properties than general PCL salt leaching-derived scaffolds. This versatile sponge-like plastic nature makes these hierarchically mesoporous–macro-porous–giant-porous BG/PCL structures highly promising for tissue engineering applications, more generally as injectable scaffolds for minimally invasive surgeries, but also as artificial cartilages. However, future evaluations are required to assess the suitability of other material properties for chondral repair so that no interference is caused between the bone and cartilage regeneration processes.

In a study by Dorj *et al.* [202], hydroxyapatite/PCL scaffolds containing ionically modified carbon nanotubes (imCNTs) were developed. A homogeneous dispersion of the imCNTs was attained in tetrahydrofuran solvent (ultrasonication for 5 min) and later mixed with the HA-PCL slurry (n.d. ratio). The CNT content utilized (0.2 wt% relative to HA-PCL) was slightly smaller than the common CNT additions in polymer-based composites but was theorized to have positive reinforcement effects in polymer matrices as, when evenly dispersed, their low concentration addition is preferable; excess addition could generate agglomerates or lumps, inducing adverse effects [203–207]. The printing procedure was held with the paste in a thermostatic syringe (50 °C) printed through a nozzle of 520 μm in diameter. The resulting HA/imCNT/PCL scaffolds had strut diameters of ~235 μm and ~227 μm of pore sizes. Mechanically, the imCNTs incorporation into HA-PCL significantly improved the elastic modulus (by ~2.5-fold) and compressive strength (by ~2.5-fold) of the structures, resulting in 40-50 and ~5.5 MPa, respectively. The HA/PCL and HA/PCL/imCNT composite scaffolds demonstrated significantly higher *in vitro* cell proliferation levels (MC3T3-E1) than pure PCL structures, with no significant difference between the composite scaffolds. The

HA/imCNT/PCL scaffolds also presented substantial induced apatite mineralization analogous to that of HA/PCL, when immersed in SBF. *In vivo*, the tissue reactions of imCNT-containing scaffolds were similar to those without this addition, indicating that the incorporated imCNTs did not induce any significant inflammatory process and did not hinder the biological beneficial roles of HA. Besides, the subcutaneous implantation in rats for 4 weeks exposed the support of cellular growth, angiogenesis, neo-blood vessel formation into the scaffold and tissue development of the imCNT-containing scaffolds with efficacy comparable to those of non-containing imCNTs. All of these results highlight the potential of reinforcing composite scaffolds with imCNTs; still, more long-term *in vivo* evaluations are required to confirm their clinical availability.

Gonçalves *et al.* [208] evaluated scaffolds composed of silicon-doped nanocrystalline hydroxyapatite, PCL and carbon nanotubes to produce electrically conductive structures for bone regeneration. The use of nanocrystalline Si-doped HA encompassed the advantage of its better biological response than conventionally used HA [209,210]. The printing paste was achieved by, concurrently, dissolving the PCL in dichloromethane (DCM) and dispersing the HA powder also in DCM, followed by the addition of the CNTs to the HA solution, mixing both the PCL and HA-CNTs solutions and heating to 35 °C to allow solvent evaporation until a viscosity suitable for printing was attained (2.5-7 Pa.s, according to the authors). The CNT content utilized varied from 0 to 10 wt% within a PCL matrix with HA as the balance. The final structure presented ~40% porosity and 450-700 μm interconnected square pore sizes. The study found that the addition of hollow CNTs induced a mesoporosity in the scaffolds of approximately 20 nm and that the scaffolds became electrically conductive with 2 wt% CNT. There was an increase in the compressive yield stress to 6.5 MPa only for the 0.75 wt% CNT scaffolds compared to unreinforced HA-PCL structures (4.2 MPa). Among the compositions studied, scaffolds with 2 wt% CNT offered the best combination of electrical conductivity and mechanical behavior – with compressive strength (~4 MPa) comparable to that of cancellous bone. The composites showed typical hydroxyapatite bioactivity as well as good cell adhesion and spreading at the surface of the scaffolds. As mentioned, cell attachment was good for all compositions. Still, it was most prominent in the scaffolds with the highest amount of CNTs (10 wt%) in agreement with the fact that the CNTs' presence enhances protein adsorption and, as a consequence, cell attachment. The study concluded that the HA/CNT/PCL scaffolds obtained are promising alternatives for the use of electrical stimulation to induce osteointegration after their implantation.

5.3.2. Composites with polymeric coating

Another strategy to profit from the interesting properties of polymers is to coat ceramic components. This approach benefits on the reinforcing mechanism of sealing defects on the surface of the strut and the prevention of crack-opening by the crack-bridging provided by polymer fibrils. Additionally, this technique allows the preservation of the predesigned macroporosity as well as cell seeding before implantation. Investigations that made use of this approach are highlighted next.

Deliormanli *et al.* [211] printed 13-93 bioactive glass scaffolds that, after sintering, were coated with a poly(ε-caprolactone) (ε-PCL) solution containing graphene nanopowder. The BG printing paste had a solid content of 35 vol% with 20 wt% Pluronic® F-127 solution, which was printed with a 410 μm cylindrical nozzle using an alumina plate as a printing substrate. Sintering took place at 690 °C for 1 h with subsequent dip coating with an ε-PCL (5 wt%) anhydrous acetone solution with graphene nanopowder in the contents of 1, 3, 5 or 10 wt% (ultrasonication for 15 min). The resulting structure had 42-48% of porosity and compressive strength of 17-30 MPa; the latter was decreased when high graphene concentrations were incorporated. The composites had no toxic response to mouse bone marrow mesenchymal stem cells (mBMSCs), which attached and proliferated well on the seeded scaffolds' surface. Besides, the ε-PCL/graphene coating had no detrimental effect on the HA-forming ability and demonstrated osteogenic differentiation under *in vitro* conditions.

Another study involving the ε-PCL coating was performed by Martínez-Vázquez *et al.* [212] with TCP scaffolds, involving the ε-CL *in-situ* ring-opening polymerization. The printing paste was composed of 45 vol% solid content, Darvan® C (1.5 wt%) Methocel® F4M (7 mg/mL of liquid) and PEI as a flocculant (2 vol% relative to the liquid content). The printing procedure used 250 μm nozzles and a paraffin oil bath to guarantee uniform drying. Debinding was conducted at 400 °C for 1 h and sintering at 1200 °C for 2 h. Subsequently, the polymerization within the scaffolds utilized lipase as a catalyst and anhydrous toluene as a solvent so that a highly homogeneous coating and full in-strut microporosity infiltration were obtained. The scaffolds had 52 ± 3% overall porosity, with 250 μm pore sizes and Young's modulus of 19 GPa. The coated scaffolds' compressive strength and toughness were significantly improved by 2- (~18 MPa) and 5-fold (~0.4 $MPa \cdot m^{1/2}$), respectively.

Motealleh *et al.* [213] analyzed the mechanical improvement on 45S5 bioactive glass scaffolds granted by deposited nanocomposite coatings, which consisted of hydroxyapatite nanoparticles (reinforcing phase) in a polycaprolactone (PCL) matrix. The BG printing paste

presented 45 vol% of solid content with 1 wt% of CMC as binder and was printed with 410 μm nozzles in an oil bath. Debinding was performed at 400 °C for 1 h and sintering at 550 °C (n.d. period). For the coating procedure (dip-coating), PCL was dissolved in toluene and the HA nanopowders (30 wt%) were added. The study evaluated the effect of particle morphology and size of the three different HA nanopowders utilized. It was found that small and round nanoparticles, as those obtained by the sol-gel process, were the most efficient reinforcements, being able to improve the mechanical performance of the coated scaffolds by over 200%, in terms of compressive strength (~11 ± 2 MPa) and also toughness (~0.42 $MPa \cdot m^{1/2}$).

In a following study [214], the same research group evaluated the performance of the same bioactive glass (45S5) scaffolds coated with natural (gelatin, alginate and chitosan) or synthetic (PCL, PLA) polymers. The same composition, printing and coating procedure was utilized with PCL and PLA being dissolved in toluene, alginate and gelatin in distilled water and chitosan in an acetic acid (2 vol%) aqueous solution. The scaffolds were sintered at 550 °C with resulting ~360 μm strut diameters and ~25% in-strut microporosity before coating. The study found that coatings from natural polymers (hydrogels) produced the greatest reinforcement, especially chitosan, which showed a compressive strength of ~13.5 MPa and ~0.85 $MPa.m^{1/2}$ of toughness. The natural polymer coatings positively affected the bioactivity, accelerating the apatite-like layer formation; an enhancement in which chitosan also stood out. Moreover, most of the coating compositions reduced the *in vitro* degradation rate, which is likely to positively impact the evolution of their mechanical properties. Overall, the prominence of coating BG (45S5) scaffolds with chitosan became evident with the superior initial strengthening and toughening found, as well as the enhanced *in vitro* bioactivity and the reduction of mechanical degradation in extents comparable to those provided by the less biodegradable synthetic polymers.

5.3.3. Composites with polymeric infiltration

It has been predicted that if scaffolds were infiltrated with a more ductile phase, providing a link between the pillars/struts, the resulting composite would, most likely, present good mechanical integrity even after the failure of the ceramic structure [215]. This approach could create damage-tolerant scaffolds for load-bearing tissue engineering applications by the infiltration of bioceramic scaffolds with biodegradable polymers; the biodegradation rate mismatch in such dense composites would develop *in situ* porosity after implantation, enabling cell ingrowth. Besides the same reinforcing mechanisms of coating and enhanced mechanical

performance (especially under flexural stresses), this technique would allow the progressive load transfer onto the regenerated bone, which would provide the required loading conditions for the development of full healing dynamics. The following paragraphs describe studies that made use of this approach.

In an innovative study, Feilden *et al.* [32] investigated dense composites with filaments composed of oriented alumina platelets infiltrated with epoxy (Fig. 17). The printing paste was composed of alumina powder mixed with alumina platelets at a mass ratio of 3:7, alongside water, Dolapix® CA deflocculant (0.5 wt%) and Pluronic® F-127 binder (8.9 wt%); the resulting solid content was 31 vol% (65 wt%). The debinding procedure occurred at 600 °C for 1 h, followed by sintering at 1550 °C for 1 h, infiltration of epoxy for 12 h under vacuum and curing (180 °C for 1 h + 200 °C for 2 h). Different nozzle lengths were studied to optimize the effect on platelet alignment (Fig. 17(a-c)). Isostatic pressing was utilized to enhance the volume fraction of platelets and powder in the green structure from ~50 to ~64 vol%. The remaining porosity (~36 vol%) was infiltrated with epoxy via vacuum infiltration, resulting in a final porosity below 0.5%. Their research's great differential was the architectured direction of the printed filaments to guide crack propagation (twisting and tilting) in three dimensions. Two structure types were evaluated in terms of fracture toughness, the first with each filament layer parallel to the others (fractured in trans-filament and inter-filament planes) and the second one with each layer's raster direction rotated 30° to the previous (a microscopic structure known as Bouligand) – Fig. 17(d). The Bouligand, trans- and inter-filament orientations had, respectively, toughness (K_{IC}), flexural and compressive strengths of ~3.1, ~3.0, ~2.4 MPa.m$^{1/2}$, ~159, ~202, ~125 MPa and 435, 452 and 452 MPa. It was noticeable that both flexural strength and toughness were higher in the trans-filament direction when compared to the inter-filament; for this reason, cracks will preferentially grow on the inter-filament plane. This way, in structures such as the Bouligand in which the directions of the planes change from one layer to the next, either the crack path to propagate through the crack preferential growing plane (inter-filament) would be increased (helical propagation, improving fracture surface area) or the crack would be required to propagate in the less favorable plane (trans-filament, higher mechanical properties); in both cases, the energy adsorption during fracture would be improved. This behavior explains why, comparatively, the Bouligand structure had similar strength and toughness values to the other orientations (trans- and inter-filament), characteristics attributed mainly to the smooth elastic modulus transition between the rotated layers and the helical crack propagation in this structure. The high volume fraction of aligned reinforcing phase of the composites obtained led to, when compared to studies with short carbon fiber reinforced epoxy

composites (CFRP), comparable compressive strength [216], higher strength and stiffness [217] and higher hardness [218]. Besides, the strength of natural analogs that utilize similar toughening mechanisms, such as cortical bone, is outperformed by a factor of two [219]. Therefore, the study inferred that printing with relative orientation between filament layers enables some control over the direction of crack propagation that is currently impossible with other approaches. Hence, the combination of DIW with microstructural control is a promising approach for fracture control, toughness and defect tolerance improvement while preserving high specific strength.

Fig. 17. Dense components of oriented alumina platelets infiltrated with epoxy. (A,B,C) SEM images of filaments printed using different nozzle lengths, evidencing its effect on the level of concentric platelet alignment. Scale bars: 30 µm. (D) Schematic diagrams of the three morphologies (trans-filament, inter-filament and Bouligand) obtained by controlling the printing direction with indicated fracture direction. (E) Crack resistance curves of each composite plotted from 6 tests. SEM images showing: (F) delamination of layers during trans-filament fracture, 300 µm scale bar; (G) deflection around filaments during inter-filament fracture, 300 µm scale bar; (H) crack deflection in the Bouligand structure, 300 µm scale bar; (I) large scale bridging, 20 µm scale bar and (J) small scale bridging of individual platelets, 10 µm scale bar.

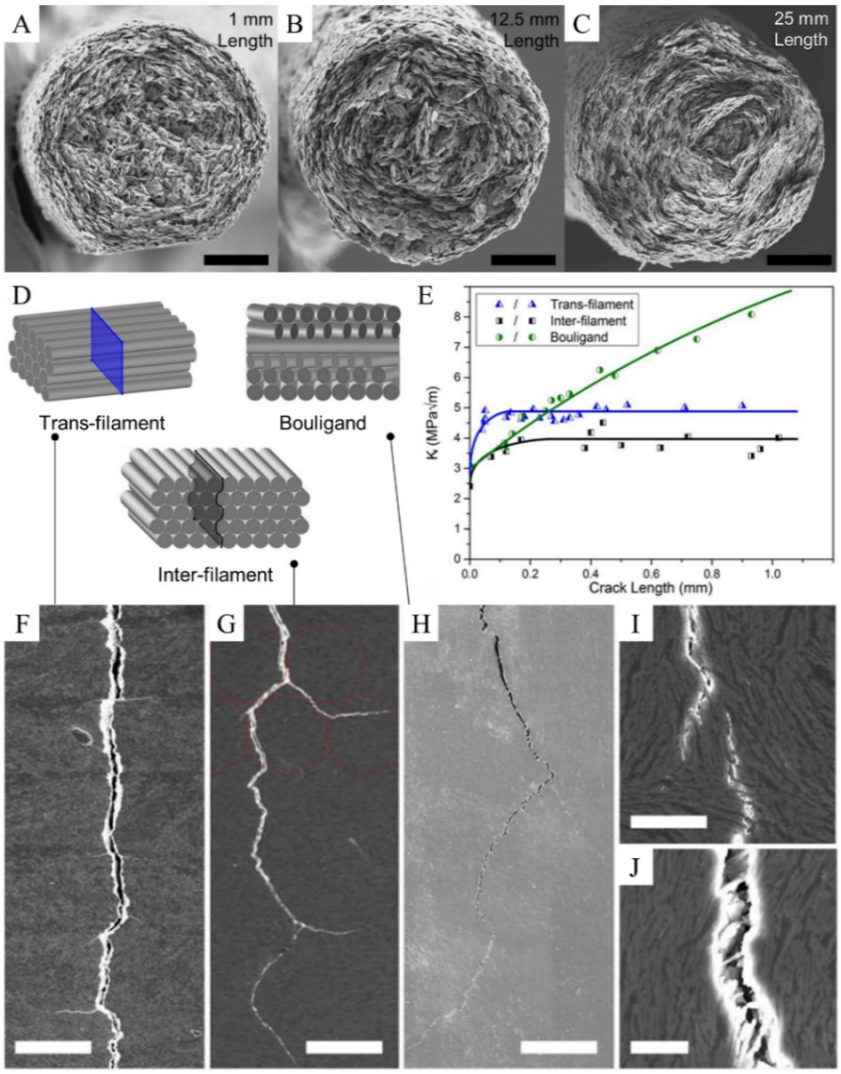

Source: Adapted from [32].

In a series of papers, Martínez-Vázquez *et al.* studied the infiltration of β-TCP scaffolds with PCL or PLA. In the first one [220], infiltration was performed by melt-immersion and the scaffolds were evaluated in terms of their mechanical response under uniaxial compression based on stress fields FEM (finite element modeling) calculations. The β-TCP paste had a solid content of 40 vol%, Darvan® C as deflocculant (1.5 wt%), Methocel® F4M (7 mg/mL of liquid) and a flocculant (PEI, 2 vol% relative to the liquid content). Printing was conducted with 250 μm cylindrical nozzles in a paraffin oil bath to ensure uniform drying. The scaffolds were debinded at 400 °C (1 h) and sintered at 1200 °C (1 h). The structures had tetragonal 3D mesh with 49% overall porosity (with 170 (PCL) and 140 μm (PLA) pore sizes) and ~25% in-strut porosity before infiltration. The PCL and PLA coatings enhanced the compressive strength of the scaffolds by a factor of three (60 ± 10 MPa) or six (130 ± 20 MPa), respectively (Weibull moduli of 7.7 ± 0.5 (PCL) and 7.6 ± 0.3 (PLA)). These improvements were attributed to the sealing of pre-existent defects in the ceramic struts' surface and the partial transfer of stress to the polymer (confirmed by the finite element analyses). For the polymers studied, defect healing alone was responsible for a three-fold strength increase in both cases, while stress shielding was only significant for PLA, granting an additional two-fold strengthening. The infiltrations also significantly enhanced the structures' mechanical integrity after initial cracking, with the retention of a considerable load-bearing capacity after the fracture of the ceramic struts. In summary, the composites produced presented great potential for bone regeneration applications, especially the β-TCP/PLA scaffolds, which had compressive strengths analogous to those of cortical bone alongside the comparable density.

In another study [221], Martínez-Vázquez *et al.* evaluated the flexural strengths of β-TCP scaffolds infiltrated with PCL or PLA produced in the same manner (the only difference was that the sintering procedure was conducted for 2 h instead of 1 h). The structures with ~68% porosity before infiltration (of which ~64% was open porosity, hence accessible) had an improvement in flexural strength by a factor of 5 (10-15 MPa) when infiltrated with PCL and 22 (43-62 MPa) with PLA infiltration. These enhancements evidenced that the strengthening and toughening effects of polymer infiltration previously reported under compressive stresses [220] were also reproducible in bending and became even more prominent under this more detrimental solicitation – a fact attributed to an improvement in the effectiveness of the stress shielding mechanism under bending. Another essential energy dissipation mechanism was the crack bridging provided by the elongation of polymeric micro- and macro-fibrils. Polymeric micro-fibrils within the filaments micropores produced a continuous crack micro-bridging toughening, whereas polymeric macro-fibrils in the macropore channels could bridge the crack

wake even after very large strains. Unfortunately, macro-fibrils are only present in ductile polymers (i.e., PCL), but micro-fibrils (if short) can be observed even in relatively brittle polymers, such as PLA. Therefore, the optimal infiltrating material would be a biodegradable polymer that combines the stiffness of PLA to improve strengthening by stress shielding and the ductility of PCL to enhance toughness.

In a complementary study [222], the group infiltrated β-TCP scaffolds with PCL or PLA with *in situ* ring-opening polymerization of ε-CL (ε-caprolactone) and LLA (l-lactide), utilizing lipase and stannous octanoate as catalysts, respectively. The composition of the paste was similar to those already used by their group with 45 vol% of solid content, Darvan® C (1.5 wt%), Methocel® F4M (7 mg/mL of liquid) and PEI (2 vol% relative to the liquids); printing with 250 μm nozzles in paraffin oil bath. Debinding and sintering were conducted at 400 °C (1 h) and 1200 °C (2 h), respectively, followed by infiltration. The mechanical properties of the infiltrated scaffolds by *in situ* polymerization (ISP) were significantly higher than those of bare structures, with values similar to those obtained by more aggressive infiltration methods (i.e., melt-immersion), with compressive strengths of 18 ± 2 MPa (ε-PCL) and 68 ± 7 MPa (PLA). When comparing this study with an already mentioned analogous study of this group [212] that utilized coating instead of infiltration, the infiltration with ε-PCL had compressive strength values in the same range as those coated with this same polymer (15 ± 2 MPa). Overall, ISP utilizing either enzymatic (for ε-CL) or conventional (for LLA) catalysts was shown a successful approach for an organic solventless infiltration of scaffolds. In this regard, *in situ* polymerization with enzymatic catalysts is even more promising – it requires a lower processing temperature (60 °C for 72 h for ε-CL), enabling the incorporation of sensible components such as drugs or growth factors, enhancing the composite scaffolds' bioactivity. Yet, to incorporate these components, the polymerization conditions (catalyst, temperature, time) may require some adjustment to retain the target biomolecule's integrity, which is likely to lead to a reduced polymeric molecular weight.

Similarly, Eqtesadi *et al.* studied the infiltration with PCL and PLA as well as coating with them; both processes were performed on bioactive glass scaffolds. In a first paper [223], 45S5 BG scaffolds (45 vol% of solid content and 1 wt% of CMC), printed with 410 μm nozzles, debinded at 400 °C (1 h), sintered at 500 or 1000 °C (1 h), were infiltrated or coated with ε-PCL (Fig. 18(a,c,e,g,h). Infiltration was performed by immersion in a polymer melt, producing fully infiltrated, dense co-continuous composites, whereas polymer-coated scaffolds were produced by dip coating (dissolution in toluene). Both processes generated structures with significant strength and toughness comparable to the properties of cancellous bone, even under

bending. The improvement found in strength and toughness provided by the polymer was higher in fully infiltrated scaffolds than in coated ones, with the toughening being especially intense under flexural stresses (≥ 2 orders of magnitude). The gain in strength and toughness with polymer infiltration, both under compressive and flexural stresses, was increased monotonically with increasing microporosity level in the ceramic struts; i.e., strength and toughness decreased with increasing sintering temperature. Despite the diminished effectiveness of polymer infiltration as a reinforcing approach once microporosity is reduced, denser ceramic struts generated stronger and tougher structures after polymer infiltration; hence, the optimization of the sintering conditions of the ceramic scaffold was a crucial aspect to maximize the mechanical properties of ceramic/polymer co-continuous composites. The study results highlighted the suitability of polymer infiltration as a strategy to mechanically reinforce ceramic scaffolds, being an excellent approach especially when full densification of the ceramic scaffold cannot be attained. Moreover, despite the higher improvements in strength and toughness provided by full infiltration, the effect of simple polymeric coating was relatively significant, even under flexural solicitations.

In a following study [224], Eqtesadi *et al.* evaluated the infiltration or coating of the same bioactive glass (45S5) this time with PLA (Fig. 18(b,d,f)). The printing pastes had the same composition as the previous study, the structures were produced similarly (melt-immersion or dip coating) and sintered at temperatures from 550 to 1000 °C. The PLA-coated scaffolds presented significantly higher toughness and strength than un-coated structures, both under compression and, especially, bending. Nevertheless, fully-infiltrated scaffolds with PLA did not exhibit a significant mechanical improvement over coated structures, as happened with infiltration with PCL in the previous study. This enhancement was prevented by chemical interactions of the molten PLA with alkaline ions from the 45S5, an interaction that has already been reported [225,226], resulting in the color change and cracking of PLA. Hence, the authors suggested shorter periods and mild processing temperatures to prepare BG/polymer composites to avoid polymer degradation in the BG presence.

Fig. 18. Bioactive glass (45S5) scaffolds infiltrated or coated with either PCL (A,C,E,G,H) [223] or PLA (B,D,F) [224]. (A,B) Compressive strength, (C,D) bending strength and (E,F) strain energy density vs. sintering temperature. (G) Strengthening and (H) toughening factors vs. in-strut porosity of the scaffolds infiltrated or coated with PCL.

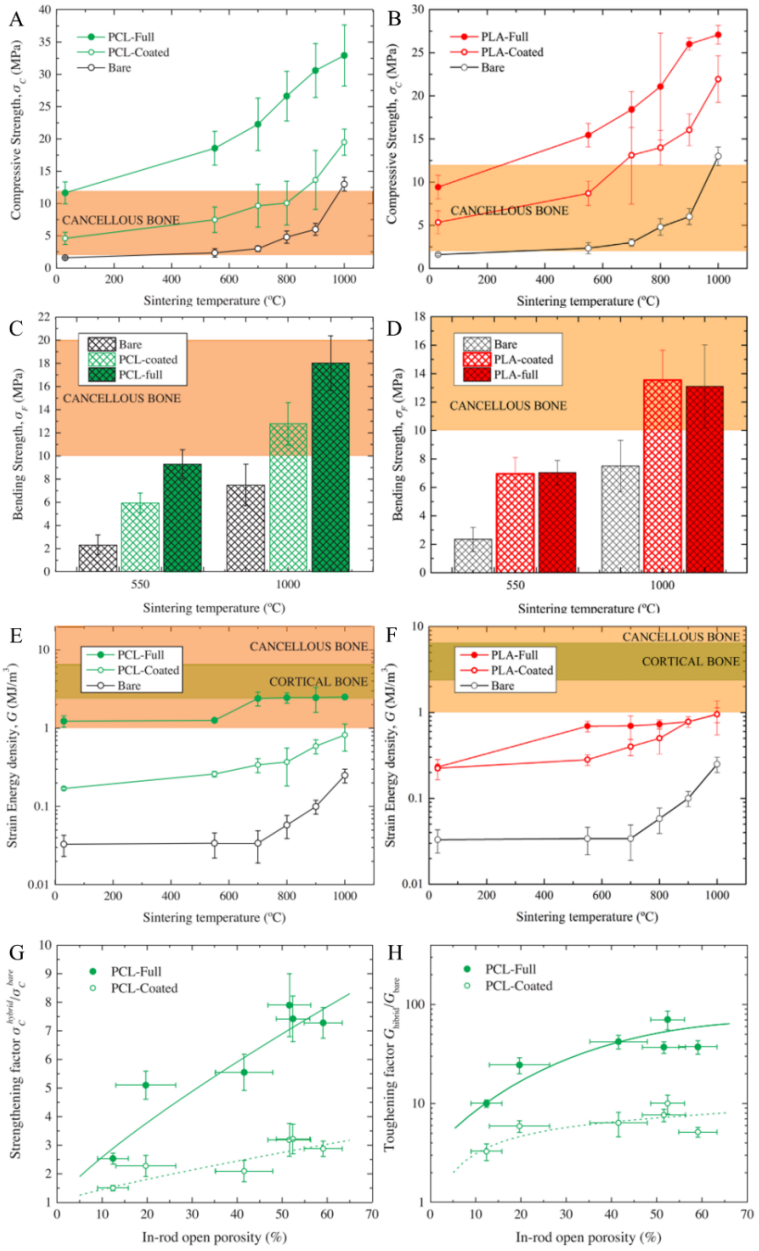

Source: Adapted from [223,224].

5.3.4. Other studies with ceramic-polymer composites worth mentioning

A particular type of injury, osteochondral (OC) defects, generally encompasses the cartilage's damage and its underneath subchondral bone. Tissue engineering has become the most promising approach for repairing OC defects in recent years, combining scaffolds, cells and growth factors. To match the hierarchical mechanical performance of natural OC tissue, the ideal OC scaffold should present a gradient structure and, as such, DIW has emerged as a technique to satisfy such requirements as a result of its precision and customizability. Thus,

Zhang *et al.* [227] used finite element simulations (FEM) to evaluate the influence of pore shape and porosity on the mechanical properties of DIW-printed HA/PCL scaffolds for osteochondral repair (Fig. 19). Different lay-down angles (15, 30, 45, 60, 70 and 90°), filament diameters (300, 400 and 600 μm), inter-filament spacing (400, 700 and 1000 μm), and layer overlaps (50-300 μm) were simulated under compressive conditions. With these parameters, porosity varied from 30 to 75%, compressive strength from ~5 to 22.5 MPa and Young's moduli from ~2 to 17 MPa (in the range of osteochondral bone); the latter linearly decreased with increasing scaffold porosity, in which the greater presence of voids facilitated deformation (i.e., lower Young's moduli). The orthotropic effect was found to increase as the lay-down angle was reduced from 90° to 15° and the most pronounced effect for scaffolds with a single lay-down angle was achieved when this value was 90°. The study also suggested that a value of ~60% of porosity separates the application between cartilage repair and cancellous bone repair. Overall, quantitative relationships were found between pore geometry and the scaffolds' mechanical properties. The investigation demonstrated that a mimetization of natural OC tissue's hierarchical mechanical properties is achievable by tuning the scaffolds' local lay-down angles and porosity.

Fig. 19. HA/PCL scaffolds for osteochondral repair. (A) Schematic illustration of the lay-down angles utilized and their associated unit cells in the XY plane. (B) Young's modulus *vs*. inter-filament spacing for scaffolds with different filament diameters. (C) Young's modulus *vs.* layer overlap. (D) Young's modulus *vs.* porosity of the scaffolds for different filament diameters, inter-filament spacing and layer overlap.

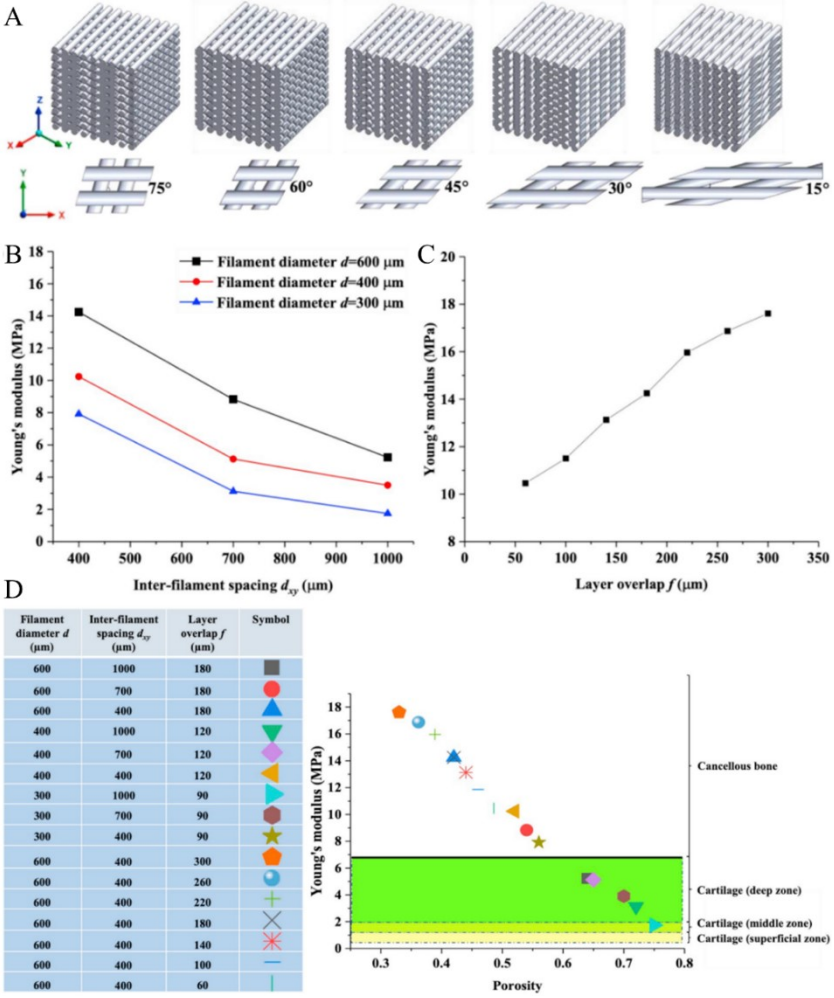

Source: Adapted from [227].

A novel fabrication method to obtain hybrid ceramic/polymer porous scaffolds with core/shell struts was developed by Paredes *et al.* [154,155]. In this technique, hollow ceramic struts are deposited by coaxial nozzles and are then filled with a polymer melt by suction (Fig. 20) – the main advantages are the conservation of the scaffolds' macroporosity required for cell ingrowth and the bioceramics surfaces' osteoconductivity. In a study utilizing this method to produce β-TCP/PCL scaffolds [154] (Fig. 20(d-f)), the printing paste had a solid content of 35 vol%, Darvan® C (1.5 wt%), Methocel® F4M (7 mg/mL of liquid), PEI (4 vol% relative to the liquids) and a fugitive graphite-based paste for the fugitive core. The coaxial printing nozzle had 1.37 mm outer internal diameter and 0.83 mm inner external diameter and printing was conducted in a paraffin oil bath. The struts' polymeric core was found to provide an outstanding toughness improvement under bending, with an increase of approximately two orders of magnitude; even after large deflections, the continuous polymeric fibers could hold the structure

together. In terms of strength, PCL infiltration improved the compressive strength over scaffolds with hollow struts, but dense-strut structures were stronger, particularly under compression. In another study [155], their group produced HA/PCL scaffolds (Fig. 20(g-k)) with a porosity of 42 ± 12% through the same method (the only difference was the solid content of 45 vol%). The results were analogous with significant toughness improvements in compression and bending over dense- and hollow-strut scaffolds, yet, in terms of strength, no significant enhancements with PCL infiltration over hollow-strut scaffolds were found. The study also evaluated the influence of a displacement of the printed layers (no offset and 50%-offset configuration) under a compressive load normal to the printing plane, which found that non-displaced layers had better performance in compression and bending. This behavior was attributed to the continuous columns of material formed via the intersections between the non-displaced layers, which support the compressive load applied. In contrast, with a 50%-offset configuration, the load produced pure bending in the struts perpendicular to the load, promptly failing under this more deleterious loading mode. These results confirm that a load perpendicular to the printing plane is more detrimental than along the strut/filament axes, as stated by Peroglio *et al.* [228]. In summary, the proposed toughening strategy of coaxial core-shell struts had the aforementioned benefits of preserving the macroporosity and osteoconductive properties of the bioceramics and, therefore, holds great promise for the mechanical improvement of scaffolds for bone regeneration applications without threatening their biological performance.

Fig. 20. Scaffolds with a core/shell strut configuration. (D-F) β-TCP/PCL [154] and (G-K) HA/PCL [155] scaffolds. The core-shell hybrid scaffolds were produced by co-extrusion, depicted in isometric and section view in (A), followed by PCL infiltration of the sintered tubular scaffold by suction (B). (C) Schematic representation comparing ceramic (gray)/polymer (blue) composites obtained through polymer infiltration of scaffolds: core/shell structures, coated and fully infiltrated. (D) SEM micrographs at different magnifications of representative cross-sections of the scaffolds fabricated with (a–c) hollow, (d–f) hybrid and (g–i) dense struts. Diagrams of average (E) strength and (F) strain energy density for all structures in compression and bending. (G) SEM micrographs of cross-sections of representative scaffold struts: (a,b) dense (c,d) hollow and (e,f) infiltrated with 30%-PCL solution. (H) Compressive strengths and (J) strain energy densities for D, H, 15-I and 30-I specimens, under uniaxial compression (D: dense; H: hollow; 15-I: infiltrated with a 15%-PCL solution; 30-I: infiltrated with 30%-PCL solution). (I) Flexural strengths and (K) strain energy densities for D, H and 30-I specimens under 3 point-bending.

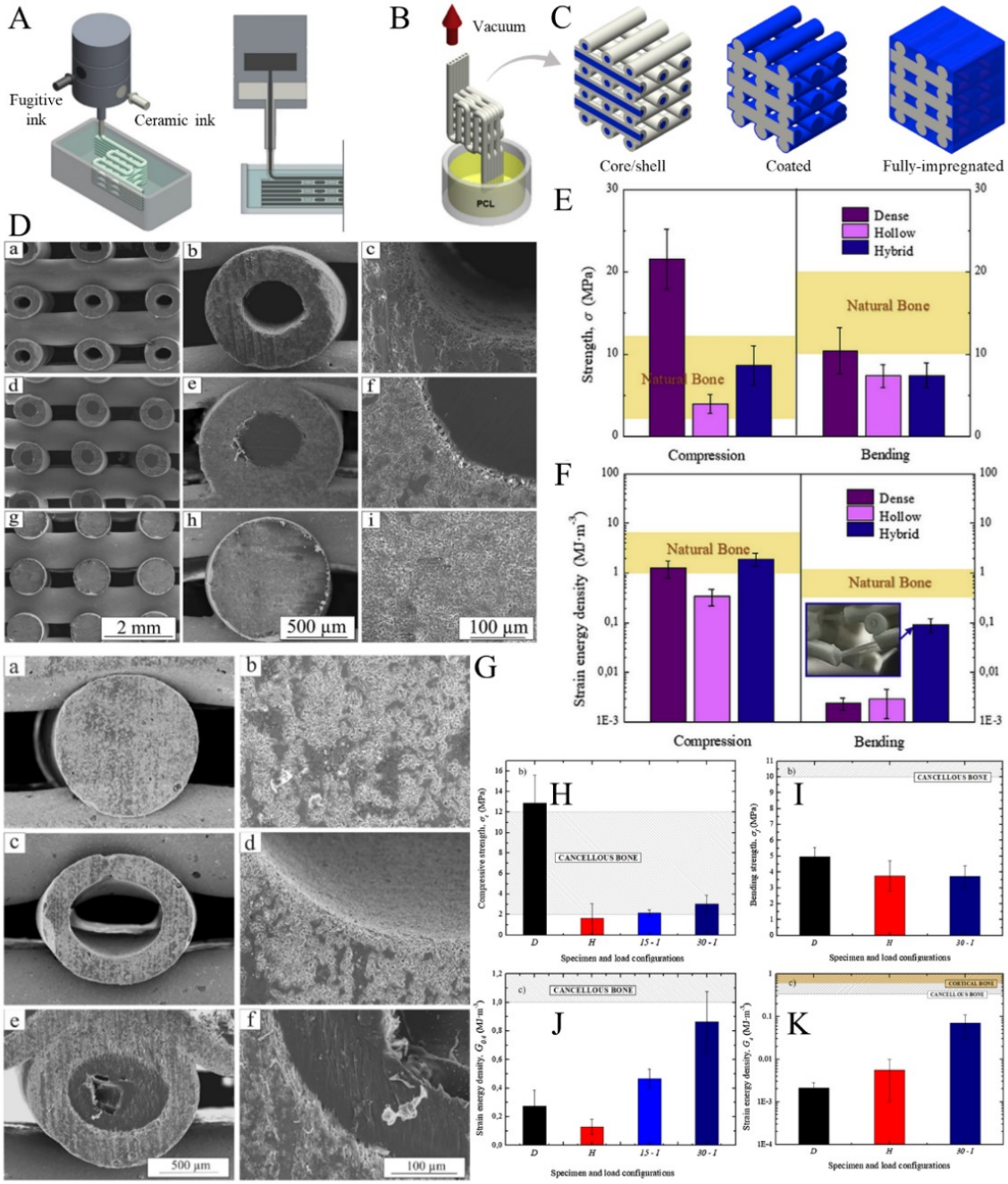

Source: Adapted from [154,155].
Natural bone values [229–231] are included for comparison.

5.4. CERAMIC-HYDROGEL COMPOSITES

Hydrogels are polymer 3D networks that can detain a large quantity of water and that can form great "soft material" microenvironments for the mimetization of ECM (extracellular matrix) as a result of their tunable mechanics, degradation and functionality [232]. The most established method to form ceramic/hydrogel composites with 3D printing is to formulate a hydrogel solution and then add ceramic powders to it [233]. After printing, this mixture immediately forms a network that can be developed (1) physically, (2) with an enzymatic mechanism, (3) through thermal/pH sensitivity [234,235] or (4) chemically by cross-linking [146,236–242]. The latter is by far the most used method for network formation with DIW and happens by the formation of covalent bonds between the added substance (usually genipin, glutaraldehyde or $CaCl_2$ solutions) and the amine groups of the hydrogels; UV light can also be used to induce cross-linking [240].

Usual hydrogels for 3D printing are those made from natural polymers such as gelatin, alginate, collagen, cellulose, hyaluronic acid, silk fibroin or those made from synthetic polymers such as polyacrylamide (PAM), poly(vinyl alcohol) (PVA) and poly(ethylene glycol) (PEG). Some made from a synthetic-natural mixture are also used. The utilization of natural polymers is linked to fewer side effects than these commonly associated with some synthetic polymers that might lead to detrimental degradation products and, consequently, reduced cell responses – the reason why the studies of DIW with ceramic-hydrogel composites are focused on natural hydrogels.

Hydrogels are promising materials for use with the DIW method once they facilitate the achievement of proper rheological behavior. Due to their gelling ability, they can be printed with other materials without any other processing additives – a fact especially beneficial as it eliminates the issues related to binder removal, which hinder the attainment of full densification. However, a limited number of hydrogels are suitable to act as binders, property modulation is still a challenge and the usual low mechanical properties obtained still need improvement. In addition, special care is required when these composites are implanted *in vivo*, considering that hydrogels swell fast in the presence of water, which can culminate in a loose structure, decreased stability and even the breaking off of the structure. Some solutions to this issue have been proposed and are being studied (e.g., methacrylation [240]). The next paragraphs describe some interesting studies with ceramic-hydrogel composites obtained via DIW that have been considered.

Martínez-Vázquez *et al.* [236] produced a highly homogeneous Si-doped HA/gelatin scaffold for bone regeneration with suitable macroporosity for vascularization and micropore architecture that allows fluid exchange. The DIW paste was produced by gradually adding the HA powder to a hydrogel of gelatin (1 wt% in distilled water, 45 °C), which was printed at 30 °C with 500 μm nozzles. Subsequently, the printed scaffolds were soaked in a glutaraldehyde solution to allow the cross-linking procedure of the gelatin. The total open porosity was 80-84%, with a compressive strength of 2.7-3.8 MPa (comparable to those of cancellous bone). The MC3T3-E1 cell differentiation in terms of gene expression and matrix mineralization was improved by incorporating gelatin into the paste. The study also included the addition of an antibiotic (vancomycin) in the slurry, which was gradually released to the medium in the short term and could efficiently hinder bacterial growth. This fact could grant a drug therapeutic concentration in the implantation site when the scaffold has not yet been vascularized.

Lin *et al.* [237] utilized the DIW method to print hydroxyapatite/collagen scaffolds with ~60-80% porosity that retained most of the properties of the raw materials after printing (Fig. 21). To obtain the printing paste, collagen and HA were individually homogenized in acetic acid solutions (0.5 M), which were then mixed at 4 °C (2 g collagen, 4 g HA in 10 mL of acetic acid solution). Printing occurred at 4 °C with nozzles of 300 μm in diameter and 90 % of relative humidity. The scaffolds were cross-linked by immersion in a genipin solution. Compared to non-printed scaffolds, those produced via DIW had a better proliferation of bone marrow stromal cells and improved *in vitro* osteogenesis. At the same time, enhanced cell penetration and mineralization improved the repair of 3D-printed scaffolds *in vivo* (rabbit femoral condyle defect model). The best results in terms of mechanical strength and *in vivo* bone repair were achieved with 600 μm-diameter struts; still, the compressive modulus (0.1 MPa) was very low.

Fig. 21. Hydroxyapatite/collagen scaffolds for bone regeneration. (A) 3D µ-CT reconstruction of the scaffolds and new bone formation at 2, 4, 8 and 12 weeks after *in vivo* implantation (rabbit femoral condyle defect model), 1 mm scale bar. (B) SEM images of BMSCs on the scaffolds' surface at 1, 4, 7 and 11 days after *in vitro* seeding. It is possible to observe the cells' growth into the printed scaffolds (Groups I, II, III) 11 days after seeding. (C) Surface morphology of the scaffolds with a grid-like microstructure with pore widths of 400 µm and strut widths of 300 µm (Group I), 600 µm (Group II) or 900 µm (Group III). Group IV represents non-printed scaffolds and Group N is the blank control. Printed bone with marrow cavity, femoral head and tibial plateau, 5 mm scale bar. (D) Histological analysis of new bone formation within and around the scaffolds (rabbit femoral condyle defect model). Van Gieson staining with newly formed bone in red and fibrous tissues in blue, 100 µm scale bar.

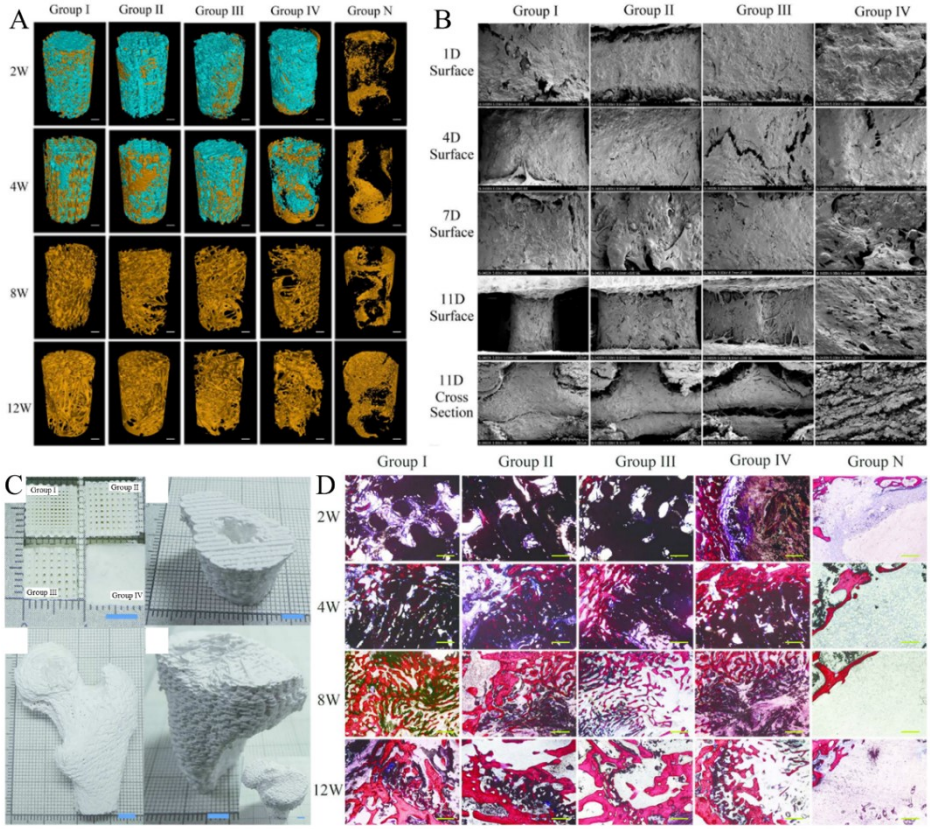

Source: Adapted from [237].

To mimic the bone native extracellular matrix (ECM) without compromising the mechanical strength, Zou *et al.* [234], in an interesting study, coated the filaments of sintered β-TCP scaffolds with type I collagen gel to obtain an ultrafine fibrous network analogous to the natural collagen nanofibers in the bone. Printing pastes had 45 vol% of solid content, ammonium polyacrylate (1.5 wt%) as a dispersant and hydroxypropyl methylcellulose 4000 (HPMC, n.d. quantity); printed nozzles had a diameter of 250 µm. For the coating procedure, the sintered β-TCP scaffolds were dipped in a collagen solution followed by the gelation of the collagen (37 °C for 2 h). The scaffolds presented a 43-44% porosity with ~250 µm pore sizes and compressive strength of 15.3 ± 3.4 MPa. The study concluded that the thin layer of biomimetic collagen nanofibers significantly stimulated the osteoblastic differentiation in mMSCs (mouse mesenchymal stromal cells) – by the up-regulation of the expression of Runx-

2, ALP, BSP, collagen I, OPN and BMP-2 – and improved the matrix mineralization – by the induction of more active biogenesis of matrix vesicles in the mMSCs.

To produce hierarchical porous scaffolds, Sommer *et al.* [238] developed concentrated oil-in-water emulsions that were stabilized by chitosan-modified silica nanoparticles. The emulsions contained 50 wt% of an oil phase (either decane (volatile) or corn oil (non-volatile)) and 50 wt% of chitosan-modified silica suspension (aqueous phase), which were mixed and centrifuged to concentrate the oil phase with the discarding of the aqueous supernatant. The resulting emulsions were printed (410 μm nozzles) into scaffolds with a hierarchical structure intended for simultaneous bone regeneration and drug delivery. After printing and drying, cross-linking took place by exposing the scaffolds to the vapor of a glutaraldehyde solution (5 wt%). The chitosan-modified silica emulsions were sufficiently stable against coalescence during centrifugation and formed droplets interconnected by a percolating network of agglomerated modified silica particles (gelled in the presence of chitosan). This good stabilization of the emulsion was derived from the fact that the particles were irreversibly adsorbed on the air/oil-water interface, hindering the droplets' coalescence. It is also the reason why particle-stabilized foams and emulsions are notably appealing templating processes as, when compared to surfactant-stabilized systems, they grant higher mechanical stability during drying as well as a more homogeneous pore-size distribution [243,244]. Besides, such emulsion-based multiphase architecture enables site-specific encapsulation of hydrophilic and hydrophobic compounds into the same structure, offering great flexibility in local compositional control. This dual-chemical nature permits the incorporation of apolar and polar functional constituents in exact positions, which can overcome the current issues with the delivery of incompatible compounds and tune the compound/drug release profile into the surrounding phase. Multiple parameters influence pore morphology and size (e.g., hydrophobicity of the particles, solid loading as well as pH and concentration of the air or oil phase), which are crucial factors for the determination of the structure-property relationship of these materials [244]. Still, further studies are required to evaluate the range of mechanical properties achievable by structures produced with this combination of techniques.

A dual-pore structure scaffold made of chitosan and nano bioactive glass (nBG) was designed by Dorj *et al.* [235]. To obtain the printing paste, chitosan powder (6% wt/vol) was dissolved in distilled water (containing 2% wt/vol acetic acid) and mixed with an nBG solution also in distilled water. The nBG concentration in relation to the chitosan utilized was 0.1 by weight. The structures of nBG ($70SiO_2$-$25CaO$-$5P_2O_5$) were obtained with the DIW process under a dry-ice cooled bath and subsequent freeze-drying since, at ambient conditions, the

solidification of the paste was troublesome. For this process, the syringe was encapsulated in a heating jacket at 37 °C and the printing nozzle had 330 μm of diameter. After printing, the scaffolds were freeze-dried at -50 °C. The study achieved nBG/chitosan scaffolds with aligned macro-channeled pores and well-developed micropores (≥ 10 μm) throughout the structure (Fig. 22), which presented a good *in vitro* biological response. The bone cells had great adherence and showed active growth with increasing culture time. It was also found that the nBG addition sped the induction of bone mineral-like apatite in SBF, demonstrating the composite *in vitro* bioactivity. In summary, the obtained composite structure was proven a favorable substrate when it comes to cell spreading and proliferation and *in vitro* apatite forming ability.

Fig. 22. Chitosan and chitosan/bioactive glass scaffolds. (A) SEM morphologies at different magnifications of the scaffolds of (A-C) chitosan/BG and (D,E) chitosan. (F) SEM morphology of cells grown on the nanocomposite scaffold for 3 days. (G) Cell proliferative potential of both Chit and Chit/nBG scaffolds, as measured by an MTS assay.

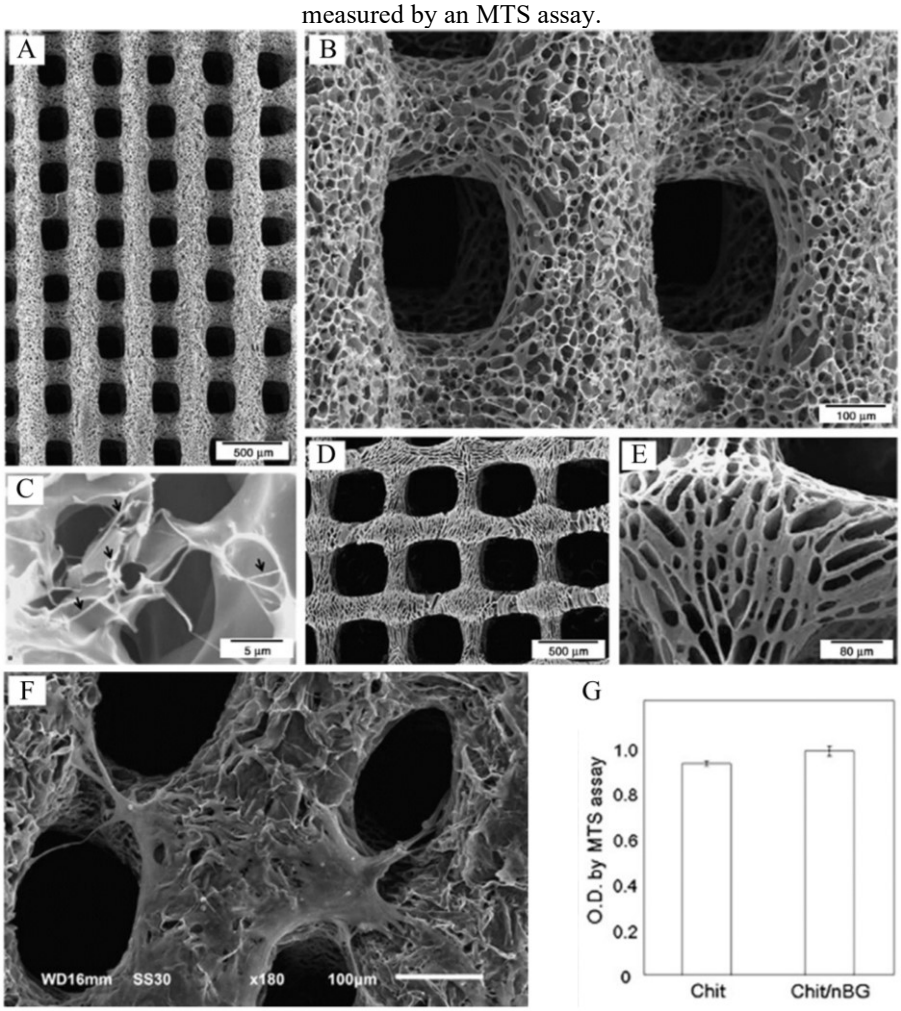

Source: Adapted from [235].

In a study by Marques *et al.* [239], composite scaffolds of BCP (HA:β-TCP; 23:77, 46:54 and 87:13)/chitosan were obtained without any processing additives. Paste preparation

first comprised of adding chitosan (3 wt%) to an acetic acid glacial (0.5 vol%) solution, then slowly adding the BCP powder (45 vol% of solid content) and later 1 wt% of genipin for the cross-linking of chitosan. The sintering-free resulting structure had ~50% of porosity and compressive strength of ~1-2 MPa. The β-TCP content in the BCP powders, which is more soluble than HA, strongly influenced the chitosan gelation behavior, hindering the achievement of suitable rheological properties; an attainment that was impossible for pastes with β-TCP content higher than 50 wt%. As the process did not require a sintering step, drug-loaded scaffolds became a possibility and levofloxacin, an antibiotic, was added to the extrudable pastes. This addition slightly changed the rheological behavior and, as a consequence, also the scaffold microstructure and mechanical properties – this effect was more pronounced in pastes with a higher content of β-TCP. The drug delivery evaluations unveiled a high burst of levofloxacin within the first 30 min. It was also found that the antibiotic preserved its bactericidal efficacy during the fabrication process since samples loaded with levofloxacin could inhibit bacterial growth. Overall, composite scaffolds with higher amounts of HA (87:13) were more promising for bi-functional bone substitutes with local bone regeneration and infection treatment abilities.

In their study, Cebe *et al.* [240] compared the effect of chitosan- and gelatin-based scaffolds on osteoblastic biomineralization. They fabricated scaffolds of laponite (a nano silicate) with chitosan (MAC-Lp) or gelatin (MAG-Lp). Both the chitosan and gelatin were previously methacrylated (methacrylate anhydride) to control their hydrolytic degradation and strengthen their network formation. These underwent a process of dialysis, freeze-drying and were then mixed with laponite (4 wt%) to enhance gelation; Irgacure® 2959 photoinitiator and sucrose (4 wt%) were also incorporated. The printing process (250 μm nozzles) took place with simultaneous *in situ* cross-linking using UV light. The methacrylation procedure improved the thixotropy of the paste and, consequently, its mechanical properties, a process that was fortunate as the achieved compressive strength was ~15 MPa. The comparison showed that MAC-Lp scaffolds had higher biomineral formation and cell viability and growth than MAG-Lp scaffolds. MAC-Lp also presented an increased formation of ECM collagen-like amide. Hence, the study established that chitosan-nanosilicate-based scaffolds favor the biomineral formation in osteoblasts and improve cell growth while creating mineral nodules in a short period compared to gelatin-based scaffolds.

Hydroxyapatite/chitosan scaffolds were developed by Zafeiris *et al.* [241] with a macropore structure attained through DIW and micropores by freeze-drying. The HA nanocrystals (Ca/P of 10/6) were biomimetically synthesized in the presence of chitosan

(HA/chitosan = 70/30, wt) and L-arginine (Ca^{2+}:arginine = 1:1, molar) and to improve ink rheology and, as a consequence, the mechanical properties, chemical cross-linking with genipin (1 wt%) was performed as well as the utilization of an acetic acid/gelatin solution; the latter was intended to increase the viscosity of the paste and avoid water-hydrogel separation during extrusion. The study encompassed several parameters, such as infill, flow and perimeter speed and showed that smaller pore sizes contribute to higher mechanical integrity. The printed scaffolds (600 μm nozzles) were later freeze-dried and the obtained porosity (61.5-92.7%) and elastic modulus (> 0.6 GPa) were comparable to those of cancellous bone. *In vitro* evaluations demonstrated the cytocompatibility of the scaffolds with good cell adherence and high levels of viability. The SEM analysis also indicated that the internal porous network favored cell attachment since the osteoblasts maintained their morphology while infiltrating the scaffolds.

Chitosan was also employed alongside calcium phosphate precursors to obtain scaffolds in a study by Caballero *et al.* [245]. The pastes were made of dispersed platelet aggregates of dicalcium phosphate dihydrate and continuous chitosan acidic aqueous solution (three different concentrations: 0.15, 0.17 and 0.19 mol/L) – the initial inorganic-to-organic ratio varied from 50/50 to 80/20 (wt%). These were printed with 400 μm nozzles into a basic water/ethanol (70/30) bath that ensured both the gelling of the solution and the conversion of the precursors into hydroxyapatite; hence with gelling by pH change occurring simultaneously to printing. Apatite was shown to be poorly crystalline, with the formation of micro-aggregates in platelet shape uniformly distributed within the chitosan matrix. The study focused on evaluating the rheological behavior of the pastes and found that chitosan concentration determined the polymer chain entanglement (higher concentration (0.19 mol/L) increased the printability of the pastes), whereas the inorganic-to-organic ratio determined both the mineral content and the ionic strength in the inks.

Alginate is another biocompatible and biodegradable hydrogel commonly utilized in applications such as tissue engineering and delivery of cells and growth factors [83,246]. Also, its sol-gel transition under mild conditions promoted by multivalent cations (i.e., Ca^{2+}) has been shown as an effective stabilization method for 3D printing, a fact that enables the encapsulation of cells, bioactive proteins and drugs into 3D-printed scaffolds [83,247].

A study that utilized this material with the DIW method was that of Kumar *et al.* [242]. They examined hydroxyapatite scaffolds with a parallelepiped porous architecture with 44% porosity and two different binders – sodium alginate (Alg) or maltodextrin (MA). For the HA/Alg paste, the HA powder was mixed with a 3 wt% Alg solution in deionized water and 1M NaOH. For the HA/MA paste, HA was mixed with MA (20 wt% in water) and PVA (12.5

wt% in water) solutions, with a subsequent pH adjustment. Printing was conducted with 410 μm nozzles and was followed either by drying, cross-linking (1 M $CaCl_2$ solution) and freeze-drying (4-6 h) or drying and sintering (1250 °C for 1 h). A higher compressive strength was found for HA/Alg scaffolds (9.5 ± 0.5 MPa) when compared to HA/MA (7.0 ± 0.6 MPa) – a difference attributed to their phase assemblage and microstructure – both in the range of cancellous bone (2-12 MPa) [53,54]. The study also compared the stabilization of the scaffolds through the processes of chemical (cross-linking) and sintering-induced stabilization. In that regard, sintering usually promotes higher compressive strengths but makes the scaffolds mostly non-biodegradable; on the other hand, chemical stabilization by a non-covalent cross-linking provides scaffolds less mechanically stable but allows them to be degradable. Besides, a sintering-free process enables the incorporation of sensitive biological components, such as drugs and proteins (like growth factors), during the printing process, as observed in some studies here highlighted.

Following the same line, Luo *et al.* [146] studied composites of alginate and bioactive glass nanoparticles (molar ratio: Si/Ca/P = 80/15/5) with dexamethasone. They produced MBG/alginate hierarchical scaffolds with good *in vitro* biocompatibility, mineralization ability and drug release properties. The DIW paste was produced by mixing the sodium alginate and MBG powders (MBG/alginate = 1:10; 3:10 or 5:10, wt), which were added into a 6% wt/vol aqueous PVA solution. After printing, the scaffolds were cross-linked in a $CaCl_2$ solution for 10 h. The structures had strut diameters of approximately 300-400 μm (printing nozzles of 406 μm) and porosity of ~50-67% but not such adequate compressive strengths (0.6-1.6 MPa). The composite had improved mechanical properties, apatite-mineralization ability, cell attachment and alkaline phosphatase activity compared to alginate scaffolds. The utilized drug, dexamethasone, was efficiently loaded in MBG particles that were incorporated into the alginate scaffolds, a fact that resulted in a more sustained release. The MBG incorporation reduced the initial drug burst and made the release concentration dependent on it. In addition, the use of a high-concentration alginate slurry and a specific printing pattern (XXYY) was able to improve pore interconnectivity and the dimensional and mechanical stability of the scaffolds.

5.5. FUNCTIONAL COMPOSITES

As highlighted before for functional ceramics, different functionality can be attained via protein/drug loading of the structures and the DIW method has been shown to be an

attractive platform to print such sensitive components. This fact is no different for ceramic composites, which are featured next with their corresponding attributed functionality.

Biphasic calcium phosphate (BCP) scaffolds coated with collagen and BMP-2 or dipyridamole – an agent that blocks cellular uptake of adenosine hence increasing local adenosine levels – were attained by Ishack *et al.* [248]. The BCP powder with a HA:β-TCP ratio of 15:85 was mixed (46 vol% solid content) with a Darvan® 821A solution (1.5 wt% of deflocculant), a 5 wt% aqueous Methocel® F4M solution (Methocel®: 7 mg/mL of ceramic) and a 10 wt% PEI solution (PEI: 5 mg per mL of paste). The scaffolds were printed (250 μm nozzles) in paraffin oil, sintered (1100 °C, 4 h), coated with collagen by crosslinking through irradiation and either immersed in a solution of BMP-2 (200 $ng.mL^{-1}$) or dipyridamole (100 μM). The scaffolds were implanted for 2-8 weeks in mice with 3 mm cranial critical bone defects. Improved bone formation and a tendency for increased remodeling were found in the micro-computed tomography (μ-CT) evaluations at 2, 4, and 8 weeks for BCP/dipyridamole and BCP/BMP-2 when compared to uncoated scaffolds. Still, no improvement in bone regeneration was found with scaffolds coated with dipyridamole in mice with knockout of adenosine receptors. Hence, coating BCP scaffolds with a growth factor and an agent that stimulates adenosine receptors could further increase bone regeneration and treat critical bone defects, with the first showing more promise than the latter.

The delivery of sufficient oxygen to an engineered tissue has been a considerable challenge to overcome the effect of hypoxia and, in this regard, scaffolds with oxygen-generating elements have shown increased oxygen levels and cell survivability in specific conditions, proving themselves good alternatives to prevent ischemia-related cell necrosis. With this intention, biphasic calcium phosphate (BCP) scaffolds (60HA:40β-TCP) were obtained by Touri *et al.* [249–251] in a series of papers in which three different contents (1, 3 and 5 wt%) of an oxygen-releasing and antimicrobial agent, calcium peroxide (CPO), particles were encapsulated within a polycaprolactone (PCL) coating (4% wt/vol in DCM) obtained via dip-coating. The BCP printed scaffolds (n.d. solid content or binder) were calcinated and sintered at 400 °C (1 h) and 1190 °C (2 h), respectively, before the coating procedure. The resulting scaffolds presented ~70% porosity with both strut diameters and pore sizes in the range of ~500 μm and compressive strengths of 21 and 23 MPa for uncoated and PCL/CPO coated structures, respectively. The oxygen release behavior was continuous and depended on the concentration of CPO encapsulated within the PCL coating. Scaffolds coated with 3% CPO presented enhanced osteoblastic viability and proliferation under hypoxic conditions and, alongside those coated with 5% CPO, had higher ALP activity. Antibacterial investigations

found that the CPO released from the scaffold was able to inhibit the growth of *S. aureus* and *E. coli*. Superior apatite precipitation of the coated scaffolds was confirmed by *in vitro* SBF tests due to the driving force role of the CPO particles in the apatite formation process. Such scaffolds could be excellent candidates for promoting bone ingrowth and simultaneous oxygen delivery for surrounding tissues, preventing cell death due to hypoxia in large bone tissue implants that present oxygen diffusion limitations.

In another study functionalizing BCP (60HA:40β-TCP), Song *et al.* [252] incorporated polyvinyl alcohol (PVA) and platelet-rich fibrin (PRF) into it and then printed the mixture through the DIW technique at low temperatures. The BCP powder was added to a 16 wt% PVA solution (powder/liquid mass-to-volume ratio of 1:1) with the subsequent addition of PRF, printing at ~4 °C with a 600 μm nozzle and freeze-drying. The resulting BCP /PVA/PRF structures had ~50% porosity and ~500-600 μm pore sizes. The printed BCP/PVA/PRF and BCP/PVA scaffolds presented significantly higher total porosities (54.7 and 49.6%, respectively) and lower compressive moduli values (~300 kPa) than the non-printed corresponding scaffolds (obtained via mold-casting, solidified at -80 °C, with resulting total porosities of 6.1 and 1.5%, respectively). The PRF incorporation enabled the sustained release of bioactive factors and improved the *in vitro* biocompatibility and biological activity of bone marrow-derived mesenchymal stem cells (BMSCs). It was shown that the PRF retained its biological activity during printing and that its presence provided cell-binding sites, promoting the BMSCs' adhesion, proliferation, and differentiation. In critical-size segmental bone defect models in rabbits, printed BCP/PVA/PRF scaffolds promoted more *in vivo* bone formation than printed and freeze-dried BCP/PVA scaffolds, demonstrating that the PRF presence likely provided osteoconductive and osteoinductive stimuli. Therefore, the BCP/PVA/PRF printed scaffolds' primary deficiency was their low mechanical strength and slow degradation rate, which require optimization. This fact does not change the potential shown by PRF growth factors' prolonged release, which could provide proliferation and differentiation stimuli.

Another critical procedure during the bone regeneration process is vascularization and its absence is acknowledged as a crucial challenge in cranial and maxillofacial defects. In this regard, to improve vascularization, Fahimipour *et al.* [253] developed β-TCP/alginate/gelatin scaffolds with PLGA (poly(lactic-co-glycolic acid)) microspheres containing vascular endothelial growth factor (VEGF); the VEGF-loaded PLGA microspheres were obtained by a modified double emulsion-solvent evaporation technique. The concentrations utilized for β-TCP and alginate were fixed at 30 and 5% wt/vol, respectively, whereas that of gelatin was varied (1, 3 or 10% wt/vol). Some difficulties with nozzle clogging related to the fact that the

mixture's gel point was above room temperature were found. These were solved by heating the syringe with the paste to 28 °C, cooling the platform for deposition to 10 °C and using a nozzle diameter of 450 μm. After printing, the scaffolds were immersed in a $CaCl_2$ solution for the cross-linking of alginate and later in EDC (N-(3-dimethylaminopropyl)-N'-ethylcarbodiimide) and NHS (N-hydroxysuccinimide) solutions for the cross-linking of gelatin. The β-TCP/gelatin/alginate scaffolds with VEGF-loaded PLGA microspheres presented porosity of 73 ± 8% and 98 ± 10 MPa of compressive modulus. The slow *in vitro* release kinetics of the VEGF was shown to fulfill the vascularization requirements for the tissue regeneration early stages. Besides, the VEGF-loaded composite structures supported cell viability, adhesion and proliferation – after 10 days, the human umbilical vein endothelial cells (HUVECs) seeded on them presented an increment of 2-fold in proliferation – and, after 2 weeks, had an improvement of 50% in the ALP activity.

6. DISCUSSION

Additive manufacturing emerged in the 1980s and promptly attained relevance in the biomedical engineering field due to the possibility of customizing objects according to the requirement of patients and clinicians [254]. Its initial motivation was to decrease the time to market of new products by minimizing the period between design, testing and implementation. Initially (in the '80s and '90s), flexibility in design was the priority, but as the essential technologies for AM were developed, the physical properties of the obtained parts became the main interest. Recently, products that cannot be produced but additively have been developed and introduced into the market, highlighting the potential of AM technologies to not only transform the way of conventional industrial manufacturing processes – adding material rather than subtracting it – but also to conceive entirely new products as well as business strategies. With the focus shifting from prototype fabrication to the fast manufacturing of end-use products in small or medium quantities, this modification in the perspective of what can be produced by AM has been stimulated. This acceleration was stimulated by the expiration of essential 3D printing patents (several expired in 2013-2015), as access to printers became easier and less expensive [254].

This shift from mass production to mass customization enabled by AM technologies comes alongside a significant decrease in production costs and an increase in efficiency when the fabrication of custom-made pieces or small series is considered [4]. In the biomedical field, mainly, the fabrication of patient-specific constructs with controllable micro-architecture

[255,256] from clinical image data of computerized tomography (CT) scans, x-rays and magnetic resonance imaging (MRI) is of crucial importance in the optimization of biological repairs, replacement and regeneration [257]. However, there are still some challenges related to the application of AM techniques. Sample surface finish, process reliability and the density of the components (for dense parts) are among the significant concerns. In ceramics, the presence of defects greatly influences mechanical properties; therefore, porosity and surface quality are critical factors.

Among AM techniques, direct ink writing has been gaining interest for the fabrication of ceramic-based components due to its simplicity, low cost and increasingly good achievable mechanical properties. As became perceptible with this review, this interest has been more prominent in the production of scaffolds that, in the area of biomedical engineering, are intended for bone regeneration applications in general. Compared to other AM technologies, scaffolds produced via DIW have been shown to have better mechanical properties than those obtained by powder-based technologies [21] – the strength is usually superior by one order of magnitude due to the high level of residual microporosity associated with powder-based approaches. In contrast, liquid-based processes, such as DIW, usually produce components that can achieve high density after sintering – once optimization of the process and the geometry has been achieved.

With such interest, some key features of the DIW method are worth highlighting, in particular the required rheological behavior of pastes, the limitations of the process and the mechanical and biological improvement strategies that have been proposed. In addition, this section describes new techniques analogous to DIW.

6.1. RHEOLOGICAL BEHAVIOR OF PASTES FOR DIW

As mentioned, the process of direct ink writing involves the computer-controlled deposition of a colloidal paste through a nozzle, forming spatially controlled continuous filaments. For a successful deposition, rigorous requirements are imposed on the rheological behavior of the pastes, as they must flow easily through a narrow opening and also, immediately after printing, resist deformation – in this regard, as it is not the scope of this review, a more throughout detailing on the parameters to predict printability can be found on [258] (more specifically on Table 3). There are two critical strategies to tailor this type of rheological behavior – one based on the phase change of the paste, the other on the achievement of a shear-thinning behavior – with some particularities related to each:

(1) Production of low-viscosity pastes that undergo viscosity change through a phase transformation after printing, rapidly developing a yield strength high enough to withstand deformation [21]. This behavior can be achieved by (a) the formation of a gel via the controlled flocculation of the paste (e.g., by the addition of polyelectrolytes, pH change, ionic strength of the solvent (when present)) [259], (b) the use of gelling/curing additives, such as (i) UV-curable pastes that are polymerized post-printing [199,200] – this method is an effective prevention of sample deformation, but is a slow process that requires a complicated setup/printing environment and leads to a complex UV-curable binder burnout process –, (ii) pastes dispersed in hydrogels [137,146,235–237,239–242] (gelling enables shape retention, but the assurance of proper gelling conditions requires additional environment control) and (iii) inverse thermo-reversible gels and (c) use of liquid pastes with high solid loading that undergo a small drying upon printing, thus going through the pseudoplastic-dilatant transition [30];

(2) Production of pastes that exhibit shear-thinning behavior, with solid loading content relatively close to the pseudoplastic to dilatant transition. Such pastes can be obtained by using a "liquid" carrier that already possesses a shear-thinning behavior, such as HPMC or Pluronic® F-127 solutions above their gelling point [29]. It is also possible to reach a shear-thinning behavior using a dispersant-binder-flocculant system (e.g. ammonium polymethacrylate-HPMC-PEI [212,220]), in which the powder is dispersed (usually in water) with the aid of a dispersant and then the paste is flocculated leading to a shear-thinning behavior (the binder is present to adjust the viscosity of the system and to provide reinforcement to the green parts) [105,125,126,260,261]. The latter has the advantage of requiring less organic material, facilitating the debinding step. In addition, powders with smaller particle sizes and low specific surface areas have been shown more appropriate for ink preparation [262].

6.2. LIMITATIONS OF THE DIW METHOD

Certain limitations are associated with the DIW method and demand consideration, special care and sometimes an association with other processing methods. The most imperative limitations are the obtained surface finish, the speed of the printing process and nozzle-clogging.

The surface quality of DIW-printed components primarily depends on the diameter of the filaments (directly related to the nozzle diameter). There is commonly a compromise

between the desired quality/resolution and processing time. A combination of DIW and computed numerical control (CNC) machining is possible and useful, especially for dense components: the near-net-shape obtained by DIW ensures that a limited volume of material is removed by CNC machining while the process of machining itself can provide an excellent surface finish [59]. Speed-wise, on first look, the DIW method might seem as if it should be further improved once the nozzle movement (with a speed typically of some $cm \cdot s^{-1}$) is much slower than the scanning speed utilized in light-based techniques (e.g., SLA and PμSL (projection micro-stereolithography)) [263]. However, when considering the building time, depending on the nozzle diameter being utilized, the DIW technique may be more advantageous. To print a cube with sides of 30 mm, for example, the SLA technique will take 100-235 min (with a typical build rate of 7.6-17.8 mm/h), whereas the DIW approach can take from 24 h (considering a nozzle of 200 μm and printing speed of 10 mm/s – 0.31 mm^3/s) to 27 min (840 μm and 30 mm/s – 16.6 mm^3/s). The DIW remains more advantageous when printing with a commonly used nozzle diameter (410 μm) with 30 mm/s (114 min) and 20 mm/s (171 min).

Another limitation of the DIW technique – nozzle clogging – usually occurs when printing pastes with strongly misoriented fibers, very high solid loadings or when using nozzles with an internal diameter less than 6.2 times the largest particle size [264]. Clogging reduces part fidelity and geometric accuracy. This process takes place by various mechanisms that depend on the nozzle geometry, fiber length and fiber volume fraction [265]. Croom *et al.* [265] deeply studied this phenomenon and have proposed some strategies to diminish the likelihood of clogging, such as improved nozzle designs (as roughness and sudden changes in diameter favor clogging), fiber pre-alignment upstream of the nozzle tip and a rotating nozzle around an internal static mandrel, which would actively mix the pastes and enable the shear strains to improve fiber alignment. As we could observe in this review, some authors utilize the strategy of printing within an oil bath to prevent nozzle clogging and to guarantee a uniform drying of the printed component. This printing of water-based inks in oil technique was developed by Smay *et al.* [266] to avoid the problems linked to simultaneous printing and drying of the component; when it comes to the materials subject of this review, the most commonly used oil is paraffin [27,29,95,111,130,154,155,212,220–222,248] but sunflower oil has also been used [161,162,187]. In addition, the utilization of powders with wide size distributions is known to favor flow through narrow printing nozzles [27].

6.3. STRATEGIES TO IMPROVE MECHANICAL PROPERTIES

Some strategies have been proposed to improve the mechanical properties of ceramic-based components produced with the DIW method. Among them, some optimize the morphological aspects of the component, whereas others change its composition. Both categories will be addressed below.

6.3.1. Reinforcement through morphological aspects

Amidst the first category are two strategies: reproduction of natural structures and obtainment of hierarchically porous structures (see Fig. 23). The first strategy, also known as mimetization, reproduces the complex hierarchical architectures of natural materials (e.g., bone, shells) that provide control over fracture and crack propagation [32,88,170]. It is estimated that the trade-off in modern composites between strength and toughness could be surpassed by the blueprints provided by natural materials, such as the Bouligand structures taken from crustacean shells, which can retain strength while improving impact resistance and toughness – characteristics that derive from the helical crack propagation and elastic modulus smooth transition between rotated layers [32]. The main advantage of this approach is the high strength-to-density ratio attained, whereas its limitations encompass (1) the production of these fine structures with complex shapes in practical times and sizes, (2) the fact that some structures may lead to lower compressive strengths and (3) the anisotropy of the structure, which, depending on the application, might be desirable.

Fig. 23. Illustration compiling the various studies that have utilized the DIW method to reproduce natural structures or to produce hierarchical porous structures. (A,B) Schematic diagram of a Bouligand structure and SEM image of the obtained composite with such structure with oriented alumina platelets infiltrated with epoxy; scale bar: 400 µm [32]. (C,D) Hexagonal honeycomb alumina structures, printed with a nozzle diameter of 200 µm [88]. (E) Schematic illustration of biomimetic vascular channeled scaffolds of β-TCP coated with rhBMP-2 [170]. (F,G,H,I) Schematic illustrations of alumina/camphene-based co-extrusion with microporous hollow struts and SEM images of the corresponding obtained structures (cross-section and strut) highlighting their hierarchical structure [84]. (J,K,L,M) Schematic illustrations of alumina/camphene-based co-extrusion with interconnected macropores and aligned micropores and SEM images of the cross-section and the aligned microporous framework developed [85]. (N,O,P) Schematic representation of the components and processing route of MBG/PCL composites obtained via DIW and subsequential salt leaching and SEM images of the overall structure and porosity [201]. (Q,R,S,T) Processing scheme of emulsion/foam templating + DIW and SEM images of emulsion-templated structures with closed porosity [90]. (U) Schematic illustration of the process of DIW of stable emulsions to obtain silica-chitosan composites and SEM images of these composites with different silica concentrations [238]. (V) Schematic illustration of the obtention of hot-dog like scaffolds of akermanite via DIW and bidirectional freezing and SEM images of the obtained microstructure [156].

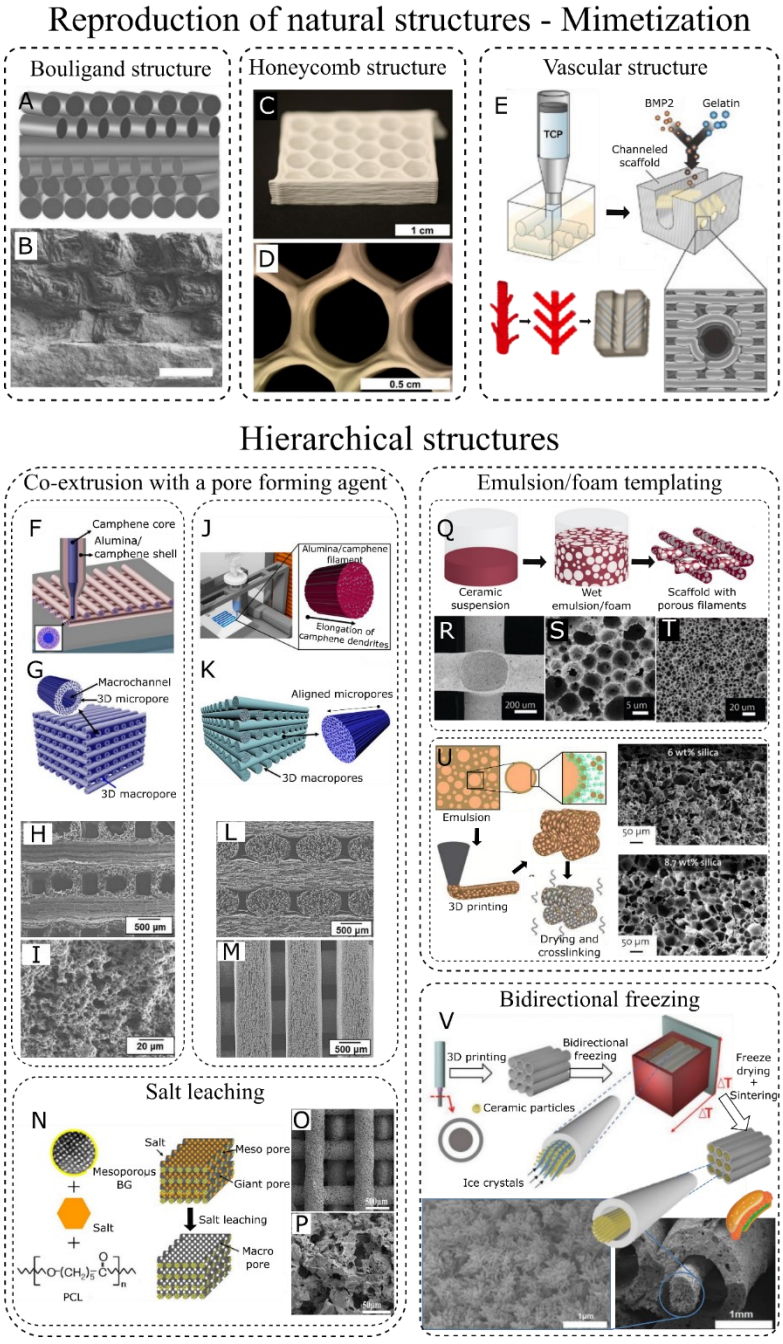

Source: Adapted from [32,84,85,88,90,156,201,238].

Most of the 3D printing research of ceramic materials so far has been focused either on the production of scaffolds with dense filaments or the obtention of dense components (not so common). Still, more recently, DIW has been associated with other ceramic processing techniques to develop hierarchically porous structures [84,85,88,90,146,156,158,170,201,238,267], another reinforcing strategy based on morphological aspects. Likewise the mimetization strategy, one of the main benefits of such structures is the alliance of low density and high relative compressive strength (high strength-to-density ratio), making them extremely attractive for load-bearing bone regeneration applications. Besides, hierarchical porous structures are known to outperform their nonhierarchical counterparts in terms of relative compressive strength and the accessibility of the material active surface [268], hence improving the *in vivo* bone-forming ability. Their potential comes from their ability to attain the design of complex biological structures, enabling load-bearing scaffolds to be loaded with functional components that can be potentially applied as drug delivery systems or that can have specific cues/signals to guide tissue regeneration. These loading/delivery capacities are extremely helpful in applications such as pharmaceuticals and cosmetics, with hierarchical structures often available in the form of emulsions utilized as vehicles for some compounds. The printing of such structures/emulsions into architectured materials has not been done until recently and unveils a new promise for the controlled delivery of sensitive compounds.

Hierarchically structured components can also be used in applications involving multi-tissue interfaces – a field in which innovative studies have been developed with hydrogels and DIW for prosthetic cartilage implants. This application was addressed by an already mentioned paper [227] that studied scaffolds to regenerate osteochondral defects by the variation of porosity and pore shape. In that regard, one recent study worth mentioning for the production of cartilage implants using DIW is that of Hirsch *et al.* [269], in which an ink composed of microgels was swollen in a monomer-containing solution and, after printing, the monomers were converted into a percolating network, which resulted in a DNGH (double network granular hydrogel) made from compartmentalized reagents that were more than one order of magnitude tougher than each pure polymeric network of which they were made. This result illustrates the potential of hierarchical structures obtained by direct ink writing for bioengineering applications.

Besides the already mentioned strategies, some other modifications on morphological aspects have been reported to improve mechanical performance as (1) pore geometry optimization (in which hexagonal [184] and honeycomb pores [150] showed promise), (2)

printing with smaller nozzle diameters [199], which produces fewer defects and enhances crystallinity and (3) production of smaller pore sizes (contributes to higher mechanical integrity) [241]. Better control of the sintering process could also improve the surface properties and the filament microporosity [262], thus improving the trade-off between mechanical properties and cell affinity with the scaffold surfaces.

6.3.2. Reinforcement through reinforcing phases

When mechanically reinforcing a component through the addition of reinforcing phases (compositional) – the other reinforcing front – the outcome greatly depends on the reinforcement material, its content and the reinforced matrix.

One strategy of reinforcing phase addition is the incorporation of a glass to assist the sintering process, which can be a glass similar in composition to the material [187] or a low-melt glass [173,174,270]. Two other strategies (polymeric full infiltration and polymeric coating) have overlapping, reinforcing mechanisms – sealing defects on the surface of the strut and preventing crack opening through crack-bridging polymer fibrils. Mechanically, full impregnation is a more efficient reinforcing strategy than coating [212]; however, the possibility of cell seeding in coated scaffolds is a useful approach to avoid or hinder colonization by undesired cell types when repairing large defects. Note that in this case, the cells are in direct contact with the polymeric material, not with the ceramic one. Conversely, the production of core-shell filaments with a polymeric core is a strategy that has shown outstanding improvements in toughness under bending [154].

A more specific summary describing the improvements reported for compositional reinforcements on ceramic-based materials obtained via DIW is displayed in Table 7. As can be observed, wollastonite-diopside [187] and bioactive glass [173,174,270] additions have been reported to increase the compressive strength, with the latter also presenting good biological outcomes. Additions of titanium fibers showed improved flexural toughness and strength with no deterioration of the biological properties of the components [192]. The other two materials utilized as reinforcement phases were carbon-based materials: graphene oxide (GO) platelets and carbon nanotubes (CNTs). Graphene oxide platelets presented excellent improvements in fracture toughness and compressive strength up to 1.5 vol% [127]; contents higher than 2 vol% caused agglomeration [178]. As a drawback, their addition hindered the viscous flow of the paste, hampering the densification of the matrix (in that case BG) [178]. Carbon nanotubes were shown to improve the compressive strength [202,208] and the elastic modulus [202] of the

components to which they were added. They have induced no significant inflammatory process or hindering of the beneficial biological properties of the other components present in the matrix [202] (their effects on the biological properties will be detailed in section 6.4.4). Their addition to a Si-doped HA/PCL matrix also induced a mesoporosity of approximately 20 nm and even enhanced cell attachment to the component [208].

Table 7. Summary of compositional reinforcements that have been studied in ceramic-based composites produced via the DIW method and their influence on the mechanical and biological properties of the printed components.

Reinforcement	Matrix	Structure	Porosity (vol%)	Influence on mechanical properties	Mechanical properties	Influence on biological properties	Remarks	Ref.
Wollastonite-diopside glass (10 wt%)	Wollastonite-diopside/ calcium carbonate/dolomite	Scaffold (BR)	68-76	Increase of ~63% in compressive strength	$\sigma_{compressive}$: 8 MPa	—	—	[187]
BG (28CaO-45SiO_2-4P_2O_5-18B_2O_3-5CuO)	Diopside ($CaMgSi_2O_6$)	Scaffold (BR)	62.5-65	5 or 10% BG enhanced the $\sigma_{compressive}$ of scaffolds sintered at 1150 °C	$\sigma_{compressive}$: 15.5-19.4 MPa	Favorable antibacterial, physicochemical and biological performance	—	[173]
BG (NCS-B, CaO-SiO_2-Na_2O-P_2O_5-B_2O_3)	Akermanite	Scaffold	62-65	Increased $\sigma_{compressive}$ by ten times (20-40 wt%)	$\sigma_{compressive}$: ~36 MPa	Improved structural and strength reliability in SBF	—	[174]
MBG	Alginate	Scaffold (BR/Drug delivery)	50-67	Improved compressive strength	$\sigma_{compressive}$: 0.6-1.6 MPa	Improved apatite-mineralization ability, cell attachment and ALP activity	Drug loaded in MBG particles (dexamethasone)	[146]
Titanium fibers	BG (13-93)	Scaffold (BR)	~50	Improved fracture toughness by ~70% and flexural strength by ~40% (0.4 vol%)	$\sigma_{flexural}$ (4PB): 15 MPa; Fracture toughness: 0.8 $MPa.m^{1/2}$	No inhibition of BG's bioactive properties and HA formation	—	[192]
Reduced graphene oxide (rGO) platelets (0-3 vol%)	BG (45S5)	Scaffold (BR)		1 vol% rGO: Increase of fracture toughness of ~850% (500 °C) and 380% (1000 °C); Increase of $\sigma_{compressive}$ of ~290% (550 °C) and 75% (1000 °C)	$\sigma_{compressive}$: 2.5 MPa (sintering 500 °C Ar); $\sigma_{compressive}$: 12 MPa (sintering 1000 °C Ar)	—	Toughness and compressive strength were improved up to 1.5 vol% GO	[127]
Graphene oxide nanoplatelets	BG (13-93)	Scaffold (BR)		2 vol% GO: Improved $\sigma_{compressive}$ by ~26% and toughness by ~894%	$\sigma_{compressive}$: 45-90 MPa; Toughness: 8 MPa	—	Hindered viscous flow, hampering the densification of the BG; Contents >2vol%: agglomeration	[178]
Carbon nanotubes (0-10 wt%)	Si-doped HA/PCL	Scaffold (BR)	~40	Increase of 55% in the compressive yield stress (2 wt% CNT)	$\sigma_{compressive}$: ~4 MPa	Enhanced cell attachment	Induced a mesoporosity of ~20 nm; With 2 wt% CNT, the scaffolds became electrically conductive	[208]
Ionically modified carbon nanotubes (0.2 wt%)	HA/PCL	Scaffold (BR)		Improved elastic modulus (by ~2.5-fold) and $\sigma_{compressive}$ (by ~2.5-fold)	$\sigma_{compressive}$: ~5.5 MPa; Elastic modulus: 40-50 MPa	No significant inflammatory process was induced; No hindering of the biological beneficial roles of HA	—	[202]

Source: Author.

BR: bone regeneration; $\sigma_{compressive}$: compressive strength; $\sigma_{flexural}$: flexural strength.

An outline of the mechanical reinforcement strategies featuring their main advantages and limitations can be found in Table 8.

Table 8. Reinforcement strategies through morphological aspects or reinforcing phases, their achieved improvements, limitations and studies that have utilized them to produce components via the DIW method.

Reinforcement strategy	Improvements/Advantages	Limitations/Disadvantages	Ref.
Reproduction of natural structures	High strength-to-density ratios	Trade-off between fine structural handling and manufacture of complex shapes in practical times and sizes; Some structures may lead to reduced compressive strength; Anisotropy (might be desirable depending on the application)	[32,88,170]
Hierarchical porous structures	Excellent strength-to-density ratios; Excellent drug/protein load and release; Improved *in vivo* bone-forming bioactivity	Some techniques still require further studies to achieve a wider porosity range	[84,85,88,90,146,156,158,170,201,238,267]
Glass addition	Increased viscous flow upon sintering, resulting in higher densities; Higher compressive strength, structural stability and strength reliability	Negative impact on phase assemblage if the glass differs in composition in relation to the matrix	[163,184,187]
Bioactive glass addition	Increased viscous flow upon sintering, resulting in higher densities; Higher compressive strength, structural stability and strength reliability; Enhancement of apatite forming ability, osteogenic cell activity and angiogenesis ability	Negative impact on phase assemblage if the glass differs in composition in relation to the matrix	[137,146,150,173,174,235,270]
Polymeric full impregnation	Improvement of strength and toughness, especially toughness under flexural stresses; Better mechanical performance than polymer-coated scaffolds; Progressive load transfer onto the regenerated bone	Loss of predesigned macroporosity; *In situ* creation of porosity for cell ingrowth during biodegradation remains a challenge	[32,220–224,271]
Polymeric coating	Preservation of predesigned macroporosity; Enables cell seeding before implantation	Lower mechanical performance than fully-impregnated scaffolds	[211–214,223,224,234,248–251]

Source: Author.

6.4. BIOLOGICAL IMPROVEMENT STRATEGIES

To improve the biological properties of ceramic-based components produced via DIW, some strategies/additions have been proposed and evaluated; these are displayed in Table 9 and explored in the next sections.

Table 9. Summary of biological improvement strategies that have been studied in ceramic-based composites produced via the DIW method and their influence on the mechanical and biological properties of the printed components.

Reinforcement	Matrix	Structure	Porosity (vol%)	Influence on mechanical properties	Mechanical properties	Influence on biological properties	Remarks	Ref.
BG (28CaO-45SiO_2-4P_2O_5-18B_2O_3-5CuO)	Diopside ($CaMgSi_2O_6$)	Scaffold (BR)	62.5-65	5 or 10% BG enhanced the $\sigma_{compressive}$ of scaffolds sintered at 1150 °C	$\sigma_{compressive}$: 15.5-19.4 MPa	Favorable antibacterial, physicochemical and biological performance	—	[173]
BG (NCS-B, CaO-SiO_2-Na_2O-P_2O_5-B_2O_3)	Akermanite	Scaffold	62-65	Increased $\sigma_{compressive}$ by ten times (20-40 wt%)	$\sigma_{compressive}$: ~36 MPa	Improved structural and strength reliability in SBF	—	[174]
nBG (70SiO_2-25CaO-5P_2O_5, 10 wt%)	Chitosan	Scaffold (BR)		—		Sped the induction of bone mineral-like apatite in SBF	—	[235]
MBG	Alginate	Scaffold (BR/Drug delivery)	50-67	Improved compressive strength	$\sigma_{compressive}$: 0.6-1.6 MPa	Improved apatite-mineralization ability, cell attachment and ALP activity	Drug loaded in MBG particles (dexamethasone)	[146]
HEA (2-hydroxyethyl acrylate)	HA/AESO	Scaffold (BR)	40.9 ± 1.5	Reduced strength and elastic modulus		Improved cell adhesion, proliferation and osteogenic differentiation;	Increased ink printability; Reduced HA distribution in the matrix	[200]
Gelatin	Si-doped HA/PCL	Scaffold (BR/Drug delivery)	80-84	—	$\sigma_{compressive}$: 2.7-3.8 MPa	Improved gene expression and matrix mineralization	No sintering; Vancomycin efficiently hindered bacterial growth	[236]
Chitosan	Laponite	Scaffold (BR)		—	$\sigma_{compressive}$: 15 MPa	Increased cell viability, cell growth and also biomineral and ECM collagen-like amide formation	No sintering procedure;	[240]
Chitosan (coating)	BG (45S5)	Scaffold (BR)	24 ± 7	Improved compressive strength and fracture toughness	$\sigma_{compressive}$: ~13.5 MPa; Toughness: ~0.85 MJ/m^3	Enhanced *in vitro* bioactivity with accelerated apatite-like layer formation; Reduction of the *in vitro* degradation rate	Sintering with subsequential coating (dip-coating)	[214]
Type I collagen (coating)	β-TCP	Scaffold (BR)	43-44	—	$\sigma_{compressive}$: 15.3 ± 3.4 MPa	Stimulated osteoblastic differentiation; Improved matrix mineralization	Sintering with subsequential coating (dip-coating)	[234]
Collagen/BMP-2 or Collagen/ dipyridamole (coating)	BCP (15HA:85β-TCP)	Scaffold (BR)		—		Improved bone formation and tendency of increased remodeling	Sintering with subsequential coating	[248]
Coating with Cu-doped bredigite or Cu-doped akermanite	Diopside ($MgCaSi_2O_6$)	Scaffold (BR)	~52	—		Induced significant angiogenesis effects, especially when coated with Cu-doped bredigite	—	[186]
PCL/CPO (coating)	BCP (60HA:40β-TCP)	Scaffold (BR/Oxygen release)	~70	—	$\sigma_{compressive}$: 23 MPa	Superior apatite precipitation; 3% CPO: enhanced osteoblastic viability and proliferation under hypoxic conditions; 5% CPO: higher ALP activity	Sintering with subsequential coating (dip-coating). CPO inhibited the growth of *S. aureus* and *E. coli*	[249–251]
PLGA microspheres containing VEGF	β-TCP/ alginate/ gelatin	Scaffold (BR/Drug delivery)	73.42 ± 8.4	—	$E_{compressive}$: 98.31 ± 10.21 MPa	Two-fold increase of cell proliferation (after 10 days); 50% improvement in ALP activity (after 2 weeks)	No sintering; Slow VEGF *in vitro* release kinetics that fulfilled vascularization requirements	[253]
Platelet-rich fibrin (PRF)	BCP (60HA:40β-TCP)/PVA	Scaffold (BR/Drug delivery)	~50	—	Low compressive moduli: ~300 kPa	Improved *in vitro* biocompatibility, biological activity, cell adhesion, proliferation, and differentiation; Enhanced *in vivo* bone formation	No sintering; Sustained release of bioactive factors; Slow degradation rate	[252]
Carbon	Larnite	Scaffold (BR/Tumor therapy)		—	$\sigma_{compressive}$: 4.8 ± 0.5 MPa	Better bone regeneration ability	Excellent photothermal effect	[191]

Reinforcement	Matrix	Structure	Porosity (vol%)	Influence on mechanical properties	Mechanical properties	Influence on biological properties	Remarks	Ref.
Graphene oxide (coating)	β-TCP	Scaffold (BR)		—		Significantly stimulated *in vitro* cell proliferation, ALP activity and osteogenic gene expression; Improved *in vivo* new bone formation	—	[179]
Fe_3O_4 particles wrapped by GO sheets (coating)	β-TCP	Scaffold (BR/Tumor therapy)	~50	—		Improved osteogenic gene expression, ALP activity and cell proliferation	≤ 1% Fe_3O_4: superparamagnetic behavior and hyperthermal effects	[180]
Carbon nanotubes (0-10 wt%)	Si-doped HA/PCL	Scaffold (BR)	~40	Increase of 55% in the compressive yield stress (2 wt% CNT)	$\sigma_{compressive}$: ~4 MPa	Enhanced cell attachment	Induced a mesoporosity of ~20 nm; With 2 wt% CNT, the scaffolds became electrically conductive	[208]

Source: Author.
BR: bone regeneration; $\sigma_{compressive}$: compressive strength; $E_{compressive}$: compressive modulus.

6.4.1. Addition of bioactive glasses

Bioactive glasses (BG) are known for their excellent biological outcomes. Besides the already mentioned increased compressive strength provided by the BG addition [146,173,174], their overall improved biological performance is translated into favorable antibacterial properties [173], enhanced structural and strength reliability in SBF (simulated body fluid) [174], improved apatite-mineralization ability [146,235], as well as enhanced cell attachment and ALP (alkaline phosphatase) activity [146].

6.4.2. Addition of hydrogels

Another strong biological reinforcement strategy is the addition of hydrogels, especially those of natural origin (e.g., chitosan, collagen and gelatin), which have shown great results. This addition can either be made to the paste to be printed, which does not undergo sintering after printing [236,240] (case in which the hydrogels generally improve the printability of the paste) or by coating after the sintering procedure of the component [214,234,248].

The incorporation of gelatin has been shown to increase gene expression and matrix mineralization [236], whereas that of chitosan improved cell viability and growth, formation of biomineral and ECM (extracellular matrix) collagen-like amide [240], *in vitro* bioactivity and accelerated apatite-like layer formation [214]. Chitosan addition has also shown a reduction of the *in vitro* degradation rate and mechanical improvements, with higher properties such as compressive strength and fracture toughness [214]. The insertion of collagen in ceramic-based

components produced via DIW has also had good results as it stimulated osteoblastic differentiation, enhanced matrix mineralization [234] and bone formation, showing a tendency for higher remodeling [248].

6.4.3. Addition of drugs/proteins

Loading with drugs or proteins has also been proven efficient. Similar to the hydrogels' additions, their incorporation can either be made to the printing paste with no post-printing sintering procedure [236,252,253] or after the sintering of the component by a coating method [249–251].

Vancomycin [236] and calcium peroxide (CPO, an oxygen-releasing antimicrobial agent) [249–251] additions have been reported to properly hinder bacterial growth, with the latter also improving ALP activity and osteoblastic viability and proliferation under hypoxic conditions. The use of vascular endothelial growth factor (VEGF) presented an excellent increase in cell proliferation and ALP activity [253], whereas that of platelet-rich fibrin enhanced *in vitro* biocompatibility, biological activity, cell adhesion, proliferation and differentiation as well as *in vivo* bone formation [252]. The known improved angiogenesis provided by materials doped with Cu has also been explored and verified in DIW components [186].

6.4.4. Addition of carbon-based materials

The last improvement strategy of the biological properties is the addition of carbon-based materials (e.g., graphene oxide and carbon nanotubes). This might not be an easy correlation, but the incorporation of such materials has been shown to modify the surface charge, improving protein adsorption and, hence, cell attachment [208,272]. This surface charge modification also enables electrical stimulation after implantation to induce osteointegration [188,189]. The incorporation of carbon has been reported to improve bone regeneration ability [191], whereas graphene oxide was shown to enhance *in vitro* cell proliferation, ALP activity, osteogenic gene expression [179,180] and *in vivo* new bone formation [179]. Likewise, the incorporation of carbon nanotubes led to enhanced cell attachment in addition to the already-mentioned increase in compressive strength [208]. Due to their photothermal effects, carbon-based materials can also be applied in applications such as tumor therapy [180,191].

6.5. ANALOGOUS TECHNIQUES

Many techniques similar in mode of operation to direct ink writing have been developed and three of these worth highlighting are presented below.

Solvent-based extrusion free-forming was conceived by Yang *et al.* [273]. Its operation is identical to DIW's, with its paste being composed of ceramic, polymer and a solvent; therefore, the phase change is induced by solvent evaporation. Among the approaches that this technique encompasses, the most prevalent is direct ink writing-solvent casting (DIW-SC), in which a sacrificial scaffold is produced through DIW, cast into resin to be cured under specific conditions and heated up in vacuum to remove the fugitive ink, making hollow vessels that can be employed in the transfer of healing agents to damaged areas. Nevertheless, solvent-based extrusion free-forming is a dangerous process, particularly when printing large components due to a large extent of solvent evaporation – reason why aqueous ceramic pastes have usually been preferred with low cost and toxicity, simple handling and slower drying process [274].

Another technique similar to DIW is bioprinting, which is gaining increasing interest as well. Also known as biofabrication, this technique enables the formation of a component with "structural organization from living cells, bioactive molecules, biomaterials, cell aggregates (e.g., micro-tissues) or hybrid cell-material constructs through bioprinting or bioassembly and subsequent tissue maturation processes" [275]. For this method, a hydrogel is used as a matrix and, hence, the overlapping with the direct ink writing technique (which can encompass these materials) becomes apparent. The further development of hydrogels in the DIW method might benefit from the advances of these materials in bioprinting and vice-versa, resulting in the parallel progress of these techniques. For instance, to improve the strength of hydrogel scaffolds, Wust *et al.* [276] designed a unique hydrogel combining alginate and gelatin through a two-step gelation process – a structure that was biofabricated and resulted in increased mechanical and structural stability. The main issue related to hydrogel-containing scaffolds obtained via DIW is their insufficient mechanical properties, so it is evident how these coordinated advances are advantageous; still, bioprinting is usually a more demanding method as cells are extremely more fragile than ceramic materials.

Besides the mentioned analogous techniques, the combination of DIW with other techniques is increasingly studied since it generates components with properties that neither technique can achieve on its own. The set of unique properties achieved, as expected, depends

on the technique being combined with direct ink writing. A distinct analogous and promising technique consists of the combination of DIW and bioprinting. That is the case of a special multi-nozzle bio-plotter developed by Khalil *et al.* [277], with its capacity to extrude biopolymeric solutions and living cells (at low pressures and room temperature to reduce cell damage) being its most appealing characteristic.

Other studies that used this combination strategy have associated the DIW method with freeze-casting [85], bidirectional freeze-casting [156], a hydrothermal method for the *in situ* growth of MoS_2 (molybdenum disulfide) nanosheets [185], emulsion/foam templating [90,238] and salt-leaching [201]. Still, the most used combination is that of DIW and freeze-drying [106,235,240–242,252] since the latter removes the water content while creating a micro-sized interconnected pore network internally and on the surface. This porosity alongside the macro-sized porosity produced by DIW generates a structure with hierarchical porosity that, as mentioned (Section 6.3.1), has been known to improve the components' mechanical and biological properties.

7. CONCLUSION

Direct ink writing is an expanding additive manufacturing technique for ceramic-based components designed for biomedical engineering applications. To remain aware of the main developments in this field, this review analyzed and discussed its overall scenario, the main characteristics of the reported studies as well as the most promising innovations proposed.

The encouraging benefits of the technique were displayed; although, some limitations remain. The main ones are the surface finish of the component, the attainment of mechanical properties in the range of cortical bone (which have been achieved only in a few cases) and also, for the dense components, the obtention of densities in the same range as other ceramic processing techniques ($\geq 99\%$). Hence, the search for improvement strategies for the properties of ceramic-based components obtained via DIW is a constant front of the field. These strategies were also reported and discussed in this review, which summarized their achieved results, advantages and limitations. [278–290]

2

CHAPTER 2: RHEOLOGICAL CHARACTERIZATION OF PASTES OF ALUMINA-TOUGHENED ZIRCONIA WITH ADDITIONS OF CARBON NANOFIBERS AND EVALUATION OF THEIR PRINTABILITY VIA DIRECT INK WRITING

1 INTRODUCTION

Additive Manufacturing (AM), commonly known as 3D printing, has emerged as a widely adopted method for fabricating solid objects. In addition to its cost and waste-saving benefits, AM also offers the ability to create intricate and personalized geometries without the need for molds. This flexibility in design and production has further contributed to the popularity of AM in various industries [291]. That includes the additive manufacturing of ceramics, a promising family of fabrication methods whose primary benefit is the capacity to create intricate shapes and eliminate the need for expensive machining procedures associated with conventional methods [292–294]. AM offers reduced waste compared to subtractive manufacturing methods [291,293,295], alongside faster production cycles and greater design freedom. Hence, as technology continues to advance, AM of ceramics is expected to play an increasingly significant role [291].

Among the existing AM techniques, Direct Ink Writing (DIW), also known as Robocasting, relies on material extrusion through fine nozzles (typically 200-900 μm) to construct three-dimensional objects through a layer-by-layer deposition process [291,293,296]. It has gained significant attention and has attracted a diverse community of researchers exploring its applications in various fields as it has shown great potential to obtain porous, hierarchical, multimaterial and multifunctional structures [297]. Amidst the fields of application, there are catalytic materials [298,299], smart composites [300,301], stretchable electronics [302], soft robotics [303,304], organ-on-a-chip systems [305] and biomedical implants [181,208,211]. DIW offers a cost-effective alternative, as the equipment required is often more affordable and user-friendly compared to other AM techniques used for ceramics [18,306]. Moreover, when needed, the printed parts can be sintered using a conventional furnace, eliminating the necessity for a high-power laser [307].

The extruded material is referred to by various names in the literature (e.g., paste, ink, feedstock), but for this paper, the term "paste" will be predominantly used. For the printing process to occur, a paste with specific rheological properties is required, as is discussed next.

General requirements for DIW

To be used in the DIW method, a paste must possess specific characteristics ensuring that throughout the printing process: (1) the formulation flows smoothly through narrow nozzles without encountering issues such as dye swell, nozzle clogging, phase separation, filter

press effects or segregation; (2) the printed filament maintains its intended shape; and (3) the final printed part demonstrates structural integrity, supporting its weight without experiencing deformation, slumping, or collapsing [64,258,293,308].

To achieve satisfactory extrudability and ensure optimal flow through fine printing nozzles, as well as filament shape retention immediately after printing, it is crucial to utilize pastes that demonstrate a significant shear thinning behavior [90,309,310]. This behavior implies that these pastes should exhibit a lower viscosity (η) at high shear rates. Several factors, including solid content, geometry, particle size distribution and surface chemistry, influence the rheological behavior of the pastes [258]. The shear-thinning behavior is attributed to changes in the structure of the paste, such as the reorganization of particles and polymers, when subjected to shear stress. Macroscopically, shear-thinning behavior can be described using the Ostwald-de Waele's relation (Eq. (2)) [311]:

$$\tau = k \cdot (\dot{\gamma})^n \quad (2)$$

Where τ is the shear stress, k is the flow consistency parameter, $\dot{\gamma}$ is the shear rate and n is the flow behavior index. The phenomenon of shear-thinning occurs when the flow index (n) is lower than 1. Alternatively, to provide a more accurate description, the Herschel-Bulkley equation (Eq. (3)) is often used, incorporating a yield stress (τ_y) [312]:

$$\tau = \tau_y + k \cdot (\dot{\gamma})^n \quad (3)$$

This value of yield stress is the critical stress required to initiate flow. It is important to note that, in this study, the term "yield stress" is not used interchangeably with "flow stress," contrary to what some authors may have done. The distinction between these two terms is significant and should be understood accordingly. Hence the three different “yield stresses”:

- Static yield stress (τ_y^{STAT} or simply τ_y) is the shear stress required to initiate flow when increasing the shear stress;
- Dynamic yield stress (τ_y^{DYN}) is the minimum stress required to maintain flow when decreasing the shear stress from a "liquid-like state";
- Flow stress (τ_f) is the stress at which the storage modulus (G') equals the loss modulus (G").

The distinction between the yield (static) and flow stress can also be visualized in Fig. 24, in which three regions can be clearly distinguished. The first region is called the linear viscoelastic region (LVR) where the storage modulus (G') is constant and greater than the loss modulus (G") – red shading area. Shear stress increases linearly with shear rate, which is linked to solid-like behavior with mainly elastic deformation. The storage modulus (G') in the LVR is equivalent to the elastic modulus of a solid material and is known as G'_{eq} (equilibrium modulus). Point 1 represents the yield point and the corresponding yield stress (τ_y) is the value of the shear stress at the LVR limit, where G' starts to decrease. This decrease is related to the start of the breakdown of the internal structure, leading to irreversible deformation. Determining the boundaries of the linear viscosity region (LVR) for DIW formulations can be highly subjective, however, its endpoint is often defined by a decrease to approximately 90% of the storage modulus at rest (G'_{eq}) [308]; this was the criterion adopted in this study for the determination of the yield point.

Fig. 24. Schematic illustration of the evolution of storage (G') and loss (G") moduli and shear stress with increasing shear strain showing the three different areas and the values of interest.

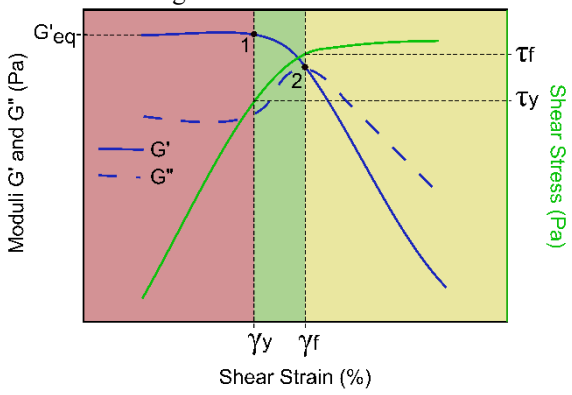

Source: Author.

In the second region (shaded in green), which lies between point 1 and point 2, the elastic behavior still dominates over the viscous (G' > G"), but the yield stress has been surpassed, indicating solid-like behavior with irreversible deformation. Point 2 represents the flow point, where G' equals G" and is the transition from solid-like to liquid-like behavior, which is attained at the flow stress (τ_f). After this point, in the flow region (shaded in yellow), the viscous behavior dominates over the elastic (G' < G"), which leads to the flow of the material due to progressive breakage and ordering of the internal structure [313].

In terms of DIW, a high yield stress (τ_y) and equilibrium modulus (G'_{eq}) help to prevent deformation and collapse of the 3D-printed structure, while a low flow stress (τ_f) reduces the force required for extrusion. However, there is a trade-off between the first two parameters and

finding the right compromise is crucial [314]; a fact that will be further addressed in the discussion section.

Types of paste – colloidal or hydrogel

There are two commonly employed methods for paste formulation: (i) transforming a colloidal paste into a gel-like paste (electrostatic mechanism of stabilization), and (ii) incorporating ceramic particles into a gel matrix (encompassing pastes based on either hydrogels (steric stabilization) or organogels (electrosteric stabilization)) [292,293]. In the first method, highly concentrated colloidal pastes are typically prepared in aqueous media by combining ceramic powders with an appropriate dispersant/deflocculant [258,315]. The colloidal approach relies on particle-particle interactions to achieve stable and homogeneous pastes with shear-thinning behavior [258]. To induce a gel-like behavior, thickening agents like carboxymethyl cellulose (CMC) are often used in conjunction with weakly flocculating agents such as polyethyleneimine (PEI). These additives enhance the rheological integrity of the ceramic paste under mechanical stresses, preventing solid-liquid phase separation during the extrusion process [258,293,316–318].

As for the second method, the development of gel systems loaded with ceramic particles has been extensively explored for several reasons: (i) the rheological properties primarily depend on the disruption of the polymer network rather than interparticle interactions, (ii) the hydrogel's steric stability can prevent solid-liquid phase separation during extrusion – enabling the accommodation even of materials that are prone to leaching, such as bioglasses [280] –, (iii) the gel matrix retains water molecules, reducing the likelihood of crack formation during the drying process and (iv) the ability to incorporate a wide variety of ceramic particles [67,293,317,318].

Pluronic® F-127 (F127) is a highly researched hydrogel system commonly used for this purpose. It is a triblock copolymer consisting of polypropylene oxide (PPO) flanked by two polyethylene oxide (PEO) blocks [319]. The viscoelastic properties of this hydrogel can be customized based on temperature, as the PPO block dehydrates with increasing temperature, transitioning from a hydrophilic to a hydrophobic state. This transformation occurs at a specific temperature known as the critical micellar temperature (CMT) for low-concentration solutions or critical gelation temperature (CGT) for higher concentrations [319]. Below this temperature, F127 behaves as a nearly Newtonian liquid, while above it, depending on the concentration, it can exhibit Newtonian or viscoelastic characteristics (e.g., shear-thinning behavior) due to core-

shell micelle formation or, at higher concentrations, the organization of micelles into a lattice that forms a gel [319]. When dissolved in water at a concentration of 25 wt%, F127 typically undergoes this transition at around 18 °C [295,318,320], resulting in a printable gel that follows the Herschel-Buckley law (Eq. (3)) [321]. Currently, Pluronic® F-127 is the most used additive in DIW due to its widespread availability, relatively low cost and ease of formulation.

The studied system

Regarding the material studied, Alumina-Toughened Zirconia (ATZ) ceramic composites have gained significant attention as potential materials for biomedical implants like hip replacements and dental implants [63,322–325]. ATZ composites stand out among oxide ceramics due to their unique combination of structural properties, including hardness, flexural strength, fracture toughness and abrasion resistance [326,327]. In the chemical composition of the ATZ composite, alumina contributes to hardness and wear resistance, while tetragonal zirconia plays a crucial role in enhancing fracture toughness and resistance through the controlled tetragonal to monoclinic (t → m) ZrO_2 phase transformation. As a composite material, ATZ may also exhibit other toughening mechanisms such as microcracking, crack deflection, bridging and controlled residual thermal stresses [325,326,328,329], which confer exceptional properties to this material. These interesting properties in conjunction with the already mentioned advantages of DIW provide an appealing combination for applications such as DIW-obtained implants. More specifically, the composition of the studied pastes (Fig. 25) includes an ATZ powder (composed of ceria stabilized tetragonal zirconia polycrystal (Ce-TZP), alumina and strontium aluminate), a deflocculant, a binder (F127 hydrogel), deionized water and, in some groups, a carbon phase (i.e., carbon nanofibers).

Fig. 25. Schematic illustration of the studied paste and its components, including those of the ATZ powder (Ce-TZP, Al_2O_3 and $SrAl_{12}O_{19}$), deflocculant, carbon phase, binder and the deionized water.

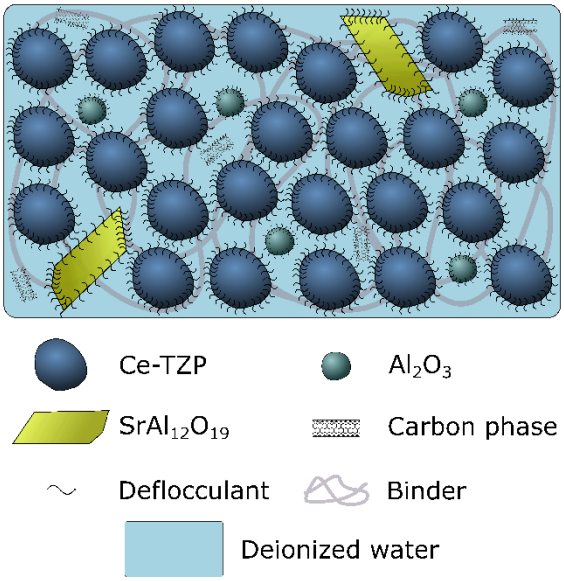

Source: Author.

2 MATERIALS AND METHODS

2.1 MATERIALS

The ATZ powder utilized is composed of 84 vol% Ce-TZP (11 mol% Ce), 8 vol% Al_2O_3 and 8 vol% $SrAl_{12}O_{19}$ (supplied by Doceram® under the name "EvoCera®") in the form of spray-dried powder. As a deflocculant, Darvan 821-A (RT Vanderbilt®) was applied and Pluronic F-127 (Sigma-Aldrich®) was used as a binder. The carbon nanofibers were Pyrograf®-III PR-19-PS and had diameters of 100-200 nm and lengths of 30-100 μm.

2.2 METHODS

2.2.1 Characterization of the ATZ powder and carbon nanofibers

The ATZ powder and the carbon nanofibers were both characterized morphologically by SEM analysis in a Thermofischer® QuattroS equipment. The powder was also assessed in terms of its particle size in a Malvern® Mastersizer 2000 laser granulometer.

2.2.2 Obtention of the pastes

The pastes were obtained as illustrated in Fig. 26. All the mixing steps involved in their preparation were performed in a SpeedMixer DAC 600 Hauschild® equipment under vacuum (30 mBar) with cycles of 800 rpm for 90 s followed by 1500 rpm for 90 s. First, the deflocculant and the deionized water were mixed – zirconia mixing balls of 1 and 2 mm were added to assist the mixing process. The binder was then added and another mixing step was applied. From this point on, every mixing step was intercalated with a cooling step of 10 min in a refrigerator at 4 °C. With the binder homogeneously mixed with the other components, the ATZ powder was added. Then, ten mixing and cooling steps were performed to ensure good homogeneity. In the case of pastes containing carbon nanofibers, these were added to the homogenized paste after ATZ powder addition, followed by another ten mixing and cooling steps. Once the paste was homogenized, the mixing balls were removed with the help of a sieve.

Fig. 26. Schematic illustration of the method of preparation of the pastes.

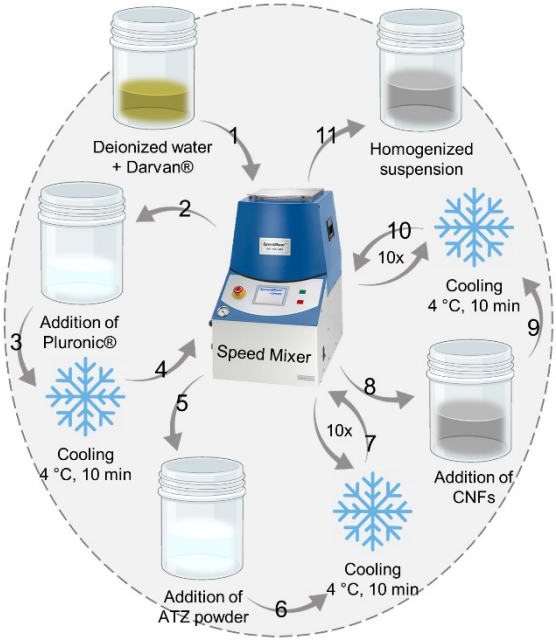

Source: Author.

The deflocculant contents evaluated were 0.5, 1.0, 1.5 and 2.0 wt% in relation to the solids, which were considered as the ATZ powder and carbon nanofibers (when present). The binder content was fixed at 25 wt% in relation to the liquids (deionized water and deflocculant) based on good outcomes of previous studies [181]. The solid contents assessed were 20, 30, 33, 36, 39, 42, 45 and 46.5 vol% and, respectively, their denominations were: 20S, 30S, 33S, 36S, 39S, 42S, 45S and 46.5S. The pastes containing carbon nanofibers had either 0.5 or 2.0 wt% of

CNFs (considered in terms of solids (ATZ + CNFs)). The composition of the studied pastes can be observed in Table 10.

Table 10. Composition of the pastes studied by the evaluation performed.

	Composition of the pastes				
Evaluation	ATZ powder	Deionized water	Deflocculant (Darvan® 821-A)	Binder (Pluronic® F-127)	CNFs
Optimization of the deflocculant content	20 vol% (T)	Remaining quantity	0-2.0 wt%	–	–
Determination of the maximum solid content	20-46.5 vol% (T)	Remaining quantity	1.0 wt% (S)	–	–
Determination of the temperature's influence	0, 30-42 vol% (T)	Remaining quantity	1.0 wt% (S)	25 wt% (L)	–
Determination of the overall behavior	0, 30, 33, 36 or 39 vol% (T)	Remaining quantity	1.0 wt% (S)	25 wt% (L)	0.0, 0.5 or 2.0 wt% (S)
Evaluation of the solid- to liquid-like transition	0, 30, 33, 36 or 39 vol% (T)	Remaining quantity	1.0 wt% (S)	25 wt% (L)	0.0, 0.5 or 2.0 wt% (S)
Determination of the time for recovery	0, 30, 33 or 36 vol% (T)	Remaining quantity	1.0 wt% (S)	25 wt% (L)	0.0, 0.5 or 2.0 wt% (S)

Source: Author.
(T): in relation to the total; (S): in relation to the solids; (L): in relation to the liquids.

2.2.3 Oscillatory rheological evaluations

The pastes were evaluated by oscillatory rheological tests in a rheometer Anton-Paar® MCR301, with a plate-plate geometry using a gap of 1 mm and a solvent trap to prevent drying of the pastes.

2.2.3.1 Optimization of the deflocculant content

To determine the optimal quantity of deflocculant to be used, an amplitude sweep test was utilized. An increasing shear amplitude (shear strain (γ)) of 0.01-1000% was applied at a constant frequency of 1 Hz and the shear stress (τ) necessary to produce this strain/deformation was recorded. The angular frequency was kept at 10 rad/s and the temperature was set at 25 °C. For this optimization, the solid content was fixed at 20 vol% (ATZ powder only). Pastes were composed only of deionized water, ATZ powder and the varying content of deflocculant.

2.2.3.2 Determination of the maximum solid content

This evaluation was performed with an identical analysis configuration to the optimization of the deflocculant content. Pastes were composed of deionized water, the optimal quantity of deflocculant established by the previous analysis (1.0 wt%) and the varying contents of ATZ powder.

2.2.3.3 Determination of the influence of temperature

Since the temperature plays an important role in the viscosity of the chosen binder, it is important to evaluate its influence on the behavior of the paste, which will assist in the specification of a temperature for the printability assessment. This test was conducted with a temperature ramp from 0 to 30 °C imposed by a Pelletier module, with a constant strain of 1% and a constant angular frequency of 10 rad/s. The pastes for this test had deionized water, deflocculant (1.0 wt%), binder (25 wt%) and varying ATZ powder content of 30, 33, 36, 39 and 42 vol%. A group with just water and the binder was also evaluated (denominated 0S).

2.2.3.4 Determination of the overall behavior

To study the overall behavior of the pastes a flow sweep test was performed. An increasing shear rate ($\dot{\gamma}$) from 10^{-4} to $5 \cdot 10^{2}$ s^{-1} was applied and the evolution of viscosity was measured. The temperature was set at 25 °C. The evaluated pastes had deionized water, deflocculant (1.0 wt%), binder (25 wt%) and ATZ powder in the amounts of 30, 33, 36 and 39 vol%. Again, a group with just water and the binder was also evaluated (0S). With this test, it was possible to establish if the pastes possess a shear-thinning behavior, a desired characteristic for the DIW process.

2.2.3.5 Evaluation of the solid- to liquid-like transition

A test with the same parameters as the tests from sections 2.2.3.1 and 0 was conducted to study the solid- to liquid-like transition of the pastes by the evolution of the storage and loss moduli. The pastes assessed included the 5 solid contents evaluated in section 2.2.3.4 with, in some cases, the incorporation of 0.5 or 2.0 wt% of CNFs. The composition of the evaluated

pastes in this test is displayed in Table 11. These pastes were also the ones assessed in the following test (2.2.3.6) and in the printability evaluation (2.2.4).

Table 11. Percentages of each component in the formulations evaluated by weight and volume.

Group	ATZ powder		CNF		Darvan® 821A		Pluronic® F-127		Deionized water	
	wt%	vol%	wt%	vol%	wt%	vol%	wt%	vol%	wt%	vol%
0S	-	-	-	-	-	-	25	23.92	75	76.08
30S	71.09	30.00	-	-	0.71	1.51	7.23	16.80	20.97	51.69
30S0.5	70.56	29.60	0.35	0.40	0.71	1.50	7.27	16.80	21.10	51.70
30S2	68.99	28.43	1.41	1.57	0.70	1.46	7.40	16.80	21.50	51.74
33S	73.85	33.00	-	-	0.74	1.66	6.54	16.09	18.87	49.25
33S0.5	73.32	32.56	0.37	0.44	0.74	1.65	6.58	16.09	19.00	49.26
33S2	71.74	31.27	1.46	1.73	0.73	1.61	6.70	16.09	19.36	49.30
36S	76.33	36.00	-	-	0.76	1.81	5.92	15.38	16.99	46.81
36S0.5	75.79	35.52	0.38	0.48	0.76	1.80	5.96	15.38	17.11	46.82
36S2	74.20	34.12	1.51	1.88	0.76	1.75	6.07	15.38	17.45	46.87
39S	78.55	39.00	-	-	0.79	1.96	5.36	14.67	15.30	44.37

Source: Author.

Densities: ATZ powder: 5.8404; CNFs: 2.16; Pluronic® F-127: 1.06; Deionized water: 1.00 and Darvan® 821A: 1.16 g/cm^3.

2.2.3.6 Determination of the time for recovery

A three-interval thixotropy test (3ITT) was utilized to determine the time for recovery of the pastes, as has been proposed by Del-Mazo-Barbara *et al.* [258]. This test mimics extrusion-based printing processes as it possesses three intervals with different shear rates:

- The first simulates a rest state before printing with a slow advance of the paste in the syringe. This is done by applying a small shear rate (10^{-3} s^{-1}), within the linear viscoelastic region (LVR, explored in the Introduction section) determined by the previous test;
- The second interval reproduces the extrusion process through the printing nozzle by the application of a shear rate above the flow point (also determined by the previous test). A shear rate of 500 s^{-1} was used for this interval, mimicking the $\dot{\gamma}_{max}$ of a 200 μm nozzle – the smallest nozzle used in this study, generating the highest shear rate;
- The last interval uses again a small shear rate, this time representing the rest state after deposition. The shear rate of 10^{-3} s^{-1} was once again applied.

The estimation of the maximum shear rate ($\dot{\gamma}_{max}$) of a 200 μm nozzle, hence the shear rate used for the second interval, is given by Eq. (4) [330]:

$$\dot{\gamma}_{max} = \frac{8 \cdot Q}{D} \quad (4)$$

Where Q is the printing speed in mm/s (10 mm/s in this study) and D is the nozzle diameter in mm. This equation assumes a no-slip condition and a Newtonian fluid.

The 3ITT assessment was conducted with an interval of 120 s for each interval and the temperature was constant at 25 °C. Values of storage moduli were recorded to establish if the recovery of a solid-like behavior is fit for good printing fidelity and the self-supporting capacity of printed filaments. The percentage of the storage modulus recovered in the third interval in relation to the first was also analyzed.

2.2.4 Evaluation of the printability via Robocasting

For this assay, the pastes were put into 5 mL syringes and underwent a centrifugation step (5000 rpm, 10 min) to avoid any air bubbles. They were later printed with a Robocasting system (3D INKS LLC®, Tulsa, Oklahoma, USA) with Robocad® software. The printing speed was fixed at 10 mm/s and conical and cylindrical nozzles were used to evaluate the printability of the pastes. The conical nozzles used had diameters of 840, 580, 410, 250 and 200 μm whereas the cylindrical nozzles had 840, 610, 410, 250 and 200 μm (Nordson®). The geometry of the printed component was a straight filament (line test). The printing process was conducted at 25 °C in a closed chamber with 95% of humidity.

3 RESULTS

3.1 CHARACTERIZATION OF THE ATZ POWDER AND CARBON NANOFIBERS

Particle morphology and size distribution play crucial roles in the design of high solids-loading pastes [331]. In the DIW technique, the use of fine particles (< 20 μm) is preferred to facilitate smoother flow during extrusion and sintering processes. Furthermore, for continuous extrusion without nozzle clogging or sudden paste release, it is recommended that the nozzle size is at least 15 times larger than the largest particle size [332]. In terms of particle

shape, spherical particles are more advantageous since they minimize internal friction between particles, preventing interlocking and enabling improved flow characteristics [295,333]. The evaluation of the ATZ powder morphology and size can be observed in Fig. 27, as well as the morphology of the CNFs.

Fig. 27. (a-e) SEM images of ATZ powder and (f) evaluation of its particles' sizes. (g-i) SEM images of the carbon nanofibers.

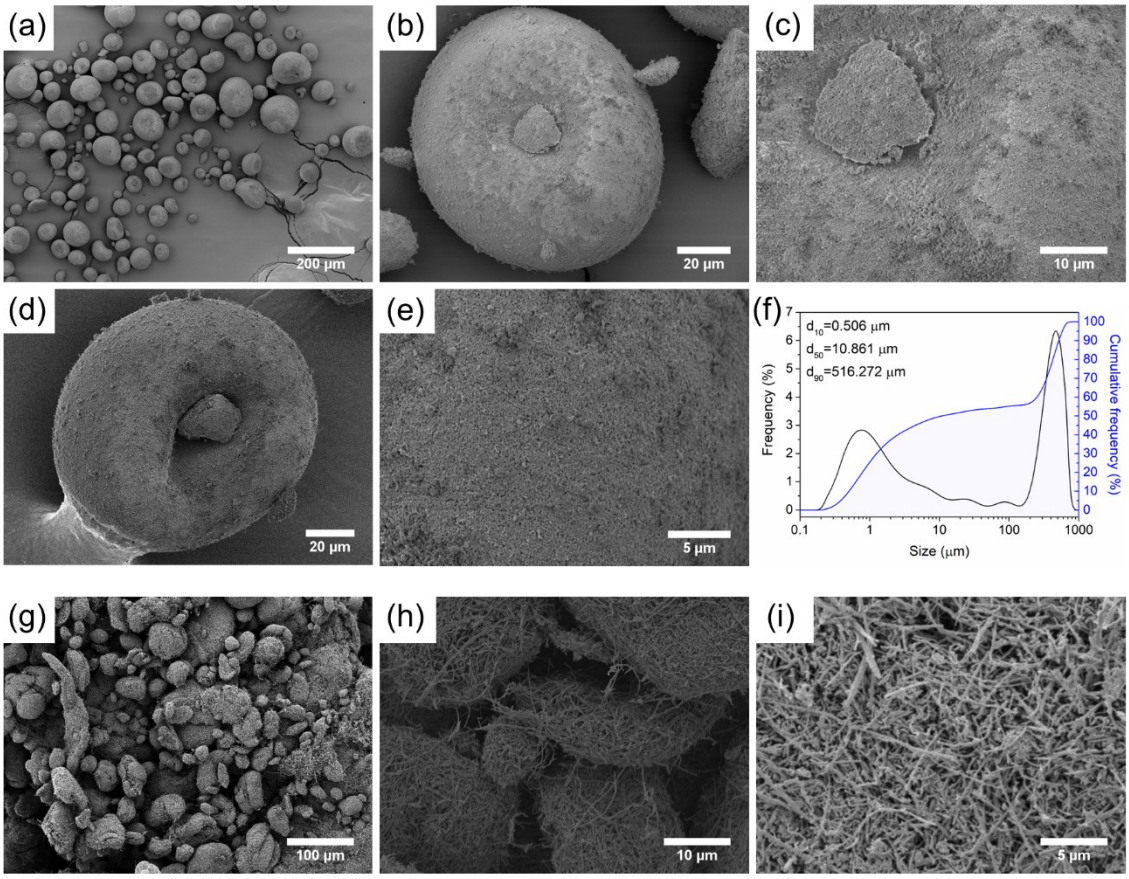

Source: Author.

The ATZ powder exhibits a granulated spherical morphology, which aligns with expectations following a spray-drying procedure. Regarding size, the distribution reveals two prominent peaks, with a prevalence of particles measuring 750 nm and 465 µm. Notably, the latter size corresponds to particle agglomerates, as becomes evident from the SEM images. This observation emphasizes the absolute need of utilizing a deflocculating agent to achieve a uniform distribution within the paste and ensure homogeneity.

The SEM images of the CNFs highlight their high aspect ratio and a strong tendency to agglomerate as expected by their high surface energy, high specific surface area and high aspect ratio (133 $mJ \cdot m^{-2}$, external SSA 17 $m^2 \cdot g^{-1}$, 200 nm diameter, 30-100 µm length), according to their datasheet and corroborated by measurements on the SEM images.

3.2 PASTE OPTIMIZATION USING RHEOLOGY

3.2.1 Optimization of the deflocculant content

The best deflocculant content to promote the deagglomeration of the composite particles was evaluated using amplitude sweep tests on pastes containing various deflocculant contents – this analysis can be observed in Fig. 28.

Fig. 28. Deflocculant content optimization. (a) Shear stress vs. shear strain for different contents of deflocculant. (b) Shear stress vs. deflocculant content with values obtained from the colored lines in (a). It is possible to notice the lower shear stress required to cause the same strain/deformation for the deflocculant content of 1.0 wt%, indicating that this quantity is the best to deflocculate the ATZ particles.

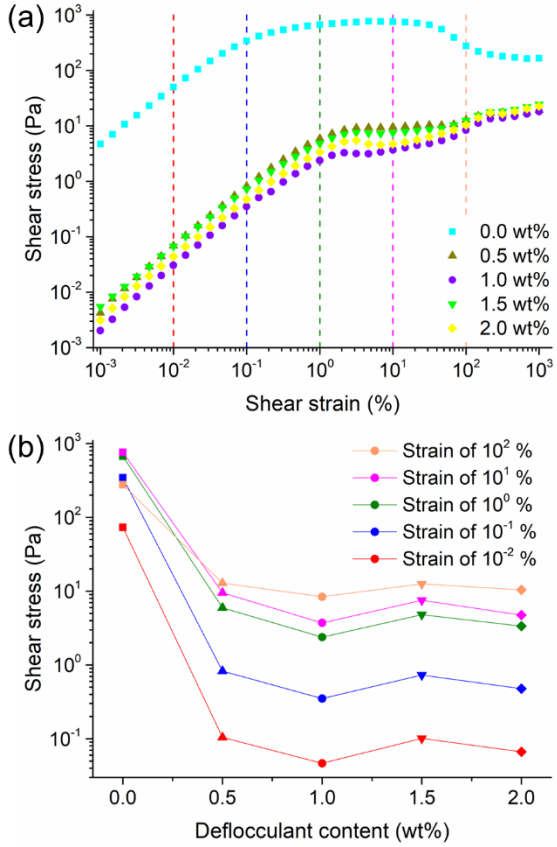

Source: Author.

The concentration of deflocculant that exhibited the highest deagglomeration efficiency was found to be 1.0 wt% (relative to the solids). This determination was based on the observation of lower shear stress requirements for inducing the same shear strain, as depicted in Fig. 28(b). Consequently, this particular concentration of deflocculant significantly improves the distribution of particles, reduces agglomeration and enhances the flowability of the powder. Moreover, it is the most effective concentration for achieving higher solid contents (which have demonstrated better shape retention in DIW [72]), resulting in increased packing

density of the paste, reduced viscosity and elevated yield stress (τ_y) [334]. All subsequent pastes were formulated with 1.0 wt% of deflocculant.

3.2.2 Determination of the maximum solid content

Achieving a high solid content in aqueous pastes is essential for successful robocasting of 3D-printed ceramics with minimal shrinkage during drying and sintering, thereby preventing the formation of cracks and ensuring the mechanical integrity of the final components [258,315,334]. However, increasing the solid content also leads to higher viscosity, yield stress (τ_y) and storage modulus (G'), which can hinder paste extrusion [292]. Hence the importance of determining the maximum solid content that a given paste can accommodate and, taking into account the aforementioned rheological properties, identify an appropriate solid content for its use. In this study, the maximum solid content that the system can accommodate was determined by evaluating the evolution of pastes with increasing solid content to increasing shear strains (Fig. 29(a)).

Fig. 29. Determination of the maximum solid content. (a) Shear stress vs. shear strain for pastes with different solid contents. (b) Fitting of Krieger-Dougherty curves with the experimental values, establishing the maximum solid content as 47 vol%.

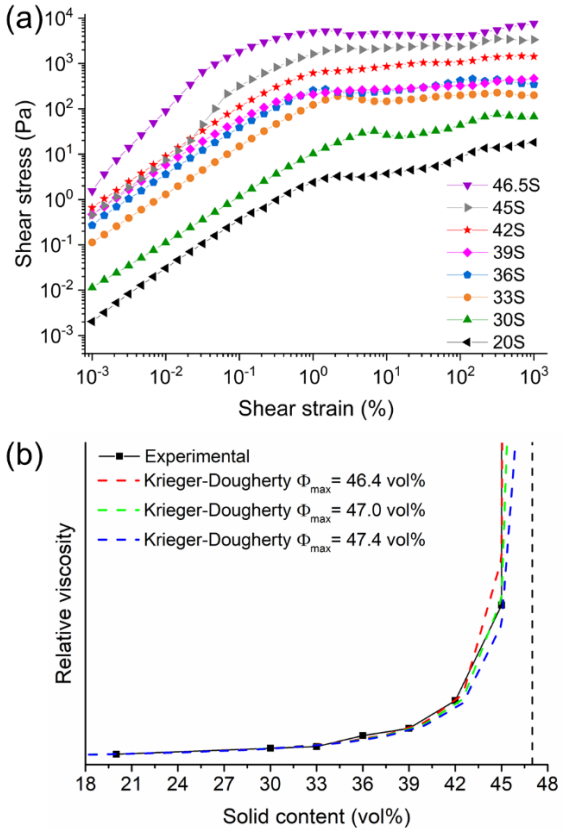

Source: Author.

As expected, the shear stress required to cause a certain strain increases with increasing solid content. From practical observations, it became clear during the preparation of the pastes that 45 vol% was already very close to the maximum solid content of the system. The paste with the highest solid content (46.5S) was more difficult to homogenize, requiring 20 cycles of mixing and cooling after the addition of the ATZ powder (instead of the 10 cycles used for the others). Pastes with solid contents higher than 46.5 vol% were unfeasible.

Then, to predict the maximum packing fraction/solid content (φ_{max}), the evolution of the viscosity with the volume fraction of solids, shown in Fig. 29(b), was fitted to the Krieger-Dougherty equation [335] (Eq. (5)):

$$\eta_r = \frac{\eta}{\eta_{medium}} = \left(1 - \frac{\varphi}{\varphi_{max}}\right)^{-[n]*\varphi_{max}} \quad (5)$$

In which, η_r is the relative viscosity, η is the viscosity of the paste, η_{medium} is the viscosity of water (10^{-3} Pa.s), φ is the solid content of the paste, φ_{max} is the maximum solid content (or maximum packing fraction) and [n] is the shape factor (usually 2.5 for spherical particles).

From the fitting of the Krieger-Dougherty curves with the experimental values, the value of 47 vol% was established as the maximum solid content of the paste – a finding that aligns with the observations made during the paste preparation process. With this value of maximum solid content in mind and considering that the viscosity would increase with the addition of the binder to the paste, it was chosen to assess pastes with 42 vol% of solid content or less in the next steps of the study.

3.2.3 Influence of the temperature

Temperature has a strong impact on viscosity due to its close correlation with molecular motion. Additionally, certain materials experience significant changes in viscosity due to temperature-dependent transitions, such as gelling processes or glass transitions in polymers. This is evident in some hydrogels that are commonly used as binders for ceramic pastes, which undergo reversible gelation at a specific temperature. As mentioned before, that is the case of Pluronic® F-127 (F127), widely used in DIW and also in this study, hence the necessity of evaluating the gelling temperature and its influence on the rheological properties of the pastes.

Therefore, to define the range of printing temperatures that can yield 'printable' ceramic pastes, Fig. 30 displays the temperature-dependent behavior of Pluronic F-127, both alone and in pastes with varying solid contents of ATZ.

Fig. 30. (a) Complex viscosity *vs.* temperature for pastes with varying solid contents. (b) Temperature of the beginning of gelation *vs.* solid content.

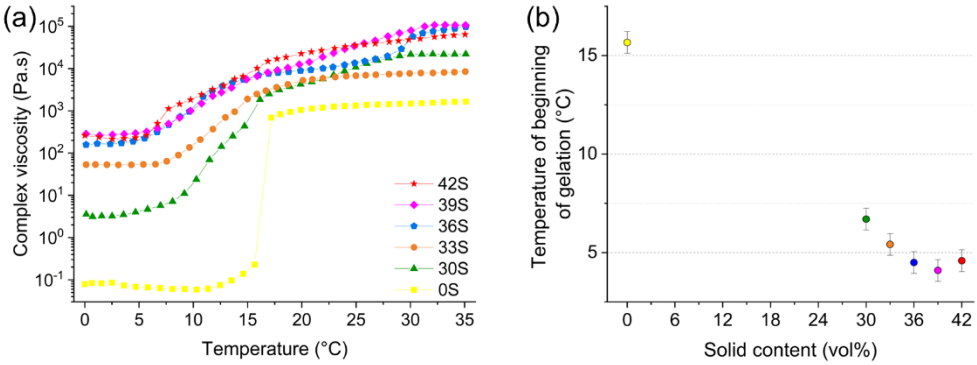

Source: Author.

It can be observed from Fig. 30 that the Pluronic hydrogel (0S) experiences a sharp increase in viscosity around 16 °C, which is its gelling temperature. Below this temperature, the viscosity is very low and the hydrogel behaves like a fluid, while above it, the hydrogel shows a solid-like behavior with much higher viscosity. This transformation is also noticeable in the ceramic pastes, but it is less pronounced and happens over a wider temperature range (usually starting earlier and continuing up to 30 °C, see Fig. 30 (b)). The presence of ceramic particles in the pastes mitigates the gelation phenomenon, resulting in a less dramatic transition. While the hydrogel undergoes a liquid-to-solid transition due to the gelation process, the ceramic pastes exhibit viscosities similar to a solid-like behavior over the range of temperatures studied.

Considering that, the temperature of 25 °C was chosen to be used in all the rheological tests as well as in the printing process for the printability evaluation, so that, at low shear rates, the paste would benefit from the viscoelastic properties of the Pluronic.

3.2.4 Determination of the overall behavior

The overall behavior of the pastes was assessed by evaluating the evolution of viscosity with increasing shear stress (Fig. 31). The tendency line of these curves follows the Ostwald-de Waele power law (Eq. (6) – an adaptation of Eq. (2)):

$$\eta = k \cdot (\dot{\gamma})^{n-1} \quad (6)$$

Where η is the viscosity, k is the flow consistency parameter, $\dot{\gamma}$ is the shear rate and n is the flow behavior index. The analysis of the values of this equation (especially the value of n) provides valuable knowledge on the rheological characteristics of the paste, as so, these values are explored in the sequence.

Fig. 31. (a) Viscosity *vs.* shear rate for varying solid contents. It is possible to observe the decrease of the viscosity as the shear rate increases, characteristic of pastes with shear-thinning behavior. The value of shear rate at which the behavior shifts from shear-thinning to shear-thickening is displayed for the three pastes that present this shift. Values of (b) k and (c) n of the Ostwald-de Waele power law for the different solid contents evaluated.

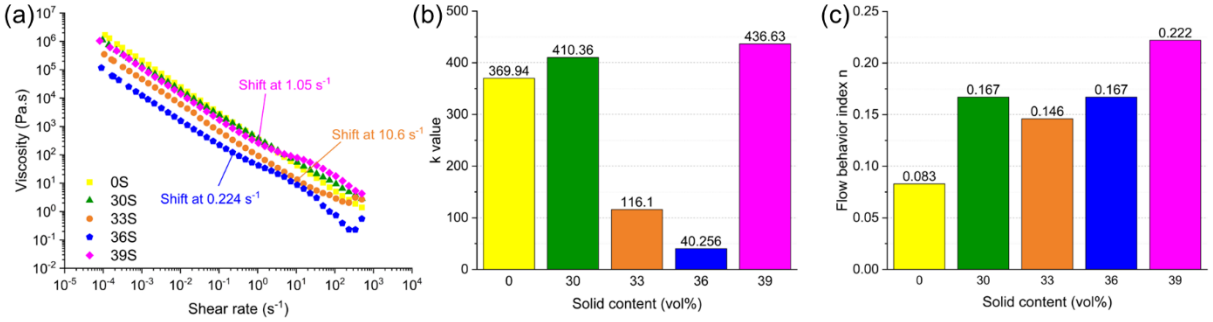

Source: Author.

The flow behavior of viscous materials can be classified based on the flow behavior index (n). Newtonian fluids have n = 1 and their viscosity is constant irrespective of the shear rate. Pseudoplastic or shear-thinning fluids, with 0 < n < 1, show a decrease in viscosity as the shear rate increases, which is due to the disruption of fluid interactions or molecular ordering in the direction of flow. Dilatant or shear-thickening fluids (n > 1), on the other hand, exhibit an increase in viscosity with increasing shear rate. From the n values obtained, it is clear the strong shear-thinning behavior of the pastes with values ranging from 0.083 to 0.222 for the 0S and 39S pastes, respectively. This fact is in agreement with previous studies on hydrogel-ceramic DIW inks, where n is always smaller than 1 [258].

Moreover, at high shear rates, a notable increase in viscosity occurs when the solid content reaches 33 vol% or higher. This is characteristic of a shear-thickening behavior and occurs when the shear is applied too quickly for the internal structure of the paste to rearrange [258] – soon after that, the shear-thinning behavior is reestablished, as observed in the graphs. Although this phenomenon occurs in all pastes, the shear rate at which the transition from shear-thinning to shear-thickening behavior takes place varies. Usually, the denser the internal structure of the paste, the lower the shear rate at which the behavior shifts from shear-thinning to shear-thickening. Still, the paste 33S exhibited this behavioral shift at a rate of 10.6 s^{-1}, while the 36S showed it at 0.224 s^{-1} and the 39S paste demonstrated it at an intermediate value of 1.05 s^{-1}. In this study, this transition was only observable with solid contents of 33 vol% or higher, because, in these cases, the shear rate of the transition has shifted to a value within the range of

shear rates evaluated. Despite happening in all pastes, this phenomenon is often omitted in the literature, where many studies tend to present graphs with a restricted range of shear rates, excluding the region where this transition occurs. However, in this study, we have intentionally chosen to present a broad range of shear rates to gain a comprehensive understanding of the behavior. This decision is especially significant considering that during the process of DIW, the pastes may experience high shear rates, of the order of magnitude where this transition is observed.

In general, increasing the solid content led to the increase of the n value, as expected – nevertheless, the n values of the 30S and 36S pastes were the same (0.167), while that of 33S was 0.146. This disrupts the tendency of increasing n with increasing solid content. It is important to note, though, that the difference between the values is very small. Altogether, in this experiment, the impact of solid content variation within the range of 30-39 vol% on the properties of the overall paste might have a lesser influence compared to the combined effect of the components. Additionally, quantifying their influence accurately is challenging since it could potentially fall below the margin of error. Conversely, no clear tendency was observed for the values of the flow consistency parameter (k) with increasing solid content.

3.2.5 Evaluation of the solid- to liquid-like transition

The evolution of the moduli (storage and loss) and shear stress with increasing shear strains for the pastes evaluated in this study is presented in Fig. 32. From this analysis, it is possible to obtain the values of the storage modulus at equilibrium (G'_{eq}), the shear strain (γ_y) and stress (τ_y) at the yield point and the shear strain (γ_f) and stress (τ_f) at the flow point. These values are displayed in Table 12.

Fig. 32. Evolution of the storage and loss moduli (left y-axis) and shear stress (right y-axis) with increasing shear strain. (a) 0S, (b) 30S, (c) 30S0.5, (d) 30S2, (e) 33S, (f) 33S0.5, (g) 33S2, (h) 36S, (i) 36S0.5, (j) 36S2 and (k) 39S.

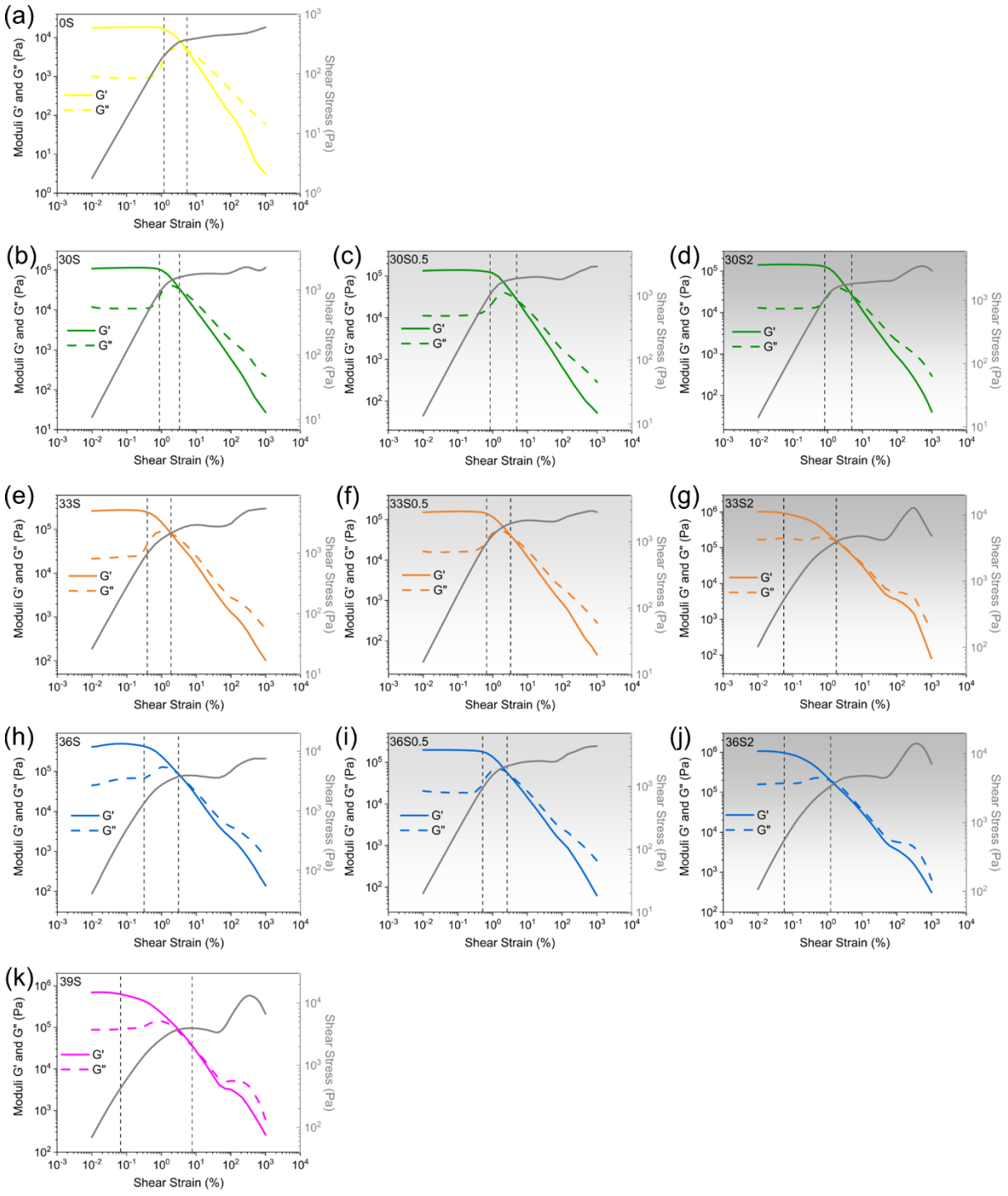

Source: Author.

Table 12. Values of equilibrium modulus (G'_{eq}), shear strain and shear stress at the yield point (γ_y and τ_y, respectively) and shear strain and shear stress at the flow point (γ_f and τ_f respectively).

Group	G'_{eq} (x10^3 Pa)	γ_y (%)	τ_y (Pa)	γ_f (%)	τ_f (Pa)
0S	18.22	1.19	198.0	5.5	372.9
30S	113.06	0.88	928.7	3.3	1 585.8
30S0.5	137.81	0.84	1031.1	4.9	1 887.8
30S2	142.10	0.81	1053.9	4.9	1 858.1
33S	270.90	0.38	962.3	1.9	2 112.7
33S0.5	157.77	0.66	962.4	3.3	1 872.6
33S2	1 002.72	0.055	518.8	1.8	3 934.5
36S	459.49	0.32	1340.3	3.1	3 712.7
36S0.5	196.79	0.52	929.7	2.6	2 116.1
36S2	1 062.65	0.057	553.3	1.2	3 397.4
39S	694.25	0.067	414.6	7.7	3 938.5

Source: Author.

When examining the equilibrium modulus, it is observed that it increases as the solid content increases in the case of pastes without CNFs. The values range from 18 kPa for the 0S paste to 694 kPa for the 39S paste. Among the pastes with 30 vol% solid content, there is minimal variation in the equilibrium modulus, with the following order being respected: 30S < 30S0.5 < 30S2. The groups with 33 and 36 vol% present the same tendency with the addition of the CNFs: surprisingly, the addition of 0.5 wt% CNFs lead to a reduction in the equilibrium modulus in both groups, whereas the addition of 2.0 wt% CNFs lead to an increase. These increases with 2.0 wt% CNF additions are significant, even surpassing the equilibrium modulus of the 39S paste in both groups.

In terms of yield stress, the 30S paste exhibits a higher τ_y value (929 Pa) compared to the F127 hydrogel (198 Pa), as expected, but a value very similar to that of the 33S paste (962 Pa). The yield stress continues to increase with the 36S paste (1340 Pa) but significantly decreases with the 39S paste (415 Pa). Within the 30 vol% group, the yield stress increases with increasing CNF addition, in agreement with the literature in which it has been demonstrated that the addition of irregular particles, even at low concentrations, can significantly increase the yield stress of ceramic pastes [336]. Another study [337] supports this finding, demonstrating that the addition of particles with large specific surface area (which is the case of CNFs) has been shown to cause an increase in the yield stress of the paste because this increased surface area promotes particle collisions and aggregation. Oddly, mostly the inverse happened with the groups of 33 and 36 vol%. For the 33 vol% group, the addition of 0.5 wt% CNFs had no effect on the yield stress but the addition of 2.0 wt% caused a significant decrease (from 962 to ~520 Pa). Conversely, the addition of 0.5 wt% CNFs lead to a reduction in the yield stress of the 36

vol% pastes, with a further decrease when 2.0 wt% was added. The yield stress value of the 39S pastes was low (414.6 Pa), being only higher than that of the F127 hydrogel.

The flow stress values also followed the tendency of augmentation with increasing solid content, spanning from 373 Pa for the 0S paste to approximately 3940 Pa for the 39S paste. Within the groups, the flow stress of the 30S0.5 paste was higher than that of the 30S paste, but very similar to the flow stress of the 30S2 paste. Both the 33 and 36 vol% groups showed a decrease in flow stress with the addition of 0.5 wt% CNF. However, adding 2.0 wt% CNF to the 33 vol% paste lead to an increase in flow stress, while adding the same amount to the 36 vol% paste resulted in slightly lower flow stress.

As the ceramic content increased, the yield point shifted towards smaller shear strains. Conversely, the flow strain decreased with increasing solid content up to 33 vol% (from 5.5% for 0S to 1.9% for 33S) but then increased for 36S (3.1%) and 39S (7.7%).

In terms of the pastes with CNFs, their addition can have a significant impact on the internal structure of the paste. This observation is supported by the behavior of pastes with 0, 30, 33, 36 and 39 vol% of solid content, which exhibited a more "linear" response compared to those containing CNF additions. This phenomenon was attributed to the fact that the presence of nano-scale particles has the potential to disrupt the colloidal paste by interfering with the deflocculant and binder that are attached to the ATZ particles. Furthermore, it may also alter the zeta potential of these particles, depending on the nature of the interaction between the nanoparticles and the paste. These findings emphasize the complexity of the system under study and explain why there was an expected variation of results within a certain range in this investigation.

Again, Fig. 32 shows that, at high shear strains (associated with high shear rates), the behavior of the pastes transitions from shear-thinning to shear-thickening, in alignment with our previous observations.

3.2.6 Determination of the recovery time

Achieving self-supporting 3D structures with good shape fidelity also depends on the kinetics of the transition from liquid-like flow to solid-like behavior. A quick recovery is necessary for the printed paste to maintain its shape, as it indicates the restoration of elastic behavior and prevents continuous paste flow immediately after extrusion. Measuring the recovery of the storage modulus when there is a sharp drop in shear stress from values above the flow point to low, near-rest shear values can quantify this behavior.

The outcome of a 3ITT assay of the different pastes is shown in Fig. 33. Additionally, Table 13 displays the values encountered in the 3ITT tests and Fig. 34 illustrates the different percentages of storage modulus recovered.

Fig. 33. Three interval thixotropy test (3ITT) highlighting the evolution of the storage modulus with time. (a) Comparison of pastes with different ceramic contents without CNFs. Display of the effect of the CNF additions in the amount of 0.5 and 2.0 wt% to the pastes with (b) 30, (c) 33 and (d) 36 vol% of solid content.

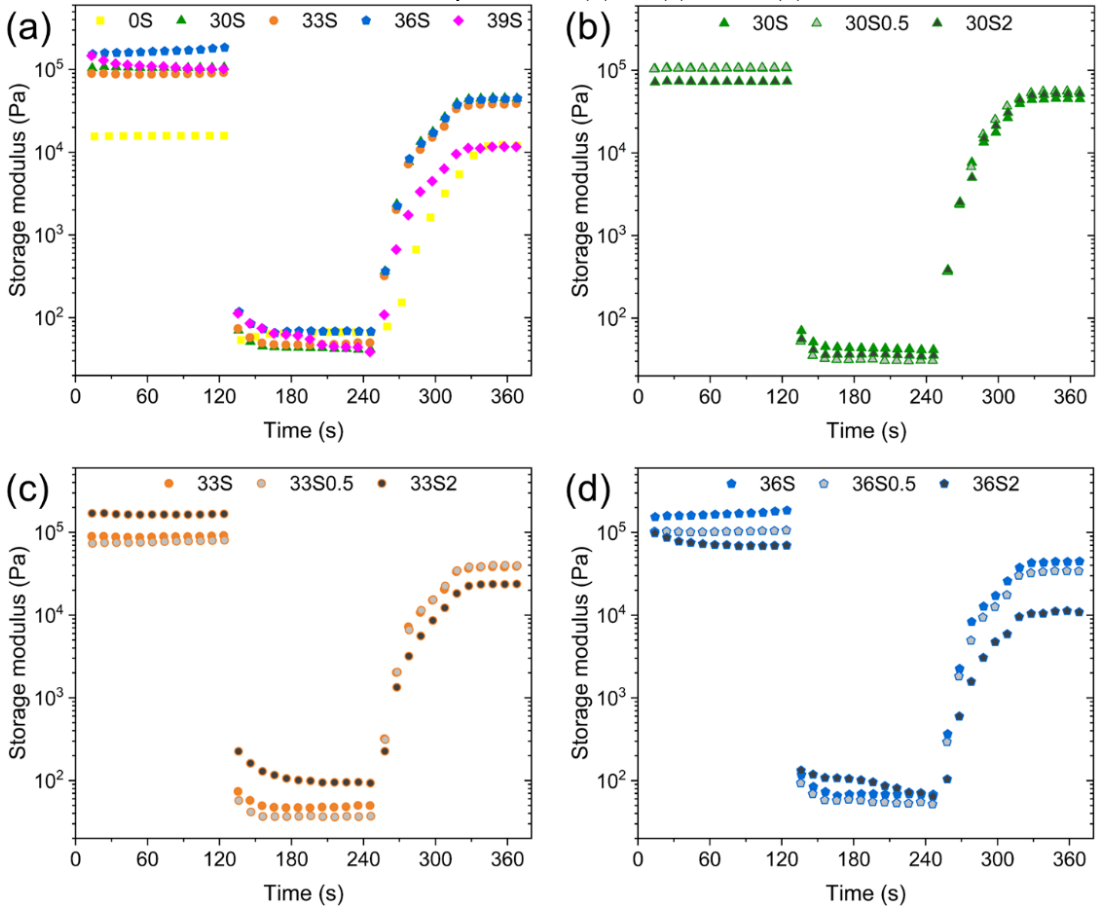

Source: Author.

Table 13. Values obtained from the three-interval thixotropy test (3ITT). Storage moduli for the first, second and third intervals, time for recovery and recovery rate. The latter was calculated by a linear fitting from the last point of the second interval to the first point of the plateau of the third interval; its associated R^2 value is also displayed.

Group	G' 1st interval (x10³ Pa)	G' 2nd interval (Pa)	G' 3rd interval (x10³ Pa)	Time for recovery (s)	Recovery rate (Pa/s) [R^2]
0S	17.81	65.90	12.08	98 ± 9	192 ± 20 [0.96]
30S	114.23	42.87	44.87	82 ± 9	701 ± 73 [0.96]
30S0.5	135.14	31.09	55.10	82 ± 9	892 ± 33 [0.99]
30S2	141.34	35.92	50.99	82 ± 9	836 ± 51 [0.98]
33S	270.4	48.12	37.99	82 ± 9	592 ± 53 [0.96]
33S0.5	159.25	36.77	39.28	82 ± 9	627 ± 50 [0.97]
33S2	1000.2	94.60	23.32	82 ± 9	358 ± 30 [0.97]
36S	461.8	68.02	43.76	82 ± 9	689 ± 50 [0.97]
36S0.5	197.1	55.57	33.63	82 ± 9	535 ± 54 [0.95]
36S2	1063.48	68.90*	10.82	82 ± 9	138 ± 7 [0.99]
39S	696.3	61.17*	11.44	82 ± 9	140 ± 7 [0.99]

Source: Author.

Asterisk (*) indicates a non-flat interval where the displayed value is a mean value of the values of that interval.

Fig. 34. Percentage of storage modulus recovered in the third interval of the 3ITT test compared to the first interval.

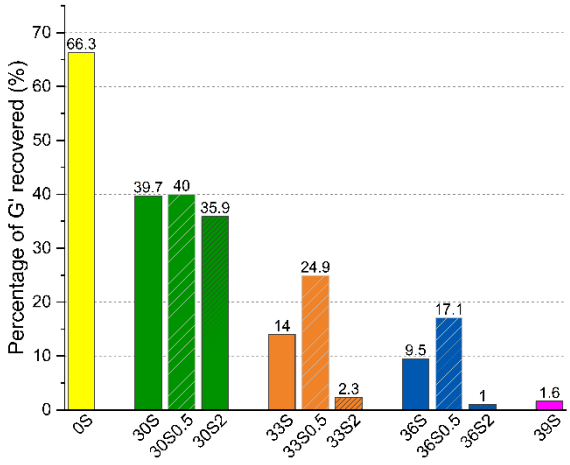

Source: Author.

All the pastes demonstrated a solid-like behavior in the first interval, followed by a swift change to a liquid-like behavior that occurs within some seconds at the start of the second interval. Then, there is a gradual return to the solid-like behavior that takes ~80 s while transitioning to the third interval. The F127 hydrogel (0S) recovered 66.3% of its storage modulus. Then, as the ceramic content increases, the percentage of the storage modulus recovered in the third interval decreases. The inclusion of 0.5 wt% of CNFs resulted in an increased percentage of G' recovered across all solid contents. Conversely, the addition of 2.0 wt% CNFs led to a reduction in these values.

Furthermore, the most concentrated pastes (36S2 and 39S) took longer to reach equilibrium in the second interval. The 36S2 paste reached equilibrium close to the end of the second interval, with G' stabilizing after 90 s, whereas the 39S paste did not reach equilibrium during that interval, as G' continued to decrease.

Interestingly, all the ceramic-loaded pastes had a recovery time in the same range of 73-91 s, a bit shorter than for the 0S paste (89-107 s). While this may seem long, it is important to note that this is the time required to reach the plateau of the third interval. However, most of the pastes presented a high recovery rate, with the lowest values observed in the pastes 0S (~190 Pa/s), 36S2 (~140 Pa/s) and 39S (~140 Pa/s). Hence, for the majority of pastes, a significant recovery of the G' value in the third interval is achieved within a few seconds of this interval.

3.3 EVALUATION OF THE PRINTABILITY VIA ROBOCASTING

The printability evaluation of the pastes, utilizing conical and cylindrical printing nozzles with diameters ranging from 200 to 840 µm, is summarized in Table 14 – a picture of printed cubes of 1 cm is present in Fig. A 1 – Annex A.

Table 14. Pastes studied and their printability (extrudability and ability to retain their shape after extrusion). Results are categorized by nozzle geometry and diameter.

	Printing nozzle									
	Geometry	Conical					Cylindrical				
	Diameter (µm)	200	250	410	580	840	250	330	410	610	840
Pastes	0S	✗	✗	✗	✗	✗	✗	✗	✗	✗	✗
	30S	✓	✓	✓	✓	✓	✗	✗	✓*	✓*	✓*
	30S0.5	✓	✓	✓	✓	✓	✗	✗	✓*	✓*	✓*
	30S2	✓	✓	✓	✓	✓	✗	✗	✓*	✓*	✓*
	33S	✓	✓	✓	✓	✓	✗	✗	✓*	✓*	✓*
	33S0.5	✓	✓	✓	✓	✓	✗	✗	✓*	✓*	✓*
	33S2	✓	✓	✓	✓	✓	✗	✗	✓*	✓*	✓*
	36S	✓	✓	✓	✓	✓	✗	✗	✗	✗	✗
	36S0.5	✓	✓	✓	✓	✓	✗	✗	✗	✗	✗
	36S2	✗	✗	✓	✓	✓	✗	✗	✗	✗	✗
	39S	✗	✗	✗	✗	✗	✗	✗	✗	✗	✗

Source: Author.

The symbol (✓) indicates that the paste was printable, whereas (✗) indicates that it was unprintable and (✓*) that it was printable but had visible defects.

Analyzing the table, it is possible to notice that the paste 39 vol% was unprintable in all conditions, disregarding the geometry of the nozzle or its diameter. This inability was attributed to a combination of factors: (i) high solid content and therefore low water content, facilitating drying and clogging; (ii) the shear-thickening behavior at high shear rates and (iii) very high flow stress to be surpassed by the printing system (~4 KPa), whose extrusion pressure was insufficient. All pastes that had 36 vol% of solid content were unprintable with cylindrical nozzles, whereas, with conical nozzles, the only unprintable conditions were utilizing the nozzles with diameters of 200 and 250 μm for the 36S2 paste. This indicates the printability threshold in relation to the diameter of the conical nozzle, probably related to a faster drying process with smaller nozzles [338]. Additionally, the viscosity of the most concentrated pastes (36S2 and 39S) is time-dependent, as observed in the second interval of the 3ITT test. This complicates the extrusion process, as the printing parameters, including printing speed, would need to be continually adjusted to maintain a constant flow of the material [339].

All pastes containing lower solids or CNF content than 36S2 were successfully printable using all conical nozzles. Pastes with a solid content of 30 and 33 vol% were only printable with cylindrical nozzles that had a diameter of 410 μm or greater. However, the filaments deposited with these nozzles exhibited defects like bubbles, which were attributed to the formation of a stirred zone in the area of nozzle reduction specific to cylindrical nozzles – this phenomenon can also increase the odds of clogging in fiber-containing pastes [265]. Regardless of the conditions tested, the 0S paste was consistently found to be unprintable as, while it was capable of being extruded, it failed to maintain its shape after printing, a phenomenon called slumping.

4 DISCUSSION

Although numerous research studies have been conducted on the DIW process, the majority of them tend to focus on post-processing techniques and the properties of the final product, rather than the optimization of paste formulation and the printing process itself [307]. Despite being necessary, this approach underestimates the fact that the DIW printing process is highly influenced by the rheological properties of the pastes [340].

The lack of comprehensive rheological characterization studies on printable formulations is concerning. Many published studies provide only a superficial discussion on the "viscosity" of the formulation or present a basic flow curve. Some studies even omit rheological characterization altogether. Furthermore, even when rheological data is reported, it

often lacks clear and meaningful analysis, casting doubts on the reliability of the data, as pointed out by Garcia-Tuñon *et al.* [308]. However, some good review papers are gradually addressing this scarcity by focusing on the printability and rheological properties of the pastes [21,258,292,307,341,342].

Rheological studies are equally crucial in bioprinting, a method that shares the same underlying principle as DIW and has evolved alongside it over the years. In the field of bioprinting, rheological studies focus on the survival of cells within hydrogels during the printing process [339,343]. Conversely, in ceramic science, the absence of printed defects is crucial to achieving sufficient mechanical properties. In addition, printable formulations can vary in their rheological properties, ranging from "soft" for the printing of relatively simple 3D shapes with limited complexity, such as in bioprinting applications [344], to "stiff" formulations that are suitable for accurately printing complex shapes with fine features. Printing large, dense parts requires an even more complex compromise (“stiff” enough for accuracy and self-support, but “soft” enough for self-healing of printing-related defects [345]). The choice of formulation stiffness (G’) depends on the specific requirements of the printing process and the desired level of detail and precision in the printed objects [308].

Definition of printability

Within the context of DIW, the term "printability" encompasses two key elements: good extrudability and appropriate shape fidelity [308,331]. Both of these factors are directly impacted by the rheological characteristics of the paste being utilized, necessitating a specific set of desired rheological properties to be defined as “printable”. The printability of the paste plays a critical role in the overall process, as it directly influences dimensional accuracy, precision manufacturing and surface finish [295].

The printability of a paste is also related to the printing nozzle utilized. Generally, conically shaped nozzles are easier to print with compared to cylindrical nozzles due to their smoother internal structure, which allows for a gradual reduction in the internal diameter. Regarding the diameter of the orifice, smaller nozzles present considerable difficulties when it comes to printing due to several factors. The accelerated drying process and increased risk of clogging are major challenges associated with smaller orifices [338]. Additionally, smaller nozzles induce higher shear rates on the paste [346], which requires the printing equipment to exert more pressure on the paste to enable extrusion – this is another requirement that can serve as a limiting factor in terms of printability. In this study, the printability of some ATZ

formulations was evaluated and an attempt was made to fit this data to the printability criteria present in the literature.

Criteria for printability

The concept of "printability" is complex and involves optimizing the entire printing process, from formulation to printing parameters. Several criteria/parameters have been proposed, but there is an ongoing discussion and further research is needed [344].

Some authors state that for a paste to be considered printable, it must possess a specific rheological property that falls either above or below a certain threshold. Whereas, other authors have developed criteria that establish a relationship between two different rheological properties. Both categories are discussed next.

Criteria based on one rheological property

Although the existing library on printable materials is still relatively limited, it has already become evident that pastes printable by DIW may exhibit a broad range of viscosity, yield stress and storage modulus values [331].

In the context of rheological properties, a printability window is commonly established based on specific values of storage modulus (G') and yield stress (τ_y) [308,344]. The latter, when too low – often associated with low solid contents – can lead to poor control of the paste during deposition and potential nozzle dripping due to a weak particle network. Conversely, a highly concentrated paste cannot be extruded from the printing nozzle if the yield stress exceeds the maximum extrusion pressure that the DIW system can apply [292]. Concerning the storage modulus, if its value is too low, the resulting struts would have low stiffness, resulting in poor shape retention. Therefore, to retain the printed filament shape against gravitational forces, support layer stacking and prevent distortion of the printed structure and solid/liquid phase separation, the paste needs to possess a high storage modulus under zero shear (i.e., equilibrium modulus (G'_{eq})) [258,292,307]. Regarding values, a graphical comparison of ranges of rheological properties found in the literature for printable pastes with the data found in this study is displayed in Fig. 35.

Fig. 35. Comparison of the properties of the studied pastes with the values/ranges found in the literature of printable pastes. (a) Yield stress, (b) equilibrium modulus, (c) flow stress and (d) flow behavior index. There is no relation of the colors specified for each range between the graphs.

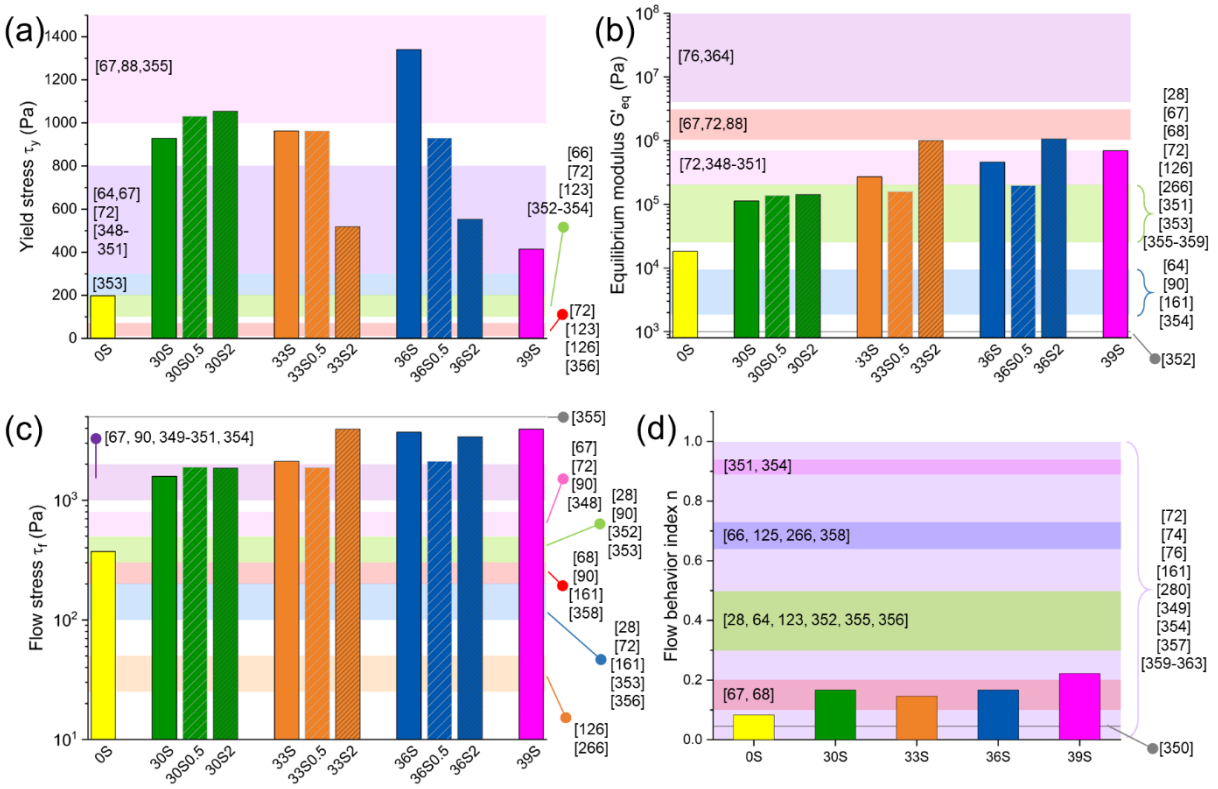

Source: Author.

First and foremost, it is clear that many authors indicate distinguished ranges of values for these rheological properties that ensure printability. Upon examining the yield stress, it becomes evident that the majority of the pastes investigated in this study align with a printable range specified in the literature [64,66,67,72,88,123,347–354]. Notably, the values of yield stress of the pastes 30S, 33S, 33S0.5 and 36S0.5 do not fall into any region deemed printable by the literature, yet, in this study, these pastes were still found to be printable.

When examining the equilibrium modulus, the majority of the studied pastes exhibit G'_{eq} values that fall within the range considered printable by many authors [28,67,68,72,88,126,266,347–350,352,354–358]. The only paste that falls outside the printable range is the 0S paste, which, according to our printability test, has a G'_{eq} value too low to maintain its shape after printing. Surprisingly, there are reports in the literature that indicate the printability of pastes with even lower G'_{eq} values [64,90,161,351,353]. While in the ceramic field, the G'_{eq} of this paste is inadequate to ensure the printability of "stiff" formulations, it can still be considered suitable for printing "soft" formulations. This is evident by the numerous studies that utilize Pluronic® F-127-based pastes for bioprinting.

An intriguing analysis emerges when considering the flow stress values. Apart from the 0S paste, which falls within the green region [28,90,351,352], and the 30S paste, positioned in the middle of the purple region [28,67,90,348–350], all the other pastes approach or exceed the defined printability limit set by the literature, specifically the purple region. Among our pastes, the highest flow stress value reached approximately 4000 Pa for the 39S paste, surpassing the capabilities of our printing system. The only reported value of flow stress higher than that of our pastes, which remained printable, was 5000 Pa [354]. Overall, the flow stress of the investigated pastes escalates to exceptionally high values starting from the composition of 33S2 and above. These excessively high τ_f values create a situation that should be avoided if possible since they have the potential to render the paste unprintable due to the mechanical limitations of the printing system, as observed in this study.

The final aspect to consider regarding printability, focusing on a single rheological property, is the flow behavior index (n). According to the underlying principles, a paste should exhibit shear-thinning behavior (which is desirable for DIW) when the value of n is less than 1, specifically within the range of $0 < n < 1$ – this guideline is followed by most authors (represented by the light purple region) [72,74,76,161,280,348,352,356,358–362]. However, some studies have specified their own range of printable n values, as depicted in Fig. 35(d). In our investigation, all the studied pastes demonstrated a flow behavior index lower than 1, specifically lower than 0.23, indicating a strong shear-thinning behavior. [125,363]

Printability criterion based on the recovery rate

Interestingly, the pastes that exhibited difficulties in terms of printability with conical nozzles were precisely the ones with lower recovery rate values: 0S, 36S2 and 39S, as depicted in Fig. 36. On the other hand, the pastes that demonstrated a recovery rate higher than 358 ± 30 Pa/s (value attributed to the paste 33S2) did not encounter any issues when printing using conical nozzles. This suggests that the recovery rate could serve as a good indicator for predicting potential printability problems. Hence, this study depicted pastes with recovery rates in the range of 328-925 Pa/s as printable, while those within the range of 133-212 Pa/s were unprintable. The printability threshold could not be defined as the examined pastes did not present values between the two regions. Still, it can be inferred that pastes with recovery rates lower than those in the unprintable region are expected to be unprintable as well. It is worth noting that, to the best of the authors' knowledge, no prior studies have utilized the recovery rate as a means to evaluate the printability of pastes.

Fig. 36. Recovery rate for the different groups evaluated, highlighting the printable and unprintable regions based on empirical data.

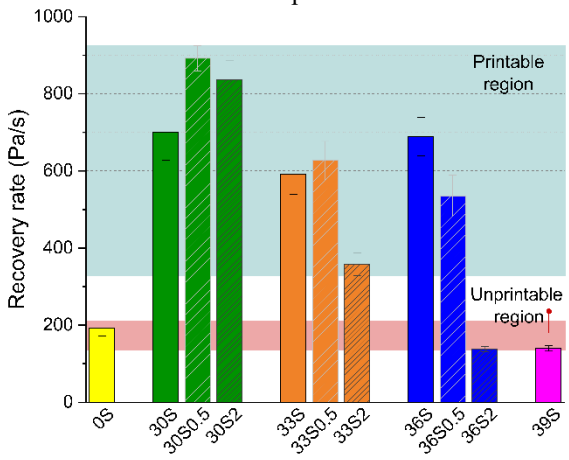

Source: Author.

Criteria based on two rheological properties

As observed, the two primary rheological properties assessed for determining the printability of a paste are the storage modulus and the yield stress. It is crucial to strike a suitable balance between these two factors to achieve an optimal equilibrium of stiffness and flowability [258,291–293,315]. Consequently, it is unsurprising that emerging printability criteria aim to reconcile these two rheological properties. Some of these criteria/parameters are discussed next.

Φ parameter

This criterion is comprised of the ratio of the equilibrium modulus (G'_{eq}) to the yield stress (τ_γ), is proportional to interparticle bond density and is referred to as "ϕ" (Eq. (7)). It was proposed by Lewis *et al.* [341] and should be higher than 20 to ensure minimal deformation (less than 5%) of overhanging structures and suitable extrudability.

$$\phi = \frac{G'_{eq}}{\tau_y} \tag{7}$$

K parameter

This criterion for printability was suggested by Chan *et al.* [364] and establishes a relationship between the storage modulus (G') and the yield stress (τ_y), as expressed in Eq. (8):

$$G' = \frac{K}{\tau_y} \quad (8)$$

Where K is a constant. In this study, the storage modulus value in the equation was considered to be the G'_{eq}. In their study [364], printable pastes exhibited K values ranging from ~6×10^6 to 1×10^7 [364]. The values of K mentioned would serve as a boundary that marks the transition from printable pastes (with higher K values) to pastes that are prone to slumping (with lower K values). This printability criterion aligns with the recommended storage modulus and yield stress values for printability as suggested by Peng *et al.* [293], Zocca *et al.* [21] and Minas *et al.* [90].

Flow Transition Index (FTI)

The FTI is a parameter commonly used to describe the "printability" of a paste and it is the ratio of yield stress to flow stress (Eq. (9)). A value lower than 20 is attributed to printable pastes and is, therefore, desirable [341,365].

$$FTI = \frac{\tau_y}{\tau_f} \quad (9)$$

The visual representation of these parameters is presented in Fig. 37 alongside the plot of the investigated pastes of this study.

Fig. 37. Printability criteria/parameters that are based on the relation of two rheological characteristics and data from the pastes of this study. Parameters: (a) ϕ and K and (b) FTI.

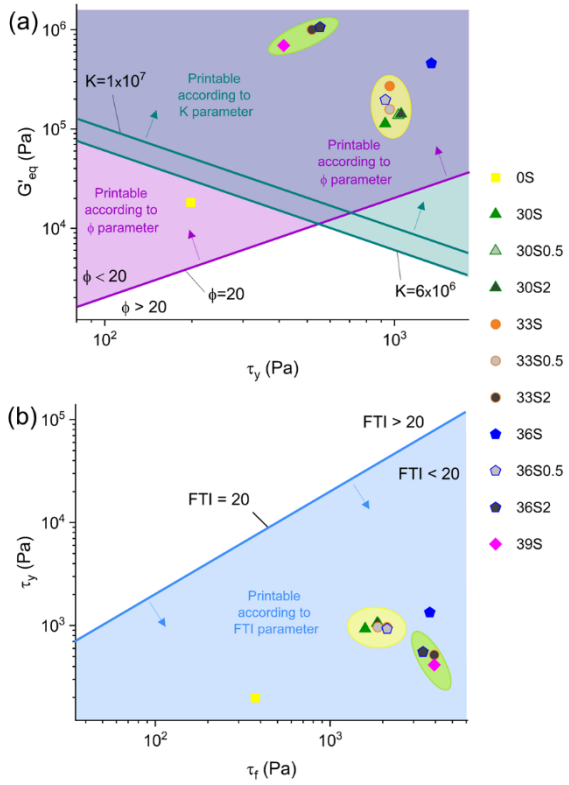

Source: Author.

Analyzing Fig. 37 provides a clearer understanding of where the pastes in this study stand in terms of the printability criteria outlined in the literature. In general, the parameters ϕ (Fig. 37(a) - purple) and FTI (Fig. 37(b)) indicate that all the pastes in this study should be printable. However, the K parameter (Fig. 37(a) - cyan) suggests the same except for the 0S paste which is likely to suffer slumping [364].

Both G'_{eq} *vs.* τ_y and τ_y *vs.* τ_f graphs exhibit a noticeable trend, with most pastes clustered closely together within a region highlighted by a yellow circle. A group of three pastes (33S2, 36S2 and 39S) deviates from the yellow region but remains close to each other within a region marked by a green circle. This group is characterized by higher values of G'_{eq} and τ_f, as well as lower values of τ_y.

Apart from these two regions, the 36S paste stands out. It has intermediate values of G'_{eq}, higher values of τ_y and τ_f values within the range observed in the green region. The other paste that deviates from the two regions is the 0S paste. In comparison to these regions, the 0S paste exhibits lower values of G'_{eq}, τ_y and τ_f. Solely based on the K parameter, this paste would be categorized as unprintable and susceptible to substantial slumping, which indeed occurred and hindered its printability, as corroborated by this study. However, none of the criteria or parameters were able to anticipate the inability to print the 39S paste under all evaluated nozzle

conditions, as well as the 36S2 paste with smaller nozzles. Usually, the ϕ and K parameters can't be used alone. They should be complemented with the highest possible value of τ_y related to the maximal force that the printer can apply (printing machine-related parameter and nozzle dependent) and the lowest τ_y value for minimal height without collapse (dependent on the paste density), as suggested by Feilden *et al.* [366]. In this study, the minimum yield stress required to print the highest filament (840 μm) is 0.8 Pa for the paste with the lowest density (1.014 g/cm^3 – 0S) and 2.4 Pa for the paste with the highest density (2.9 g/cm^3 – 39S) – calculated via Eq. (10) [64]:

$$h_{max} = \frac{\tau_y^{Dyn}}{\rho g} \quad (10)$$

Where h_{max} is the maximum printable height, τ_y^{Dyn} is the dynamic yield stress, ρ is the density of the paste and g is the gravitational force (9.81 m/s^2). Every paste examined in this study had a higher τ_y^{Dyn} compared to these values (ranging from 98.5 to 808.2 Pa for the groups 39S and 33S, respectively). As a result, all of them were expected to resist slumping during filament printing. However, as observed, the paste 0S was found to experience this phenomenon, emphasizing a limitation of the approach.

Moreover, the investigation of the upper limit of yield stress (static) associated with the maximum force the printer can exert was not within the scope of this study, as the manufacturer did not provide this information. Additionally, this value is rarely explored in the literature due to the challenges involved in preparing pastes that surpass this τ_y threshold. However, if we solely consider the yield stress values, the 36S paste exhibited the highest value and could be printed using all conical nozzles examined. On the contrary, the 39S paste, despite having a lower yield stress value, was unprintable with all nozzles tested, likely due to the limitations of the printing machine. This highlights another limitation when evaluating yield stress values in isolation.

Taking these factors into consideration, we can conclude that the three parameters exhibit a reasonable level of agreement with the printability data obtained in this study. Among them, the K parameter was the sole criterion capable of predicting the incapability to print the 0S paste. Therefore, they serve as a valid method for assessing printability. Nevertheless, it is crucial to acknowledge their limitation, as none of them anticipated the inability to print certain pastes.

5 CONCLUSIONS

This study focused on investigating the rheological properties of ATZ pastes with and without CNFs and assessing the applicability of printability criteria found in the existing literature. Many studies tend to overlook the crucial role of rheological characterization in determining the printability of a paste, often relying solely on a single test to establish its shear-thinning behavior and deeming it printable, which can be an erroneous assumption.

As discussed in this research, the concept of printability encompasses more than just the extrudability of a paste; it also entails the ability of the paste to retain its shape after printing. To address this, the present paper defined that the printability criteria outlined in the literature, particularly those that correlate two rheological properties such as G'_{eq}, τ_y, or τ_f, provide a valid approach for predicting the printability of a paste, although presenting some limitations. Additionally, a new criterion based on the recovery rate was presented, which has the potential to predict printability with a single three-interval test.

The field of rheology is vast and intricate, with even slight variations in test conditions significantly impacting the obtained results. This complexity can make result interpretation challenging at times. Therefore, the use of printability criteria that explicitly define the essential properties to evaluate is immensely valuable, benefiting both experienced researchers and newcomers entering the domain of direct ink writing.

By taking into account the established printability criteria and conducting the correct rheological analysis, researchers can be closer to a comprehensive evaluation of a paste's printability. This approach not only enables the development of superior printable pastes but also paves the way for compositions that are increasingly sophisticated and capable of producing structures with growing complexity.

3

CHAPTER 3: MECHANICAL EVALUATION OF DIW-PRINTED CARBON NANOFIBERS - ALUMINA-TOUGHENED ZIRCONIA COMPOSITES

1. INTRODUCTION

Ceria-stabilized zirconia stands out as one of the mostly developed ceramic materials in the field of biomedical applications. Its notable advantage arises from a stress-induced phase transformation, shifting from a tetragonal (t) to a monoclinic (m) phase. This transition brings about a significant volumetric expansion of approximately 4%, effectively impeding the propagation of cracks. Consequently, this mechanism greatly enhances the strength and toughness of tetragonal zirconia polycrystals (TZP) [367]. Another material that capitalizes on this stress-induced phase transformation is yttria-stabilized zirconia (Y-TZP). Due to this fact, these two materials, ceria-stabilized zirconia (Ce-TZP) and Y-TZP, are the most used materials among the TZP systems.

When comparing the two, Y-TZP demonstrates remarkable strength (800-1200 MPa) and a moderate level of toughness (~6 MPa·√m). In contrast, Ce-TZP typically exhibits extraordinarily high toughness (15-20 MPa·√m) but limited strength (≤ 600 MPa). The latter arises from the challenge of producing dense Ce-TZP materials with small grain sizes (< 0.5 μm) [368], as the mobility of grain boundaries during sintering is considerably greater in Ce-TZP compared to Y-TZP [181]. Moreover, Ce-TZP ceramics display significantly reduced susceptibility to aging when compared to Y-TZP, owing to the presence of a tetravalent ion (Ce^{4+}) as the stabilizer. Notably, due to the exceptional transformability of Ce-TZP, notable non-linear, permanent ("plastic") deformation is observable before failure, with the most pronounced pseudoplastic/non-linear behavior among ceramic materials [369–373].

Consequently, significant research efforts have been directed toward incorporating an immiscible secondary phase to immobilize the grain boundaries and controlling grain growth within Ce-TZP [181,374,375]. Among these second-phase materials, alumina is by far the most explored. Various studies have developed Ce-TZP/Al_2O_3 composites [376–379], in which the addition of alumina demonstrated improvements in hardness, Young's modulus and fracture strength. However, it was noted that an increase in alumina content corresponded to a reduction in fracture toughness, aligning with the decrease in transformability. This type of material comprising zirconia and alumina (at higher and lower contents, respectively) is usually referred to as alumina-toughened zirconia (ATZ).

To further improve the mechanical properties, the introduction of elongated third-phase materials has been suggested. These elongated phases offer the potential to help hinder the growth of zirconia grains and further enhance toughness through mechanisms like bridging

and crack deflection [380–384]. Among the explored candidates for third-phase integration are strontium aluminate platelets (more specifically strontium hexaaluminate, $SrAl_{12}O_{19}$), initially investigated by Cutler *et al.* [371,372]. Their incorporation resulted in improved toughness and strength via crack branching and bridging mechanisms. However, it's worth noting that the composite with three phases also exhibited a reduced level of transformability in comparison to pure Ce-TZP ceramics.

More recent investigations have been performed on this composition of three-phase composites [374,375,385]. Specifically, they have focused on 10.0-11.5Ce-TZP/Al_2O_3/$SrAl_{12}O_{19}$ composites with a volume ratio of 84/8/8. This particular configuration of Al_2O_3 and $SrAl_{12}O_{19}$ contents at 8 vol% was determined to yield the most refined microstructures post-sintering [374]. Notably, these composites demonstrated remarkable strength (> 1 GPa) and toughness (> 10 MPa·√m), accompanied by an exceptional flaw tolerance, evident in a notably high Weibull modulus (m = 60) [385]. Given these favorable mechanical properties, the three-phase composite system (11Ce-TZP/Al_2O_3/$SrAl_{12}O_{19}$) was selected for utilization in the present study.

In terms of processing methods, in recent years, additive manufacturing (AM) has gained significant attention and experienced rapid development. AM, also known as 3D printing, is a manufacturing technique that constructs computer-generated models by adding materials, typically layer by layer. It enables the production of complex geometries without the need for micromachining processes or costly molds. The utilization of AM technologies offers several distinct advantages, including rapid prototyping, predictable production, reduced assembly requirements, design flexibility, and the ability to meet specific customer requirements. Consequently, it has emerged as an attractive alternative to conventional manufacturing processes across various fields, including ceramics [386,387] – a field where traditional processing methods are limited by the need for special equipment and tooling as well as by the complexity of the molds.

There are diverse AM techniques available for fabricating ceramic structures, such as stereolithography (SLA), selective laser sintering (SLS), fused deposition modeling (FDM), inkjet printing, binder jet and direct ink writing (DIW or robocasting) [388–390]. Among these techniques, DIW stands out as a simple, emerging, cost-effective, environmentally friendly and rapid fabrication method. It enables the direct production of net or near-net complex-shaped ceramic structures with self-supporting properties and high aspect ratios by the extrusion of a paste through a printing nozzle.

Nevertheless, the mechanical properties of ceramic materials produced through DIW require further improvements, particularly concerning their mechanical reliability, often expressed through Weibull modulus (m) values. To achieve better mechanical properties, this study suggests the incorporation of carbon nanofibers (CNFs) oriented by the shear stresses from the process of nozzle reduction during DIW printing (Fig. 38).

Fig. 38. Schematic representation of the direct ink writing process and the orientation of elongated phases promoted by it.

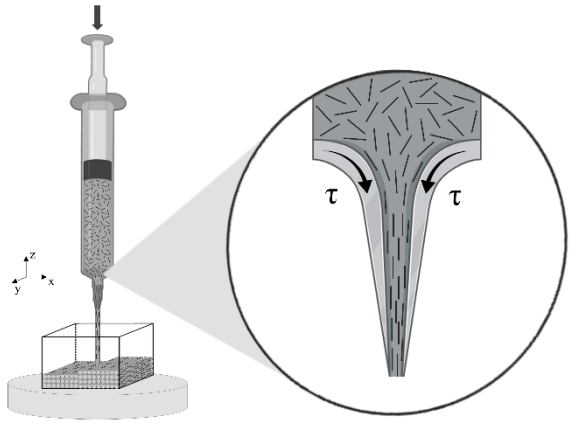

Source: Author.
τ: shear stress

Carbon nanofibers exhibit exceptional mechanical properties, elevated electrical and thermal conductivity and a remarkable strength-to-weight ratio [391]. Their incorporation has demonstrated enhancements in compressive strength, flexural strength, Young's modulus and fracture toughness [392–395]. By strategically orienting them in a specific direction, it is expected that these improvements could be further amplified through mechanisms such as microcrack bridging and crack deflection.

Still, some challenges arise when adding carbon nanofibers to a ceramic matrix. These encompass the achievement of a homogeneous dispersion of the CNFs, their orientation during DIW printing and the sintering of the obtained component. To address the first, two methods were employed in this study: a deflocculant was added to the printing paste and a high-speed mixing technique was applied to the production procedure of the paste. The latter is a method that has already been utilized to achieve a homogeneous dispersion of CNFs in pastes for DIW [396].

Considering the orientation, this behavior observed in DIW happens as non-equiaxed particles tend to rotate and align themselves parallel to the shear direction under shear stresses [397]. This orientation phenomenon has been documented in DIW studies involving various

materials, such as alumina particles [398], platelets [32], carbon nanofibers [346,396,399,400] and graphene nanoplatelets (GNP) [176]. According to Folgar-Tucker [397], the factors that affect these particles' orientation are the particles' shape (length/diameter ratio), interactions between these particles (particles' solid loading) and shear rate and time. Hence, the achievement of proper orientation needs to consider such parameters. In this study, the length/diameter ratio of the CNFs was not varied and ranged from 150 to 1000. The solid loading/content utilized (30 vol%) was not varied either, since it was optimized in Chapter 2. Meanwhile, the shear rate was altered by modifying the diameter of the printing nozzle. The influence of the nozzle diameter on the maximum shear rate induced by the nozzle ($\dot{\gamma}_{max}$) is depicted in Eq. (11):

$$\dot{\gamma}_{max} = \frac{8 \cdot Q}{D} \tag{11}$$

Where Q is the printing speed in mm/s (10 mm/s in this study) and D is the nozzle diameter in mm. As so, in this study, the nozzle diameter was assessed in terms of its influence on the orientation of the CNFs and the mechanical properties achieved.

Sintering with CNFs inside a ceramic also poses a significant challenge, because of the thermal decomposition of the CNFs in the presence of oxygen. The thermal stability and decomposition behavior of carbon nanofibers are the subject of ongoing research and the exact decomposition temperature range can differ based on the specific type of nanofibers, their structural properties, impurities, catalyst residues and surface functionalization. Nevertheless, there have been studies that have reported the thermal decomposition of the CNFs from 480-550 °C [401]. To address these difficulties and maintain the structural integrity of CNF materials while achieving sintering at reduced temperatures or shorter timeframes, the Spark Plasma Sintering (SPS) technique has been proven advantageous [402]. This method's high heating rate facilitates rapid completion of the sintering process, thereby minimizing potential damage to the CNF structures. To assess the impact of Spark Plasma Sintering (SPS), a control group was established by conducting conventional sintering (CS). This comparison allowed for the evaluation of the specific influence of the SPS sintering process.

Summarizing, this study aimed to improve the mechanical properties of ATZ composites by the addition of oriented CNFs. For that, the influence of CNF content, nozzle diameter and sintering method on the mechanical properties was evaluated. Processes that

influence the final mechanical properties such as debinding and sintering were carefully studied and conducted to reduce the likelihood of defects and ensure smaller grain sizes.

2. MATERIALS AND METHODS

2.1.MATERIALS

The ATZ powder used in this study consists of 84 vol% Ce-TZP (11.0 mol% Ce), 8 vol% Al_2O_3, and 8 vol% $SrAl_{12}O_{19}$, which was obtained from Doceram® under the trade name "EvoCera®" in the form of a spray-dried powder. For deflocculation purposes, Darvan® 821-A from RT Vanderbilt® was employed, while Pluronic® F-127 from Sigma-Aldrich® served as the binder. The carbon nanofibers used in the experiments were Pyrograf®-III PR-19-PS.

2.2.METHODS

2.2.1. Preparation of the pastes

The preparation of the pastes depicted in Fig. 39 was carried out as follows. All mixing procedures were conducted in a SpeedMixer DAC 600 Hauschild® under a vacuum of 30 mBar, employing cycles of 800 rpm for 90 s, followed by 1500 rpm for 90 s. Initially, the deflocculant and deionized water were combined and zirconia mixing balls measuring 1 and 2 mm were introduced to facilitate the mixing process. Then, the binder was added and another round of mixing was performed. Subsequently, each mixing step was alternated with a cooling step of 10 min in a refrigerator at 4 °C. Once the binder was uniformly blended with the other components, the ATZ powder was introduced. Ten rounds of mixing and cooling were carried out to ensure optimal homogeneity. In cases where carbon nanofibers were included in the paste, they were added after the ATZ powder, followed by an additional ten cycles of mixing and cooling. Once the paste achieved homogeneity, the mixing balls were separated using a sieve. Before printing, the pastes were put inside 5 mL syringes with a subsequent centrifugation step at 3000 rpm for 12 min to remove any bubbles.

Fig. 39. Schematic illustration of the obtention of the filaments, including the steps of paste preparation, printing and post-printing thermal processes.

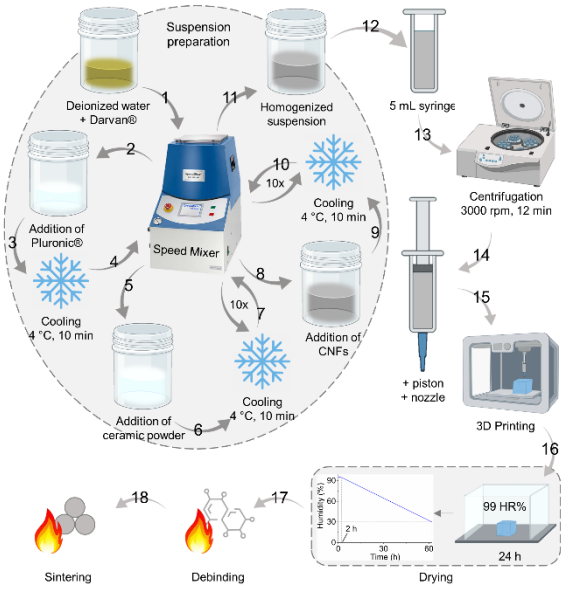

Source: Author.

Four groups were prepared with three different compositions that were later sintered either by conventional sintering (CS) or spark plasma sintering (SPS). The composition and sintering method of the groups evaluated in this study are displayed in Table 15.

Table 15. The four groups evaluated, their composition and sintering approach.

Group	ATZ	CNFs	Darvan® 821A	Pluronic® F-127	Deionized water	Sintering method
CS-ATZ	30 vol% (T)	–	1.0 wt% (S)	25 wt% (L)	Remaining quantity	CS
SPS-ATZ	30 vol% (T)	–	1.0 wt% (S)	25 wt% (L)	Remaining quantity	SPS
SPS0.5	30 vol% (T)	0.5 wt% (S)	1.0 wt% (S)	25 wt% (L)	Remaining quantity	SPS
SPS2	30 vol% (T)	2.0 wt% (S)	1.0 wt% (S)	25 wt% (L)	Remaining quantity	SPS

Source: Author.

(T): in relation to the total; (S): in relation to the solids (ATZ + CNFs); (L): in relation to the liquids (deionized water + Darvan); CS: conventional sintering; SPS: spark plasma sintering.

2.2.2. Obtention of the filaments

The filaments were printed via the Direct Ink Writing (DIW) method using a robocasting manufactured by 3D INKS, LLC® (Tulsa, USA) with nozzles of diameters of 200, 250, 410, 580 or 840 µm (Nordson®, Fig. 40(a)). The printing procedure took place in an enclosure with 25 °C of temperature and 95% of humidity. The filaments were deposited on a glass plate on top of which a fine layer of coconut oil was previously applied to facilitate the

detachment of the filaments. The printing speed utilized was 10 mm/s. For the nozzle diameters of 200, 250, 410, 580 and 840 µm, the nozzle offset (distance between the end of the nozzle and printing plate) was 230 (115%), 270 (108%), 450 (110%), 650 (112%) and 900 µm (107%), respectively. The printing pattern was a zig-zag (Fig. 40(b)) leading to 25 mm long filaments (Fig. 40(c)).

Fig. 40. (a) The different nozzles used in this study with their corresponding diameters and obtained filaments. The color of the nozzles was utilized for the graphs of the filaments that were printed with each specific nozzle (gray for 200 µm, red for 250 µm, blue for 410 µm, pink for 580 µm and green for 840 µm). (b) Zig-zag printing pattern after printing and (c) after drying and cutting out the curves/edges.

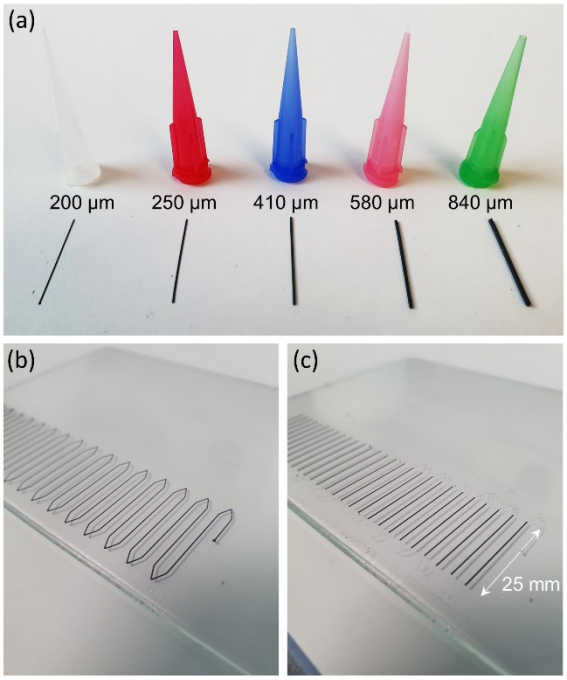

Source: Author.

The filaments, still on the glass plate, were dried in a climatic chamber (Weisstechnik® WKL 34/+10) at 25 °C (relative humidity of 95% for 2 h, then decreased to 30% over 60 h). After the drying process, the curves/edges of the zig-zag pattern were cut out with a cutter, the glass plate was heated to 30 °C on a hot plate to melt the coconut oil and the filaments were detached from the glass plate with the aid of a razor blade. Subsequentially, the filaments were placed in alumina crucibles (Fig. 41) and stored in a box with 30% relative humidity. After the debinding process, the filaments became extremely fragile (particularly those with smaller diameters) and any attempt to handle them directly would inevitably lead to breakage. Hence, the placement of the filaments inside crucibles was an essential procedure to ensure their protection due to the requirement to transfer them between the debinding and sintering furnaces.

Fig. 41. Alumina crucible into which the filaments were placed after drying to reduce the need to handle them and prevent their breakage. (a) CAD model and (b) photograph of the crucibles – the inset photograph of (b) shows a broken crucible to better observe its bottom configuration. Since one of the main advantages of the DIW technique is its versatility in terms of shape creation with ceramics, it seemed natural to produce the crucibles by DIW. Nozzles of 410 µm were used and the crucibles had 1 cm of diameter with 2.8 cm of height. The first five layers were designed to be *"fully printed"* whereas the subsequent layers were *"hollow"*.

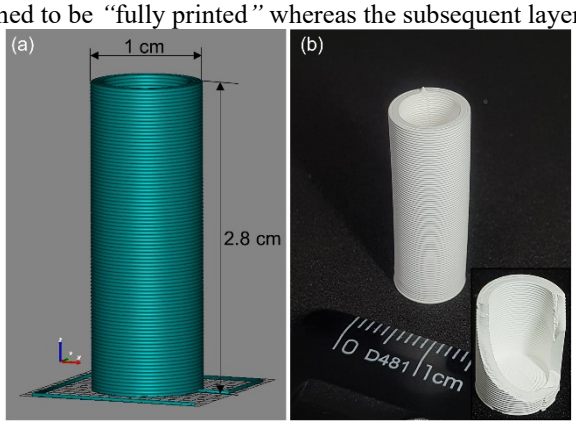

Source: Author.

2.2.3. Debinding study

The optimal debinding condition was determined by thermogravimetric analyses (TGA, SETARAM®) in an Argon atmosphere with a heating rate of 10 °C/min and a cooling rate of 30 °C/min. The samples were placed in an alumina crucible suitable for the equipment, on which a blank analysis was conducted. The resulting curve from this blank analysis was subtracted from the curves obtained during the analysis of the materials.

Two types of materials were examined: ATZ powder and small fragments of printed and dried filaments of ATZ with a 2.0 wt% content of carbon nanofibers (CNFs). The ATZ powder was evaluated up to 1300 °C with no plateau and up to 400 °C with a 3 h plateau. The ATZ with 2.0 wt% of CNFs underwent three types of evaluations: (i) up to 1300 °C, (ii) up to 350 °C with a 3 h plateau at this temperature and (iii) up to 400 °C also with a 3 h plateau. The dried filament of ATZ with 2 wt% of CNFs had, after water removal, a composition of 0.89 wt% of Darvan® 821A, 9.55 wt% of Pluronic® F-127, 1.80 wt% of CNFs and 87.76 wt% of ATZ powder. It is worth noting that small amounts of a polymer may be present in the ATZ powder as a result of its addition during the powder mixing process in an aqueous solution, followed by spray-drying. According to its datasheet, the Darvan has a boiling point of ~100 °C, hence should decompose around this temperature. According to the literature, the CNFs decompose approximately at 480-550 °C [401] (the exact temperature range is still debatable) and the Pluronic® F-127 decomposes between 200 and 400 °C (in nitrogen) [403].

2.2.4. Sintering study

The filaments utilized in this evaluation were previously debinded at 400 °C for 30 min. For this part of the study, filaments of 840 µm in diameter were either sintered by conventional sintering (CS) or by Spark Plasma Sintering (SPS). For the CS, only ATZ filaments (no CNFs) were sintered whereas, for the SPS, filaments with and without CNFs were sintered for comparison. To determine the optimal sintering temperature, the filaments were sintered by CS in a Pyrox® chamber furnace at 1350, 1400, 1450, 1500 or 1550°C, with a heating rate of 2.5 °C/min, cooling rate of 5 °C/min and a 1 h plateau. For the filaments sintered by SPS, the temperatures of 1350, 1400 and 1450°C were investigated (secondary vacuum, heating rate of 100 °C/min and 1 h plateau, furnace HP D25 from FCT®), without applied pressure (Fig. 42). The results of the sintering process were evaluated by density measurements and SEM images (Thermofischer® QuattroS equipment).

Fig. 42. Schematic illustration of the configuration of the samples within the SPS furnace to avoid the application of pressure.

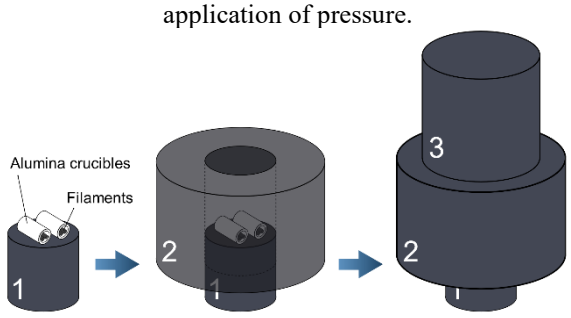

Source: Author.

The density of the sintered filaments was determined via Archimedes' method (Eq. (12)) utilizing deionized water as the liquid phase. In the equation, ρ_{sample} is the measured density of the sintered filament, m_{air} is the mass of the sample in air, m_{liquid} is the mass of the sample in the liquid phase, ρ_{liquid} is the density of the liquid and ρ_{air} is the density of air.

$$\rho_{sample} = \frac{m_{air}}{m_{air} - m_{liquid}} * (\rho_{liquid} - \rho_{air}) + \rho_{air} \quad (12)$$

The relative density was calculated by the ratio of the measured density of the sample to the theoretical density calculated with the following values: the theoretical density of the ATZ powder considered was 5.8404 g/cm^3 and that of the CNFs was 2.16 g/cm^3. The value of

relative density had an associated measurement uncertainty of ±2% linked to the precision of the scale utilized (0.0001 g) and the very low weight of the filaments (0.0147-0.0221 g).

2.2.5. Mechanical study under flexion of filaments

The printed filaments were mechanically characterized by 3-point flexural tests in a BOSE EF3200 multi-test machine with a 20 N force cell, displacement sensor LVDT (linear variable differential transformer) with 50 nm displacement resolution and 15 mm lower span distance (Fig. 43(a)).

For the samples utilized in this test, the CS process was done at 1500 °C for 1 h, whereas the SPS process was performed at 1400 °C for 1 h. The evaluated groups were the same as those displayed in Table 15 (CS-ATZ, SPS-ATZ, SPS0.5 and SPS2) and, in each group, 30 filaments were tested.

Fig. 43. (a) 3-point bending device utilized for the mechanical evaluations. (b) Optical microscopy image of the cross-section of a printed filament and (c) schematic representation of the diameter (D) and dimensions A and B used for the calculation of the quadratic moment.

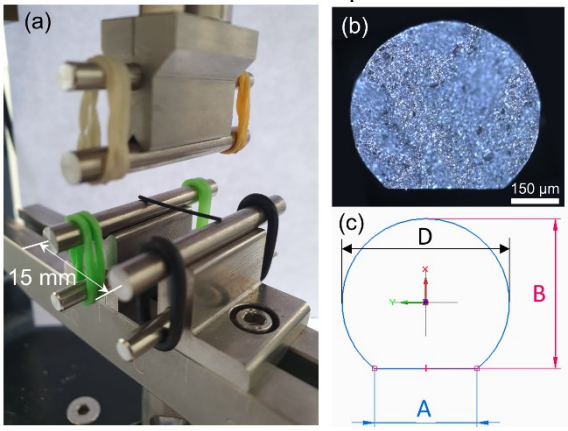

Source: Author.

The stress-strain curves were deduced from the load-displacement curves using the following method. The stress (σ) and strain (ε) were calculated from the applied load (F) and displacement (u_x) using Eq. (13), (14) – Catigliano theorem – and (15):

$$\sigma = \frac{F \cdot L \cdot x}{4 \cdot I_y} \tag{13}$$

$$u_x = \frac{L^3 \cdot F}{48 \cdot E \cdot I_y} \leftrightarrow E = \frac{L^3 \cdot F}{48 \cdot u_x \cdot I_y} \tag{14}$$

$$\varepsilon = \frac{\sigma}{E} = \frac{F \cdot L \cdot x}{4 \cdot I_y} \cdot \frac{48 \cdot u_x \cdot I_y}{L^3 \cdot F} = \frac{12 \cdot u_x \cdot x}{L^2} \quad (15)$$

Where L is the length between cylinders (lower span, 15 mm, in this case), E is the Young's modulus, x is the distance from the tensile side of the filament to the neutral axis and I_y is the quadratic moment. As the printed filaments have a flat side where they touched the printing substrate, their quadratic moment is not that of a round filament. Hence, I_y and x were calculated individually for each tested filament by SolidEdge® after measurements of thickness (dimension A) and height (dimension B) of each filament by optical microscopy (Fig. 43(b) and (c)). The value of Young's modulus (E) was directly calculated as the slope of the linear part of the stress-strain curve.

From the stress-strain curves, a few key characteristic mechanical values were defined as shown in Fig. 44. Whenever the behavior was not purely linear elastic, the yield stress (σ_{yield}) was defined as the stress necessary to reach $\delta = 0.1\%$ of plastic deformation, corresponding to a yield strain ε_{yield}. Fracture stress ($\sigma_{fracture}$) was defined as the maximum stress attained before fracture; the corresponding strain was denoted as $\varepsilon_{fracture}$. In addition, a non-linear strain ($\varepsilon_{non\text{-}linear}$) was calculated by removing the elastic part of the strain from the fracture strain (Eq. (16)):

$$\varepsilon_{non-linear} = \varepsilon_{fracture} - \frac{\sigma_{fracture}}{E} \quad (16)$$

Fig. 44. Schematic illustration of how the characteristic values were obtained from the stress *vs.* deformation curves.

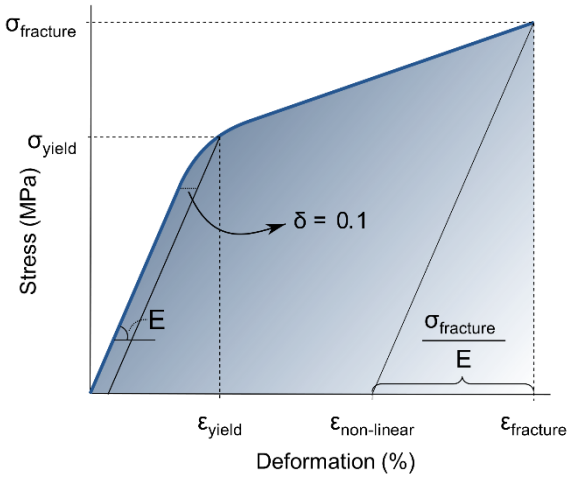

Source: Author.

A Weibull analysis was also conducted on each group, utilizing Eq. (17):

$$F = 1 - \exp\left(\frac{-\sigma_f}{\sigma_0}\right)^m \quad (17)$$

Where F is the probability of failure ($0 < F < 1$) under applied stress σ_f, whereas σ_0 is the characteristic strength of the material. The Weibull modulus (m) was determined by the slope of the curve $\ln\left(\ln\left(\frac{1}{1-F}\right)\right)$ *vs.* $\ln(\sigma_f)$.

In addition, after observing a certain inelastic deformation in the filaments that underwent conventional sintering, these were tested in flexural cycles. This was done by applying five cycles of increasing imposed force at regular intervals aiming to achieve the maximum deformation while avoiding sample breakage (force intervals from 0.3-0.4 to 2.0-4.2 N). Intermediary and larger nozzle sizes were preferred for the evaluation under flexural cycles to enable a more comprehensive observation of results with an increased volume of material. In another test, six cycles with the same imposed force (from 0.37 to 2 N) were applied to study fatigue on the filaments. SEM evaluations of the filaments' surface were also conducted on conventionally sintered filaments tested under flexion where the test was stopped right before failure.

2.2.6. Data analysis

Results were expressed as mean value ± standard deviation and were statistically analyzed using ONE-WAY Analysis of Variance (ANOVA). The influence of the variables CNF content, nozzle diameter and sintering method was evaluated in relation to the fracture strain and stress and Young's and Weibull moduli values by correlation and regression analysis. A correlation was established by a value higher than |0.25| and differences were considered significant if p-value ≤ 0.05. The percent chance that there was a true relationship between the variables was calculated by CTR (chance of true relationship) = (1 – p-value) x 100. The 95% interval of confidence of the Weibull modulus was calculated according to the study of Griggs *et al.* [404].

3. RESULTS

3.1.DEBINDING STUDY

The results of the TGA analyses of ATZ powder and a dried filament obtained from the paste containing 2 wt.% CNFs are displayed in Fig. 45.

Fig. 45. TGA analyses to determine the debinding temperature. Evolution of the mass with increasing temperature for the (a) ATZ powder up to 1300 °C and (b) ATZ with 2 wt% of CNFs up to 1300 °C. Evolution of the mass with time for the group of ATZ with 2 wt% of CNFs when treated at (c) 350 °C for 3 h and (d) 400 °C for 3 h. (e) Evolution of the mass with time for the ATZ powder treated at 400 °C for 3h.

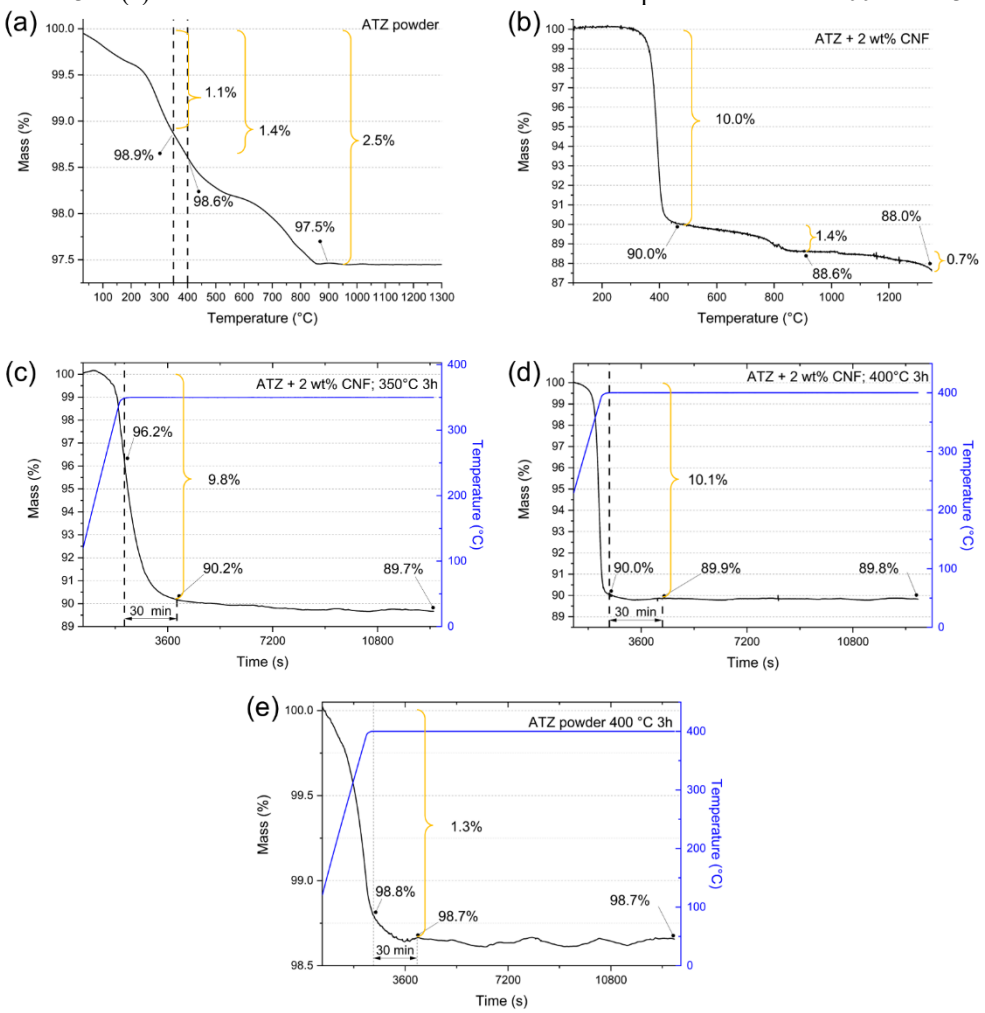

Source: Author.

The TGA analysis of the ATZ powder (Fig. 45(a)) revealed the presence of residual polymer in the powder, as indicated by a continuous decrease in mass up to 900 °C (followed by a stable mass up to 1300 °C). This mass reduction was more pronounced in three distinct intervals: $T < 225$ °C, $250 < T < 550$ °C and $T > 650$ °C. These reductions cannot be attributed

to any of the ceramic materials present (Ce-TZP, Al_2O_3 and $SrAl_{12}O_{19}$), as the evaluated temperatures are not sufficiently high to affect them. Hence the inference that the presence of a polymer caused these reductions. The overall mass loss up to 900 °C was 2.5%, with values of 1.1% and 1.4% up to 350 °C and 400 °C, respectively.

Regarding the ATZ with 2.0 wt% of CNFs (Fig. 45(b)), a significant mass reduction of 10.0% occurred around the temperature range of ~350-400 °C. A smaller decrease of 1.4% was observed up to 900 °C, followed by an additional decrease of 0.7% with further temperature increase. Analyzing the first decrease (10.0%), it is estimated that 0.9% resulted from the decomposition of Darvan, 1.2% from the decomposition of the residual polymer within the ATZ powder (which corresponds to 1.4% of 87.8%) and the remaining 7.9% was associated with the decomposition of Pluronic. Although CNFs decompose in the temperature range of 480-550 °C [401], no CNF decomposition is expected as the analyses were conducted in an argon atmosphere. Regarding the second mass decrease of 1.4%, 1.0% was attributed to the decomposition of the residual polymer within the ATZ powder (equivalent to 1.1% of 87.8%) and 0.4% to the decomposition of Pluronic. The third decrease (0.7%) was likely entirely linked to the decomposition of Pluronic. At the end of this analysis, from the remaining 88.0% mass, 85.5% was the mass of ATZ, 1.8% was attributed to CNFs and 0.6% corresponded to the remaining Pluronic. Overall, in comparison to the ATZ powder, Fig. 45(b) shows an additional mass loss at low temperatures, attributed to the decomposition of Pluronic, but no sign of CNF decomposition at high temperatures.

Considering that the extraction of the majority of Pluronic occurs in the range of 350-400 °C, two conditions were taken into account for the debinding process, which were, therefore, assessed through TGA analysis: heating up to 350 °C with a 3-hour plateau at this temperature (Fig. 45(c)) and heating up to 400 °C, also with a 3-hour plateau (Fig. 45(d)).

Under the first condition, when the temperature reached 350 °C, 96.2% of the initial mass remained. After a 30-minute plateau, there was a decrease of 9.8% compared to the starting point. This decrease consisted of 0.9% Darvan, 1.0% of the residual polymer within the ATZ powder (equivalent to 1.1% of 87.8%) and 7.9% of Pluronic. Hence, after the 30-minute plateau, the remaining quantity of Pluronic was 1.6%. Following a 3-hour plateau, the mass further decreased by 0.5%, which was attributed entirely to the Pluronic. At the end of the analysis, the remaining mass (89.7%) was distributed as follows: 86.8% was attributed to ATZ, 1.8% to CNFs and 1.1% to the remaining quantity of Pluronic.

Under the second condition, when the plateau temperature of 400 °C was reached, 90.0% of the initial mass remained. After a 30-minute plateau, there was a mass reduction of 10.1% compared to the starting point. However, there was no significant change in the mass value observed after 30 minutes (89.9%) compared to that after 3 hours (89.8%) of the plateau. Considering this and the objective of achieving a shorter debinding period to prevent CNF decomposition in the air atmosphere inside the debinding furnace, the condition of heating up to 400 °C with a 30-minute plateau was chosen as the preferred debinding condition.

To determine the precise quantity of Pluronic remaining in the sample under the latter condition, the ATZ powder was analyzed under the same conditions (Fig. 45(e)). After a 30-minute plateau at 400 °C, 1.3% of the polymer within the ATZ powder was decomposed. Therefore, out of the 10.1% mass decrease observed in Fig. 45(d), 1.2% was attributed to the decomposition of the polymer within the ATZ powder (equivalent to 1.3% of 87.8%), 0.9% to Darvan and 8.1% to Pluronic. Consequently, following the debinding procedure of 400 °C with a 30-minute plateau, it is expected that the samples contain a remaining quantity of Pluronic of approximately 1.5%. This remaining Pluronic is likely to decompose during the subsequent sintering procedure, posing a low potential for defect generation as it leaves the samples.

Moreover, it's important to consider the evaluation provided in this section as an approximation of the amount of mass attributed to each component of the material. This approximation arises due to the constraints posed by a basic TGA analysis (without integration with a spectrometer), the inherent uncertainty in the initial mass measurement and the possible existence of small amounts of water at low temperatures (which could alter the relative mass variations).

3.2.SINTERING STUDY

The sintering study encompassed density and morphological evaluations. The density results are presented in Table 16 for both sintering approaches: conventional sintering (CS) and Spark Plasma Sintering (SPS).

Table 16. Density results of the sintering study with different sintering methods/approaches and temperatures.

Sintering approach	Sample	$T_{sintering}$ (°C)	$t_{sintering}$ (h)	Measured density (g/cm^3)	Theoretical density (g/cm^3)	Relative density (%)
CS	ATZ	1350	1	5.398	5.840	92.4
	ATZ	1400	1	5.485	5.840	93.9
	ATZ	1450	1	5.589	5.840	95.7
	ATZ	1500	1	5.726	5.840	98.0
	ATZ	1550	1	5.757	5.840	98.6
SPS	ATZ	1350	1	5.368	5.840	91.9
	0.5 wt% CNF		1	5.326	5.791	92.0
	ATZ	1400	1	5.728	5.840	98.0
	0.5 wt% CNF		1	5.728	5.791	99.0
	ATZ	1450	1	5.661	5.840	97.0
	0.5 wt% CNF		1	5.570	5.791	96.2

Source: Author.

$T_{sintering}$: temperature of the sintering plateau; $t_{sintering}$: time at the plateau.

In the conventional sintering (CS), the relative density of the ATZ samples increased with increasing temperatures ranging from 92.4 to 98.6% for the 1350 and 1550 °C, respectively. Nevertheless, with an associated measurement uncertainty of ±2%, there is no significant difference between some of the values. Still, the tendency of increased relative density with increasing sintering temperature remains when sintering by a conventional approach.

When employing Spark Plasma Sintering (SPS), the evaluation of three different temperatures revealed distinct ranges of relative densities. Sintering at 1350 °C resulted in densities of approximately 91-92%, while sintering at 1400 °C yielded densities around 98-99% and at 1450 °C, densities were approximately 96-97%. In this particular case, unlike the outcome with CS, the samples sintered at the highest temperature (1450 °C) exhibited lower densities than those sintered at 1400 °C; however, these values fall within the respective error ranges, failing to reach a significant difference. The inclusion of 0.5 wt% of carbon nanofibers (CNFs) did not present any distinct trend.

To further understand the effect of the sintering temperatures, morphological evaluations were performed on the sintered samples. The outcomes of this evaluation, alongside the density results, assisted in the definition of the sintering temperature for both approaches. The microstructural images of the sintered samples are depicted in Fig. 46 for the CS method and in Fig. 47 for the SPS approach. The grain size evaluation of the sintered samples is displayed in Fig. 48.

Fig. 46. Microstructural evaluation of ATZ filaments sintered by Conventional Sintering (CS). Sintering at (a) 1350, (b) 1400, (c) 1450, (d) 1500 or (e) 1550 °C. It is possible to notice larger zirconia grains with smaller alumina grains predominantly at the grain boundaries.

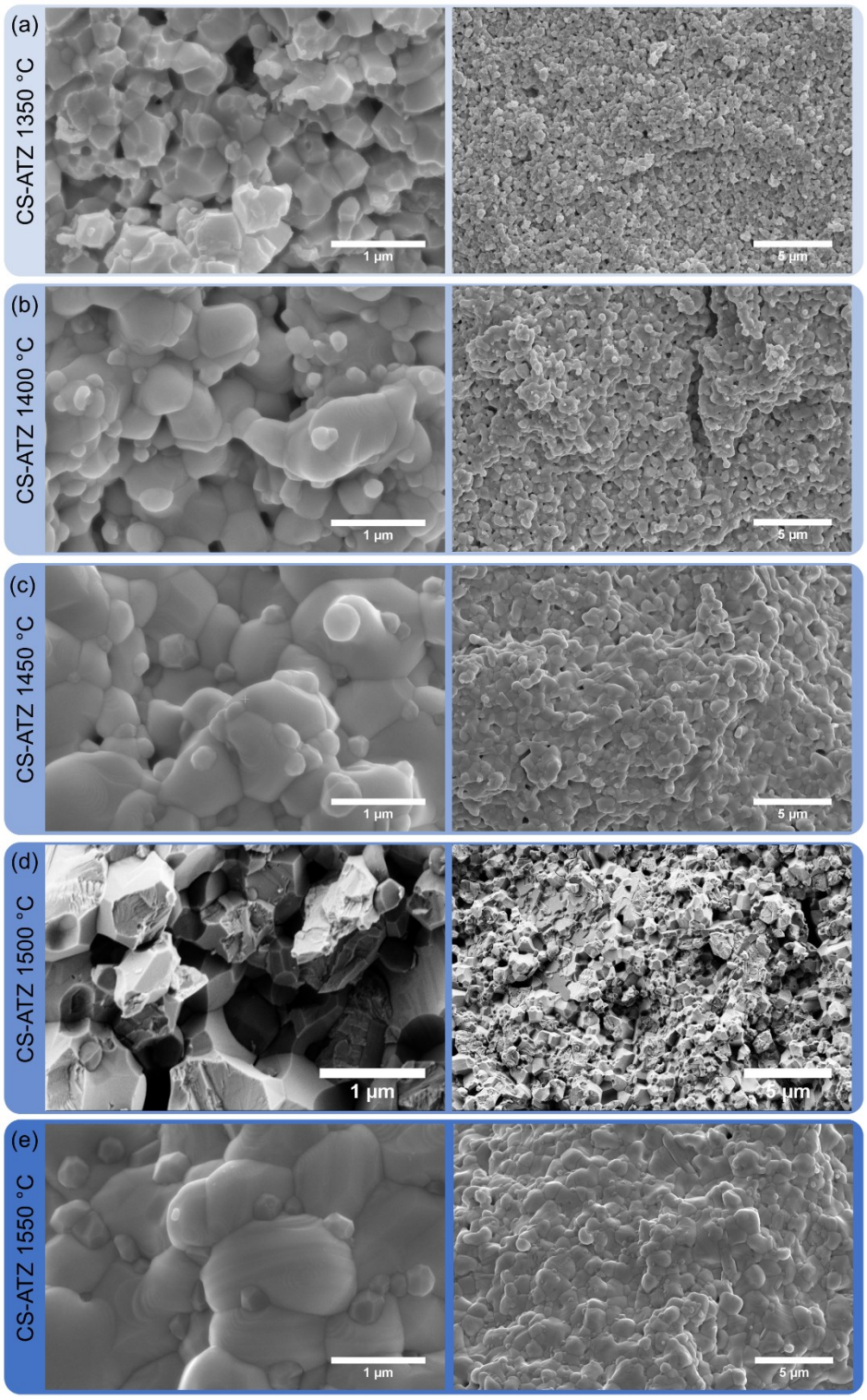

Source: Author.

Fig. 47. Microstructural evaluation of filaments sintered by Spark Plasma Sintering (SPS). ATZ filaments in yellow (a, c and e) and ATZ with 0.5 wt% of CNFs in orange (b, d and f). Sintering at (a and b) 1350, (c and d) 1400 or (e and f) 1450 °C.

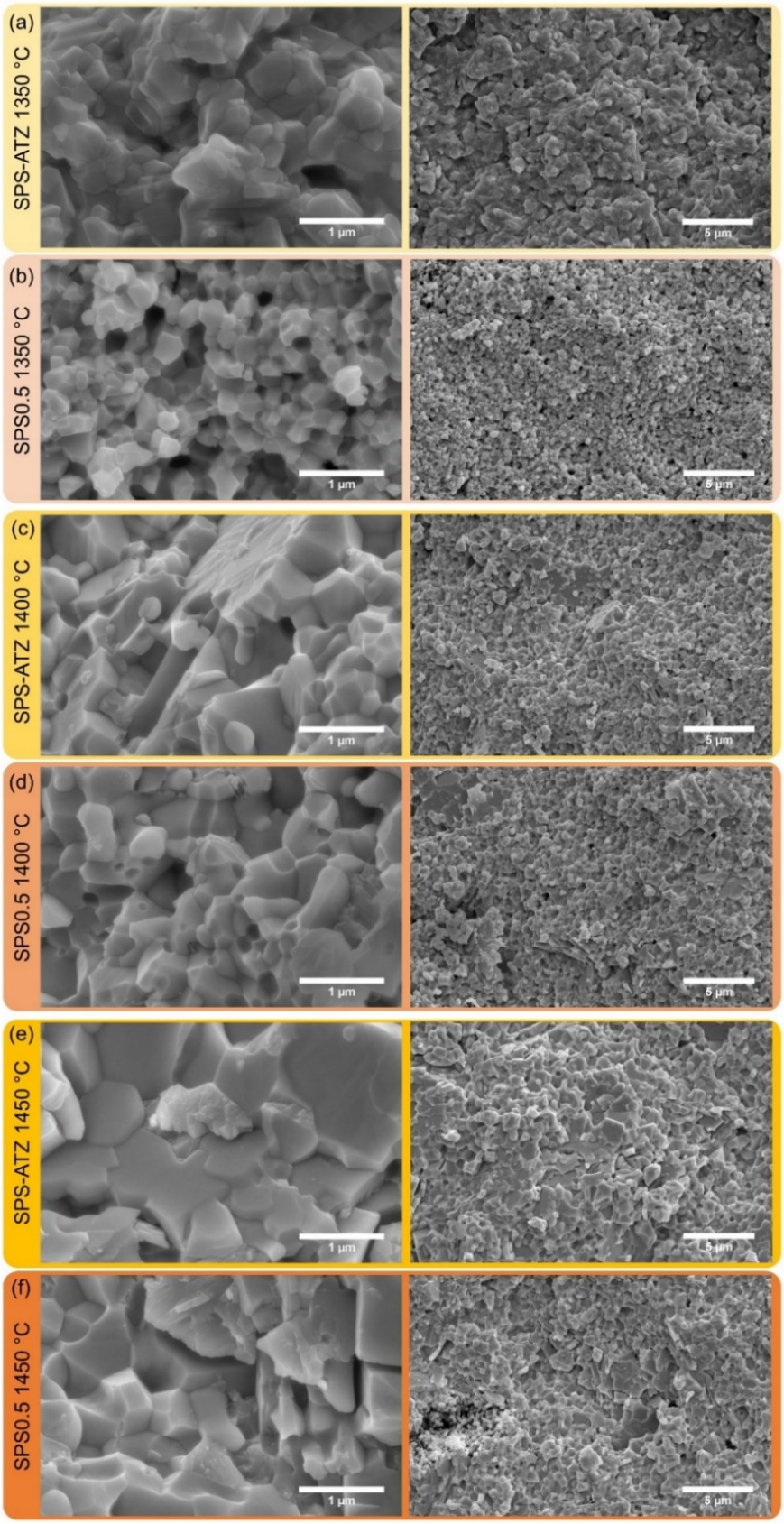

Source: Author.

Fig. 48. Grain size evaluation for (a) ATZ samples sintered by conventional sintering and (b) ATZ and ATZ with 0.5 wt% CNF samples sintered by Spark Plasma Sintering. Comparison of the grain sizes obtained by CS and SPS at (c) 1350 °C, (d) 1400 °C and (e) 1450 °C. The orange color represents alumina grains, whereas the blue color represents Ce-TZP grains. In some samples, it was not possible to visually distinguish the alumina (usually smaller and more angular) from the Ce-TZP grains – the green color represents these samples and contains the sizes of both kinds of grains. When it was not possible to distinguish the alumina and zirconia grains in one group, the comparison with a second group was made in relation to the average grain size of alumina and zirconia together, regardless of whether in that second group it was possible to distinguish the grains.

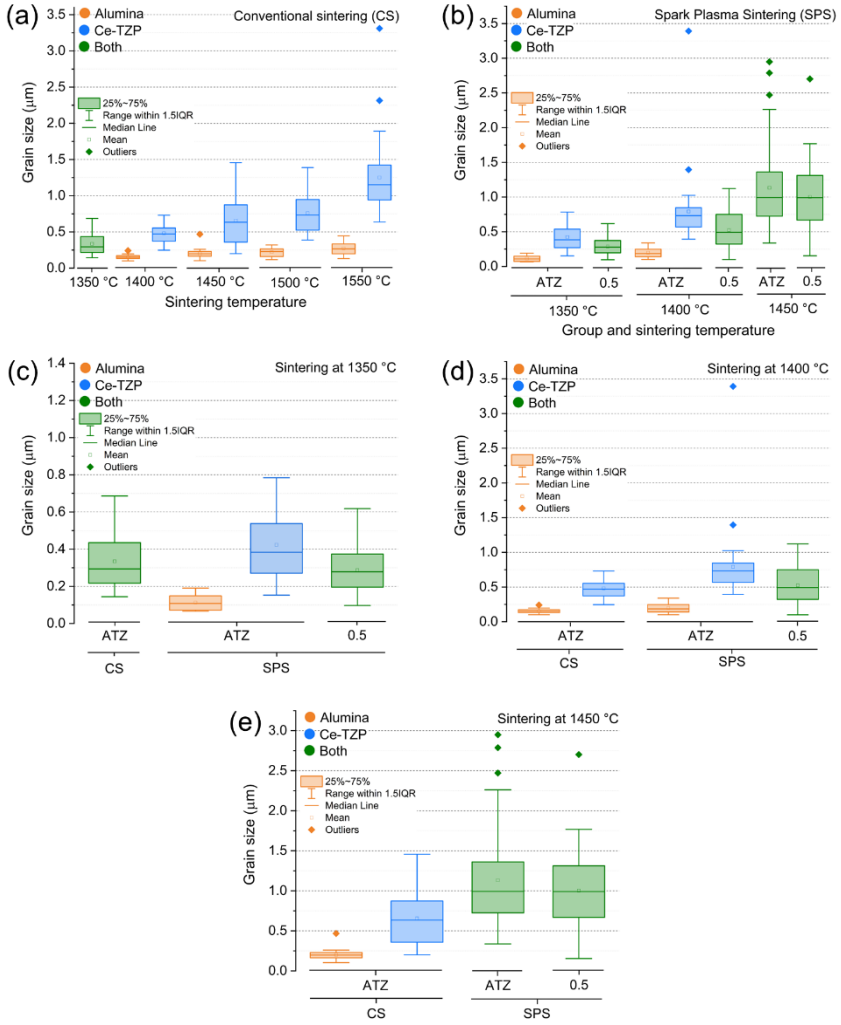

Source: Author.

As the sintering temperature increased in both sintering approaches, a significant reduction in the number of pores was observed. The presence of larger grains also became evident with increasing temperature, as expected. This observation is supported by Fig. 48(a) for the CS samples and Fig. 48(b) for the SPS samples. Upon analyzing the conventionally sintered samples shown in Fig. 48(a), it was observed that the increase in the size of alumina grains was less pronounced compared to the increase in the size of Ce-TZP grains. While the samples sintered at 1500 °C had a higher mean value of Ce-TZP grain size compared to those sintered at 1450 °C, their range of grain size fell within the range of the latter. However, at a

slightly higher temperature of 1550 °C, very large grains (~2.25 and ~3.25 μm) were present. In terms of density, the CS samples sintered at 1500 and 1550 °C exhibited the highest densities, with very similar values of 98.0 and 98.6%, respectively. Therefore, the smaller grain sizes observed in the samples sintered at 1500 °C were crucial in selecting this temperature as the sintering temperature for the Conventional Sintering (CS) approach.

When considering the samples sintered using the Spark Plasma Sintering (SPS) method, a similar trend of increasing grain sizes with higher temperatures was observed for both types of samples: ATZ and ATZ with 0.5 wt% CNF. Interestingly, the samples containing 0.5 wt% CNFs exhibited slightly smaller grain sizes compared to the samples without CNFs. Additionally, in all CNF-containing samples, it was not possible to distinguish between the alumina and Ce-TZP grains. Comparing the grain sizes of the SPS samples sintered at 1400 °C and 1450 °C, it was found that the former had smaller mean values and narrower ranges. This, coupled with the higher density values observed in the 1400 °C samples (~98-99%) compared to the 1450 °C samples (~96-97%), supported the decision to select 1400 °C as the sintering temperature for the SPS approach.

When comparing the grain sizes obtained through the CS and SPS methods (as shown in Fig. 48(c-e)), it was observed that the samples sintered using SPS had higher mean values of grain size and wider ranges. This particular observation could harm the mechanical properties, which will be discussed in the upcoming sections.

During the microstructural evaluations conducted to optimize the sintering process, it was noted that the samples containing CNFs exhibited their agglomeration (Fig. 49). The presence of CNF agglomerates is expected to have a detrimental effect on the mechanical properties, which will be assessed in the subsequent sections and on density since the CNFs form very porous agglomerates with no ceramic inside (however this effect was not observed (Table 16)).

Fig. 49. SEM image evidencing the agglomeration of CNFs in samples containing 0.5 wt% CNFs.

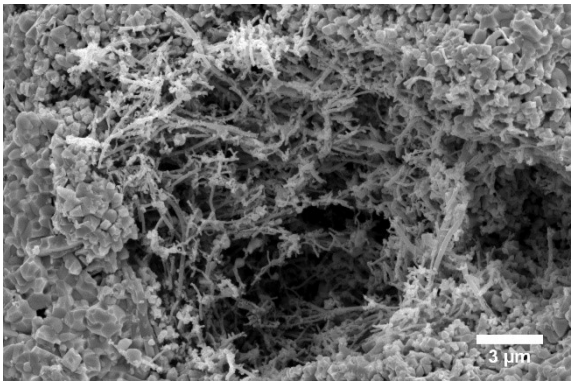

Source: Author.

3.3.MECHANICAL STUDY

3.3.1. Stress *vs.* deformation graphs

The curves of stress *vs.* deformation for a single sample from each group are illustrated in Fig. 50. The key characteristic mechanical values for all 30 samples within each group are presented in Fig. 51, which were utilized for group-to-group or nozzle-to-nozzle comparisons. The characteristic mechanical properties of all the groups and nozzles are shown in Table 17.

Fig. 50. Stress *vs.* deformation for the groups CS-ATZ, SPS-ATZ, SPS0.5 and SPS2 and printed with nozzles of diameters of (a) 200, (b) 250, (c) 410, (d) 580 and (e) 840 µm.

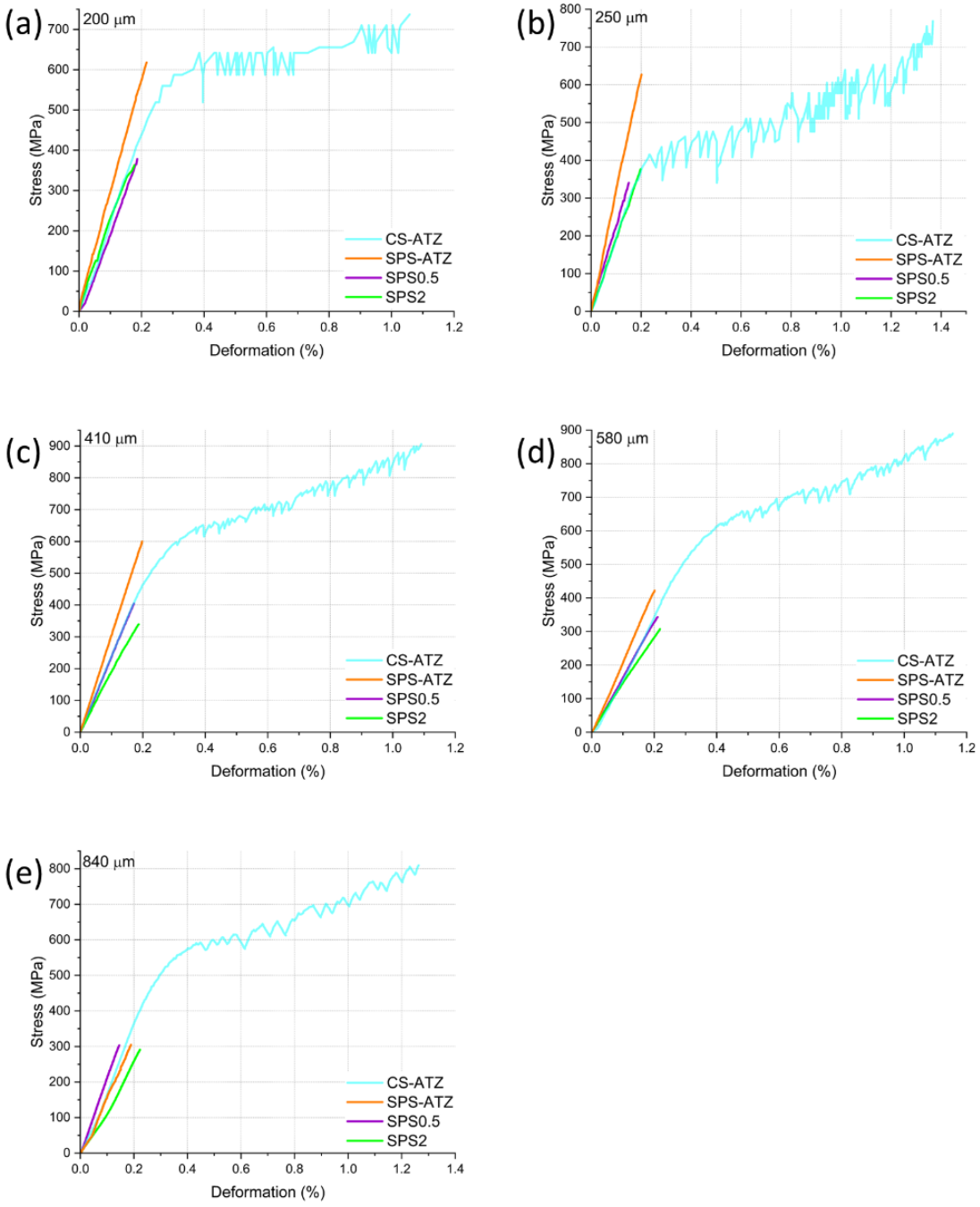

Source: Author.

Fig. 51. Mechanical properties of the filaments that underwent 3PB by nozzle diameter for the groups CS-ATZ, SPS-ATZ, SPS0.5 and SPS2. (a) Young's modulus, (b) Fracture stress/flexural strength and (c) Fracture strain.

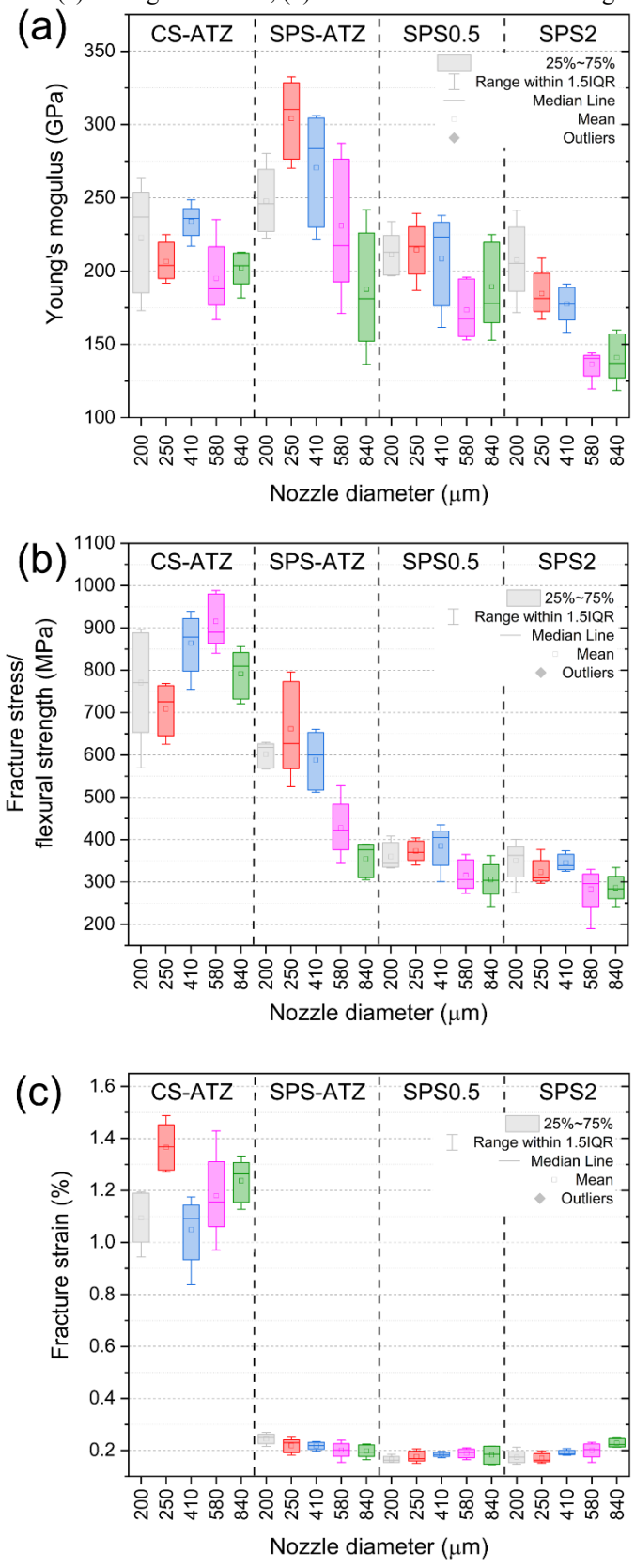

Source: Author.

Table 17. Properties of the filaments by group and by the nozzle diameter utilized in the printing process.

			CS-ATZ		
Nozzle diameter (μm)	200	250	410	580	840
E (GPa)	223 ± 33	207 ± 12	234 ± 11	195 ± 22	202 ± 11
$\varepsilon_{fracture}$ (%)	1.09 ± 0.09	1.37 ± 0.08	1.05 ± 0.11	1.18 ± 0.15	1.24 ± 0.07
$\varepsilon_{non\text{-}linear}$ (%)	0.75 ± 0.07	1.02 ± 0.07	0.68 ± 0.09	0.70 ± 0.10	0.84 ± 0.07
$\sigma_{fracture}$ (MPa)	770.8 ± 117.8	708.8 ± 55.1	863.9 ± 63.3	915.7 ± 55.9	791.6 ± 51.2
ε_{yield} (%)	0.27 ± 0.01	0.22 ± 0.01	0.27 ± 0.02	0.35 ± 0.05	0.31 ± 0.03
σ_{yield} (MPa)	526 ± 71	396 ± 15	561 ± 29	594 ± 46	490 ± 6
			SPS-ATZ		
	200	250	410	580	840
E (GPa)	248 ± 20	304 ± 24	270 ± 34	231 ± 41	188 ± 36
$\varepsilon_{fracture}$ (%)	0.24 ± 0.02	0.22 ± 0.02	0.22 ± 0.01	0.20 ± 0.03	0.20 ± 0.02
$\sigma_{fracture}$ (MPa)	602 ± 27	662 ± 98	588 ± 61	428 ± 59	355 ± 37
			SPS0.5		
	200	250	410	580	840
E (GPa)	211 ± 13	215 ± 17	208 ± 28	173 ± 18	189 ± 26
$\varepsilon_{fracture}$ (%)	0.16 ± 0.01	0.18 ± 0.02	0.18 ± 0.01	0.19 ± 0.02	0.18 ± 0.03
$\sigma_{fracture}$ (MPa)	360 ± 29	373 ± 22	385 ± 46	316 ± 33	306 ± 39
			SPS2		
	200	250	410	580	840
E (GPa)	208 ± 23	185 ± 14	178 ± 11	136 ± 9	141 ± 15
$\varepsilon_{fracture}$ (%)	0.17 ± 0.02	0.17 ± 0.02	0.19 ± 0.01	0.20 ± 0.03	0.23 ± 0.01
$\sigma_{fracture}$ (MPa)	350 ± 41	323 ± 28	346 ± 18	283 ± 48	286 ± 30

Source: Author.

E: Young's modulus; $\varepsilon_{fracture}$: fracture strain; $\varepsilon_{non\text{-}linear}$: non-linear strain; $\sigma_{fracture}$: fracture stress; ε_{yield}: yield strain; σ_{yield}: yield stress.

Influence of the composition and sintering method

Regarding the Young's modulus (depicted in Fig. 51(a)), no significant differences were observed between the evaluated groups when using the 200 μm printing nozzle. However, when the 250 μm nozzle was used, the SPS-ATZ group exhibited the highest Young's modulus, while the remaining groups showed no significant differences between them. When utilizing the 410 μm nozzle, both the CS-ATZ and SPS-ATZ groups demonstrated higher Young's modulus values compared to the SPS2 group, with the highest mean value belonging to the SPS-ATZ group. Similar trends were observed with the 580 and 840 μm nozzles, respectively, with the SPS0.5 group also exhibiting a higher Young's modulus than the SPS2 group. In summary, the SPS-ATZ group consistently displayed the highest Young's modulus values, while the SPS2 group exhibited the lowest values, with a noticeable tendency of reduction in the Young's modulus with the addition of CNFs.

Upon analyzing the filaments obtained using 200 and 250 μm nozzles, it was evident that both the CS-ATZ and SPS-ATZ groups exhibited higher fracture stress/flexural strength values compared to the SPS0.5 or SPS2 groups (Fig. 51(b)). This observation supports the

expectation that the agglomeration of CNFs indeed impairs flexural strength. The same trend was observed for filaments printed with 410 µm nozzles, with the additional finding of a significant difference between the CS-ATZ and SPS-ATZ groups, where the former displayed higher fracture stress. In the case of filaments produced using 580 or 840 µm nozzles, the CS-ATZ group demonstrated higher fracture stresses compared to all other groups. In summary, the agglomeration of CNFs negatively affected flexural strength across all nozzle diameters. Notably, with larger nozzles (580 and 840 µm), ATZ filaments sintered via SPS exhibited lower flexural strength than those sintered using CS.

When examining the fracture strain (depicted in Fig. 51(c)), the CS-ATZ group exhibited significantly higher fracture strains compared to the other groups. Indeed, only the CS-ATZ samples displayed inelastic deformation, while all other groups exhibited only elastic deformations (Fig. 50) as expected from most ceramics. Among these three groups, the SPS-ATZ group demonstrated a higher fracture strain when using the 200 µm printing nozzle, with no significant difference observed between the SPS0.5 and SPS2 groups. However, when using other printing nozzles, there were no significant differences among these three groups in terms of fracture strain.

Influence of the printing nozzle diameter

Regarding Young's modulus (Fig. 51(a)), the CS-ATZ group exhibited higher Young's modulus for filaments printed with 410 µm nozzles compared to those printed with 250, 580 or 840 µm nozzles. In the SPS-ATZ group, filaments printed with 250 µm nozzles had higher Young's modulus than those printed with 200, 580 or 840 µm nozzles. Within the SPS0.5 group, filaments printed with 200 or 250 µm nozzles displayed higher Young's modulus than those printed with 580 µm nozzles. In the meantime, in the SPS2 group, filaments printed with one of the three smaller nozzles (200, 250 or 410 µm) exhibited higher Young's modulus than those printed with 580 or 840 µm nozzles. In general, when sintered by SPS, the smaller nozzles produced filaments with higher Young's modulus. However, for filaments that underwent sintering by CS, there was no clear trend regarding the influence of nozzle diameter on Young's modulus.

In terms of the fracture stress (Fig. 51(b)), in the CS-ATZ group, filaments printed with 580 µm nozzles exhibited higher fracture stress compared to those printed with 250 µm nozzles. Within the SPS-ATZ group, filaments obtained with 200 or 250 µm nozzles displayed

higher flexural strength than those obtained with 840 µm nozzles. Notably, the fracture stress of filaments printed with 250 µm nozzles had a wide range of values in that group. On the other hand, no significant difference was observed when varying the nozzle diameter within the SPS0.5 and SPS2 groups. Overall, the only discernible trend was that for ATZ filaments sintered by SPS, in which smaller nozzles produced filaments with higher flexural strength.

Relative to the fracture strains (Fig. 51(c)), in the CS-ATZ group, the filaments printed with 250 µm nozzles exhibited greater deformation before fracture compared to those printed with 200 and 410 µm nozzles, while no significant differences were observed between the other nozzle diameters. Similarly, within the SPS-ATZ group, filaments printed with 200 µm nozzles showed higher deformation before fracture compared to those printed with 840 µm nozzles. On the other hand, no significant difference was observed within the SPS0.5 group. In the SPS2 group, the filaments printed with 840 µm nozzles displayed higher fracture strain than those printed with 200, 250 or 410 µm nozzles. Overall, there was no clear trend observed in terms of fracture strains when varying the printing nozzle diameter.

Inelastic deformation of the CS-ATZ filaments

As could be observed in Fig. 50, the CS-ATZ filaments undergo both elastic and inelastic deformations. The value of fracture strain ($\varepsilon_{fracture}$) of this group was around 1.2%. When the elastic component is removed, the non-linear strain value ($\varepsilon_{non\text{-}linear}$) is approximately 0.7-0.8%. It is noteworthy that the values of yield strain (ε_{yield}) for the CS-ATZ filaments (ranging from 0.22 to 0.35% on average) are close to the $\varepsilon_{fracture}$ values for the SPS-ATZ filaments (ranging from 0.20 to 0.24% on average, see Table 17). This deformation will be further investigated in section 3.3.3, particularly to determine whether it is plastic in nature or associated with the formation of microcracks.

3.3.2. Mechanical reliability – Weibull analysis

The reliability of the mechanical evaluations performed can be assessed via the Weibull modulus, which was calculated and is present in Fig. 52.

Fig. 52. Results of the Weibull analysis. ln(ln(1/(1-F)) vs. ln(σ_f) for different nozzle diameters in the groups (a) CS-ATZ, (b) SPS-ATZ, (c) SPS0.5 and (d) SPS2. (e) Weibull modulus of the four groups by the nozzle diameter utilized in the printing process.

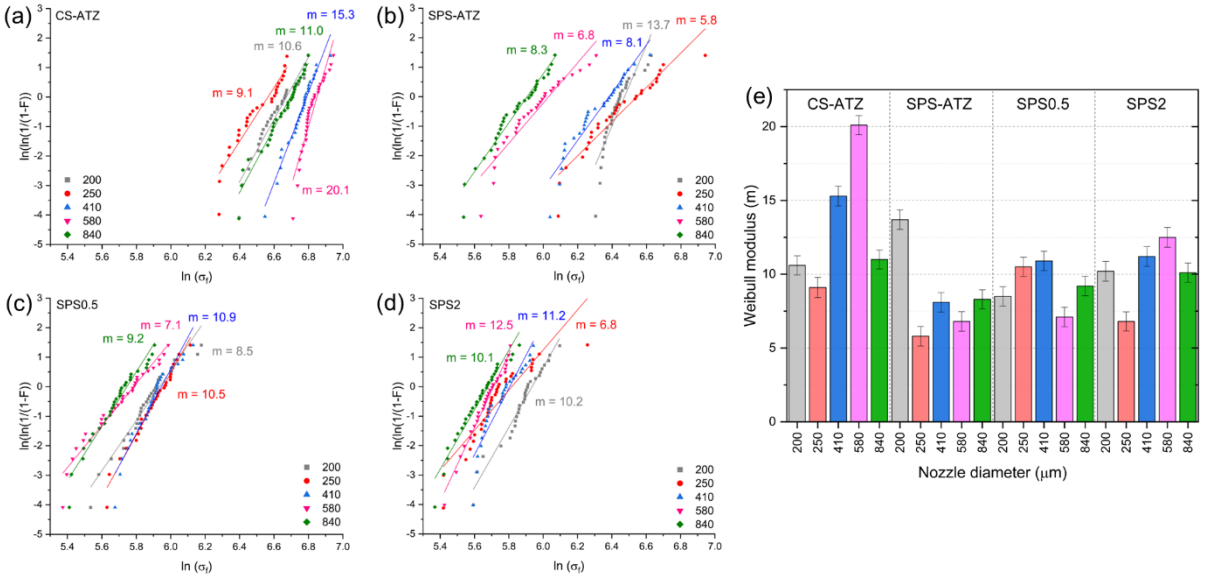

Source: Author.

In terms of individual values, the lowest Weibull modulus recorded was 5.8, observed in the SPS-ATZ filaments printed with 250 μm nozzles. On the other hand, the highest Weibull modulus observed was 20.1, which was associated with CS-ATZ filaments printed using 580 μm nozzles. The majority of Weibull moduli found stay between 8 to 11 – values that underline the good mechanical reliability of the printed filaments. Similar to the previous sections, the influence of composition, sintering approach and printing nozzle diameter on the reliability of the mechanical evaluations can be analyzed.

Influence of the composition and sintering approach

For the filaments printed with 200 μm nozzles, the SPS-ATZ group had the highest Weibull modulus, followed by CS-ATZ and SPS2 (with no significant difference between these two) and SPS0.5. Analyzing the filaments obtained with 250 μm nozzles, the group SPS0.5 had the highest Weibull modulus with CS-ATZ, SPS2 and SPS-ATZ in the sequence, with no significant difference between the last two. Considering the filaments printed with the other nozzle diameters, they all presented the same group sequence in terms of Weibull modulus: CS-ATZ > SPS2 > SPS0.5 > SPS-ATZ. Some particularities include that, for the 410 μm nozzles, there was no significant difference between the groups SPS2 and SPS0.5, for the 580 μm

nozzles, the same happened between the groups SPS0.5 and SPS-ATZ, whereas, for the 840 µm nozzles, that occurred between the groups CS-ATZ, SPS2 and SPS0.5.

In summary, the CS-ATZ group was associated with higher Weibull moduli, indicating greater mechanical reliability, while the SPS-ATZ group exhibited lower Weibull moduli, indicating relatively lower mechanical reliability.

Influence of the printing nozzle diameter

In the CS-ATZ group, the highest Weibull modulus was achieved with 580 µm nozzles, followed by 410, 840, 200 (no significant difference between the last two) and 250 µm. In the meantime, in the SPS-ATZ group, the filaments printed with 200 µm nozzles had the highest value of Weibull modulus, with 840 and 410 µm in the sequence (no significant difference between these two) and 580 and 250 µm (also without significant difference between them). Within the SPS0.5 group, the sequence was 410 > 250 > 840 > 200 > 580 µm. There were no significant differences between the nozzles 410 and 250 µm and between 840 and 20 µm. In the last group, SPS2, the 580 µm nozzles generated the filaments with the highest Weibull modulus with 410, 200 and 840 µm in the sequence (no significant difference between these three) followed by 250 µm nozzles.

To summarize, it is important to highlight the main trend observed: the 250 µm nozzles exhibited the lowest mechanical reliability in three out of the four groups. However, this trend does not apply to the only nozzle diameter smaller than 250 µm (200 µm).

3.3.3. Transformation-induced plasticity (TRIP)

Based on the observations made on the flexural curves of the CS-ATZ filaments, it was decided to conduct cyclic three-point flexion at regular intervals, taking into account the maximum force that could be applied to these filaments. The force *vs.* displacement curves for the filaments printed with 410 and 840 µm are presented in Fig. 53, along with the calculated slopes for the descending portion of each cycle. Additionally, a photograph of the filaments before and after this test is shown in Fig. 54.

Fig. 53. Force *vs.* displacement for CS-ATZ filaments printed with nozzle diameters of (a) 410 and (b) 840 µm that underwent cycles of deformation.

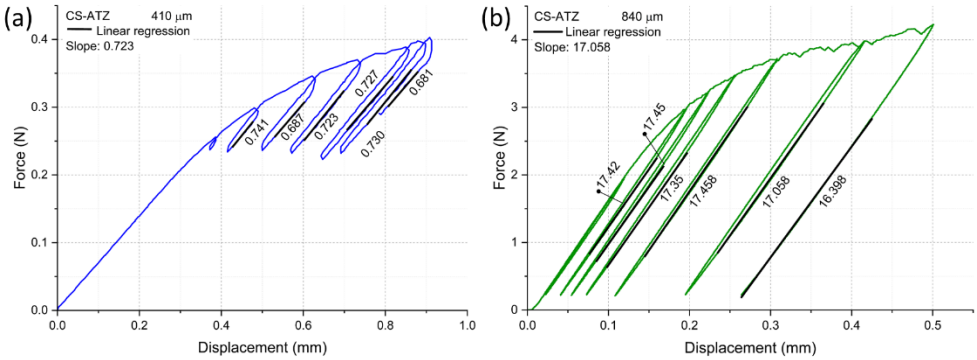

Source: Author.

Fig. 54. Photograph of a CS-ATZ filament that had been printed with a 410 µm nozzle before and after undergoing cycles of deformation. It is possible to observe the expressive inelastic deformation presented by the CS-ATZ filaments after 3PB and before fracture.

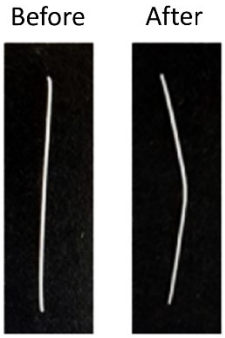

Source: Author.

Based on the findings shown in Fig. 53, it can be observed that there was a minimal reduction in Young's modulus (slope) between the cycles, with only a slight decrease occurring just before filament fracture. This suggests that the phenomenon of microcracking did not occur within the filaments before the last cycle. Similarly, flexural cycles were conducted with a constant applied load (Fig. 55), just below the fracture load. Throughout these cycles, minimal changes in slope were observed. There was a slight hysteresis between the load descent and ascent and the filaments exhibited a slight shift in the cycles as they progressed.

Fig. 55. Force vs. displacement for CS-ATZ filaments printed with nozzle diameters of 410 µm that underwent cycles with a constant applied load.

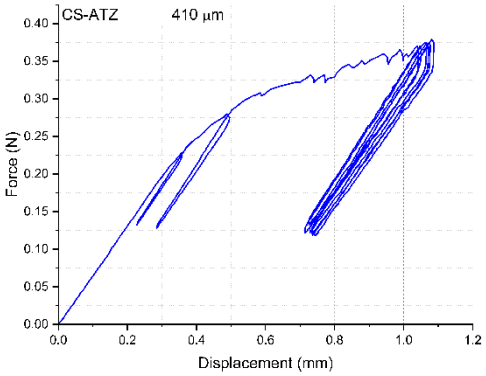

Source: Author.

Microstructural evaluations were also conducted on the surfaces of highly deformed filaments (Fig. 56). In Fig. 56(a), the surface near the edge of a filament printed with a 200 µm nozzle is depicted. This region, which remains undistorted, reveals the presence of large zirconia grains (indicated by blue arrows), small alumina grains (yellow arrows) and strontium aluminate platelets (purple arrows). Moving to Fig. 56(b), which represents the center of that filament (zone submitted to highest stress), fine circular streaks can be observed on the zirconia grains (highlighted in green). These streaks correspond to the crystalline growth of the grains during the sintering process. Additionally, twinning is visible (highlighted in red), which is a sure sign that the t-m transformation took place in these grains [405].

Fig. 56. SEM images of highly deformed CS-ATZ filaments. Filament printed with a 200 µm nozzle (a) at the edge of the filament (unloaded zone) and (b) at the center of the filament (zone of maximum tensile stress). (c) Filament printed with a 580 µm nozzle deformed until right before fracture and (d) deformed by cycles of different forces. (e) Filament printed with a 410 µm nozzle deformed by cycles of the same force.

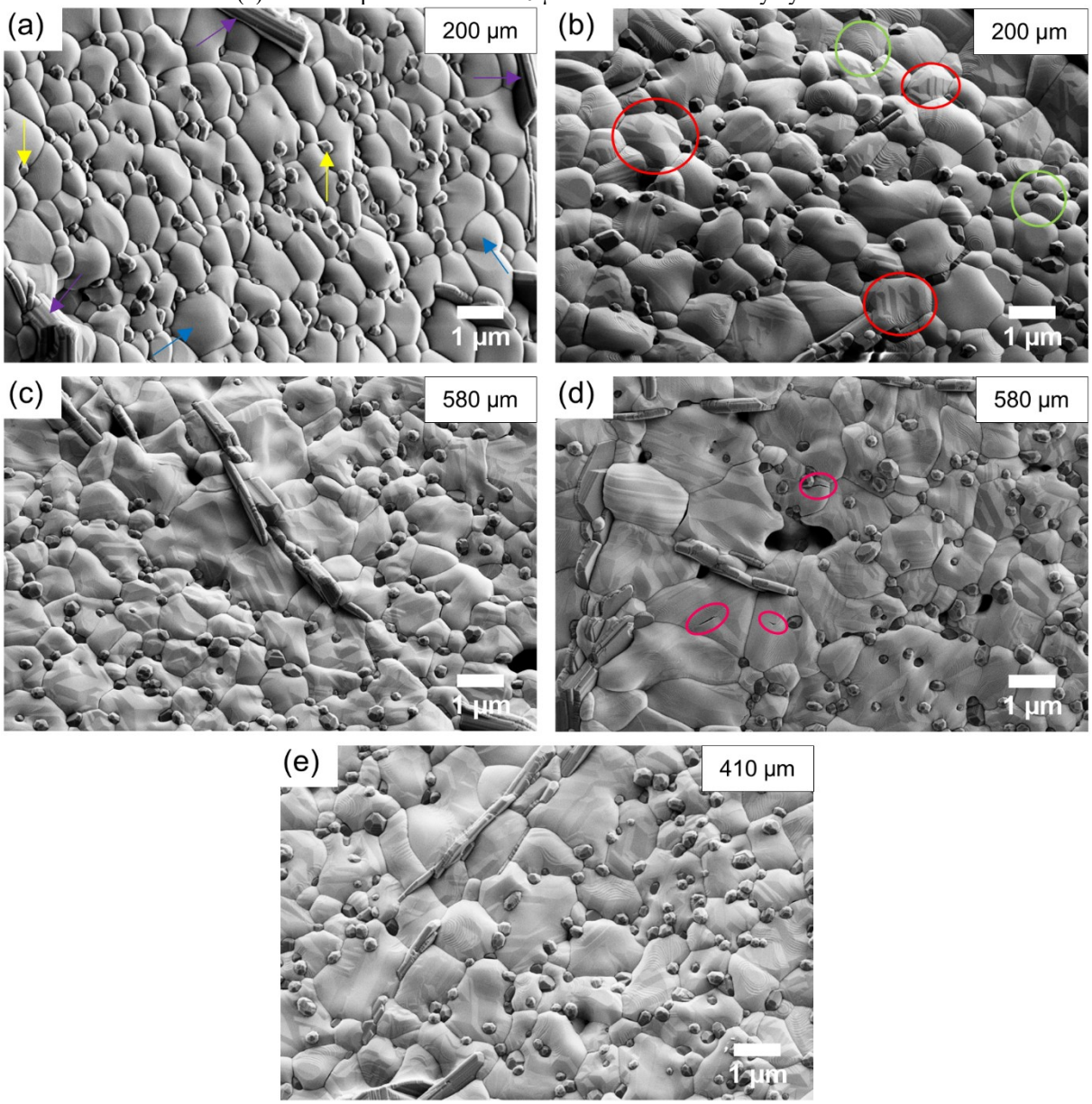

Source: Author.

Fig. 56 (c) and (d) display the surface of a filament printed with a larger diameter (580 µm). Larger zirconia grains were visible surrounding the strontium aluminate platelets, exhibiting a distinct pattern compared to the rest of the material. Additionally, the alumina grains tended to cluster in areas away from the strontium aluminate platelets. The images also revealed the presence of a few pores. Particularly in Fig. 56(d), a few microcracks could be observed, highlighted in pink.

The microstructure of a filament printed with a 410 μm nozzle, which underwent flexural cycles with a constant identical imposed load (mechanically evaluated in Fig. 55), was also examined. The microstructure is depicted in Fig. 56(e). In this image, there was no indicative of an increased presence of microcracks specifically. However, it appeared that the entire material had undergone some t-m transformation. Overall, no significant noticeable differences were observed compared to the other samples.

4. DISCUSSION

Over the past few years, there has been rapid growth in Additive Manufacturing (AM) techniques due to their ability to ease the production of intricate shapes and potentially streamline the manufacturing process. However, the application of AM in ceramics poses several challenges. Unlike metals, ceramics are more susceptible to defects caused during processing, making the AM process less forgiving. Moreover, current AM methods for ceramics often yield larger material defects compared to other established industrial technologies [181]. In the DIW method, increasing the mechanical reliability of the ceramic components obtained has been a challenge.

This study aimed to enhance the mechanical properties and reliability of alumina-toughened zirconia (ATZ) composites. This was pursued through careful debinding and sintering processes, alongside the intended carbon nanofiber (CNF) orientation within the composite.

Debinding optimization

Multiple approaches exist to create an aqueous paste with optimal rheology for DIW to obtain a ceramic component. Frequently, organic additives are incorporated into the pastes to facilitate the preservation of the printed geometry through polymer chain bridging [71,358,365], an incorporation that requires a post-printing debinding step. Still, some studies avoid the debinding process by reducing the volume of organics in the paste composition [69,406–408]. In this study, in addition to the ATZ powder and CNFs, a deflocculant (Darvan® 821-A), a binder (Pluronic® F-127) and deionized water composed the printing paste. Hence, as our study utilized an organic additive (Pluronic), after drying, a debinding study was performed by TGA analyses defining the temperature of 400 °C with a 30 min plateau as the

best condition to remove the Pluronic from the dried printed material. After this process, a minimal quantity of organic materials (estimated at around 1%) remained in the printed samples. This quantity is likely to exit the filaments without causing defects on its way out.

Challenges of CNF addition

When incorporating carbon nanofibers (CNFs) into a ceramic matrix, three primary challenges need to be addressed: achieving a homogeneous dispersion, achieving proper orientation (if desired, as in the case of this study) and ensuring sintering without inducing thermal degradation of the CNFs. In the following paragraphs, we will discuss each of these challenges.

Homogeneous dispersion of CNFs

Achieving proper dispersion of CNFs within a material presents a significant challenge, as their near-perfect nanostructure makes it very difficult to disperse them into both organic and inorganic materials [202]. In the literature, various strategies have been employed to enhance the dispersion of CNFs and also carbon nanotubes (CNTs) [409], including molecular level mixing, hydrothermal synthesis, ultrasonication [410,411], sol-gel synthesis, use of deflocculants or surfactants [412–414], ball milling and high-speed mixing methods [415,416]. Overall, the CNFs' dispersion is limited by their weight fraction and this limit varies with the dispersion process [409]. In this study, a deflocculant (Darvan® 821-A) was utilized, along with a high-speed mixing technique. Nevertheless, these measures were proven insufficient to deagglomerate the CNFs. For the sequence of the study, it is necessary to explore alternative deflocculants that are more suitable and to improve the deflocculation procedure to achieve better results.

Proper orientation of the CNFs

Direct Ink Writing (DIW) is an additive manufacturing technique that enables the fabrication of intricate three-dimensional structures. It has emerged as a promising method for producing anisotropic materials containing highly oriented phases or particles with high aspect ratios. The orientation behavior observed in DIW aligns with Jeffery's Obit theory [417] and

the Folgar-Tucker equation [397], which propose that non-equiaxed particles tend to rotate and align themselves parallel to the shear direction under shear stresses.

In that regard, Lu *et al.* [346] conducted an exemplary study in which highly oriented carbon fiber-reinforced SiC composites were produced using DIW and analyzed using SEM and X-ray Diffraction (XRD). The researchers observed that the distribution of additions, in this case, fibers, within the extruded filament was not uniform. The fiber orientation and arrangement were more pronounced and denser closer to the nozzle wall, while the middle region exhibited a less orderly and sparser arrangement. This gradient distribution from the filament's center to the wall was attributed to the non-uniform shear rate distribution during extrusion [398]. The distribution patterns differed between Newtonian and non-Newtonian fluids. In the case of Newtonian fluids, there was a linear increase in shear rate from the middle to the edge of the nozzle. On the other hand, non-Newtonian fluids displayed a non-linear shear rate distribution, with a practically shear-free zone (referred to as the "0" shear rate area) in the center of the nozzle. The width of this "0" shear rate area increased with larger nozzle diameters. In their study, the "0" shear rate area nearly vanished when the nozzle diameter was reduced to 500 µm, indicating that with nozzle diameters smaller than 500 µm, the fibers throughout the entire nozzle area experienced shear stresses and tended to align parallel to the shear direction. Therefore, the potential for orientation in DIW relies on optimizing a balanced combination of factors, which can be summarized as follows [346,397]:

- Particle shape (length/diameter ratio): Higher aspect ratios enhance orientation potential.
- Interaction between particles (solid content): Optimization is required to prevent interference among particles (referred to as the "bridging" effect), avoid nozzle blockage due to excessive particle content, and maintain the desired reinforcement effect.
- Shear rate controlled by nozzle diameter: Decreasing the diameter increases the shear rate. Finding the optimal diameter is crucial to ensure sufficient shear stress and orientation throughout the entire nozzle area, as well as achieve desired finishing aspects of the printed component.
- Shear time controlled by nozzle length: Increasing the nozzle length prolongs the shear time and can be adjusted in combination with other parameters to achieve proper orientation.

In this study, when considering the particle shape, the added CNFs possess a high aspect ratio (from 150 to 1000.) and, therefore, a good orientation potential, as corroborated by other studies that have reported the orientation of CNFs with DIW [346,396,400]. The solid content utilized (30 vol%) was optimized in Chapter 2 and was found to be far from the maximum solid content of the system of the studied paste (47 vol%). The shear time was not varied in this study, but the studies that did achieve CNF orientation utilized the same nozzle length as this study (31 mm) [400] or bigger (50 mm) [346]. The focus of this paper was the variation of the nozzle diameter, ranging from 840 to 200 μm. The latter is estimated by Eq. (1) to induce a considerable shear rate of approximately 400 s^{-1}. Other studies reporting CNF orientation utilized nozzles of a diameter of 500 μm [346], 250, 400 or 610 μm [396] and even 1250 μm [400]. Therefore, it is expected that the diameters employed in this study would also lead to CNF orientation. Nevertheless, no orientation of the CNFs was observed in this study. The primary obstacle in achieving orientation was likely the agglomeration of CNFs, which, once agglomerated, do not experience the same shear forces as individual, deagglomerated CNFs would. The studies that have reported CNF orientation utilized a quantity of 3-15 vol% [396] or even 23 wt% [346] – in this study, the quantities were much lower: 1.34 vol% (equivalent to 0.5 wt%) or 5.23 vol% (2.0 wt%). Hence, the quantity of CNFs is unlikely to be the main issue. The aspect that requires optimization is the deflocculation process.

Sintering with CNFs

After removing the water by drying and the Pluronic by debinding, the printed structure was left with the ATZ particles, which required a sintering process to achieve an adequate level of density. This achieved level of density largely influences the mechanical properties of ceramics, highlighting the importance of the sintering approach and parameters utilized. However, incorporating the CNFs adds a challenge to this process.

Traditional sintering methods for carbon nanofiber-ceramic composites involve the use of high temperatures over prolonged periods [418]. However, such prolonged exposure to high temperatures can lead to damage or destruction of the CNFs, significantly diminishing their reinforcement effect [419]. Previous studies have demonstrated that composites containing a carbon-phase content below 1.5 wt% can be sintered with ceramics (e.g., CNT-alumina) using an air atmosphere furnace, provided an appropriate anti-oxidation sagger (protective fireclay box) and carbon black packing powder [420]. Nevertheless, although there were no significant

differences observed in terms of microstructure, composites sintered using Spark Plasma Sintering (SPS) techniques exhibited higher hardness and toughness compared to those sintered in air furnaces [420]. Apart from the temperature issue, sintering carbon-based phases and oxide ceramic phases together poses challenges, as it necessitates a low-oxygen sintering atmosphere to prevent carbon oxidation, which can potentially degrade the oxide ceramics [421]. Other studies that have used carbon nanofibers as reinforcement performed sintering by hot pressing (1300 °C, 40 MPa [422]; 1300 °C 41 MPa [402], both in argon with 3Y-TZP matrix material) or SPS (60 MPa, 1400 or 1500 °C) [402]. None of them reported degradation of the CNFs.

To overcome these challenges and retain the integrity of CNF structures while achieving sintering at lower temperatures or shorter durations, the Spark Plasma Sintering (SPS) process was employed in this study. In this process, a pulsed-electric-current passes through a graphitic mold and the sample under vacuum, resulting in a heating rate of approximately 300 °C/min (100 °C/min in this specific study). This rapid heating rate achieved through SPS enables quick completion of the sintering process while minimizing damage to the CNFs. Of the tested approaches, the SPS method was the only one that allowed the preservation of the CNFs, as has been observed in Fig. 49, in which their integrity after the SPS process was attested. Furthermore, the addition of CNFs did not present any distinct trend in the sintering procedure, despite the literature suggesting that they could hinder the sintering process by pinning off the grain boundaries [423] or facilitate it by lowering the activation energy, as has been reported with carbon nanotubes in a zirconia matrix [424].

To determine the influence of sintering with the SPS method, conventional sintering (CS) was performed to serve as a control group. The sintering temperatures for both sintering approaches were optimized by density evaluations and microstructural evaluations assessing the overall aspect and grain sizes. In terms of the latter, smaller grain sizes are desirable to achieve higher strength and improved mechanical properties [374] – the grain size has also been reported to be closely related to the wear resistance of Y-TZP and alumina materials [425]. The fracture strength of sintered components containing less than 10 mol% CeO_2 has also been shown to be strongly dependent on grain-size [426]. Although the ATZ powder utilized in this study had 11 mol%, special attention was given to selecting a sintering temperature that maximized the density and minimized the grain size. The results found indicated that the higher the sintering temperature, the higher the grain size, a fact that has been reported by other studies [68,426]. In the CS approach, the optimum sintering temperature of the ATZ filaments was

1500 °C, whereas, in the case of SPS, a temperature of 1400 °C was selected for sintering filaments with and without CNFs.

Comparative of mechanical properties

A schematic illustration of the influence of CNF content, nozzle diameter and sintering method on the mechanical properties evaluated in this study is displayed in Fig. 57.

Fig. 57. Schematic illustration of the influence of CNF content, nozzle diameter and sintering method on the mechanical properties of the printed filaments. The values obtained from the correlation and regression analyses such as the chance of true relationship (CTR) and p-value are also shown.

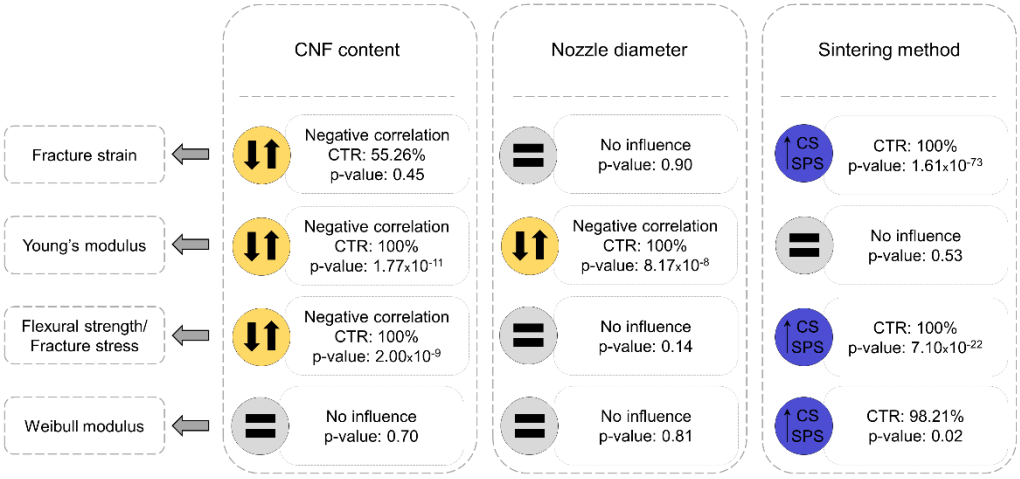

Source: Author.

Considering the fracture strain, the correlation and regression analyses showed that there was no influence of the printing nozzle diameter on the fracture strain values (p-value: 0.90). Furthermore, with increasing CNF content, the fracture strain values tended to decrease (p-value: 0.45). In the meantime, samples sintered with the CS method tended to have higher fracture strain (p-value: 1.16×10^{-73}). Regarding the Young's modulus, there was no influence of the sintering method on the Young's modulus values (p-value: 0.53). Also, as CNF content increased, the Young's modulus values tended to decrease (p-value: 1.77×10^{-11}). Still, the Young's modulus values tended to increase with decreasing nozzle diameter (p-value: 8.17×10^{-8}).

In terms of flexural strength/fracture stress values, there was no influence of the nozzle diameter (p-value: 0.14). Similarly to the previous mechanical properties, increasing CNF content tended to decrease the flexural strength (p-value: 2×10^{-9}) whereas the CS method tended to increase it (p-value: 7.10×10^{-22}). When the Weibull modulus was considered, there

was no influence of the CNF content (p-value: 0.70) or of the nozzle diameter (p-value: 0.81). However, samples sintered by CS tended to have a higher Weibull modulus (p-value: 0.02).

The decrease in fracture stress and Young's modulus as the CNF content increases was probably connected to the agglomeration of CNFs within the samples. Additionally, the reduction in fracture strain can be attributed to the fact that this property is a balance between the two properties mentioned earlier.

One would expect that reducing the nozzle diameter would lead to an increase in fracture stress due to a size-effect – smaller nozzles produce filaments with reduced volume and, therefore, with a decreased likelihood of defects. Surprisingly, this anticipated trend was not observed. Conversely, smaller nozzle diameters tended to yield filaments with higher Young's modulus, indicating greater stiffness. This outcome likely originated from higher density values of filaments printed using smaller nozzles. When subjected to the same sintering conditions, a sample with less volume would experience more significant densification compared to one with more volume. However, it's important to note that there were no density measurements conducted while varying the nozzle diameter to validate this hypothesis.

The superiority of conventionally sintered samples compared to those subjected to Spark Plasma Sintering (SPS) in terms of fracture strain, fracture stress and Weibull modulus can be attributed to the occurrence of transformation-induced plasticity (TRIP). This phenomenon occurred within the conventionally sintered (CS) samples through t-m transformations, resulting in inelastic deformation. On the other hand, it is hypothesized that the mechanical properties of the SPS samples were hindered due to the presence of a reducing atmosphere within the SPS furnace (primary vacuum). This atmosphere can lead to the creation of oxygen vacancies within the ATZ, reducing the oxides present and thereby hindering the mechanical properties in the SPS-treated samples (as a consequence, the TRIP effect is also unachievable). Usually, the SPS method is utilized with the application of pressure [402], nevertheless, in this study, this was not desirable due to the delicate nature of the printed filaments that would break even under the minimal pressure applied by the SPS (3 N). Hence, a “mini furnace” was created within the SPS equipment to avoid pressure application as depicted by Fig. 42. The filaments were, therefore, exposed to the atmosphere of the furnace, which was unfortunately deleterious to them.

To facilitate comparison with existing literature, Table 18 provides an overview of the processing and sintering methods, as well as the key mechanical properties reported for various

materials, including zirconia and ATZ composites, as well as, the materials produced in this study.

Table 18. Comparison of the processing methods and properties of different ceramics obtained either by traditional ceramic processing methods or DIW, including the results found in this study.

Material	Processing method	Sintering method and temperature	Density (%)	Grain size (μm)	Young's modulus (GPa)	Flexural strength (MPa)	Testing methodology	Weibull modulus	Sample size (mm)	Number of samples	Ref.
3Y-TZP	CIP	CS; 1475 °C 2h	99.5	0.29	203	945 ± 105	3PB	-	3 × 4 × 40	6	[427]
12Ce-TZP	CIP	CS; 1550 °C 2h	-	3.49	-	273 ± 6	4PB	-	3 × 4 × 45	-	[428]
7-16Ce-TZP	CIP	CS; 1400-1600 °C 2h	99	0.5-2.5	-	350-800	3PB	-	3 × 4 × 4	-	[426]
ZTA	DIW	CS; 1570 °C 6h	97.5-99	0.84-1.31	-	422.5	3PB	-	-	-	[429]
ATZ (Y-TZP/Al_2O_3) 80:20%*	CIP	HIP; 1450 °C 2h 1200 bar	>99.5	0.4	-	793-1163	Biaxial bending	7.3-16.5	Ø36 × 2	30	[430]
ATZ (3Y-TZP/Al_2O_3) 80:20 wt%	DIW	CS; 1600 °C 2h	97.3-98.1	Z:0.63-0.9; A:0.62-0.76	-	530-611	P-3B	4.7-5.1	Ø20 × 5	25	[431]
ATZ (10Ce-TZP/Al_2O_3) 70:30 vol%	CIP	CS; 1440 °C 4h	-	0.25 for both	269	1000	4PB	12.6	4 × 6 × 50	10-20	[432]
ATZ (10Ce-TZP/Al_2O_3) 70:30 vol%	CIP	CS; 1440 °C 4h	-	0.59	247	941 ± 34	3PB	-	3 × 4 × 40	6	[427]
ATZ (10Ce-TZP/Al_2O_3) 70:30 vol%	CIP	CS; 1450 °C 2h	-	Z: 1; A: 0.01-0.1	-	950	4PB	-	-	-	[433]
ATZ (12Ce-TZP/Al_2O_3) 90:10 wt%	CIP	CS; 1550 °C 2h	-	2.49	-	632 ± 34	4PB	-	3 × 4 × 45	-	[428]
ATZ (10-11.5Ce-TZP/Al_2O_3/$SrAl_{12}O_{19}$) 84:8:8 vol%	SC	CS; 1450 °C 1h	99.9	Z: 0.6 ± 0.2; A: 0.3 ± 0.1	216	680-1100	Biaxial bending	60	Ø12-15 × 1.2	10	[385]
ATZ (11Ce-TZP/Al_2O_3/$SrAl_{12}O_{19}$) 84:8:8 vol%	DIW	CS; 1350 °C 1h	86	-	-	850 ± 22	Biaxial bending (P-3B)	-	Ø12 × 1.5	8	[181]
ATZ (11Ce-TZP/Al_2O_3/$SrAl_{12}O_{19}$) 84:8:8 vol%	DIW	CS; 1500 °C 1h	98.04 ± 2	Z: 0.76 ± 0.3; A: 0.22 ± 0.06	172.5-244.2	585.6-1113.2	3PB	9.1-20.1	ØVarying × 25	30	This study
ATZ (11Ce-TZP/Al_2O_3/$SrAl_{12}O_{19}$) 84:8:8 vol%	DIW	SPS; 1400 °C 1h	98.08 ± 2	Z: 0.79 ± 0.5; A: 0.20 ± 0.07	151.3-304.9	296.6-779.4	3PB	5.8-13.7	ØVarying × 25	30	This study

Source: Author.

ZTA: zirconia-toughened alumina; CIP: cold isostatic pressing; DIW: direct ink writing; SC: slip casting; HIP: hot isostatic pressing; CS: conventional sintering; Z: zirconia; A: alumina: 3PB: 3-point bending; 4PB: 4-point bending; P-3B: piston-on-three balls. Asterisk (*) indicates a value that was not disclosed if wt% or vol%.

Comparing the Young's modulus, the values found in this study are in the same range or higher than those obtained for ATZ (10Ce-TZP/Al_2O_3) via cold isostatic pressing [427,432] and ATZ (10-11.5Ce-TZP/Al_2O_3/$SrAl_{12}O_{19}$) via slip casting [385]. Regarding flexural strength, high values were found in this study. These were in the same range or higher than flexural strength values of all the studies in Table 18 regardless of the processing method (DIW, CIP or SC) and also in comparison to same-composition-ATZ obtained both by slip casting [385] and DIW in previous studies [181].

Finally, the main issue that has been found in most components printed via DIW is the lack of mechanical reliability, which can be translated into low Weibull modulus. The Weibull modulus is a measure of the material's reliability and its value can vary based on the inherent properties of the material, the testing methodology employed and the intended use of the ceramic in practical applications [434]. In general, high Weibull modulus values above 10 or even 20 are considered to indicate good mechanical reliability and strength in ceramics [434]. Usually, the Weibull moduli obtained from ceramics produced through additive manufacturing are lower than those obtained by conventional ceramic processing methods. Indeed, DIW leads to a wider distribution of defects and consequently lower robustness compared to more established ceramic technologies [67,345]. That would raise concerns for structural applications that demand minimal risk of failure. Still, the results found in this study show that a good level of mechanical reliability is achievable by DIW. The obtained values of Weibull modulus were found to be higher than DIW-produced ATZ (3Y-TZP/Al_2O_3) [431], as well as ATZ obtained by CIP (Y-TZP/Al_2O_3 [430] and 10Ce-TZP/Al_2O_3 [432]). The Weibull moduli found were only lower than those of the same composition ATZ obtained by slip casting (m=60, number of samples=23) [385].

The good Weibull moduli found indicate a lower sensitivity to the presence of defects, which has been attributed to the exceptional toughness imparted by the TRIP effect [432]. This, alongside the other good mechanical properties observed of the ductile Ce-TZP-based composites, demonstrates encouraging potential for DIW of these ceramic materials. However, it is important to note that this study focused on evaluating individual filaments. Printing a complete piece/component introduces greater complexity, as factors like inter-filament distance must be carefully considered in both the x-y plane and the z-direction. Making incorrect choices regarding these parameters may result in porosity, which could hinder the mechanical properties of the final component.

5. CONCLUSIONS

Filaments of an ATZ composite (84 vol% Ce-TZP, 8% Al_2O_3, 8% $SrAl_{12}O_{19}$) with and without carbon nanofibers (CNFs) were fabricated using Direct Ink Writing (DIW), an additive manufacturing method. The objective was to enhance the mechanical properties of these composites through careful debinding and sintering processes, as well as the orientation of CNFs induced by the shear rate associated with the printing nozzles. The nozzle diameter was varied in the range of 200 to 840 μm. Optimal debinding and sintering conditions were determined, utilizing both Conventional Sintering (CS) and Spark Plasma Sintering (SPS) methods. Evaluation of the filaments included mechanical properties such as fracture stress/flexural strength, fracture strain, Young's modulus and mechanical reliability determined by the Weibull modulus.

The addition of the CNFs, which was expected to improve the mechanical properties, had an adverse effect in this study. The negative impact can be attributed to the agglomeration of CNFs, highlighting the need to explore alternative deflocculants and improve the deflocculation procedure for better results. Theoretically, smaller nozzle diameters should promote more uniform fiber alignment and orientation throughout the filament in the longitudinal direction. However, this phenomenon was not observed due to the poor dispersion of CNFs. Nevertheless, printing with smaller nozzles showed improvements in the Young's modulus. Conventionally sintered ATZ samples exhibited transformation-induced plasticity, while those sintered by SPS did not, a fact that led to CS samples presenting higher fracture strains, flexural strengths and Weibull moduli.

The mechanical properties obtained were comparable to or higher than those achieved through conventional ceramic processing techniques like cold isostatic pressing and slip casting. Similarly, mechanical reliability, which is often a concern with DIW, was also satisfactory. Overall, these results demonstrate the promising potential of DIW for ceramic materials, especially ductile Ce-TZP-based composites.

GENERAL CONCLUSION AND PERSPECTIVES

Direct ink writing is an expanding additive manufacturing technique for ceramic-based components with complex structures. The DIW technique has encouraging benefits, nevertheless, some limitations remain. The main ones include the surface finish and the attainment of densities (in the case of dense components) and also mechanical reliability in the range of traditional processing ceramic techniques. The objective of this thesis was to improve these points by a comprehensive study of the rheology of pastes with focus on their printability – what helps in the obtention of pastes that are printable even with smaller nozzles enhancing surface finish – and also of the optimization of the debinding and sintering conditions (density improvement) as well as of the mechanical properties by the incorporation of oriented carbon nanofibers.

As we could observe, the printability criteria outlined in the literature (particularly ϕ, K and FTI) provide a valid approach for predicting the printability of a paste, although presenting some limitations. Furthermore, a new criterion based on the recovery rate of the storage modulus was presented, with the potential to predict printability with a single three-interval test, facilitating the achievement of printable pastes for DIW. Given the vastitude and complexity of the rheology field, even minor deviations in testing conditions can exert a substantial influence on the outcomes obtained rendering challenging the interpretation of results. Thus, the employment of printability criteria that expressly define the essential properties to be assessed could benefit both experienced researchers and newcomers entering the field of direct ink writing. This not only facilitates the creation of enhanced printable pastes but also lays the groundwork for progressively advanced formulations, enabling the fabrication of structures characterized by escalating intricacy.

The addition of the CNFs, which was expected to improve the mechanical properties, had an adverse effect, which was attributed to the agglomeration of CNFs. This highlights the need to explore alternative deflocculants and improve the deflocculation procedure for better results in future studies. In addition, the sintering method of components with CNFs needs to be improved since it was likely reducing the oxides of the ceramic. These points, once optimized, could increase the mechanical properties of the ATZ samples that already benefit from the transformation-induced plasticity that led to higher fracture strains, flexural strengths and Weibull moduli.

Although seeming to be close to its limits, the DIW technique was proven capable of obtaining mechanical properties comparable to or higher than those achieved through conventional ceramic processing techniques like cold isostatic pressing and slip casting. Similarly, mechanical reliability, which is often a concern with DIW, was also satisfactory. The limitations of the study here conducted need to be taken into consideration, as complexity increases when working with structured components rather than individual filaments, nevertheless, the results demonstrate a promising potential of DIW for ceramic materials, especially ductile Ce-TZP-based composites.

REFERENCES

[1] S. Vinodh, G. Sundararaj, S.R. Devadasan, D. Kuttalingam, D. Rajanayagam, Agility through rapid prototyping technology in a manufacturing environment using a 3D printer, Journal of Manufacturing Technology Management. 20 (2009) 1023–1041. https://doi.org/10.1108/17410380910984267.

[2] D. Tang, R.S. Tare, L.-Y. Yang, D.F. Williams, K.-L. Ou, R.O.C. Oreffo, Biofabrication of bone tissue: approaches, challenges and translation for bone regeneration, Biomaterials. 83 (2016) 363–382. https://doi.org/10.1016/j.biomaterials.2016.01.024.

[3] I. Schwartz, B. Robinson, J. Hollinger, E. Szachowicz, J. Brekke, Calvarial bone repair with porous D,L-polylactide, Otolaryngology - Head and Neck Surgery. 112 (1995) 707–713. https://doi.org/10.1016/S0194-5998(95)70180-X.

[4] R. Galante, C.G. Figueiredo-Pina, A.P. Serro, Additive manufacturing of ceramics for dental applications: A review, Dental Materials. 35 (2019) 825–846. https://doi.org/10.1016/j.dental.2019.02.026.

[5] J. Akmal, M. Salmi, A. Mäkitie, R. Björkstrand, J. Partanen, Implementation of industrial additive manufacturing: Intelligent implants and drug delivery systems, J Funct Biomater. 9 (2018) 41. https://doi.org/10.3390/jfb9030041.

[6] S. Derakhshanfar, R. Mbeleck, K. Xu, X. Zhang, W. Zhong, M. Xing, 3D bioprinting for biomedical devices and tissue engineering: A review of recent trends and advances, Bioact Mater. 3 (2018) 144–156. https://doi.org/10.1016/j.bioactmat.2017.11.008.

[7] J.K. Placone, A.J. Engler, Recent advances in extrusion-based 3D printing for biomedical applications, Adv Healthc Mater. 7 (2018) 1701161. https://doi.org/10.1002/adhm.201701161.

[8] J. Ten Kate, G. Smit, P. Breedveld, 3D-printed upper limb prostheses: A review, Disabil Rehabil Assist Technol. 12 (2017) 300–314. https://doi.org/10.1080/17483107.2016.1253117.

[9] J.S. Cuellar, G. Smit, A.A. Zadpoor, P. Breedveld, Ten guidelines for the design of non-assembly mechanisms: The case of 3D-printed prosthetic hands, Proc Inst Mech Eng H. 232 (2018) 962–971. https://doi.org/10.1177/0954411918794734.

[10] M. Randazzo, J. Pisapia, N. Singh, J. Thawani, 3D printing in neurosurgery: A systematic review, Surg Neurol Int. 7 (2016) 801. https://doi.org/10.4103/2152-7806.194059.

[11] C. Culmone, G. Smit, P. Breedveld, Additive manufacturing of medical instruments: A state-of-the-art review, Addit Manuf. 27 (2019) 461–473. https://doi.org/https://doi.org/10.1016/j.addma.2019.03.015.

[12] M. Zangheri, L. Cevenini, L. Anfossi, C. Baggiani, P. Simoni, F. Di Nardo, A. Roda, A simple and compact smartphone accessory for quantitative chemiluminescence-based lateral flow immunoassay for salivary cortisol detection, Biosens Bioelectron. 64 (2015) 63–68. https://doi.org/10.1016/j.bios.2014.08.048.

[13] W. Lee, D. Kwon, W. Choi, G.Y. Jung, A.K. Au, A. Folch, S. Jeon, 3D-Printed microfluidic device for the detection of pathogenic bacteria using size-based separation in helical channel with trapezoid cross-section, Sci Rep. 5 (2015) 7717. https://doi.org/10.1038/srep07717.

[14] A. Mäkitie, R. Kontio, K. Mesimäki, M. Paloheimo, R. Björkstrand, K. Paloheimo, J. Tuomi, M. Salmi, Digital design and rapid manufacturing in orbital wall reconstruction,

Innovative Developments in Design and Manufacturing. (2009). https://doi.org/10.1201/9780203859476.ch52.

[15] J. Poukens, P. Laeven, M. Beerens, G. Nijenhuis, J. Vander Sloten, P. Stoelinga, P. Kessler, A classification of cranial implants based on the degree of difficulty in computer design and manufacture, The International Journal of Medical Robotics and Computer Assisted Surgery. 4 (2008) 46–50. https://doi.org/10.1002/rcs.171.

[16] D.B. Jones, R. Sung, C. Weinberg, T. Korelitz, R. Andrews, Three-dimensional modeling may improve surgical education and clinical practice, Surg Innov. 23 (2016) 189–195. https://doi.org/10.1177/1553350615607641.

[17] M. Salmi, Possibilities of preoperative medical models made by 3D printing or additive manufacturing, J Med Eng. 2016 (2016) 1–6. https://doi.org/10.1155/2016/6191526.

[18] W. Gao, Y. Zhang, D. Ramanujan, K. Ramani, Y. Chen, C.B. Williams, C.C.L. Wang, Y.C. Shin, S. Zhang, P.D. Zavattieri, The status, challenges, and future of additive manufacturing in engineering, CAD Computer Aided Design. 69 (2015) 65–89. https://doi.org/10.1016/j.cad.2015.04.001.

[19] N.O. Shanti, D.B. Hovis, M.E. Seitz, J.K. Montgomery, D.M. Baskin, K.T. Faber, Ceramic laminates by gelcasting, Int J Appl Ceram Technol. 6 (2009) 593–606. https://doi.org/10.1111/j.1744-7402.2008.02312.x.

[20] F. Mohd Foudzi, N. Muhamad, A. Bakar Sulong, H. Zakaria, Yttria stabilized zirconia formed by micro ceramic injection molding: Rheological properties and debinding effects on the sintered part, Ceram Int. 39 (2013) 2665–2674. https://doi.org/10.1016/j.ceramint.2012.09.033.

[21] A. Zocca, P. Colombo, C.M. Gomes, J. Günster, Additive manufacturing of ceramics: Issues, potentialities, and opportunities, Journal of the American Ceramic Society. 98 (2015) 1983–2001. https://doi.org/10.1111/jace.13700.

[22] J.W. Halloran, Ceramic stereolithography: Additive manufacturing for ceramics by photopolymerization, Annu Rev Mater Res. 46 (2016) 19–40. https://doi.org/10.1146/annurev-matsci-070115-031841.

[23] J. Wilkes, Y.C. Hagedorn, W. Meiners, K. Wissenbach, Additive manufacturing of ZrO_2-Al_2O_3 ceramic components by selective laser melting, Rapid Prototyp J. 19 (2013) 51–57. https://doi.org/10.1108/13552541311292736.

[24] J. Cesarano, P.D. Calvert, Freeforming objects with low-binder slurry, US patent 6027326 A, 2000.

[25] J.A. Lewis, Direct Ink Writing of 3D Functional Materials, Adv Funct Mater. 16 (2006) 2193–2204. https://doi.org/10.1002/adfm.200600434.

[26] K. Rane, M. Strano, A comprehensive review of extrusion-based additive manufacturing processes for rapid production of metallic and ceramic parts, Adv Manuf. 7 (2019) 155–173. https://doi.org/10.1007/s40436-019-00253-6.

[27] J. Franco, P. Hunger, M.E. Launey, A.P. Tomsia, E. Saiz, Direct write assembly of calcium phosphate scaffolds using a water-based hydrogel, Acta Biomater. 6 (2010) 218–228. https://doi.org/10.1016/j.actbio.2009.06.031.

[28] E. Peng, X. Wei, U. Garbe, D. Yu, B. Edouard, A. Liu, J. Ding, Robocasting of dense yttria-stabilized zirconia structures, J Mater Sci. 53 (2018) 247–273. https://doi.org/10.1007/s10853-017-1491-x.

[29] Q. Fu, E. Saiz, A.P. Tomsia, Direct ink writing of highly porous and strong glass scaffolds for load-bearing bone defects repair and regeneration, Acta Biomater. 7 (2011) 3547–3554. https://doi.org/10.1016/j.actbio.2011.06.030.

[30] J.A. Lewis, J.E. Smay, J. Stuecker, J. Cesarano III, Direct ink writing of three-dimensional ceramic structures, Journal of the American Ceramic Society. 89 (2006) 3599–3609. https://doi.org/10.1111/j.1551-2916.2006.01382.x.

[31] G. Franchin, L. Wahl, P. Colombo, Direct ink writing of ceramic matrix composite structures, Journal of the American Ceramic Society. 100 (2017) 4397–4401. https://doi.org/10.1111/jace.15045.

[32] E. Feilden, C. Ferraro, Q. Zhang, E. Garcia-Tunon, E. D'Elia, F. Giuliani, L. Vandeperre, E. Saiz, 3D Printing bioinspired ceramic composites, Sci Rep. 7 (2017). https://doi.org/10.1038/s41598-017-14236-9.

[33] B.G. Compton, J.A. Lewis, 3D-Printing of lightweight cellular composites, Advanced Materials. 26 (2014) 5930–5935. https://doi.org/10.1002/adma.201401804.

[34] J. Zhang, S. Zhao, Y. Zhu, Y. Huang, M. Zhu, C. Tao, C. Zhang, Three-dimensional printing of strontium-containing mesoporous bioactive glass scaffolds for bone regeneration, Acta Biomater. 10 (2014) 2269–2281. https://doi.org/10.1016/j.actbio.2014.01.001.

[35] Z. Min, Z. Shichang, X. Chen, Z. Yufang, Z. Changqing, 3D-printed dimethyloxallyl glycine delivery scaffolds to improve angiogenesis and osteogenesis, Biomater Sci. 3 (2015) 1236–1244. https://doi.org/10.1039/C5BM00132C.

[36] A.J. Salgado, O.P. Coutinho, R.L. Reis, Bone tissue engineering: State of the art and future trends, Macromol Biosci. 4 (2004) 743–765. https://doi.org/10.1002/mabi.200400026.

[37] E. Tamjid, A. Simchi, J.W.C. Dunlop, P. Fratzl, R. Bagheri, M. Vossoughi, Tissue growth into three-dimensional composite scaffolds with controlled micro-features and nanotopographical surfaces, J Biomed Mater Res A. 101 (2013) 2796–2807. https://doi.org/10.1002/jbm.a.34584.

[38] C.M.B. Ho, S.H. Ng, Y.-J. Yoon, A review on 3D printed bioimplants, International Journal of Precision Engineering and Manufacturing. 16 (2015) 1035–1046. https://doi.org/10.1007/s12541-015-0134-x.

[39] K. Rezwan, Q.Z. Chen, J.J. Blaker, A.R. Boccaccini, Biodegradable and bioactive porous polymer/inorganic composite scaffolds for bone tissue engineering, Biomaterials. 27 (2006) 3413–3431. https://doi.org/10.1016/j.biomaterials.2006.01.039.

[40] K.F. Leong, C.M. Cheah, C.K. Chua, Solid freeform fabrication of three-dimensional scaffolds for engineering replacement tissues and organs, Biomaterials. 24 (2003) 2363–2378. https://doi.org/10.1016/S0142-9612(03)00030-9.

[41] D.W. Hutmacher, Scaffold design and fabrication technologies for engineering tissues - state of the art and future perspectives, J Biomater Sci Polym Ed. 12 (2001) 107–124. https://doi.org/10.1163/156856201744489.

[42] J.O. Hollinger, J. Brekke, E. Gruskin, D. Lee, Role of bone substitutes, Clin Orthop Relat Res. 324 (1996) 55–65. https://doi.org/10.1097/00003086-199603000-00008.

[43] V. Karageorgiou, D. Kaplan, Porosity of 3D biomaterial scaffolds and osteogenesis, Biomaterials. 26 (2005) 5474–5491. https://doi.org/10.1016/j.biomaterials.2005.02.002.

[44] D. Massai, F. Pennella, P. Gentile, D. Gallo, G. Ciardelli, C. Bignardi, A. Audenino, U. Morbiducci, Image-based three-dimensional analysis to characterize the texture of porous scaffolds, Biomed Res Int. 2014 (2014) 1–8. https://doi.org/10.1155/2014/161437.

[45] E. M Zanetti, A. Aldieri, M. Terzini, M. Calì, G. Franceschini, C. Bignardi, Additively manufactured custom load-bearing implantable devices, Australasian Medical Journal. 10 (2017). https://doi.org/10.21767/AMJ.2017.3093.

[46] J.W. Lee, G. Ahn, J.Y. Kim, D.-W. Cho, Evaluating cell proliferation based on internal pore size and 3D scaffold architecture fabricated using solid freeform fabrication technology, J Mater Sci Mater Med. 21 (2010) 3195–3205. https://doi.org/10.1007/s10856-010-4173-7.

[47] T.L. Tuan, L.C. Keller, D. Sun, M.E. Nimni, D. Cheung, Dermal fibroblasts activate keratinocyte outgrowth on collagen gels, J Cell Sci. 107 (Pt 8 (1994) 2285–9.
[48] S.J. Eichhorn, W.W. Sampson, Statistical geometry of pores and statistics of porous nanofibrous assemblies, J R Soc Interface. 2 (2005) 309–318. https://doi.org/10.1098/rsif.2005.0039.
[49] A. Muthutantri, J. Huang, M. Edirisinghe, Novel preparation of graded porous structures for medical engineering, J R Soc Interface. 5 (2008) 1459–1467. https://doi.org/10.1098/rsif.2008.0092.
[50] M. Mozafari, F. Moztarzadeh, M. Rabiee, M. Azami, S. Maleknia, M. Tahriri, Z. Moztarzadeh, N. Nezafati, Development of macroporous nanocomposite scaffolds of gelatin/bioactive glass prepared through layer solvent casting combined with lamination technique for bone tissue engineering, Ceram Int. 36 (2010) 2431–2439. https://doi.org/10.1016/j.ceramint.2010.07.010.
[51] E.F. Morgan, G.U. Unnikrisnan, A.I. Hussein, Bone mechanical properties in healthy and diseased states, Annu Rev Biomed Eng. 20 (2018) 119–143. https://doi.org/10.1146/annurev-bioeng-062117-121139.
[52] R. Murugan, S. Ramakrishna, Development of nanocomposites for bone grafting, Compos Sci Technol. 65 (2005) 2385–2406. https://doi.org/10.1016/j.compscitech.2005.07.022.
[53] F. Zhang, J. Chang, J. Lu, K. Lin, C. Ning, Bioinspired structure of bioceramics for bone regeneration in load-bearing sites, Acta Biomater. 3 (2007) 896–904. https://doi.org/10.1016/j.actbio.2007.05.008.
[54] L.L. Hench, Bioceramics: From Concept to Clinic, Journal of the American Ceramic Society. 74 (1991) 1487–1510. https://doi.org/10.1111/j.1151-2916.1991.tb07132.x.
[55] J.Y. Rho, M.C. Hobatho, R.B. Ashman, Relations of mechanical properties to density and CT numbers in human bone, Med Eng Phys. 17 (1995) 347–355. https://doi.org/10.1016/1350-4533(95)97314-F.
[56] Y.-C. Fung, Biomechanics: Mechanical properties of living tissues, 2nd ed., Springer-Verlag, New York, 1993.
[57] W.W. Wu, Y.B. Zhu, W. Chen, S. Li, B. Yin, J.Z. Wang, X.J. Zhang, G.B. Liu, Z.S. Hu, Y.Z. Zhang, Bone hardness of different anatomical regions of human radius and its impact on the pullout strength of screws, Orthop Surg. 11 (2019) 270–276. https://doi.org/10.1111/os.12436.
[58] P. Tack, J. Victor, P. Gemmel, L. Annemans, 3D-printing techniques in a medical setting: a systematic literature review, Biomed Eng Online. 15 (2016) 115. https://doi.org/10.1186/s12938-016-0236-4.
[59] N. Travitzky, A. Bonet, B. Dermeik, T. Fey, I. Filbert-Demut, L. Schlier, T. Schlordt, P. Greil, Additive manufacturing of ceramic-based materials, Adv Eng Mater. 16 (2014) 729–754. https://doi.org/10.1002/adem.201400097.
[60] U. Scheithauer, E. Schwarzer, H.J. Richter, T. Moritz, Thermoplastic 3D printing - An additive manufacturing method for producing dense ceramics, Int J Appl Ceram Technol. 12 (2015) 26–31. https://doi.org/10.1111/ijac.12306.
[61] M.S. Mason, T. Huang, R.G. Landers, M.C. Leu, G.E. Hilmas, Aqueous-based extrusion of high solids loading ceramic pastes: Process modeling and control, J Mater Process Technol. 209 (2009) 2946–2957. https://doi.org/10.1016/j.jmatprotec.2008.07.004.
[62] R. Vaidyanathan, J. Walish, J.L. Lombardi, S. Kasichainula, P. Calvert, K.C. Cooper, The extrusion freeforming of functional ceramic prototypes, JOM. 52 (2000) 34–37. https://doi.org/10.1007/s11837-000-0066-4.
[63] I. Rodrigues, M. Guedes, S. Olhero, A. Chefdor, A.C. Branco, M. Leite, A.P. Serro, C.G. Figueiredo-Pina, Development of free binder zirconia-based pastes for the production of

dental pieces by robocasting, J Manuf Process. 57 (2020) 1–9. https://doi.org/10.1016/j.jmapro.2020.06.015.

[64] A. M'Barki, L. Bocquet, A. Stevenson, Linking rheology and printability for dense and strong ceramics by direct ink writing, Sci Rep. 7 (2017) 1–10. https://doi.org/10.1038/s41598-017-06115-0.

[65] P. Palmero, F. Cambier, E. De Barra, eds., Advances in ceramic biomaterials: Materials, devices and challenges, Woodhead Publishing, Cambridge, 2017.

[66] L. Rueschhoff, W. Costakis, M. Michie, J. Youngblood, R. Trice, Additive manufacturing of dense ceramic parts via direct ink writing of aqueous alumina suspensions, Int J Appl Ceram Technol. 13 (2016) 821–830. https://doi.org/10.1111/ijac.12557.

[67] E. Feilden, E.G.T. Blanca, F. Giuliani, E. Saiz, L. Vandeperre, Robocasting of structural ceramic parts with hydrogel inks, J Eur Ceram Soc. 36 (2016) 2525–2533. https://doi.org/10.1016/j.jeurceramsoc.2016.03.001.

[68] D. Glymond, L.J. Vandeperre, Robocasting of MgO-doped alumina using alginic acid slurries, Journal of the American Ceramic Society. 101 (2018) 3309–3316. https://doi.org/10.1111/jace.15509.

[69] L. Yang, X. Zeng, Y. Zhang, 3D printing of alumina ceramic parts by heat-induced solidification with carrageenan, Mater Lett. 255 (2019) 126564. https://doi.org/10.1016/j.matlet.2019.126564.

[70] A.C. Branco, R. Silva, H. Jorge, T. Santos, K. Lorenz, M. Polido, R. Colaço, A.P. Serro, C.G. Figueiredo-Pina, Tribological performance of the pair human teeth vs 3D printed zirconia: An *in vitro* chewing simulation study, J Mech Behav Biomed Mater. 110 (2020) 103900. https://doi.org/10.1016/j.jmbbm.2020.103900.

[71] T. Yu, Z. Zhang, Q. Liu, R. Kuliiev, N. Orlovskaya, D. Wu, Extrusion-based additive manufacturing of yttria-partially-stabilized zirconia ceramics, Ceram Int. (2019) 1–8. https://doi.org/10.1016/j.ceramint.2019.10.245.

[72] T. Chen, A. Sun, C. Chu, H. Wu, J. Wang, J. Wang, Z. Li, J. Guo, G. Xu, Rheological behavior of titania ink and mechanical properties of titania ceramic structures by 3D direct ink writing using high solid loading titania ceramic ink, J Alloys Compd. 783 (2019) 321–328. https://doi.org/10.1016/j.jallcom.2018.12.334.

[73] U.K. Roopavath, S. Malferrari, A. Van Haver, F. Verstreken, S.N. Rath, D.M. Kalaskar, Optimization of extrusion based ceramic 3D printing process for complex bony designs, Mater Des. 162 (2019) 263–270. https://doi.org/10.1016/j.matdes.2018.11.054.

[74] S. Zhao, W. Xiao, M.N. Rahaman, D. O'Brien, J.W. Seitz-Sampson, B. Sonny Bal, Robocasting of silicon nitride with controllable shape and architecture for biomedical applications, Int J Appl Ceram Technol. 14 (2017) 117–127. https://doi.org/10.1111/ijac.12633.

[75] E.L. Corral, J. Cesarano III, A. Shyam, E. Lara-Curzio, N. Bell, J. Stuecker, N. Perry, M. Di Prima, Z. Munir, J. Garay, E. V Barrera, Engineered nanostructures for multifunctional single-walled carbon nanotube reinforced silicon nitride nanocomposites, Journal of the American Ceramic Society. 91 (2008) 3129–3137. https://doi.org/10.1111/j.1551-2916.2008.02533.x.

[76] L. Goyos-Ball, E. García-Tuñón, E. Fernández-García, R. Díaz, A. Fernández, C. Prado, E. Saiz, R. Torrecillas, Mechanical and biological evaluation of 3D printed 10CeTZP-Al2O3 structures, J Eur Ceram Soc. 37 (2017) 3151–3158. https://doi.org/10.1016/j.jeurceramsoc.2017.03.012.

[77] V.P. Galván-Chacón, S. Eqtesadi, A. Pajares, P. Miranda, F. Guiberteau, Elucidating the role of 45S5 bioglass content in the density and flexural strength of robocast β-TCP/45S5

composites, Ceram Int. 44 (2018) 12717–12722. https://doi.org/10.1016/j.ceramint.2018.04.074.
[78] S. Eqtesadi, A. Motealleh, A. Pajares, F. Guiberteau, P. Miranda, Improving mechanical properties of 13-93 bioactive glass robocast scaffold by poly (lactic acid) and poly (ε-caprolactone) melt infiltration, J Non Cryst Solids. 432 (2016) 111–119. https://doi.org/10.1016/j.jnoncrysol.2015.02.025.
[79] L.-H. Hu, Y.-K. Wang, S.-C. Wang, Polymer derived gel-like preceramic precursor of core-shell silicon oxycarbide ceramic for robocasting, Ceram Int. 45 (2019) 23475–23481. https://doi.org/10.1016/j.ceramint.2019.08.053.
[80] L.L. Hench, E.C. Ethridge, Biomaterials: An interfacial approach, New York, 1982. https://doi.org/10.1002/jbm.820190515.
[81] D.T.-J. Barone, J.-M. Raquez, Ph. Dubois, Bone-guided regeneration: from inert biomaterials to bioactive polymer (nano)composites, Polym Adv Technol. 22 (2011) 463–475. https://doi.org/10.1002/pat.1845.
[82] V. V. Lashneva, Yu.N. Kryuchkov, S. V. Sokhan, Bioceramics based on aluminum oxide, Glass and Ceramics. 55 (1998) 357–359. https://doi.org/10.1007/BF02694271.
[83] X. Du, S. Fu, Y. Zhu, 3D printing of ceramic-based scaffolds for bone tissue engineering: An overview, J Mater Chem B. 6 (2018) 4397–4412. https://doi.org/10.1039/c8tb00677f.
[84] Y.W. Moon, I.J. Choi, Y.H. Koh, H.E. Kim, Macroporous alumina scaffolds consisting of highly microporous hollow filaments using three-dimensional ceramic/camphene-based co-extrusion, J Eur Ceram Soc. 35 (2015) 4623–4627. https://doi.org/10.1016/j.jeurceramsoc.2015.08.017.
[85] Y.-W. Moon, I.-J. Choi, Y.-H. Koh, H.-E. Kim, Porous alumina ceramic scaffolds with biomimetic macro/micro-porous structure using three-dimensional (3-D) ceramic/camphene-based extrusion, Ceram Int. 41 (2015) 12371–12377. https://doi.org/10.1016/j.ceramint.2015.06.069.
[86] J. Dittmann, E. Koos, N. Willenbacher, Ceramic capillary suspensions: Novel processing route for macroporous ceramic materials, Journal of the American Ceramic Society. 96 (2013) 391–397. https://doi.org/10.1111/jace.12126.
[87] J. Dittmann, N. Willenbacher, Micro structural investigations and mechanical properties of macro porous ceramic materials from capillary suspensions, Journal of the American Ceramic Society. 97 (2014) 3787–3792. https://doi.org/10.1111/jace.13184.
[88] J. Maurath, N. Willenbacher, 3D printing of open-porous cellular ceramics with high specific strength, J Eur Ceram Soc. 37 (2017) 4833–4842. https://doi.org/10.1016/j.jeurceramsoc.2017.06.001.
[89] M.F. Ashby, The properties of foams and lattices, Philosophical Transactions of the Royal Society A: Mathematical, Physical and Engineering Sciences. 364 (2006) 15–30. https://doi.org/10.1098/rsta.2005.1678.
[90] C. Minas, D. Carnelli, E. Tervoort, A.R. Studart, 3D printing of emulsions and foams into hierarchical porous ceramics, ADVANCED MATERIALS. 28 (2016) 9993–9999. https://doi.org/10.1002/adma.201603390.
[91] A.R. Studart, U.T. Gonzenbach, E. Tervoort, L.J. Gauckler, Processing Routes to Macroporous Ceramics: A Review, Journal of the American Ceramic Society. 89 (2006) 1771–1789. https://doi.org/10.1111/j.1551-2916.2006.01044.x.
[92] H.-C. Ko, J.-S. Han, M. Bächle, J.-H. Jang, S.-W. Shin, D.-J. Kim, Initial osteoblast-like cell response to pure titanium and zirconia/alumina ceramics, Dental Materials. 23 (2007) 1349–1355. https://doi.org/10.1016/j.dental.2006.11.023.
[93] R.H.J. Hannink, Transformation toughening in zirconia-containing ceramics, Journal of the American Ceramic Society. 83 (2000) 461–87.

[94] S. Gobain, ZirPro CY3Z-P Technical Data Sheet. Available at http:// www.zirpro.com/zirconia-beads-powders/yttria-stabilized- zirconia, n.d.
[95] M.A. Sainz, S. Serena, M. Belmonte, P. Miranzo, M.I. Osendi, Protein adsorption and in vitro behavior of additively manufactured 3D-silicon nitride scaffolds intended for bone tissue engineering, Materials Science and Engineering C. 115 (2020) 110734. https://doi.org/10.1016/j.msec.2020.110734.
[96] L.-C. Gerhardt, A.R. Boccaccini, Bioactive Glass and Glass-Ceramic Scaffolds for Bone Tissue Engineering, Materials. 3 (2010) 3867–3910. https://doi.org/10.3390/ma3073867.
[97] S. Bose, D. Ke, H. Sahasrabudhe, A. Bandyopadhyay, Additive manufacturing of biomaterials, Prog Mater Sci. 93 (2018) 45–111. https://doi.org/10.1016/j.pmatsci.2017.08.003.
[98] S. Bose, S. Tarafder, Calcium phosphate ceramic systems in growth factor and drug delivery for bone tissue engineering: A review, Acta Biomater. 8 (2012) 1401–1421. https://doi.org/10.1016/j.actbio.2011.11.017.
[99] H. Liu, H. Yazici, C. Ergun, T.J. Webster, H. Bermek, An in vitro evaluation of the Ca/P ratio for the cytocompatibility of nano-to-micron particulate calcium phosphates for bone regeneration, Acta Biomater. 4 (2008) 1472–1479. https://doi.org/10.1016/j.actbio.2008.02.025.
[100] X. Cao, H. Lu, J. Liu, W. Lu, L. Guo, M. Ma, B. Zhang, Y. Guo, 3D plotting in the preparation of newberyite, struvite, and brushite porous scaffolds: using magnesium oxide as a starting material, J Mater Sci Mater Med. 30 (2019) 1–12. https://doi.org/10.1007/s10856-019-6290-2.
[101] X. Chen, Q. Xin, Z. Min, Z. Shi-Chang, Z. Yu-Fang, Hydroxyapatite Whisker-reinforced Composite Scaffolds Through 3D Printing for Bone Repair, Journal of Inorganic Materials. 32 (2017) 837. https://doi.org/10.15541/jim20160628.
[102] P.H. Warnke, H. Seitz, F. Warnke, S.T. Becker, S. Sivananthan, E. Sherry, Q. Liu, J. Wiltfang, T. Douglas, Ceramic scaffolds produced by computer-assisted 3D printing and sintering: Characterization and biocompatibility investigations, J Biomed Mater Res B Appl Biomater. 9999B (2010) NA-NA. https://doi.org/10.1002/jbm.b.31577.
[103] S. Shkarina, R. Shkarin, V. Weinhardt, E. Melnik, G. Vacun, P.J. Kluger, K. Loza, M. Epple, S.I. Ivlev, T. Baumbach, M.A. Surmeneva, R.A. Surmenev, 3D biodegradable scaffolds of polycaprolactone with silicate-containing hydroxyapatite microparticles for bone tissue engineering: high-resolution tomography and in vitro study, Sci Rep. 8 (2018) 8907. https://doi.org/10.1038/s41598-018-27097-7.
[104] S. Maji, T. Agarwal, J. Das, T.K. Maiti, Development of gelatin/carboxymethyl chitosan/nano-hydroxyapatite composite 3D macroporous scaffold for bone tissue engineering applications, Carbohydr Polym. 189 (2018) 115–125. https://doi.org/10.1016/j.carbpol.2018.01.104.
[105] P. Miranda, A. Pajares, E. Saiz, A.P. Tomsia, F. Guiberteau, Mechanical properties of calcium phosphate scaffolds fabricated by robocasting, J Biomed Mater Res A. 85 (2008) 218–227. https://doi.org/10.1002/jbm.a.31587.
[106] F. Martínez-Vázquez, A. Pajares, P. Miranda, Effect of the drying process on the compressive strength and cell proliferation of hydroxyapatite-derived scaffolds, Int J Appl Ceram Technol. 14 (2017) 1101–1106. https://doi.org/10.1111/ijac.12755.
[107] A.M. Mocioiu, R. Tutuianu, L.M. Cursaru, R.M. Piticescu, P. Stanciu, S.V. Bogdan, R. Trusca, V. Sereanu, A. Meghea, 3D structures of hydroxyapatite obtained from Rapana venosa shells using hydrothermal synthesis followed by 3D printing, J Mater Sci. 54 (2019) 13901–13913. https://doi.org/10.1007/s10853-019-03872-3.

[108] M.C. Matesanz, J. Linares, M. Oñaderra, M.J. Feito, F.J. Martínez-Vázquez, S. Sánchez-Salcedo, D. Arcos, M.T. Portolés, M. Vallet-Regí, Response of osteoblasts and preosteoblasts to calcium deficient and Si substituted hydroxyapatites treated at different temperatures, Colloids Surf B Biointerfaces. 133 (2015) 304–313. https://doi.org/10.1016/j.colsurfb.2015.06.014.

[109] S. Raymond, Y. Maazouz, E.B. Montufar, R.A. Perez, B. González, J. Konka, J. Kaiser, M.-P. Ginebra, Accelerated hardening of nanotextured 3D-plotted self-setting calcium phosphate inks, Acta Biomater. 75 (2018) 451–462. https://doi.org/10.1016/j.actbio.2018.05.042.

[110] N. Tovar, L. Witek, P. Atria, M. Sobieraj, M. Bowers, C.D. Lopez, B.N. Cronstein, P.G. Coelho, Form and functional repair of long bone using 3D-printed bioactive scaffolds, J Tissue Eng Regen Med. 12 (2018) 1986–1999. https://doi.org/10.1002/term.2733.

[111] C.D. Lopez, J.R. Diaz-Siso, L. Witek, J.M. Bekisz, B.N. Cronstein, A. Torroni, R.L. Flores, E.D. Rodriguez, P.G. Coelho, Three dimensionally printed bioactive ceramic scaffold osseoconduction across critical-sized mandibular defects, Journal of Surgical Research. 223 (2018) 115–122. https://doi.org/10.1016/j.jss.2017.10.027.

[112] M. Casas-Luna, H. Tan, S. Tkachenko, D. Salamon, E.B. Montufar, Enhancement of mechanical properties of 3D-plotted tricalcium phosphate scaffolds by rapid sintering, J Eur Ceram Soc. 39 (2019) 4366–4374. https://doi.org/10.1016/j.jeurceramsoc.2019.05.055.

[113] H. Seitz, U. Deisinger, B. Leukers, R. Detsch, G. Ziegler, Different calcium phosphate granules for 3-D printing of bone tissue engineering scaffolds, Adv Eng Mater. 11 (2009) 41–46. https://doi.org/10.1002/adem.200800334.

[114] B.A.E. Ben-Arfa, R.C. Pullar, A Comparison of Bioactive Glass Scaffolds Fabricated by Robocasting from Powders Made by Sol–Gel and Melt-Quenching Methods, Processes. 8 (2020) 615. https://doi.org/10.3390/pr8050615.

[115] L.L. Hench, Third-Generation Biomedical Materials, Science (1979). 295 (2002) 1014–1017. https://doi.org/10.1126/science.1067404.

[116] L.L. Hench, The story of Bioglass®, J Mater Sci Mater Med. 17 (2006) 967–978. https://doi.org/10.1007/s10856-006-0432-z.

[117] M.N. Rahaman, D.E. Day, B. Sonny Bal, Q. Fu, S.B. Jung, L.F. Bonewald, A.P. Tomsia, Bioactive glass in tissue engineering, Acta Biomater. 7 (2011) 2355–2373. https://doi.org/10.1016/j.actbio.2011.03.016.

[118] X. Yan, C. Yu, X. Zhou, J. Tang, D. Zhao, Highly ordered mesoporous bioactive glasses with superior in vitro bone-forming bioactivities, Angewandte Chemie - International Edition. 43 (2004) 5980–5984. https://doi.org/10.1002/anie.200460598.

[119] W. Xiao, M.A. Zaeem, B.S. Bal, M.N. Rahaman, Creation of bioactive glass (13–93) scaffolds for structural bone repair using a combined finite element modeling and rapid prototyping approach, Materials Science and Engineering C. 68 (2016) 651–662. https://doi.org/10.1016/j.msec.2016.06.011.

[120] X. Liu, M.N. Rahaman, G.E. Hilmas, B.S. Bal, Mechanical properties of bioactive glass (13-93) scaffolds fabricated by robotic deposition for structural bone repair, Acta Biomater. 9 (2013) 7025–7034. https://doi.org/10.1016/j.actbio.2013.02.026.

[121] W. Jia, G.Y. Lau, W. Huang, C. Zhang, A.P. Tomsia, Q. Fu, Bioactive glass for large bone repair, Adv Healthc Mater. 4 (2015) 2842–2848. https://doi.org/10.1002/adhm.201500447.

[122] L. Bi, B. Zobell, X. Liu, M.N. Rahaman, L.F. Bonewald, Healing of critical-size segmental defects in rat femora using strong porous bioactive glass scaffolds, Materials Science and Engineering: C. 42 (2014) 816–824. https://doi.org/10.1016/j.msec.2014.06.022.

[123] A.M. Deliormanli, M.N. Rahaman, Direct-write assembly of silicate and borate bioactive glass scaffolds for bone repair, J Eur Ceram Soc. 32 (2012) 3637–3646. https://doi.org/10.1016/j.jeurceramsoc.2012.05.005.
[124] Y. Gu, W. Huang, M.N. Rahaman, *In vivo* evaluation of scaffolds with a grid-like microstructure composed of a mixture of silicate (13-93) and borate (13-93B3) bioactive glasses, Advances in Bioceramics and Porous Ceramics VII. (2015) 53–64. https://doi.org/10.1002/9781119040392.ch6.
[125] S. Eqtesadi, A. Motealleh, P. Miranda, A. Pajares, A. Lemos, J.M.F. Ferreira, Robocasting of 45S5 bioactive glass scaffolds for bone tissue engineering, J Eur Ceram Soc. 34 (2014) 107–118. https://doi.org/10.1016/j.jeurceramsoc.2013.08.003.
[126] S. Eqtesadi, A. Motealleh, P. Miranda, A. Lemos, A. Rebelo, J.M.F. Ferreira, A simple recipe for direct writing complex 45S5 Bioglass® 3D scaffolds, Mater Lett. 93 (2013) 68–71. https://doi.org/10.1016/j.matlet.2012.11.043.
[127] S. Eqtesadi, A. Motealleh, R. Wendelbo, A.L. Ortiz, P. Miranda, Reinforcement with reduced graphene oxide of bioactive glass scaffolds fabricated by robocasting, J Eur Ceram Soc. 37 (2017) 3695–3704. https://doi.org/10.1016/j.jeurceramsoc.2016.12.047.
[128] A. Motealleh, S. Eqtesadi, A. Civantos, A. Pajares, P. Miranda, Robocast 45S5 bioglass scaffolds: *In vitro* behavior, J Mater Sci. 52 (2017) 9179–9191. https://doi.org/10.1007/s10853-017-0775-5.
[129] F. Baino, J. Barberi, E. Fiume, G. Orlygsson, J. Massera, E. Verné, Robocasting of bioactive SiO_2-P_2O_5-CaO-MgO-Na_2O-K_2O glass scaffolds, J Healthc Eng. 2019 (2019) 1–12. https://doi.org/10.1155/2019/5153136.
[130] Q. Fu, E. Saiz, A.P. Tomsia, Bioinspired strong and highly porous glass scaffolds, Adv Funct Mater. 21 (2011) 1058–1063. https://doi.org/10.1002/adfm.201002030.
[131] S.M. Olhero, H.R. Fernandes, C.F. Marques, B.C.G. Silva, J.M.F. Ferreira, Additive manufacturing of 3D porous alkali-free bioactive glass scaffolds for healthcare applications, J Mater Sci. 52 (2017) 12079–12088. https://doi.org/10.1007/s10853-017-1347-4.
[132] S. Zhao, J. Zhang, M. Zhu, Y. Zhang, Z. Liu, C. Tao, Y. Zhu, C. Zhang, Three-dimensional printed strontium-containing mesoporous bioactive glass scaffolds for repairing rat critical-sized calvarial defects, Acta Biomater. 12 (2015) 270–280. https://doi.org/10.1016/j.actbio.2014.10.015.
[133] S. Zhao, M. Zhu, J. Zhang, Y. Zhang, Z. Liu, Y. Zhu, C. Zhang, Three dimensionally printed mesoporous bioactive glass and poly(3-hydroxybutyrate-co-3-hydroxyhexanoate) composite scaffolds for bone regeneration, J Mater Chem B. 2 (2014) 6106–6118. https://doi.org/10.1039/c4tb00838c.
[134] B.A.E. Ben-Arfa, A.S. Neto, I.E. Palamá, I.M. Miranda Salvado, R.C. Pullar, J.M.F. Ferreira, Robocasting of ceramic glass scaffolds: Sol–gel glass, new horizons, J Eur Ceram Soc. 39 (2019) 1625–1634. https://doi.org/10.1016/j.jeurceramsoc.2018.11.019.
[135] B.A.E. Ben-Arfa, A.S. Neto, I.M. Miranda Salvado, R.C. Pullar, J.M.F. Ferreira, Robocasting: Prediction of ink printability in solgel bioactive glass, Journal of the American Ceramic Society. 102 (2019) 1608–1618. https://doi.org/10.1111/jace.16092.
[136] B.A.E. Ben-Arfa, S. Neto, I.M. Miranda Salvado, R.C. Pullar, J.M.F. Ferreira, Robocasting of Cu^{2+} & La^{3+} doped sol–gel glass scaffolds with greatly enhanced mechanical properties: Compressive strength up to 14 MPa, Acta Biomater. 87 (2019) 265–272. https://doi.org/10.1016/j.actbio.2019.01.048.
[137] Y. Luo, D. Zhai, Z. Huan, H. Zhu, L. Xia, J. Chang, C. Wu, Three-dimensional printing of hollow-struts-packed bioceramic scaffolds for bone regeneration, ACS Appl Mater Interfaces. 7 (2015) 24377–24383. https://doi.org/10.1021/acsami.5b08911.

[138] A.M. Deliormanli, X. Liu, M.N. Rahaman, Evaluation of borate bioactive glass scaffolds with different pore sizes in a rat subcutaneous implantation model, J Biomater Appl. 28 (2014) 643–653. https://doi.org/10.1177/0885328212470013.
[139] Y. Zhu, C. Wu, Y. Ramaswamy, E. Kockrick, P. Simon, S. Kaskel, H. Zreiqat, Preparation, characterization and in vitro bioactivity of mesoporous bioactive glasses (MBGs) scaffolds for bone tissue engineering, Microporous and Mesoporous Materials. 112 (2008) 494–503. https://doi.org/10.1016/j.micromeso.2007.10.029.
[140] C.K. Sen, S. Khanna, M. Venojarvi, P. Trikha, E.C. Ellison, T.K. Hunt, S. Roy, Copper-induced vascular endothelial growth factor expression and wound healing, American Journal of Physiology-Heart and Circulatory Physiology. 282 (2002) H1821–H1827. https://doi.org/10.1152/ajpheart.01015.2001.
[141] M. Frangoulis, P. Georgiou, C. Chrisostomidis, D. Perrea, I. Dontas, N. Kavantzas, A. Kostakis, O. Papadopoulos, Rat Epigastric Flap Survival and VEGF Expression after Local Copper Application, Plast Reconstr Surg. 119 (2007) 837–843. https://doi.org/10.1097/01.prs.0000252000.59231.5e.
[142] Y. Lin, R.F. Brown, S.B. Jung, D.E. Day, Angiogenic effects of borate glass microfibers in a rodent model, J Biomed Mater Res A. (2014) n/a-n/a. https://doi.org/10.1002/jbm.a.35120.
[143] S. Zhao, L. Li, H. Wang, Y. Zhang, X. Cheng, N. Zhou, M.N. Rahaman, Z. Liu, W. Huang, C. Zhang, Wound dressings composed of copper-doped borate bioactive glass microfibers stimulate angiogenesis and heal full-thickness skin defects in a rodent model, Biomaterials. 53 (2015) 379–391. https://doi.org/10.1016/j.biomaterials.2015.02.112.
[144] Y. Lin, W. Xiao, B.S. Bal, M.N. Rahaman, Effect of copper-doped silicate 13-93 bioactive glass scaffolds on the response of MC3T3-E1 cells in vitro and on bone regeneration and angiogenesis in rat calvarial defects in vivo, Materials Science and Engineering C. 67 (2016) 440–452. https://doi.org/10.1016/j.msec.2016.05.073.
[145] A.F. Wells, Structural Inorganic Chemistry, 4th ed., Oxford University Press, London, 1975.
[146] Y. Luo, C. Wu, A. Lode, M. Gelinsky, Hierarchical mesoporous bioactive glass/alginate composite scaffolds fabricated by three-dimensional plotting for bone tissue engineering, Biofabrication. 5 (2013). https://doi.org/10.1088/1758-5082/5/1/015005.
[147] G.G. dos Santos, E.C.A. Meireles, F.B. Miguel, Wollastonite/TCP composites for bone regeneration: systematic review and meta-analysis, Cerâmica. 66 (2020) 277–283. https://doi.org/10.1590/0366-69132020663792926.
[148] S. Kunjalukkal Padmanabhan, F. Gervaso, M. Carrozzo, F. Scalera, A. Sannino, A. Licciulli, Wollastonite/hydroxyapatite scaffolds with improved mechanical, bioactive and biodegradable properties for bone tissue engineering, Ceram Int. 39 (2013) 619–627. https://doi.org/10.1016/j.ceramint.2012.06.073.
[149] H. Shao, A. Liu, X. Ke, M. Sun, Y. He, X. Yang, J. Fu, L. Zhang, G. Yang, Y. Liu, S. Xu, Z. Gou, 3D robocasting magnesium-doped wollastonite/TCP bioceramic scaffolds with improved bone regeneration capacity in critical sized calvarial defects, J Mater Chem B. 5 (2017) 2941–2951. https://doi.org/10.1039/c7tb00217c.
[150] H. Shao, M. Sun, F. Zhang, A. Liu, Y. He, J. Fu, X. Yang, H. Wang, Z. Gou, Custom repair of mandibular bone defects with 3D printed bioceramic scaffolds, J Dent Res. 97 (2018) 68–76. https://doi.org/10.1177/0022034517734846.
[151] A. Liu, M. Sun, H. Shao, X. Yang, C. Ma, D. He, Q. Gao, Y. Liu, S. Yan, S. Xu, Y. He, J. Fu, Z. Gou, The outstanding mechanical response and bone regeneration capacity of robocast dilute magnesium-doped wollastonite scaffolds in critical size bone defects, J Mater Chem B. 4 (2016) 3945–3958. https://doi.org/10.1039/c6tb00449k.

[152] H. Shao, X. Ke, A. Liu, M. Sun, Y. He, X. Yang, J. Fu, Y. Liu, L. Zhang, G. Yang, S. Xu, Z. Gou, Bone regeneration in 3D printing bioactive ceramic scaffolds with improved tissue/material interface pore architecture in thin-wall bone defect, Biofabrication. 9 (2017) 025003. https://doi.org/10.1088/1758-5090/aa663c.

[153] Z. Jin, R. Wu, J. Shen, X. Yang, M. Shen, W. Xu, R. Huang, L. Zhang, G. Yang, C. Gao, Z. Gou, S. Xu, Nonstoichiometric wollastonite bioceramic scaffolds with core-shell pore struts and adjustable mechanical and biodegradable properties, J Mech Behav Biomed Mater. 88 (2018) 140–149. https://doi.org/10.1016/j.jmbbm.2018.08.018.

[154] C. Paredes, F.J. Martínez-Vázquez, A. Pajares, P. Miranda, Novel strategy for toughening robocast bioceramic scaffolds using polymeric cores, Ceram Int. 45 (2019) 19572–19576. https://doi.org/10.1016/j.ceramint.2019.06.175.

[155] C. Paredes, F.J. Martínez-Vázquez, A. Pajares, P. Miranda, Development by robocasting and mechanical characterization of hybrid HA/PCL coaxial scaffolds for biomedical applications, J Eur Ceram Soc. 39 (2019) 4375–4383. https://doi.org/10.1016/j.jeurceramsoc.2019.05.053.

[156] T. Li, D. Zhai, B. Ma, J. Xue, P. Zhao, J. Chang, M. Gelinsky, C. Wu, 3D Printing of hot dog-like biomaterials with hierarchical architecture and distinct bioactivity, Advanced Science. 6 (2019). https://doi.org/10.1002/advs.201901146.

[157] C. Vakifahmetoglu, D. Zeydanli, P. Colombo, Porous polymer derived ceramics, Materials Science and Engineering: R: Reports. 106 (2016) 1–30. https://doi.org/10.1016/j.mser.2016.05.001.

[158] A. Dasan, H. Elsayed, J. Kraxner, D. Galusek, E. Bernardo, Hierarchically porous 3D-printed akermanite scaffolds from silicones and engineered fillers, J Eur Ceram Soc. 39 (2019) 4445–4449. https://doi.org/10.1016/j.jeurceramsoc.2019.06.021.

[159] L. Fiocco, H. Elsayed, D. Badocco, P. Pastore, D. Bellucci, V. Cannillo, R. Detsch, A.R. Boccaccini, E. Bernardo, Direct ink writing of silica-bonded calcite scaffolds from preceramic polymers and fillers, Biofabrication. 9 (2017) 025012. https://doi.org/10.1088/1758-5090/aa6c37.

[160] S. Fu, W. Liu, S. Liu, S. Zhao, Y. Zhu, 3D printed porous β-Ca_2SiO_4 scaffolds derived from preceramic resin and their physicochemical and biological properties, Sci Technol Adv Mater. 19 (2018) 495–506. https://doi.org/10.1080/14686996.2018.1471653.

[161] A. Zocca, G. Franchin, H. Elsayed, E. Gioffredi, E. Bernardo, P. Colombo, A. Bandyopadhyay, Direct ink writing of a preceramic polymer and fillers to produce hardystonite (Ca2ZnSi2O7) bioceramic scaffolds, Journal of the American Ceramic Society. 99 (2016) 1960–1967. https://doi.org/10.1111/jace.14213.

[162] H. Elsayed, M. Sinico, M. Secco, F. Zorzi, P. Colombo, E. Bernardo, B-doped hardystonite bioceramics from preceramic polymers and fillers: Synthesis and application to foams and 3D-printed scaffolds, J Eur Ceram Soc. 37 (2017) 1757–1767. https://doi.org/10.1016/j.jeurceramsoc.2016.12.002.

[163] H. Elsayed, C. Gardin, L. Ferroni, B. Zavan, P. Colombo, E. Bernardo, Highly porous Sr/Mg-doped hardystonite bioceramics from preceramic polymers and reactive fillers: Direct foaming and direct ink writing, Adv Eng Mater. 21 (2019) 1–7. https://doi.org/10.1002/adem.201800900.

[164] J. Yuan, P. Zhen, H. Zhao, K. Chen, X. Li, M. Gao, J. Zhou, X. Ma, The preliminary performance study of the 3D printing of a tricalcium phosphate scaffold for the loading of sustained release anti-tuberculosis drugs, J Mater Sci. 50 (2015) 2138–2147. https://doi.org/10.1007/s10853-014-8776-0.

[165] V. Devescovi, E. Leonardi, G. Ciapetti, E. Cenni, Growth factors in bone repair, Chir Organi Mov. 92 (2008) 161–168. https://doi.org/10.1007/s12306-008-0064-1.

[166] J.O. Hollinger, C.E. Hart, S.N. Hirsch, S. Lynch, G.E. Friedlaender, Recombinant Human Platelet-Derived Growth Factor: Biology and Clinical Applications, The Journal of Bone and Joint Surgery-American Volume. 90 (2008) 48–54. https://doi.org/10.2106/JBJS.G.01231.

[167] X. Liu, M.N. Rahaman, Y. Liu, B.S. Bal, L.F. Bonewald, Enhanced bone regeneration in rat calvarial defects implanted with surface-modified and BMP-loaded bioactive glass (13-93) scaffolds, Acta Biomater. 9 (2013) 7506–7517. https://doi.org/10.1016/j.actbio.2013.03.039.

[168] Y. Lin, W. Xiao, X. Liu, B.S. Bal, L.F. Bonewald, M.N. Rahaman, Long-term bone regeneration, mineralization and angiogenesis in rat calvarial defects implanted with strong porous bioactive glass (13-93) scaffolds, J Non Cryst Solids. 432 (2016) 120–129. https://doi.org/10.1016/j.jnoncrysol.2015.04.008.

[169] J.G. Dellinger, J.A.C. Eurell, R.D. Jamison, Bone response to 3D periodic hydroxyapatite scaffolds with and without tailored microporosity to deliver bone morphogenetic protein 2, J Biomed Mater Res A. 76 (2006) 366–376. https://doi.org/10.1002/jbm.a.30523.

[170] M. Zhou, X. Yang, S. Li, K. Kapat, K. Guo, F.H. Perera, L. Qian, P. Miranda, Y. Che, Bioinspired channeled, rhBMP-2-coated β-TCP scaffolds with embedded autologous vascular bundles for increased vascularization and osteogenesis of prefabricated tissue-engineered bone, Materials Science and Engineering C. 118 (2021) 111389. https://doi.org/10.1016/j.msec.2020.111389.

[171] L. Meseguer-Olmo, V. Vicente-Ortega, M. Alcaraz-Baños, J.L. Calvo-Guirado, M. Vallet-Regí, D. Arcos, A. Baeza, In-vivo behavior of Si-hydroxyapatite/polycaprolactone/DMB scaffolds fabricated by 3D printing, J Biomed Mater Res A. 101A (2013) 2038–2048. https://doi.org/10.1002/jbm.a.34511.

[172] R. Detsch, S. Schaefer, U. Deisinger, G. Ziegler, H. Seitz, B. Leukers, In vitro - Osteoclastic Activity Studies on Surfaces of 3D Printed Calcium Phosphate Scaffolds, J Biomater Appl. 26 (2011) 359–380. https://doi.org/10.1177/0885328210373285.

[173] J. Wang, C. Wang, K. Jin, X. Yang, L. Gao, C. Yao, X. Dai, J. He, C. Gao, J. Ye, P. Li, Z. Gou, Simultaneous enhancement of vascularization and contact-active antibacterial activity in diopside-based ceramic orbital implants, Materials Science and Engineering C. 105 (2019). https://doi.org/10.1016/j.msec.2019.110036.

[174] X. Wang, L. Zhang, X. Ke, J. Wang, G. Yang, X. Yang, D. He, H. Shao, Y. He, J. Fu, S. Xu, Z. Gou, 45S5 Bioglass analogue reinforced akermanite ceramic favorable for additive manufacturing mechanically strong scaffolds, RSC Adv. 5 (2015) 102727–102735. https://doi.org/10.1039/c5ra19272b.

[175] G. Franchin, H.S. Maden, L. Wahl, A. Baliello, M. Pasetto, P. Colombo, Optimization and characterization of preceramic inks for Direct Ink Writing of Ceramic Matrix Composite structures, Materials. 11 (2018) 1–14. https://doi.org/10.3390/ma11040515.

[176] B. Román-Manso, F.M. Figueiredo, B. Achiaga, R. Barea, D. Pérez-Coll, A. Morelos-Gómez, M. Terrones, M.I. Osendi, M. Belmonte, P. Miranzo, Electrically functional 3D-architectured graphene/SiC composites, Carbon N Y. 100 (2016) 318–328. https://doi.org/10.1016/j.carbon.2015.12.103.

[177] A.E. Jakus, R.N. Shah, Multi and mixed 3D-printing of graphene-hydroxyapatite hybrid materials for complex tissue engineering, J Biomed Mater Res A. 105 (2017) 274–283. https://doi.org/10.1002/jbm.a.35684.

[178] A. Motealleh, S. Eqtesadi, F.H. Perera, A.L. Ortiz, P. Miranda, A. Pajares, R. Wendelbo, Reinforcing 13–93 bioglass scaffolds fabricated by robocasting and pressureless spark plasma sintering with graphene oxide, J Mech Behav Biomed Mater. 97 (2019) 108–116. https://doi.org/10.1016/j.jmbbm.2019.05.016.

[179] C. Wu, L. Xia, P. Han, M. Xu, B. Fang, J. Wang, J. Chang, Y. Xiao, Graphene-oxide-modified β-tricalcium phosphate bioceramics stimulate in vitro and in vivo osteogenesis, Carbon N Y. 93 (2015) 116–129. https://doi.org/10.1016/j.carbon.2015.04.048.
[180] Y. Zhang, D. Zhai, M. Xu, Q. Yao, J. Chang, C. Wu, 3D-printed bioceramic scaffolds with a Fe_3O_4/graphene oxide nanocomposite interface for hyperthermia therapy of bone tumor cells, J Mater Chem B. 4 (2016) 2874–2886. https://doi.org/10.1039/c6tb00390g.
[181] J. Chevalier, A. Liens, H. Reveron, F. Zhang, P. Reynaud, T. Douillard, L. Preiss, V. Sergo, V. Lughi, M. Swain, N. Courtois, Forty years after the promise of «ceramic steel?»: Zirconia-based composites with a metal-like mechanical behavior, Journal of the American Ceramic Society. 103 (2020) 1482–1513. https://doi.org/10.1111/jace.16903.
[182] E. Kocyło, G. Franchin, P. Colombo, A. Chmielarz, M. Potoczek, Hydroxyapatite-coated ZrO_2 scaffolds with a fluorapatite intermediate layer produced by direct ink writing, J Eur Ceram Soc. 41 (2021) 920–928. https://doi.org/10.1016/j.jeurceramsoc.2020.08.021.
[183] M. Houmard, Q. Fu, M. Genet, E. Saiz, A.P. Tomsia, On the structural, mechanical, and biodegradation properties of HA/β-TCP robocast scaffolds, J Biomed Mater Res B Appl Biomater. 101 (2013) 1233–1242. https://doi.org/10.1002/jbm.b.32935.
[184] S.I. Roohani-Esfahani, P. Newman, H. Zreiqat, Design and fabrication of 3D printed scaffolds with a mechanical strength comparable to cortical bone to repair large bone defects, Sci Rep. 6 (2016) 1–8. https://doi.org/10.1038/srep19468.
[185] X. Wang, T. Li, H. Ma, D. Zhai, C. Jiang, J. Chang, J. Wang, C. Wu, A 3D-printed scaffold with MoS_2 nanosheets for tumor therapy and tissue regeneration, NPG Asia Mater. 9 (2017) e376-14. https://doi.org/10.1038/am.2017.47.
[186] D. He, C. Zhuang, C. Chen, S. Xu, X. Yang, C. Yao, J. Ye, C. Gao, Z. Gou, Rational design and fabrication of porous calcium-magnesium silicate constructs that enhance angiogenesis and improve orbital implantation, ACS Biomater Sci Eng. 2 (2016) 1519–1527. https://doi.org/10.1021/acsbiomaterials.6b00282.
[187] H. Elsayed, P. Colombo, E. Bernardo, Direct ink writing of wollastonite-diopside glass-ceramic scaffolds from a silicone resin and engineered fillers, J Eur Ceram Soc. 37 (2017) 4187–4195. https://doi.org/10.1016/j.jeurceramsoc.2017.05.021.
[188] M. Griffin, A. Bayat, Electrical stimulation in bone healing: Critical analysis by evaluating levels of evidence, Eplasty. 11 (2011) e34.
[189] S. Meng, M. Rouabhia, Z. Zhang, Electrical stimulation in tissue regeneration, in: Applied Biomedical Engineering, InTech, 2011. https://doi.org/10.5772/18874.
[190] S. Eqtesadi, A. Motealleh, A. Pajares, P. Miranda, Effect of milling media on processing and performance of 13-93 bioactive glass scaffolds fabricated by robocasting, Ceram Int. 41 (2015) 1379–1389. https://doi.org/10.1016/j.ceramint.2014.09.071.
[191] S. Fu, H. Hu, J. Chen, Y. Zhu, S. Zhao, Silicone resin derived larnite/C scaffolds via 3D printing for potential tumor therapy and bone regeneration, Chemical Engineering Journal. 382 (2020) 122928. https://doi.org/10.1016/j.cej.2019.122928.
[192] A. Thomas, K.C.R. Kolan, M.C. Leu, G.E. Hilmas, Freeform extrusion fabrication of titanium fiber reinforced 13–93 bioactive glass scaffolds, J Mech Behav Biomed Mater. 70 (2017) 43–52. https://doi.org/10.1016/j.jmbbm.2016.12.025.
[193] Y.-C. Fung, Bone and cartilage, in: Biomechanics, Springer, New York, NY, 1993.
[194] B.K. Hall, K. Brian, Bone, Telford Press, 1990.
[195] M. Casas-Luna, S. Tkachenko, M. Horynová, L. Klakurková, P. Gejdos, S. Diaz-De-La-Torre, L. Celko, J. Kaiser, E.B. Montufar, Interpenetrated magnesium-tricalcium phosphate composite: Manufacture, characterization and in vitro degradation test, Acta Metallurgica Sinica (English Letters). 30 (2017) 319–325. https://doi.org/10.1007/s40195-017-0560-0.

[196] J.F. Mano, R.A. Sousa, L.F. Boesel, N.M. Neves, R.L. Reis, Bioinert, biodegradable and injectable polymeric matrix composites for hard tissue replacement: state of the art and recent developments, Compos Sci Technol. 64 (2004) 789–817. https://doi.org/10.1016/j.compscitech.2003.09.001.

[197] X. Wang, B.Z. Molino, S. Pitkänen, M. Ojansivu, C. Xu, M. Hannula, J. Hyttinen, S. Miettinen, L. Hupa, G. Wallace, 3D Scaffolds of Polycaprolactone/Copper-Doped Bioactive Glass: Architecture Engineering with Additive Manufacturing and Cellular Assessments in a Coculture of Bone Marrow Stem Cells and Endothelial Cells, ACS Biomater Sci Eng. 5 (2019) 4496–4510. https://doi.org/10.1021/acsbiomaterials.9b00105.

[198] Q. Peng, Z.-R. Zhang, T. Gong, G.-Q. Chen, X. Sun, A rapid-acting, long-acting insulin formulation based on a phospholipid complex loaded PHBHHx nanoparticles, Biomaterials. 33 (2012) 1583–1588. https://doi.org/10.1016/j.biomaterials.2011.10.072.

[199] D. Mondal, T.L. Willett, Mechanical properties of nanocomposite biomaterials improved by extrusion during direct ink writing, J Mech Behav Biomed Mater. 104 (2020) 103653. https://doi.org/10.1016/j.jmbbm.2020.103653.

[200] D. Mondal, A. Srinivasan, P. Comeau, Y.C. Toh, T.L. Willett, Acrylated epoxidized soybean oil/hydroxyapatite-based nanocomposite scaffolds prepared by additive manufacturing for bone tissue engineering, Materials Science and Engineering C. 118 (2021) 111400. https://doi.org/10.1016/j.msec.2020.111400.

[201] H. Yun, S. Kim, E.K. Park, Bioactive glass–poly (ε-caprolactone) composite scaffolds with 3 dimensionally hierarchical pore networks, Materials Science and Engineering: C. 31 (2011) 198–205. https://doi.org/10.1016/j.msec.2010.08.020.

[202] B. Dorj, J.-E. Won, J.-H. Kim, S.-J. Choi, U.S. Shin, H.-W. Kim, Robocasting nanocomposite scaffolds of poly(caprolactone)/hydroxyapatite incorporating modified carbon nanotubes for hard tissue reconstruction, J Biomed Mater Res A. 101A (2013) 1670–1681. https://doi.org/10.1002/jbm.a.34470.

[203] X. Xie, Y. Mai, X. Zhou, Dispersion and alignment of carbon nanotubes in polymer matrix: A review, Materials Science and Engineering: R: Reports. 49 (2005) 89–112. https://doi.org/10.1016/j.mser.2005.04.002.

[204] D. Lahiri, F. Rouzaud, S. Namin, A.K. Keshri, J.J. Valdés, L. Kos, N. Tsoukias, A. Agarwal, Carbon Nanotube Reinforced Polylactide−Caprolactone Copolymer: Mechanical Strengthening and Interaction with Human Osteoblasts in Vitro, ACS Appl Mater Interfaces. 1 (2009) 2470–2476. https://doi.org/10.1021/am900423q.

[205] U.S. Shin, I.-K. Yoon, G.-S. Lee, W.-C. Jang, J.C. Knowles, H.-W. Kim, Carbon Nanotubes in Nanocomposites and Hybrids with Hydroxyapatite for Bone Replacements, J Tissue Eng. (2011). https://doi.org/10.4061/2011/674287.

[206] J. Ramontja, S.S. Ray, S.K. Pillai, A.S. Luyt, High-Performance Carbon Nanotube-Reinforced Bioplastic, Macromol Mater Eng. (2009) NA-NA. https://doi.org/10.1002/mame.200900197.

[207] W.-M. Chiu, Y.-A. Chang, H.-Y. Kuo, M.-H. Lin, H.-C. Wen, A study of carbon nanotubes/biodegradable plastic polylactic acid composites, J Appl Polym Sci. 108 (2008) 3024–3030. https://doi.org/10.1002/app.27796.

[208] E.M. Gonçalves, F.J. Oliveira, R.F. Silva, M.A. Neto, M.H. Fernandes, M. Amaral, M. Vallet-Regí, M. Vila, Three-dimensional printed PCL-hydroxyapatite scaffolds filled with CNTs for bone cell growth stimulation, J Biomed Mater Res B Appl Biomater. 104 (2016) 1210–1219. https://doi.org/10.1002/jbm.b.33432.

[209] N. Patel, S.M. Best, W. Bonfield, I.R. Gibson, K.A. Hing, E. Damien, P.A. Revell, A comparative study on the in vivo behavior of hydroxyapatite and silicon substituted

hydroxyapatite granules., J Mater Sci Mater Med. 13 (2002) 1199–206. https://doi.org/10.1023/a:1021114710076.

[210] A. Bianco, I. Cacciotti, M. Lombardi, L. Montanaro, Si-substituted hydroxyapatite nanopowders: Synthesis, thermal stability and sinterability, Mater Res Bull. 44 (2009) 345–354. https://doi.org/10.1016/j.materresbull.2008.05.013.

[211] A.M. Deliormanli, M. Türk, H. Atmaca, Response of mouse bone marrow mesenchymal stem cells to graphene-containing grid-like bioactive glass scaffolds produced by robocasting, J Biomater Appl. 33 (2018) 488–500. https://doi.org/10.1177/0885328218799610.

[212] F.J. Martínez-Vázquez, P. Miranda, F. Guiberteau, A. Pajares, Reinforcing bioceramic scaffolds with *in situ* synthesized ε-polycaprolactone coatings, J Biomed Mater Res A. 101 (2013) 3551–3559. https://doi.org/10.1002/jbm.a.34657.

[213] A. Motealleh, S. Eqtesadi, A. Pajares, P. Miranda, D. Salamon, K. Castkova, Case study: Reinforcement of 45S5 bioglass robocast scaffolds by HA/PCL nanocomposite coatings, J Mech Behav Biomed Mater. 75 (2017) 114–118. https://doi.org/10.1016/j.jmbbm.2017.07.012.

[214] A. Motealleh, S. Eqtesadi, A. Pajares, P. Miranda, Enhancing the mechanical and *in vitro* performance of robocast bioglass scaffolds by polymeric coatings: Effect of polymer composition, J Mech Behav Biomed Mater. 84 (2018) 35–45. https://doi.org/10.1016/j.jmbbm.2018.04.022.

[215] P. Miranda, A. Pajares, E. Saiz, A.P. Tomsia, F. Guiberteau, Fracture modes under uniaxial compression in hydroxyapatite scaffolds fabricated by robocasting, J Biomed Mater Res A. 83 (2007) 646–655. https://doi.org/10.1002/jbm.a.31272.

[216] Y. Zhou, S. Jeelani, T. Lacy, Experimental study on the mechanical behavior of carbon/epoxy composites with a carbon nanofiber-modified matrix, J Compos Mater. 48 (2014) 3659–3672. https://doi.org/10.1177/0021998313512348.

[217] H. Zhang, Z. Zhang, C. Breidt, Comparison of short carbon fibre surface treatments on epoxy composites, Compos Sci Technol. 64 (2004) 2021–2029. https://doi.org/10.1016/j.compscitech.2004.02.009.

[218] Y.H. Sheng, Different Content of Short Carbon Fiber Influence on the Hardness of Thermo Plastic Resin Composite Material, Applied Mechanics and Materials. 490–491 (2014) 280–283. https://doi.org/10.4028/www.scientific.net/AMM.490-491.280.

[219] U.G.K. Wegst, H. Bai, E. Saiz, A.P. Tomsia, R.O. Ritchie, Bioinspired structural materials, Nat Mater. 14 (2015) 23–36. https://doi.org/10.1038/nmat4089.

[220] F.J. Martínez-Vázquez, F.H. Perera, P. Miranda, A. Pajares, F. Guiberteau, Improving the compressive strength of bioceramic robocast scaffolds by polymer infiltration, Acta Biomater. 6 (2010) 4361–4368. https://doi.org/10.1016/j.actbio.2010.05.024.

[221] F.J. Martínez-Vázquez, A. Pajares, F. Guiberteau, P. Miranda, Effect of polymer infiltration on the flexural behavior of β-tricalcium phosphate robocast scaffolds, Materials. 7 (2014) 4001–4018. https://doi.org/10.3390/ma7054001.

[222] F.J. Martínez-Vázquez, F.H. Perera, I. Van Der Meulen, A. Heise, A. Pajares, P. Miranda, Impregnation of β-tricalcium phosphate robocast scaffolds by in situ polymerization, J Biomed Mater Res A. 101 (2013) 3086–3096. https://doi.org/10.1002/jbm.a.34609.

[223] S. Eqtesadi, A. Motealleh, A. Pajares, F. Guiberteau, P. Miranda, Influence of sintering temperature on the mechanical properties of ε-PCL-impregnated 45S5 bioglass-derived scaffolds fabricated by robocasting, J Eur Ceram Soc. 35 (2015) 3985–3993. https://doi.org/10.1016/j.jeurceramsoc.2015.06.021.

[224] S. Eqtesadi, A. Motealleh, F.H. Perera, A. Pajares, P. Miranda, Poly-(lactic acid) infiltration of 45S5 Bioglass® robocast scaffolds: Chemical interaction and its

deleterious effect in mechanical enhancement, Mater Lett. 163 (2016) 196–200. https://doi.org/10.1016/j.matlet.2015.10.073.
[225] J.J. Blaker, A. Bismarck, A.R. Boccaccini, A.M. Young, S.N. Nazhat, Premature degradation of poly(α-hydroxyesters) during thermal processing of Bioglass®-containing composites, Acta Biomater. 6 (2010) 756–762. https://doi.org/10.1016/j.actbio.2009.08.020.
[226] N. Ginsac, J.-M. Chenal, S. Meille, E. Pacard, R. Zenati, D.J. Hartmann, J. Chevalier, Crystallization processes at the surface of polylactic acid-bioactive glass composites during immersion in simulated body fluid, J Biomed Mater Res B Appl Biomater. 99B (2011) 412–419. https://doi.org/10.1002/jbm.b.31913.
[227] B. Zhang, L. Guo, H. Chen, Y. Ventikos, R.J. Narayan, J. Huang, Finite element evaluations of the mechanical properties of polycaprolactone/hydroxyapatite scaffolds by direct ink writing: Effects of pore geometry, J Mech Behav Biomed Mater. 104 (2020) 103665. https://doi.org/10.1016/j.jmbbm.2020.103665.
[228] M. Peroglio, L. Gremillard, J. Chevalier, L. Chazeau, C. Gauthier, T. Hamaide, Toughening of bio-ceramics scaffolds by polymer coating, J Eur Ceram Soc. 27 (2007) 2679–2685. https://doi.org/10.1016/j.jeurceramsoc.2006.10.016.
[229] D. Taylor, J.-H. Kuiper, The prediction of stress fractures using a 'stressed volume' concept, Journal of Orthopaedic Research. 19 (2001) 919–926. https://doi.org/10.1016/S0736-0266(01)00009-2.
[230] L.L. Hench, J.R. Jones, Materials Minerals, Mining, Biomaterials, Artificial Organs and Tissue Engineering, Woodhead Publishing, 2005.
[231] T.M. Keaveny, W.C. Hayes, Mechanical properties of cortical and trabecular bone, in: Bone, 1992: pp. 285–344.
[232] D. Seliktar, Designing Cell-Compatible Hydrogels for Biomedical Applications, Science (1979). 336 (2012) 1124–1128. https://doi.org/10.1126/science.1214804.
[233] J. Malda, J. Visser, F.P. Melchels, T. Jüngst, W.E. Hennink, W.J.A. Dhert, J. Groll, D.W. Hutmacher, 25th Anniversary Article: Engineering Hydrogels for Biofabrication, Advanced Materials. 25 (2013) 5011–5028. https://doi.org/10.1002/adma.201302042.
[234] F. Zou, N. Zhao, X. Fu, J. Diao, Y. Ma, X. Cao, S. Wan, S. Zhong, Y. Wang, Enhanced osteogenic differentiation and biomineralization in mouse mesenchymal stromal cells on a β-TCP robocast scaffold modified with collagen nanofibers, RSC Adv. 6 (2016) 23588–23598. https://doi.org/10.1039/c5ra26670j.
[235] B. Dorj, J.-H. Park, H.-W. Kim, Robocasting chitosan/nanobioactive glass dual-pore structured scaffolds for bone engineering, Mater Lett. 73 (2012) 119–122. https://doi.org/10.1016/j.matlet.2011.12.107.
[236] F.J. Martínez-Vázquez, M. V. Cabañas, J.L. Paris, D. Lozano, M. Vallet-Regí, Fabrication of novel Si-doped hydroxyapatite/gelatine scaffolds by rapid prototyping for drug delivery and bone regeneration, Acta Biomater. 15 (2015) 200–209. https://doi.org/10.1016/j.actbio.2014.12.021.
[237] K.-F. Lin, S. He, Y. Song, C.-M. Wang, Y. Gao, J.-Q. Li, P. Tang, Z. Wang, L. Bi, G.-X. Pei, Low-temperature additive manufacturing of biomimic three-dimensional hydroxyapatite/collagen scaffolds for bone regeneration, ACS Appl Mater Interfaces. 8 (2016) 6905–6916. https://doi.org/10.1021/acsami.6b00815.
[238] M.R. Sommer, L. Alison, C. Minas, E. Tervoort, P.A. Rühs, A.R. Studart, 3D printing of concentrated emulsions into multiphase biocompatible soft materials, Soft Matter. 13 (2017) 1794–1803. https://doi.org/10.1039/C6SM02682F.
[239] C.F. Marques, S.M. Olhero, P.M.C. Torres, J.C.C. Abrantes, S. Fateixa, H.I.S. Nogueira, I.A.C. Ribeiro, A. Bettencourt, A. Sousa, P.L. Granja, J.M.F. Ferreira, Novel sintering-free scaffolds obtained by additive manufacturing for concurrent bone regeneration and

drug delivery: Proof of concept, Materials Science and Engineering C. 94 (2019) 426–436. https://doi.org/10.1016/j.msec.2018.09.050.

[240] T. Cebe, N. Ahuja, F. Monte, K. Awad, K. Vyavhare, P. Aswath, J. Huang, M. Brotto, V. Varanasi, Novel 3D-printed methacrylated chitosan-laponite nanosilicate composite scaffolds enhance cell growth and biomineral formation in MC3T3 pre-osteoblasts, (2018). https://doi.org/10.1557/jmr.2018.260.

[241] K. Zafeiris, D. Brasinika, A. Karatza, E.P. Koumoulos, I.K. Karoussis, K. Kyriakidou, C.A. Charitidis, Additive manufacturing of hydroxyapatite – Chitosan – Genipin composite scaffolds for bone tissue engineering applications, Materials Science and Engineering: C. (2020) 111639. https://doi.org/10.1016/j.msec.2020.111639.

[242] A. Kumar, A.R. Akkineni, B. Basu, M. Gelinsky, Three-dimensional plotted hydroxyapatite scaffolds with predefined architecture: Comparison of stabilization by alginate cross-linking versus sintering, J Biomater Appl. 30 (2016) 1168–1181. https://doi.org/10.1177/0885328215617058.

[243] P. Rattanakit, S.E. Moulton, K.S. Santiago, S. Liawruangrath, G.G. Wallace, Extrusion printed polymer structures: A facile and versatile approach to tailored drug delivery platforms, Int J Pharm. 422 (2012) 254–263. https://doi.org/10.1016/j.ijpharm.2011.11.007.

[244] D. Therriault, S.R. White, J.A. Lewis, Chaotic mixing in three-dimensional microvascular networks fabricated by direct-write assembly, Nat Mater. 2 (2003) 265–271. https://doi.org/10.1038/nmat863.

[245] S.S. Ramirez Caballero, E. Saiz, A. Montembault, S. Tadier, E. Maire, L. David, T. Delair, L. Gremillard, 3-D printing of chitosan-calcium phosphate inks: rheology, interactions and characterization, J Mater Sci Mater Med. 30 (2019). https://doi.org/10.1007/s10856-018-6201-y.

[246] K. Ziv, H. Nuhn, Y. Ben-Haim, L.S. Sasportas, P.J. Kempen, T.P. Niedringhaus, M. Hrynyk, R. Sinclair, A.E. Barron, S.S. Gambhir, A tunable silk–alginate hydrogel scaffold for stem cell culture and transplantation, Biomaterials. 35 (2014) 3736–3743. https://doi.org/10.1016/j.biomaterials.2014.01.029.

[247] E. West, M. Xu, T. Woodruff, L. Shea, Physical properties of alginate hydrogels and their effects on in vitro follicle development, Biomaterials. 28 (2007) 4439–4448. https://doi.org/10.1016/j.biomaterials.2007.07.001.

[248] S. Ishack, A. Mediero, T. Wilder, J.L. Ricci, B.N. Cronstein, Bone regeneration in critical bone defects using three-dimensionally printed β-tricalcium phosphate/hydroxyapatite scaffolds is enhanced by coating scaffolds with either dipyridamole or BMP-2, J Biomed Mater Res B Appl Biomater. 105 (2017) 366–375. https://doi.org/10.1002/jbm.b.33561.

[249] M. Touri, F. Moztarzadeh, N.A.A. Osman, M.M. Dehghan, M. Mozafari, 3D–printed biphasic calcium phosphate scaffolds coated with an oxygen generating system for enhancing engineered tissue survival, Materials Science and Engineering C. 84 (2018) 236–242. https://doi.org/10.1016/j.msec.2017.11.037.

[250] M. Touri, F. Moztarzadeh, N.A.A. Osman, M.M. Dehghan, M. Mozafari, Breathable tissue engineering scaffolds: An efficient design-optimization by additive manufacturing, Mater Today Proc. 5 (2018) 15813–15820. https://doi.org/10.1016/j.matpr.2018.05.079.

[251] M. Touri, F. Moztarzadeh, N.A.A. Osman, M.M. Dehghan, M. Mozafari, Optimisation and biological activities of bioceramic robocast scaffolds provided with an oxygen-releasing coating for bone tissue engineering applications, Ceram Int. 45 (2019) 805–816. https://doi.org/10.1016/j.ceramint.2018.09.247.

[252] Y. Song, K. Lin, S. He, C. Wang, S. Zhang, D. Li, J. Wang, T. Cao, L. Bi, G. Pei, Nano-biphasic calcium phosphate/polyvinyl alcohol composites with enhanced bioactivity for bone repair via low-temperature three-dimensional printing and loading with platelet-rich fibrin, Int J Nanomedicine. 13 (2018) 505–523. https://doi.org/10.2147/IJN.S152105.

[253] F. Fahimipour, M. Rasoulianboroujeni, E. Dashtimoghadam, K. Khoshroo, M. Tahriri, F. Bastami, D. Lobner, L. Tayebi, 3D printed TCP-based scaffold incorporating VEGF-loaded PLGA microspheres for craniofacial tissue engineering, Dental Materials. 33 (2017) 1205–1216. https://doi.org/10.1016/j.dental.2017.06.016.

[254] C.-Y. Liaw, M. Guvendiren, Current and emerging applications of 3D printing in medicine, Biofabrication. 9 (2017) 024102. https://doi.org/10.1088/1758-5090/aa7279.

[255] A. Zadpoor, Design for additive bio-manufacturing: From patient-specific medical devices to rationally designed meta-biomaterials, Int J Mol Sci. 18 (2017) 1607. https://doi.org/10.3390/ijms18081607.

[256] C. Lee Ventola, Medical applications for 3D printing: Current and projected uses, P and T. 39 (2014) 704–711.

[257] R.R. Jose, J.E. Brown, K.E. Polido, F.G. Omenetto, D.L. Kaplan, Polyol-silk bioink formulations as two-part room-temperature curable materials for 3D printing, ACS Biomater Sci Eng. 1 (2015) 780–788. https://doi.org/10.1021/acsbiomaterials.5b00160.

[258] L. Del-Mazo-Barbara, M.P. Ginebra, Rheological characterisation of ceramic inks for 3D direct ink writing: A review, J Eur Ceram Soc. 41 (2021) 18–33. https://doi.org/10.1016/j.jeurceramsoc.2021.08.031.

[259] A.M. Stanciuc, C.M. Sprecher, J. Adrien, L.I. Roiban, M. Alini, L. Gremillard, M. Peroglio, Robocast zirconia-toughened alumina scaffolds: Processing, structural characterisation and interaction with human primary osteoblasts, J Eur Ceram Soc. 38 (2018) 845–853. https://doi.org/10.1016/j.jeurceramsoc.2017.08.031.

[260] R.C. Richard, R.N. Oliveira, G.D.A. Soares, R.M.S.M. Thiré, Direct-write assembly of 3D scaffolds using colloidal calcium phosphates inks, Revista Matéria. 19 (2014) 61–67. https://doi.org/10.1590/S1517-70762014000100009.

[261] C.F. Marques, F.H. Perera, A. Marote, S. Ferreira, S.I. Vieira, S. Olhero, P. Miranda, J.M.F. Ferreira, Biphasic calcium phosphate scaffolds fabricated by direct write assembly: Mechanical, anti-microbial and osteoblastic properties, J Eur Ceram Soc. 37 (2017) 359–368. https://doi.org/10.1016/j.jeurceramsoc.2016.08.018.

[262] P. Miranda, E. Saiz, K. Gryn, A.P. Tomsia, Sintering and robocasting of β-tricalcium phosphate scaffolds for orthopaedic applications, Acta Biomater. 2 (2006) 457–466. https://doi.org/10.1016/j.actbio.2006.02.004.

[263] M. Mao, J. He, X. Li, B. Zhang, Q. Lei, Y. Liu, D. Li, The emerging frontiers and applications of high-resolution 3D printing, Micromachines (Basel). 8 (2017). https://doi.org/10.3390/mi8040113.

[264] T. Beran, T. Mulholland, F. Henning, N. Rudolph, T.A. Osswald, Nozzle clogging factors during fused filament fabrication of spherical particle filled polymers, Addit Manuf. 23 (2018) 206–214. https://doi.org/10.1016/j.addma.2018.08.009.

[265] B.P. Croom, A. Abbott, J.W. Kemp, L. Rueschhoff, L. Smieska, A. Woll, S. Stoupin, H. Koerner, Mechanics of nozzle clogging during direct ink writing of fiber-reinforced composites, Addit Manuf. (2020) 101701. https://doi.org/10.1016/j.addma.2020.101701.

[266] J.E. Smay, J. Cesarano, J.A. Lewis, Colloidal inks for directed assembly of 3-D periodic structures, Langmuir. 18 (2002) 5429–5437. https://doi.org/10.1021/la0257135.

[267] J.G. Dellinger, J. Cesarano III, R.D. Jamison, Robotic deposition of model hydroxyapatite scaffolds with multiple architectures and multiscale porosity for bone

tissue engineering, J Biomed Mater Res A. 82 (2007) 383–394. https://doi.org/10.1002/jbm.a.31072.

[268] E. García-Tuñon, S. Barg, J. Franco, R. Bell, S. Eslava, E. D'Elia, R.C. Maher, F. Guitian, E. Saiz, Printing in three dimensions with graphene, Advanced Materials. 27 (2015) 1688–1693. https://doi.org/10.1002/adma.201405046.

[269] M. Hirsch, A. Charlet, E. Amstad, 3D printing of strong and tough double network granular hydrogels, Adv Funct Mater. 2005929 (2020). https://doi.org/10.1002/adfm.202005929.

[270] H. Shao, X. Yang, Y. He, J. Fu, L. Liu, L. Ma, L. Zhang, G. Yang, C. Gao, Z. Gou, Bioactive glass-reinforced bioceramic ink writing scaffolds: Sintering, microstructure and mechanical behavior, Biofabrication. 7 (2015). https://doi.org/10.1088/1758-5090/7/3/035010.

[271] S.S. Ramirez Caballero, H. Elsayed, S. Tadier, A. Montembault, E. Maire, L. David, T. Delair, P. Colombo, L. Gremillard, Fabrication and characterization of hardystonite-chitosan biocomposite scaffolds, Ceram Int. 45 (2019) 8804–8814. https://doi.org/10.1016/j.ceramint.2019.01.206.

[272] M. Vila, M. Cicuéndez, J. Sánchez-Marcos, V. Fal-Miyar, M. Manzano, C. Prieto, M. Vallet-Regi, Electrical stimuli to increase cell proliferation on carbon nanotubes/mesoporous silica composites for drug delivery, J Biomed Mater Res A. 101A (2013) 213–221. https://doi.org/10.1002/jbm.a.34325.

[273] H. Yang, S. Yang, X. Chi, J.R.G. Evans, Fine ceramic lattices prepared by extrusion freeforming, J Biomed Mater Res B Appl Biomater. 79B (2006) 116–121. https://doi.org/10.1002/jbm.b.30520.

[274] S. Michna, W. Wu, J.A. Lewis, Concentrated hydroxyapatite inks for direct-write assembly of 3-D periodic scaffolds, Biomaterials. 26 (2005) 5632–5639. https://doi.org/10.1016/j.biomaterials.2005.02.040.

[275] J. Groll, T. Boland, T. Blunk, J.A. Burdick, D.-W. Cho, P.D. Dalton, B. Derby, G. Forgacs, Q. Li, V.A. Mironov, L. Moroni, M. Nakamura, W. Shu, S. Takeuchi, G. Vozzi, T.B.F. Woodfield, T. Xu, J.J. Yoo, J. Malda, Biofabrication: reappraising the definition of an evolving field, Biofabrication. 8 (2016) 013001. https://doi.org/10.1088/1758-5090/8/1/013001.

[276] S. Wüst, M.E. Godla, R. Müller, S. Hofmann, Tunable hydrogel composite with two-step processing in combination with innovative hardware upgrade for cell-based three-dimensional bioprinting, Acta Biomater. 10 (2014) 630–640. https://doi.org/10.1016/j.actbio.2013.10.016.

[277] S. Khalil, J. Nam, W. Sun, Multi-nozzle deposition for construction of 3D biopolymer tissue scaffolds, Rapid Prototyp J. 11 (2005) 9–17. https://doi.org/10.1108/13552540510573347.

[278] A. Barba, Y. Maazouz, A. Diez-Escudero, K. Rappe, M. Espanol, E.B. Montufar, C. Öhman-Mägi, C. Persson, P. Fontecha, M.C. Manzanares, J. Franch, M.P. Ginebra, Osteogenesis by foamed and 3D-printed nanostructured calcium phosphate scaffolds: Effect of pore architecture, Acta Biomater. 79 (2018) 135–147. https://doi.org/10.1016/j.actbio.2018.09.003.

[279] M.-W. Sa, J.Y. Kim, Fabrication and evaluation of 3D β-TCP scaffold by novel direct-write assembly method, Journal of Mechanical Science and Technology. 29 (2015) 5369–5376. https://doi.org/10.1007/s12206-015-1138-2.

[280] A. Nommeots-Nomm, P.D. Lee, J.R. Jones, Direct ink writing of highly bioactive glasses, J Eur Ceram Soc. 38 (2018) 837–844. https://doi.org/10.1016/j.jeurceramsoc.2017.08.006.

[281] J. Barberi, F. Baino, E. Fiume, G. Orlygsson, A. Nommeots-Nomm, J. Massera, E. Verné, Robocasting of SiO_2-based bioactive glass scaffolds with porosity gradient for bone regeneration and potential load-bearing applications, Materials. 12 (2019). https://doi.org/10.3390/ma12172691.

[282] M. Houmard, Q. Fu, E. Saiz, A.P. Tomsia, Sol-gel method to fabricate CaP scaffolds by robocasting for tissue engineering, J Mater Sci Mater Med. 23 (2012) 921–930. https://doi.org/10.1007/s10856-012-4561-2.

[283] G. Pierin, C. Grotta, P. Colombo, C. Mattevi, Direct Ink Writing of micrometric SiOC ceramic structures using a preceramic polymer, J Eur Ceram Soc. 36 (2016) 1589–1594. https://doi.org/10.1016/j.jeurceramsoc.2016.01.047.

[284] H. Elsayed, F. Carraro, S. Agnoli, D. Bellucci, V. Cannillo, L. Ferroni, C. Gardin, B. Zavan, E. Bernardo, Direct ink writing of silica-carbon-calcite composite scaffolds from a silicone resin and fillers, J Eur Ceram Soc. 38 (2018) 5200–5207. https://doi.org/10.1016/j.jeurceramsoc.2018.07.049.

[285] C. Gao, M.N. Rahaman, Q. Gao, A. Teramoto, K. Abe, Robotic deposition and *in vitro* characterization of 3D gelatin-bioactive glass hybrid scaffolds for biomedical applications, J Biomed Mater Res A. 101 A (2013) 2027–2037. https://doi.org/10.1002/jbm.a.34496.

[286] Y. Maazouz, E.B. Montufar, J. Guillem-Marti, I. Fleps, C. Öhman, C. Persson, M.P. Ginebra, Robocasting of biomimetic hydroxyapatite scaffolds using self-setting inks, J Mater Chem B. 2 (2014) 5378–5386. https://doi.org/10.1039/c4tb00438h.

[287] L.J. Gibson, The hierarchical structure and mechanics of plant materials, J R Soc Interface. 9 (2012) 2749–2766. https://doi.org/10.1098/rsif.2012.0341.

[288] C. Polzin, D. Günther, H. Seitz, 3D printing of porous Al_2O_3 and SiC ceramics, Journal of Ceramic Science and Technology. 6 (2015) 141–146. https://doi.org/10.4416/JCST2015-00013.

[289] J. Maurath, J. Dittmann, N. Schultz, N. Willenbacher, Fabrication of highly porous glass filters using capillary suspension processing, Sep Purif Technol. 149 (2015) 470–478. https://doi.org/10.1016/j.seppur.2015.06.022.

[290] H. Elsayed, M. Picicco, A. Dasan, J. Kraxner, D. Galusek, E. Bernardo, Glass powders and reactive silicone binder: Interactions and application to additive manufacturing of bioactive glass-ceramic scaffolds, Ceram Int. 45 (2019) 13740–13746. https://doi.org/10.1016/j.ceramint.2019.04.070.

[291] S.M. Olhero, P.M.C. Torres, J. Mesquita-Guimarães, J. Baltazar, J. Pinho-da-Cruz, S. Gouveia, Conventional versus additive manufacturing in the structural performance of dense alumina-zirconia ceramics: 20 years of research, challenges and future perspectives, J Manuf Process. 77 (2022) 838–879. https://doi.org/10.1016/j.jmapro.2022.02.041.

[292] S. Lamnini, H. Elsayed, Y. Lakhdar, F. Baino, F. Smeacetto, E. Bernardo, Robocasting of advanced ceramics: ink optimization and protocol to predict the printing parameters - A review, Heliyon. 8 (2022) e10651. https://doi.org/10.1016/j.heliyon.2022.e10651.

[293] E. Peng, D. Zhang, J. Ding, Ceramic Robocasting: Recent Achievements, Potential, and Future Developments, Advanced Materials. 30 (2018). https://doi.org/10.1002/adma.201802404.

[294] J. Cesarano III, Review of robocasting technology, Materials Research Society Symposium - Proceedings. 542 (1999) 133–139.

[295] A. Shahzad, I. Lazoglu, Direct ink writing (DIW) of structural and functional ceramics: Recent achievements and future challenges, Compos B Eng. 225 (2021) 109249. https://doi.org/10.1016/j.compositesb.2021.109249.

[296] E.N. Udofia, W. Zhou, Microextrusion based 3D printing - A review, Solid Freeform Fabrication 2018: Proceedings of the 29th Annual International Solid Freeform Fabrication Symposium - An Additive Manufacturing Conference, SFF 2018. (2020) 2033–2060.
[297] H. Yuk, X. Zhao, A New 3D Printing Strategy by Harnessing Deformation, Instability, and Fracture of Viscoelastic Inks, Advanced Materials. 30 (2018). https://doi.org/10.1002/adma.201704028.
[298] J. Lefevere, S. Mullens, V. Meynen, The impact of formulation and 3D-printing on the catalytic properties of ZSM-5 zeolite, Chemical Engineering Journal. 349 (2018) 260–268. https://doi.org/10.1016/j.cej.2018.05.058.
[299] A.J. Young, R. Guillet-Nicolas, E.S. Marshall, F. Kleitz, A.J. Goodhand, L.B.L. Glanville, M.R. Reithofer, J.M. Chin, Direct ink writing of catalytically active UiO-66 polymer composites, Chemical Communications. 55 (2019) 2190–2193. https://doi.org/10.1039/c8cc10018g.
[300] J.R. Raney, N. Nadkarni, C. Daraio, D.M. Kochmann, J.A. Lewis, K. Bertoldi, Stable propagation of mechanical signals in soft media using stored elastic energy, Proceedings of the National Academy of Sciences. 113 (2016) 9722–9727. https://doi.org/10.1073/pnas.1604838113.
[301] A. Sydney Gladman, E.A. Matsumoto, R.G. Nuzzo, L. Mahadevan, J.A. Lewis, Biomimetic 4D printing, Nat Mater. 15 (2016) 413–418. https://doi.org/http://dx.doi.org/10.1038/nmat4544.
[302] K. Tian, J. Bae, S.E. Bakarich, C. Yang, R.D. Gately, G.M. Spinks, M. in het Panhuis, Z. Suo, J.J. Vlassak, 3D Printing of Transparent and Conductive Heterogeneous Hydrogel–Elastomer Systems, Advanced Materials. 29 (2017) 1604827. https://doi.org/10.1002/adma.201604827.
[303] D. Rus, M.T. Tolley, Design, fabrication and control of soft robots, Nature. 521 (2015) 467–475. https://doi.org/10.1038/nature14543.
[304] M. Wehner, R.L. Truby, D.J. Fitzgerald, B. Mosadegh, G.M. Whitesides, J.A. Lewis, R.J. Wood, An integrated design and fabrication strategy for entirely soft, autonomous robots, Nature. 536 (2016) 451–455. https://doi.org/10.1038/nature19100.
[305] D.B. Kolesky, K.A. Homan, M.A. Skylar-Scott, J.A. Lewis, Three-dimensional bioprinting of thick vascularized tissues, Proceedings of the National Academy of Sciences. 113 (2016) 3179–3184. https://doi.org/10.1073/pnas.1521342113.
[306] N. Guo, M.C. Leu, Additive manufacturing: technology, applications and research needs, Frontiers of Mechanical Engineering. 8 (2013) 215–243. https://doi.org/10.1007/s11465-013-0248-8.
[307] X. Ang, J.Y. Tey, W.H. Yeo, K.P.Y. Shak, A review on metallic and ceramic material extrusion method: Materials, rheology, and printing parameters, J Manuf Process. 90 (2023) 28–42. https://doi.org/10.1016/j.jmapro.2023.01.077.
[308] E. García-Tuñón, R. Agrawal, B. Ling, D.J.C. Dennis, Fourier-transform rheology and printability maps of complex fluids for three-dimensional printing, Physics of Fluids. 35 (2023). https://doi.org/10.1063/5.0128658.
[309] M.S. Faria, M.F.R.P. Alves, R. Cintra, F.J. Oliveira, C.M. Fernandes, D. Figueiredo, S.M. Olhero, Influence of ink rheology and post processing in the structural performance of silicon nitride-based ceramics fabricated by robocasting, Ceram Int. 49 (2023) 20968–20979. https://doi.org/10.1016/j.ceramint.2023.03.231.
[310] M. Yarahmadi, P. Barcelona, G. Fargas, E. Xuriguera, J.J. Roa, Optimization of the ceramic ink used in Direct Ink Writing through rheological properties characterization of zirconia-based ceramic materials, Ceram Int. 48 (2022) 4775–4781. https://doi.org/10.1016/j.ceramint.2021.11.013.

[311] F.W. Ostwald, W.J.L. de Waele, Über die Viskosität von Suspensionen, Kolloid Zeitschrift. 39 (1926).
[312] W.H. Herschel, R. Bulkley, Konsistenzmessungen von Gummi-Benzollösungen, Kolloid-Zeitschrift. 39 (1926) 291–300. https://doi.org/10.1007/BF01432034.
[313] M. Instruments, Understanding yield stress measurements, Annual Transactions of the Nordic Rheology Society. 21 (2012).
[314] N. Paxton, W. Smolan, T. Böck, F. Melchels, J. Groll, T. Jungst, Proposal to assess printability of bioinks for extrusion-based bioprinting and evaluation of rheological properties governing bioprintability, Biofabrication. 9 (2017). https://doi.org/10.1088/1758-5090/aa8dd8.
[315] J. Cesarano, A review of robocasting technology, Materials Research Society Symposium - Proceedings. 542 (1999) 133–139. https://doi.org/10.1557/proc-542-133.
[316] A. Paterlini, S. Le Grill, F. Brouillet, C. Combes, D. Grossin, G. Bertrand, Robocasting of self-setting bioceramics: from paste formulation to 3D part characteristics, Open Ceramics. 5 (2021) 100070. https://doi.org/10.1016/j.oceram.2021.100070.
[317] J. Baltazar, P.M.C. Torres, J. Dias-de-Oliveira, J. Pinho-da-Cruz, S. Gouveia, S. Olhero, Influence of filament patterning in structural properties of dense alumina ceramics printed by robocasting, J Manuf Process. 68 (2021) 569–582. https://doi.org/10.1016/j.jmapro.2021.05.043.
[318] M.H. Monfared, A. Nemati, F. Loghman, M. Ghasemian, A. Farzin, N. Beheshtizadeh, M. Azami, A deep insight into the preparation of ceramic bone scaffolds utilizing robocasting technique, Ceram Int. 48 (2022) 5939–5954. https://doi.org/10.1016/j.ceramint.2021.11.268.
[319] X. Li, K. Hyun, Rheological study of the effect of polyethylene oxide (PEO) homopolymer on the gelation of PEO-PPO-PEO triblock copolymer in aqueous solution, Korea-Australia Rheology Journal. 30 (2018) 109–125. https://doi.org/10.1007/s13367-018-0012-z.
[320] B. Basu, Toughening of yttria-stabilised tetragonal zirconia ceramics, International Materials Reviews. 50 (2005) 239–256. https://doi.org/10.1179/174328005X41113.
[321] C. Wei, G. Montagnac, B. Reynard, N. Le Roux, L. Gremillard, Interplay between internal stresses and matrix stiffness influences hydrothermal ageing behaviour of zirconia-toughened-alumina, Acta Mater. 185 (2020) 55–65. https://doi.org/10.1016/j.actamat.2019.11.061.
[322] S. Sequeira, M.H. Fernandes, N. Neves, M.M. Almeida, Development and characterization of zirconia–alumina composites for orthopedic implants, Ceram Int. 43 (2017) 693–703. https://doi.org/10.1016/j.ceramint.2016.09.216.
[323] B.C. Spies, M. Sperlich, J. Fleiner, S. Stampf, R.J. Kohal, Alumina reinforced zirconia implants: 1-year results from a prospective cohort investigation, Clin Oral Implants Res. 27 (2016) 481–490. https://doi.org/10.1111/clr.12560.
[324] R.J. Kohal, M. Wolkewitz, C. Mueller, Alumina-reinforced zirconia implants: Survival rate and fracture strength in a masticatory simulation trial, Clin Oral Implants Res. 21 (2010) 1345–1352. https://doi.org/10.1111/j.1600-0501.2010.01954.x.
[325] J. Grech, E. Antunes, Zirconia in dental prosthetics: A literature review, Journal of Materials Research and Technology. 8 (2019) 4956–4964. https://doi.org/10.1016/j.jmrt.2019.06.043.
[326] A. Maji, G. Choubey, Microstructure and Mechanical Properties of Alumina Toughened Zirconia (ATZ), Mater Today Proc. 5 (2018) 7457–7465. https://doi.org/10.1016/j.matpr.2017.11.417.
[327] E. Schwarzer, S. Holtzhausen, U. Scheithauer, C. Ortmann, T. Oberbach, T. Moritz, A. Michaelis, Process development for additive manufacturing of functionally graded

alumina toughened zirconia components intended for medical implant application, J Eur Ceram Soc. 39 (2019) 522–530. https://doi.org/10.1016/j.jeurceramsoc.2018.09.003.
[328] C. Santos, L.H.P. Teixeira, J.K.M.F. Daguano, S.O. Rogero, K. Strecker, C.N. Elias, Mechanical properties and cytotoxicity of 3Y-TZP bioceramics reinforced with Al_2O_3 particles, Ceram Int. 35 (2009) 709–718. https://doi.org/10.1016/j.ceramint.2008.02.004.
[329] A. Nevarez-Rascon, A. Aguilar-Elguezabal, E. Orrantia, M.H. Bocanegra-Bernal, Compressive strength, hardness and fracture toughness of Al_2O_3 whiskers reinforced ZTA and ATZ nanocomposites: Weibull analysis, Int J Refract Metals Hard Mater. 29 (2011) 333–340. https://doi.org/10.1016/j.ijrmhm.2010.12.008.
[330] William.S. Janna, Introduction to Fluid Mechanics, 4th ed., CRC Press, Boston, 2010.
[331] S.S. Hossain, K. Lu, Recent progress of alumina ceramics by direct ink writing: Ink design, printing and post-processing, Ceram Int. 49 (2023) 10199–10212. https://doi.org/10.1016/j.ceramint.2023.01.143.
[332] J. Qiu, J. Tani, N. Yanada, Y. Kobayashi, H. Takahashi, Fabrication of Pb(Nb,Ni)O3-Pb(Zr,Ti)O3 Piezoelectric Ceramic Fibers by Extrusion of a Sol-Powder Mixture, J Intell Mater Syst Struct. 15 (2004) 643–653. https://doi.org/10.1177/1045389X04043949.
[333] J. Hlosta, D. Žurovec, L. Jezerská, J. Neas, Effect of particle shape and size on the compressibility and bulk properties of powders in powder metallurgy, in: n.d.
[334] M. Faes, J. Vleugels, F. Vogeler, E. Ferraris, Extrusion-based additive manufacturing of ZrO2 using photoinitiated polymerization, CIRP J Manuf Sci Technol. 14 (2016) 28–34. https://doi.org/10.1016/j.cirpj.2016.05.002.
[335] I.M. Krieger, T.J. Dougherty, A Mechanism for Non-Newtonian Flow in Suspensions of Rigid Spheres, Transactions of the Society of Rheology. 3 (1959) 137–152. https://doi.org/10.1122/1.548848.
[336] R.L. Walton, M.A. Fanton, R.J. Meyer, G.L. Messing, Dispersion and rheology for direct writing lead-based piezoelectric ceramic pastes with anisotropic template particles, Journal of the American Ceramic Society. 103 (2020) 6157–6168. https://doi.org/10.1111/jace.17350.
[337] S.S. Hossain, H.J. Son, S. Park, C.J. Bae, Extrusion-based 3D printing alumina-silica inks: Adjusting rheology and sinterability incorporating waste derived nanoparticles, J Eur Ceram Soc. (2023). https://doi.org/10.1016/j.jeurceramsoc.2023.03.068.
[338] S. Eqtesadi, A. Motealleh, F.H. Perera, P. Miranda, A. Pajares, R. Wendelbo, F. Guiberteau, A.L. Ortiz, Fabricating geometrically-complex B4C ceramic components by robocasting and pressureless spark plasma sintering, Scr Mater. 145 (2018) 14–18. https://doi.org/10.1016/j.scriptamat.2017.10.001.
[339] A. Schwab, R. Levato, M. D'Este, S. Piluso, D. Eglin, J. Malda, Printability and Shape Fidelity of Bioinks in 3D Bioprinting, Chem Rev. 120 (2020) 11028–11055. https://doi.org/10.1021/acs.chemrev.0c00084.
[340] K. Huang, H. Elsayed, G. Franchin, P. Colombo, Embedded direct ink writing of freeform ceramic components, Appl Mater Today. 23 (2021) 101005. https://doi.org/10.1016/j.apmt.2021.101005.
[341] J.A. Lewis, Direct ink writing of 3D functional materials, Adv Funct Mater. 16 (2006) 2193–2204. https://doi.org/10.1002/adfm.200600434.
[342] S.S.L. Chan, R.M. Pennings, L. Edwards, G. V. Franks, 3D printing of clay for decorative architectural applications: Effect of solids volume fraction on rheology and printability, Addit Manuf. 35 (2020). https://doi.org/10.1016/j.addma.2020.101335.
[343] S. Naghieh, X. Chen, Printability–A key issue in extrusion-based bioprinting, J Pharm Anal. 11 (2021) 564–579. https://doi.org/10.1016/j.jpha.2021.02.001.

[344] A. Corker, H.C.H. Ng, R.J. Poole, E. García-Tuñón, 3D printing with 2D colloids: Designing rheology protocols to predict "printability" of soft-materials, Soft Matter. 15 (2019) 1444–1456. https://doi.org/10.1039/c8sm01936c.
[345] M. Maillard, J. Chevalier, L. Gremillard, G.P. Baeza, E.J. Courtial, S. Marion, V. Garnier, Optimization of mechanical properties of robocast alumina parts through control of the paste rheology, J Eur Ceram Soc. 43 (2023) 2805–2817. https://doi.org/10.1016/j.jeurceramsoc.2022.12.008.
[346] Z. Lu, Y. Xia, K. Miao, S. Li, L. Zhu, H. Nan, J. Cao, D. Li, Microstructure control of highly oriented short carbon fibres in SiC matrix composites fabricated by direct ink writing, Ceram Int. 45 (2019) 17262–17267. https://doi.org/10.1016/j.ceramint.2019.05.283.
[347] Y.Y. Li, B. Li, J.B. Sun, K.P. Cai, J. Zhou, L.T. Li, Direct Write Assembly of 3-Dimensional Structures with Aqueous-Based Piezoelectric Inks, Key Eng Mater. 512–515 (2012) 390–394. https://doi.org/10.4028/www.scientific.net/KEM.512-515.390.
[348] C.M. Larson, J.J. Choi, P.A. Gallardo, S.W. Henderson, M.D. Niemack, G. Rajagopalan, R.F. Shepherd, Direct Ink Writing of Silicon Carbide for Microwave Optics, Adv Eng Mater. 18 (2016) 39–45. https://doi.org/10.1002/adem.201500298.
[349] T. Schlordt, F. Keppner, N. Travitzky, P. Greil, Robocasting of alumina lattice truss structures, Journal of Ceramic Science and Technology. 3 (2012) 81–88. https://doi.org/10.4416/JCST2012-00003.
[350] T. An, K.-T. Hwang, J.-H. Kim, J. Kim, Extrusion-based 3D direct ink writing of NiZn-ferrite structures with viscoelastic ceramic suspension, Ceram Int. 46 (2020) 6469–6476. https://doi.org/10.1016/j.ceramint.2019.11.127.
[351] W.J. Costakis, L.M. Rueschhoff, A.I. Diaz-Cano, J.P. Youngblood, R.W. Trice, Additive manufacturing of boron carbide via continuous filament direct ink writing of aqueous ceramic suspensions, J Eur Ceram Soc. 36 (2016) 3249–3256. https://doi.org/10.1016/j.jeurceramsoc.2016.06.002.
[352] J.E. Smay, S.S. Nadkarni, J. Xu, Direct Writing of Dielectric Ceramics and Base Metal Electrodes, Int J Appl Ceram Technol. 4 (2007) 47–52. https://doi.org/10.1111/j.1744-7402.2007.02118.x.
[353] Q. Sun, Z. Yang, H. Cheng, Y. Peng, Y. Huang, M. Chen, Creation of three-dimensional structures by direct ink writing with kaolin suspensions, J Mater Chem C Mater. 6 (2018) 11392–11400. https://doi.org/10.1039/c8tc03152e.
[354] Q. Sun, Y. Peng, H. Cheng, Y. Mou, Z. Yang, D. Liang, M. Chen, Direct ink writing of 3D cavities for direct plated copper ceramic substrates with kaolin suspensions, Ceram Int. 45 (2019) 12535–12543. https://doi.org/10.1016/j.ceramint.2019.03.191.
[355] Y.-Y. Li, L.-T. Li, B. Li, Direct ink writing of 3-3 piezoelectric composite, J Alloys Compd. 620 (2015) 125–128. https://doi.org/10.1016/j.jallcom.2014.09.124.
[356] Y. Chen, Y. Wang, Q. Yang, Y. Liao, B. Zhu, G. Zhao, R. Shen, X. Lu, S. Qu, A novel thixotropic magnesium phosphate-based bioink with excellent printability for application in 3D printing, J Mater Chem B. 6 (2018) 4502–4513. https://doi.org/10.1039/C8TB01196F.
[357] H. Elsayed, A. Chmielarz, M. Potoczek, T. Fey, P. Colombo, Direct ink writing of three dimensional Ti2AlC porous structures, Addit Manuf. 28 (2019) 365–372. https://doi.org/10.1016/j.addma.2019.05.018.
[358] H. Jin, D. Jia, Z. Yang, Y. Zhou, Direct ink writing of Si2N2O porous ceramic strengthened by directional β-Si3N4 grains, Ceram Int. 46 (2020) 15709–15713. https://doi.org/10.1016/j.ceramint.2020.03.077.

[359] X. Lu, Y. Lee, S. Yang, Y. Hao, J.R.G. Evans, C.G. Parini, Solvent-based paste extrusion solid freeforming, J Eur Ceram Soc. 30 (2010) 1–10. https://doi.org/10.1016/j.jeurceramsoc.2009.07.019.
[360] D. Brazete, A.S. Neto, J.M.F. Ferreira, Optimization of zirconia inks to fabricate 3D porous scaffolds by robocasting, Lekar a Technika. 49 (2019) 5–10. https://doi.org/10.14311/CTJ.2019.1.
[361] Y. Sun, C. Peng, X. Wang, R. Wang, J. Yang, D. Zhang, Rheological behavior of Al2O3 suspensions containing polyelectrolyte complexes for direct ink writing, Powder Technol. 320 (2017) 223–229. https://doi.org/10.1016/j.powtec.2017.07.049.
[362] P. Diloksumpan, M. de Ruijter, M. Castilho, U. Gbureck, T. Vermonden, P.R. van Weeren, J. Malda, R. Levato, Combining multi-scale 3D printing technologies to engineer reinforced hydrogel-ceramic interfaces, Biofabrication. 12 (2020) 025014. https://doi.org/10.1088/1758-5090/ab69d9.
[363] B. Nan, F.J. Galindo-Rosales, J.M.F. Ferreira, 3D printing vertically: Direct ink writing free-standing pillar arrays, Materials Today. 35 (2020) 16–24. https://doi.org/10.1016/j.mattod.2020.01.003.
[364] S.S.L. Chan, R.M. Pennings, L. Edwards, G. V. Franks, 3D printing of clay for decorative architectural applications: Effect of solids volume fraction on rheology and printability, Addit Manuf. 35 (2020) 101335. https://doi.org/10.1016/j.addma.2020.101335.
[365] J.A. Lewis, Colloidal processing of ceramics, Journal of the American Ceramic Society. 83 (2000) 2341–2359. https://doi.org/10.1111/j.1151-2916.2000.tb01560.x.
[366] E. Feilden, F. Giuliani, L. Vandeperre, E. Saiz, Additive Manufacturing of Ceramics and Ceramic Composites via Robocasting, 2017.
[367] J. Chevalier, L. Gremillard, A. V. Virkar, D.R. Clarke, The tetragonal-monoclinic transformation in zirconia: Lessons learned and future trends, Journal of the American Ceramic Society. 92 (2009) 1901–1920. https://doi.org/10.1111/j.1551-2916.2009.03278.x.
[368] J. Chevalier, L. Gremillard, Ceramics for medical applications: A picture for the next 20 years, J Eur Ceram Soc. 29 (2009) 1245–1255. https://doi.org/10.1016/j.jeurceramsoc.2008.08.025.
[369] R.C. Garvie, R.H. Hannink, R.T. Pascoe, Ceramic steel?, Nature. 258 (1975) 703–704. https://doi.org/10.1038/258703a0.
[370] G. Rauchs, T. Fett, D. Munz, R. Oberacker, Tetragonal-to-monoclinic phase transformation in CeO2-stabilized zirconia under uniaxial loading, J Eur Ceram Soc. 21 (2001) 2229–41.
[371] R.A. Cutler, J.M. Lindemann, J.H. Ulvensøen, H.I. Lange, Damage-resistant SrO-doped Ce-TZP/Al2O3 composites, Mater Des. 15 (1994) 123–133. https://doi.org/10.1016/0261-3069(94)90111-2.
[372] R.A. Cutler, R.J. Mayhew, K.M. Prettyman, A. V. Virkar, High-Toughness Ce-TZP/Al2O3 Ceramics with Improved Hardness and Strength, Journal of the American Ceramic Society. 74 (1991) 179–186. https://doi.org/10.1111/j.1151-2916.1991.tb07315.x.
[373] R.H.J. Hannnink, M. V. Swain, Metastability of the Martensitic Transformation in a 12 mol% Ceria-Zirconia Alloy: I, Deformation and Fracture Observations, Journal of the American Ceramic Society. 72 (1989) 90–98. https://doi.org/10.1111/j.1151-2916.1989.tb05959.x.
[374] P. Palmero, M. Fornabaio, L. Montanaro, H. Reveron, C. Esnouf, J. Chevalier, Towards long lasting zirconia-based composites for dental implants. Part I: Innovative synthesis,

microstructural characterization and in vitro stability, Biomaterials. 50 (2015) 38–46. https://doi.org/10.1016/j.biomaterials.2015.01.018.

[375] M. Fornabaio, P. Palmero, R. Traverso, C. Esnouf, H. Reveron, J. Chevalier, L. Montanaro, Zirconia-based composites for biomedical applications: Role of second phases on composition, microstructure and zirconia transformability, J Eur Ceram Soc. 35 (2015) 4039–4049. https://doi.org/10.1016/j.jeurceramsoc.2015.04.027.

[376] J.-F. Tsai, C.-S. Yu, D.K. Shetty, Fatigue Crack Propagation in Ceria-Partially-Stabilized Zirconia (Ce-TZP)-Alumina Composites, Journal of the American Ceramic Society. 73 (1990) 2992–3001. https://doi.org/10.1111/j.1151-2916.1990.tb06706.x.

[377] C.-S. Yu, D.K. Shetty, M.C. Shaw, D.B. Marshall, Transformation Zone Shape Effects on Crack Shielding in Ceria-Partially-Stabilized Zirconia (Ce-TZP)-Alumina Composites, Journal of the American Ceramic Society. 75 (1992) 2991–2994. https://doi.org/10.1111/j.1151-2916.1992.tb04376.x.

[378] H.K. Schmid, R. Pennefather, S. Meriani, C. Schmid, Redistribution of Ce and La during processing of Ce(La)-TZP/Al2O3 composites, J Eur Ceram Soc. 10 (1992) 381–392. https://doi.org/10.1016/0955-2219(92)90012-3.

[379] M. Nawa, S. Nakamoto, T. Sekino, K. Niihara, Tough and strong Ce-TZP/Alumina nanocomposites doped with titania, Ceram Int. 24 (1998) 497–506. https://doi.org/10.1016/S0272-8842(97)00048-5.

[380] J. -F Tsai, U. Chon, N. Ramachandran, D.K. Shetty, Transformation Plasticity and Toughening in CeO2-Partially-Stabilized Zirconia–Alumina (Ce-TZP/Al2O3) Composites Doped with MnO, Journal of the American Ceramic Society. 75 (1992) 1229–1238. https://doi.org/10.1111/j.1151-2916.1992.tb05562.x.

[381] S. Maschio, G. Pezzotti, O. Sbaizero, Effect of LaNbO4 addition on the mechanical properties of ceria-tetragonal zirconia polycrystal matrices, J Eur Ceram Soc. 18 (1998) 1779–1785. https://doi.org/10.1016/S0955-2219(98)00104-6.

[382] M. Miura, H. Hongoh, T. Yogo, S. Hirano, T. Fujll, Formation of plate-like lanthanum-β-Aluminate crystal in Ce-TZP matrix, J Mater Sci. 29 (1994) 262–268. https://doi.org/10.1007/BF00356602.

[383] S. Ori, T. Kojima, T. Hara, N. Uekawa, K. Kakegawa, Fabrication of Ce-TZP/Ba hexaaluminate composites using amorphous precursor of the second phase, Journal of the Ceramic Society of Japan. 120 (2012) 111–115. https://doi.org/10.2109/jcersj2.120.111.

[384] T. Yamaguchi, W. Sakamoto, T. Yogo, T. Fujii, S.-I. Hirano, In Situ Formation of Ce-TZP/Ba Hexaaluminate Composites, Journal of the Ceramic Society of Japan. 107 (1999) 814–819.

[385] H. Reveron, M. Fornabaio, P. Palmero, T. Fürderer, E. Adolfsson, V. Lughi, A. Bonifacio, V. Sergo, L. Montanaro, J. Chevalier, Towards long lasting zirconia-based composites for dental implants: Transformation induced plasticity and its consequence on ceramic reliability, Acta Biomater. 48 (2017) 423–432. https://doi.org/10.1016/j.actbio.2016.11.040.

[386] J.J. Beaman, D.L. Bourell, C.C. Seepersad, D. Kovar, Additive Manufacturing Review: Early Past to Current Practice, J Manuf Sci Eng. 142 (2020). https://doi.org/10.1115/1.4048193.

[387] M. Bhuvanesh Kumar, P. Sathiya, Methods and materials for additive manufacturing: A critical review on advancements and challenges, Thin-Walled Structures. 159 (2021) 107228. https://doi.org/10.1016/j.tws.2020.107228.

[388] Z. Chen, Z. Li, J. Li, C. Liu, C. Lao, Y. Fu, C. Liu, Y. Li, P. Wang, Y. He, 3D printing of ceramics: A review, J Eur Ceram Soc. 39 (2019) 661–687. https://doi.org/10.1016/j.jeurceramsoc.2018.11.013.

[389] Z. Chen, X. Sun, Y. Shang, K. Xiong, Z. Xu, R. Guo, S. Cai, C. Zheng, Dense ceramics with complex shape fabricated by 3D printing: A review, Journal of Advanced Ceramics. 10 (2021) 195–218. https://doi.org/10.1007/s40145-020-0444-z.
[390] Y. Lakhdar, C. Tuck, J. Binner, A. Terry, R. Goodridge, Additive manufacturing of advanced ceramic materials, Prog Mater Sci. 116 (2021) 100736. https://doi.org/10.1016/j.pmatsci.2020.100736.
[391] P. Morgan, Carbon Fibers and Their Composites, CRC Press, 2005. https://doi.org/10.1201/9781420028744.
[392] N. Yazdani, E. Brown, Carbon nanofibers in cement composites, in: Innovative Developments of Advanced Multifunctional Nanocomposites in Civil and Structural Engineering, Elsevier, 2016: pp. 47–58. https://doi.org/10.1016/B978-1-78242-326-3.00003-8.
[393] Y. Zhou, S. Jeelani, T. Lacy, Experimental study on the mechanical behavior of carbon/epoxy composites with a carbon nanofiber-modified matrix, J Compos Mater. 48 (2014) 3659–3672. https://doi.org/10.1177/0021998313512348.
[394] S. Maensiri, P. Laokul, J. Klinkaewnarong, V. Amornkitbamrung, Carbon nanofiber-reinforced alumina nanocomposites: Fabrication and mechanical properties, Materials Science and Engineering: A. 447 (2007) 44–50. https://doi.org/10.1016/j.msea.2006.08.009.
[395] A. Sayam, A.N.M.M. Rahman, Md.S. Rahman, S.A. Smriti, F. Ahmed, Md.F. Rabbi, M. Hossain, Md.O. Faruque, A review on carbon fiber-reinforced hierarchical composites: mechanical performance, manufacturing process, structural applications and allied challenges, Carbon Letters. 32 (2022) 1173–1205. https://doi.org/10.1007/s42823-022-00358-2.
[396] J.P. Lewicki, J.N. Rodriguez, C. Zhu, M.A. Worsley, A.S. Wu, Y. Kanarska, J.D. Horn, E.B. Duoss, J.M. Ortega, W. Elmer, R. Hensleigh, R.A. Fellini, M.J. King, 3D-Printing of Meso-structurally Ordered Carbon Fiber/Polymer Composites with Unprecedented Orthotropic Physical Properties, Sci Rep. 7 (2017). https://doi.org/10.1038/srep43401.
[397] F. Folgar, C.L. Tucker, Orientation Behavior of Fibers in Concentrated Suspensions, Journal of Reinforced Plastics and Composites. 3 (1984) 98–119. https://doi.org/10.1177/073168448400300201.
[398] Z. Fu, M. Freihart, L. Wahl, T. Fey, P. Greil, N. Travitzky, Micro- and macroscopic design of alumina ceramics by robocasting, J Eur Ceram Soc. 37 (2017) 3115–3124. https://doi.org/10.1016/j.jeurceramsoc.2017.03.052.
[399] J.P. Lewicki, J.N. Rodriguez, C. Zhu, M.A. Worsley, A.S. Wu, Y. Kanarska, J.D. Horn, E.B. Duoss, J.M. Ortega, W. Elmer, R. Hensleigh, R.A. Fellini, M.J. King, 3D-Printing of Meso-structurally Ordered Carbon Fiber/Polymer Composites with Unprecedented Orthotropic Physical Properties, Sci Rep. 7 (2017) 43401. https://doi.org/10.1038/srep43401.
[400] P. Huang, Z. Xia, S. Cui, 3D printing of carbon fiber-filled conductive silicon rubber, Mater Des. 142 (2018) 11–21. https://doi.org/10.1016/j.matdes.2017.12.051.
[401] S. Kumar, T. Rath, R.N. Mahaling, C.K. Das, Processing and characterization of carbon nanofiber/syndiotactic polystyrene composites in the absence and presence of liquid crystalline polymer, Compos Part A Appl Sci Manuf. 38 (2007) 1304–1317. https://doi.org/10.1016/j.compositesa.2006.11.006.
[402] J. Dusza, G. Blugan, J. Morgiel, J. Kuebler, F. Inam, T. Peijs, M.J. Reece, V. Puchy, Hot pressed and spark plasma sintered zirconia/carbon nanofiber composites, J Eur Ceram Soc. 29 (2009) 3177–3184. https://doi.org/10.1016/j.jeurceramsoc.2009.05.030.

[403] Q. Dou, A. Abdul Karim, X. Loh, Modification of Thermal and Mechanical Properties of PEG-PPG-PEG Copolymer (F127) with MA-POSS, Polymers (Basel). 8 (2016) 341. https://doi.org/10.3390/polym8090341.
[404] J.A. Griggs, Y. Zhang, Determining the confidence intervals of Weibull parameters estimated using a more precise probability estimator, n.d.
[405] W.D. Scott, Deformation Twinning in Ceramics, in: Deformation of Ceramic Materials II, Springer US, Boston, MA, 1984: pp. 235–249. https://doi.org/10.1007/978-1-4615-6802-5_17.
[406] T.J. Hensen, T.G. Aguirre, C.L. Cramer, A.S. Wand, K. Ma, D.A. Prawel, J.D. Williams, T.B. Holland, Additive manufacturing of ceramic nanopowder by direct coagulation printing, Addit Manuf. 23 (2018) 140–150. https://doi.org/10.1016/j.addma.2018.07.010.
[407] Z. Goharibajestani, O. Akhlaghi, C. Akaoglu, F. Afghah, N. Khani, A. Hodaei, B. Koc, O. Akbulut, Incorporating Steric Hindrance into the Additive Design Enables a Robust Formulation of Alumina Ink for Extrusion-based 3D Printing, ACS Appl Polym Mater. 1 (2019) 3279–3285. https://doi.org/10.1021/acsapm.9b00704.
[408] Y. Yang, D. Cai, Z. Yang, X. Duan, P. He, D. Jia, Y. Zhou, Rheology of organics-free aqueous ceramic suspensions for additive manufacturing of dense silicon nitride ceramics, Ceram Int. 48 (2022) 31941–31951. https://doi.org/10.1016/j.ceramint.2022.07.130.
[409] K.K. Kar, Composite materials: Processing, applications, characterizations, Composite Materials: Processing, Applications, Characterizations. (2016) 1–686. https://doi.org/10.1007/978-3-662-49514-8.
[410] F. Ye, L. Liu, Y. Wang, Y. Zhou, B. Peng, Q. Meng, Preparation and mechanical properties of carbon nanotube reinforced barium aluminosilicate glass–ceramic composites, Scr Mater. 55 (2006) 911–914. https://doi.org/10.1016/j.scriptamat.2006.07.045.
[411] C. Balázsi, B. Fényi, N. Hegman, Z. Kövér, F. Wéber, Z. Vértesy, Z. Kónya, I. Kiricsi, L.P. Biró, P. Arató, Development of CNT/Si3N4 composites with improved mechanical and electrical properties, Compos B Eng. 37 (2006) 418–424. https://doi.org/10.1016/j.compositesb.2006.02.006.
[412] J. Sun, L. Gao, X. Jin, Reinforcement of alumina matrix with multi-walled carbon nanotubes, Ceram Int. 31 (2005) 893–896. https://doi.org/10.1016/j.ceramint.2004.10.002.
[413] J. Sun, L. Gao, W. Li, Colloidal processing of carbon nanotube/alumina composites, Chemistry of Materials. 14 (2002) 5169–5172. https://doi.org/10.1021/cm020736q.
[414] N. Garmendia, I. Santacruz, R. Moreno, I. Obieta, Slip casting of nanozirconia/MWCNT composites using a heterocoagulation process, J Eur Ceram Soc. 29 (2009) 1939–1945. https://doi.org/10.1016/j.jeurceramsoc.2008.12.014.
[415] S. Maensiri, P. Laokul, J. Klinkaewnarong, V. Amornkitbamrung, Carbon nanofiber-reinforced alumina nanocomposites: Fabrication and mechanical properties, Materials Science and Engineering: A. 447 (2007) 44–50. https://doi.org/10.1016/j.msea.2006.08.009.
[416] Cs. Balázsi, F. Wéber, Zs. Kövér, Z. Shen, Z. Kónya, Zs. Kasztovszky, Z. Vértesy, L.P. Biró, I. Kiricsi, P. Arató, Application of carbon nanotubes to silicon nitride matrix reinforcements, Current Applied Physics. 6 (2006) 124–130. https://doi.org/10.1016/j.cap.2005.07.024.
[417] G.B. Jeffery, P.R.S.L. A, The motion of ellipsoidal particles immersed in a viscous fluid, Proceedings of the Royal Society of London. Series A, Containing Papers of a

Mathematical and Physical Character. 102 (1922) 161–179. https://doi.org/10.1098/rspa.1922.0078.
[418] J.-P. Fan, D.-M. Zhuang, D.-Q. Zhao, G. Zhang, M.-S. Wu, F. Wei, Z.-J. Fan, Toughening and reinforcing alumina matrix composite with single-wall carbon nanotubes, Appl Phys Lett. 89 (2006) 121910. https://doi.org/10.1063/1.2336623.
[419] A. Duszová, J. Dusza, K. Tomášek, G. Blugan, J. Kuebler, Microstructure and properties of carbon nanotube/zirconia composite, J Eur Ceram Soc. 28 (2008) 1023–1027. https://doi.org/10.1016/j.jeurceramsoc.2007.09.011.
[420] J. Sun, M. Iwasa, T. Nakayama, Þ.K. Niihara, L.G.A.O. Þ, X.J.I.N. Þ, Pressureless Sintering of Alumina Carbon Nanotubes Composites in Air Atmosphere Furnace and Their Mechanical Properties, 406 (2004) 403–406.
[421] L. Gremillard, J. Chevalier, T. Epicier, G. Fantozzi, Improving the Durability of a Biomedical-Grade Zirconia Ceramic by the Addition of Silica, Journal of the American Ceramic Society. 85 (2002) 401–7.
[422] A. Duszová, J. Dusza, K. Tomášek, J. Morgiel, G. Blugan, J. Kuebler, Zirconia/carbon nanofiber composite, Scr Mater. 58 (2008) 520–523. https://doi.org/10.1016/j.scriptamat.2007.11.002.
[423] M. Mazaheri, D. Mari, R. Schaller, G. Bonnefont, G. Fantozzi, Processing of yttria stabilized zirconia reinforced with multi-walled carbon nanotubes with attractive mechanical properties, J Eur Ceram Soc. 31 (2011) 2691–2698. https://doi.org/10.1016/j.jeurceramsoc.2010.11.009.
[424] B. Milsom, G. Viola, Z. Gao, F. Inam, T. Peijs, M.J. Reece, The effect of carbon nanotubes on the sintering behaviour of zirconia, J Eur Ceram Soc. 32 (2012) 4149–4156. https://doi.org/10.1016/j.jeurceramsoc.2012.07.028.
[425] K.-H. Zum Gahr, W. Bundschuh, B. Zimmerlin, Effect of grain size on friction and sliding wear of oxide ceramics, Wear. 162–164 (1993) 269–279. https://doi.org/10.1016/0043-1648(93)90509-K.
[426] K. Tsukuma, Strength, fracture toughness and Vickers hardness of CeO2-stabilized tetragonal Zr02 polycrystals (Ce-TZP), J Mater Sci. 20 (1985) 1178–1184.
[427] K. Tanaka, J. Tamura, K. Kawanabe, M. Nawa, M. Oka, M. Uchida, T. Kokubo, T. Nakamura, Ce-TZP/Al2O3 nanocomposite as a bearing material in total joint replacement, J Biomed Mater Res. 63 (2002) 262–270. https://doi.org/10.1002/jbm.10182.
[428] J.-F. Tsai, U. Chon, N. Ramachandran, D.K. Shetty, Transformation Plasticity and Toughening in CeO2-Partially-Stabilized Zirconia-Alumina (Ce-TZP/Al2O3) Composites Doped with MnO, Journal of the American Ceramic Society. 75 (1992) 1229–1238. https://doi.org/10.1111/j.1151-2916.1992.tb05562.x.
[429] T. Yu, X. Zhu, H. Yu, P. Wu, C. Li, X. Han, M. Chen, Material extrusion-based additive manufacturing of zirconia toughened alumina: Machinability, mechanical properties and biocompatibility, J Manuf Process. 94 (2023) 120–132. https://doi.org/10.1016/j.jmapro.2023.03.052.
[430] S. Begand, T. Oberbach, W. Glien, Investigations of the Mechanical Properties of an Alumina Toughened Zirconia Ceramic for an Application in Joint Prostheses, Key Eng Mater. 284–286 (2005) 1019–1022. https://doi.org/10.4028/www.scientific.net/KEM.284-286.1019.
[431] N.R.M. Lévaro, M.F.R.P. Alves, C. Santos, V. Sencadas, S. Olhero, Direct ink writing of ATZ composites based on inks prepared by colloidal or hydrogel route: Linking inks rheology with mechanical properties, Colloids Surf A Physicochem Eng Asp. 668 (2023) 131426. https://doi.org/10.1016/j.colsurfa.2023.131426.

[432] R. Benzaid, J. Chevalier, M. Saâdaoui, G. Fantozzi, M. Nawa, L.A. Diaz, R. Torrecillas, Fracture toughness, strength and slow crack growth in a ceria stabilized zirconia-alumina nanocomposite for medical applications, Biomaterials. 29 (2008) 3636–3641. https://doi.org/10.1016/j.biomaterials.2008.05.021.

[433] M. Nawa, N. Kurizoe, Y. Okamoto, A. Ueno, Transformation-induced plastic deformation in Ce-TZP/alumina nanocomposite generated during fatigue tests at room temperature, J Eur Ceram Soc. 34 (2014) 4337–4345. https://doi.org/10.1016/j.jeurceramsoc.2014.06.025.

[434] W. Weibull, A Statistical Theory of the Strength of Materials, Generalstabens Litografiska Anstalts Förlag, Stockholm, 1939.

ANNEX A – Supplementary material

Fig. A 1. Photo of a 1 cm printed cube with the paste 30S2 (30 vol% of solid content and 2.0 wt% of CNFs) with the 410 µm nozzle diameter. To maximize the density, the starting point for each layer was deliberately dislocated by half the diameter of the nozzle to place the filaments of the upper layer in the middle of the filaments of the lower layer. It is noticeable the paste's ability to support the weight of subsequent layers.

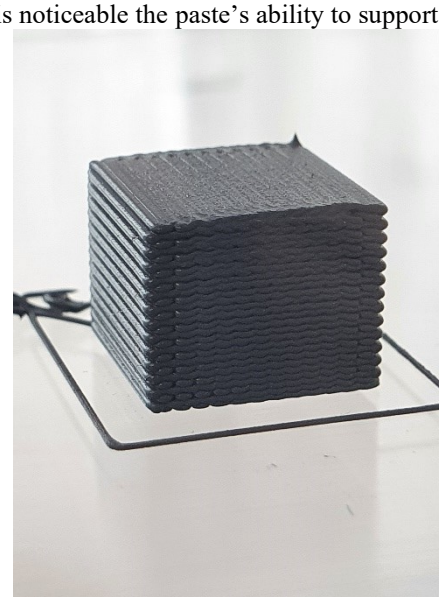

Source: Author.